Autophagy regulator ATG5 maintains cerebellar function by preventing excessive glycolytic activity

Inaugural-Dissertation

zur

Erlangung des Doktorgrades

der Mathematisch-Naturwissenschaftlichen Fakultät

der Universität zu Köln

vorgelegt von

Janine Tutas

aus Leverkusen, Deutschland

Köln, 2023

1. Gutachterin: Prof. Dr. Natalia Kononenko

2. Gutachter: Prof. Dr. Ansgar Büschges

Tag der mündlichen Prüfung: 26.02.2024

Table of contents

Abbreviations **1**

Summary **4**

Zusammenfassung **5**

I. Introduction **6**

1. Autophagy 6
   1.1 Physiological role of autophagy 6
   1.2 The autophagic process 7
      1.2.1 Initiation of the phagophore formation 8
      1.2.2 Nucleation 9
      1.2.3 Phagophore expansion and autophagosome maturation 9
      1.2.4 Fusion of the autophagosome with the lysosome 10
   1.3 Autophagy in the central nervous system 11
   1.4 Selective autophagy 12
      1.4.1 Mitophagy 13
      1.4.2 ER-phagy 14
      1.4.3 Aggrephagy 14
   1.5 Autophagy and neurodegeneration 15
      1.5.1 Alzheimer's disease (AD) 16
      1.5.2 Parkinson's disease (PD) 16
      1.5.3 Amyotrophic lateral sclerosis (ALS) 17
      1.5.4 Huntington's disease (HD) 17

2. Metabolism 18
   2.1 Brain energy metabolism 18
   2.2 Blood brain barrier and metabolite transporters 18
   2.3 Glucose transporters (*SLC2*) in the brain 20
      2.3.1 GLUT1 (SLC2A1) 20
      2.3.2 GLUT2 (SLC2A2) 20
      2.3.3 GLUT3 (SLC2A3) 21
      2.3.4 GLUT4 (SLC2A4) 22
   2.4 Glucose metabolic pathways 22
      2.4.1 Glycolysis 23
      2.4.2 Tricarbyxlic acid (TCA) cycle 25
      2.4.3 Oxidative phosphorylation (OXPHOS) 26
   2.5 Mitochondria 27

2.6 Metabolic regulation ... 28
2.7 Autophagy and metabolism ... 29
2.8 Brain metabolism in diseases ... 30
2.8.1 Metabolism in aging ... 30
2.8.2 Metabolism in neurodegenerative diseases ... 31
3. Cerebellum ... 33
3.1 Anatomy ... 33
3.2 Cerebellar functions ... 35
3.3 Cerebellar dysfunction ... 36
3.3.1 Ataxia ... 36
II. Aims ... 38
III. Material and Methods ... 39
1. Materials ... 39
2. Methods ... 43
2.1 Animals ... 43
2.1.1 Mouse breeding and maintenance ... 43
2.1.2. Conditional gene activation of ATG5 and GLUT2 in GABAergic neurons ... 43
2.2 Genotyping ... 44
2.2.1 Tissue sample and DNA extraction ... 44
2.2.2 PCR and gel electrophoresis ... 44
2.3 Primary cultures ... 46
2.3.1 PDL-coating ... 46
2.3.2 Primary cortical culture ... 46
2.3.3 Primary cerebellar culture ... 47
2.5 Seahorse assay ... 48
2.5.1 Mito Stress test ... 48
2.5.2 Glycolysis Stress Test ... 48
2.4 Cerebellar organotypic slice culture (OTC) ... 49
2.4.1 Viral transduction and live imaging of OTCs ... 50
2.4.1.1 FRET-based imaging ... 50
2.4.1.1.1 Laconic imaging ... 51
2.4.1.1.2 ATeam imaging ... 51
2.4.1.2 GcamP7f$^{CamKII\alpha}$ imaging ... 51
2.4.1.3 2-NBDG uptake ... 51
2.5 Ex vivo acute slices ... 52
2.5.1 Starvation and chloroquine treatment ... 52
2.5.2 Surface biotinylation assay ... 52

2.5.3 Isotope labeling (In collaboration with Patrick Giavalisco, MPI Cologne) 53
2.5.3.1 Semi-targeted liquid chromatography-high-resolution mass spectrometry- based (LC-HRS-MS) analysis of amine-containing metabolites 53
2.5.3.2 Anion-Exchange Chromatography Mass Spectrometry (AEX-MS) for the analysis of anionic metabolites 54
2.6 Animal behavior 56
2.6.1 SIMI Motion 56
2.6.2 Rotarod 56
2.7 Histology methods 56
2.7.1 Perfusion 56
2.7.2 Immunohistochemistry 57
2.7.2.1 Reconstruction and colocalization analysis 58
2.7.3 Cresyl-violet (Nissl) staining 58
2.7.4 Electron microscopy 59
2.8 Immunoblot 59
2.8.1 Tissue preparation and lysis 59
2.8.2 SDS-PAGE and western blot 60
2.9 Multi-omics analysis 61
2.9.1 Metabolomics analysis 61
2.9.1.1 Untargeted metabolomics (in collaboration with AG Frezza, CECAD, Cologne) 61
2.9.1.2 Targeted metabolomics (performed by Susanne Brodesser) 63
2.9.1.2.1 Intermediates of glycolysis and tricarboxylic acid (TCA) cycle 63
2.9.1.2.2 Amino acids and γ- Aminobutyric acid (GABA) 63
2.9.2 Proteomics 64
2.9.2.1 Protein extraction 64
2.9.2.2 Data Acquisition 65
2.9.2.3 Sample Processing in DIA-NN 65
2.10 PET imaging 66
2.10.1 [18F]UCB-H-/[18F]MNI1126-PET 66
2.10.2 [18F]FDG-PET 66
2.10.3 Image reconstruction 67
2.10.4 Image statistics 67
2.11 Stereotactic surgeries into cerebellar lobes IV/V 68
2.12 Statistical analysis 69
IV. Results 70
1. Region-specific vulnerability to autophagy loss 70

1.1 PET imaging reveals region-specific vulnerability to autophagy loss.......................... 70
1.2 Cell type-specific vulnerability of Purkinje cells to autophagy loss.............................. 71
1.3 Loss of autophagy results in region-specific astrogliosis 73
1.4 Loss of autophagy results in region specific changes in AKT/mTORC1 signaling..... 74
1.5 Loss of Purkinje cells does not correlate with accumulation of protein aggregates upon ATG5 deficiency... 77
2. Proteomics analysis reveals metabolic changes in ATG5 deficient cerebellum prior to Purkinje cell loss 80
3. Metabolomic analysis reveals increased glycolytic metabolism in ATG5 cKO cerebellum 82
3.1 Untargeted metabolomics reveals increased glycolysis upon loss of ATG5 82
3.2 Targeted metabolomics reveals global changes in amino acid metabolism in ATG5 cKO cerebellum 83
3.3 Targeted metabolomics reveals increased glycolytic metabolites in ATG5 cKO cerebellum... 85
3.4 Isotope labeling reveals increased glycolytic flux in ATG5 cKO cerebellum 88
4. Purkinje cell loss upon loss of autophagy dysfunction does not correlate with impaired mitochondrial function.. 90
5. ATG5 deficient Purkinje cells display increased glycolysis... 93
5.1 *Ex vivo* ATG5 cKO Purkinje cells display increased glycolysis indicators 93
5.2 Hexokinase II levels are increased in one-month old Purkinje cells........................... 95
6. Loss of ATG5 results in upregulation of GLUT2 in Purkinje cells..................................... 97
6.1 GLUT1 expression is not altered upon the loss of ATG5 in GABAergic neurons 97
6.2 Loss of ATG5 results in upregulation of GLUT2 in Purkinje cells............................... 98
6.3 GLUT3 expression is not altered upon loss the of ATG5 in GABAergic neurons 99
6.4 GLUT4 expression is not altered upon the loss of ATG5 in GABAergic neurons 100
6.5 Loss of ATG5 results in increased levels of GLUT2 in Purkinje cell plasma membrane 102
7. Autophagy regulates cerebellar GLUT2 levels 102
8. Increased cerebellar glycolytic metabolism causes Purkinje cell loss 105
9. Loss of GLUT2 ameliorates ATG5 - deficient caused Purkinje cell loss......................... 108
9.1 Loss of GLUT2 reduced glycolytic capacity of ATG5 cKO Purkinje cells 108
9.2 Loss of GLUT2 ameliorates ataxic phenotype of ATG5 cKO animals 110
9.3 Loss of GLUT2 rescues Purkinje cell loss in cerebellar lobes VIII-X 110

V. Discussion **112**

1. Region-specific vulnerability to autophagy loss 112
2. Metabolic alterations precede Purkinje cell loss in ATG5 cKO cerebellum 113
3. Autophagy regulates GLUT2 levels in Purkinje cell.......... 119

VI. Conclusion.......... **122**

VII. Outlook **122**

VIII. References.......... **124**

IX. Acknowledgements.......... **155**

X. Declaration/ Erklärung.......... **156**

Abbreviations

2-NBDG	2-(N-(7-Nitrobenz-2-Oxa-1,3-Diazol-4-yl)Amino)-2-Desoxyglucose
AAV	Adeno-associated virus
AD	Alzheimer's disease
AGE	Advanced glycation end products
ALS	Amyotrophic lateral sclerosis
AMPA	α-amino-3-hydroxy-5-methyl-4-isoxazolepropionic acid receptor
AMPK	AMP-activated kinase
ATG	Autophagy-related protein/gene
ATP	Adenosine triphosphate
AVs	Autophagic vacuoles
BafA1	Bafilomycin A1
BBB	Blood-brain-barrier
°C	Celsius
CALCOCO2	Nuclear dot protein 52
cKO	Conditional knockout
CMA	Chaperone-mediated autophagy
cntr	Control
CQ	Chloroquine
DKO	Double knockout
DNA	Deoxyribunucleotic acid
ECAR	Extraacidifcation rate
EM	Electronmicroscopy
FBS	Fetal bovine serum
F-1,6-P	Fructose-1,6-bisphophate
F-6-P	Fructose-6-phosphate
FC	Fold change
Fer-1	Ferrostatin
FRET	Förster resonance energy transfer
G-6-P	Glucose-6-phosphate
G-6-PD	Glucose-6-phosphate dehydrogenase
GABA	γ-aminobutyric acid
GFAP	Glial fibrillary acidic protein

GFP	Green fluorescent protein
GO	Gene ontology
GLUT	Glucose transporter
h	hours
HK	Hexokinase
HTT	Huntingtin
HD	Huntington's disease
Hz	Hertz
IHC	Immunohistochemistry
kDa	Kilodalton
KEGG	Kyoto Encyclopedia of Genes and Genomes
KO	Knockout
IRES	internal ribosomal entry site
LC3	Microtubule-associated protein 1 light chain 3
LC3 I	Non-lipidated LC3
LC3 II	Lipidated LC3
LIR	LC3-interacting region
LRRK2	Leucine-rich repeat kinase
LPA	Lysophosphatidic acid
MAPK	Mitogen-activated protein kinase
MG	Methylglyoxal
min	Minutes
mm	Millimeter
MS	Mass spectrometry
mt-CYB	Mitochondrial cytochrome B
mHTT	Mutant huntingtin
mTOR	Mammalian target of rapamycin
mTORC1	Mammalian target of rapamycin complex 1
NADPH	Nicotinamide adenine dinucleotide phosphate hydrogen
NBR1	Next to BRCA1 protein
NDD	Neurodegenerative disease
NDP52	Nuclear domain 10 protein, also termed CALCOCO2
OCR	Oxygen consumption rate
OPTN	Optineurin
OTC	Organotypic slice culture
OXPHOS	Oxidative phosphorylation

p62	Sequestosome 1/SQSTM1
PAS	Phagophore assembly site
PCR	Polymerase chain reaction
PD	Parkinson’s disease
PET	Positron emission tomography
PI3K	Phosphatidylinositol 3-kinase
PI3P	Phosphatidylinositol 3-phosphate
PINK	PTEN-induced kinase
PPP	Pentose-phosphate pathway
pS6	S6 ribosomal protein
P/S	Penicilin Streptomycin
RSL3	nicotinamide adenine dinucleotide phosphate hydrogen
RT	Room temperature
SEM	standard error of the mean
SDS	Sodium dodecyl sulfate
SOD1	Superoxide dismutase 1
TCA	Tricarboxylic acid
WT	Wild-type

Summary

Autophagy is an evolutionary conserved catabolic process that provides nutrients to maintain cellular homeostasis. Under physiological and stress conditions, cytosolic components are sequestered into autophagosomes and ultimately delivered to lysosomes for degradation.

This role of autophagy is critical in neurons because of their postmitotic nature. Autophagy is believed to contribute to neuronal health by eliminating defective proteins and organelles. However, recent studies show that neurons are resistant to autophagy-deficiency in-vivo, with an exception of cerebellar Purkinje cells, which are selectively vulnerable to autophagy loss, compared to forebrain GABAergic neurons. This study aims to understand the cell-type specific vulnerability of Purkinje cells to autophagy loss. The cerebellum of conditional ATG5 knockout (cKO) mice is highly glycolytic, whereas these changes are not observed in ATG5- deficient cortex. These alterations depend on glucose transporter 2 (GLUT2), which is degraded in Purkinje cells by autophagy. Loss of ATG5 results in increased GLUT2 levels, a phenotype that leads to elevated levels of glycolysis-derived metabolites such as lactate, serine and ATP without affecting mitochondrial respiration. Progressive Purkinje cell degeneration in ATG5 cKO animals results in impairment in motor coordination such as motor balance.

Concomitant loss of GLUT2 in ATG5 cKO cerebellum mitigates glycolytic metabolism and ameliorates Purkinje cell loss, resulting in improved motor coordination. This research suggests that the selective vulnerability of Purkinje cells under dysfunctional autophagy conditions stems from a metabolic shift towards glycolysis induced by elevated GLUT2 expression. The detrimental effects of excessive glycolysis on Purkinje cells highlight the significance of maintaining low glycolytic activity, offering a potential avenue to extend their survival even in the absence of functional autophagy.

Zusammenfassung

Autophagie ist ein evolutionär konservierter katabolischer Prozess, der Nährstoffe zur Aufrechterhaltung der zellulären Homöostase liefert. Unter physiologischen und stressinduzierten Bedingungen werden zytosolische Komponenten in Autophagosomen gesammelt und anschließend in Lysosomen abgebaut. Diese Rolle der Autophagie ist in Neuronen aufgrund ihrer postmitotischen Natur von entscheidender Bedeutung. Es wird angenommen, dass Autophagie zur neuronalen Gesundheit beiträgt, indem sie defekte Proteine und Organellen eliminiert. Jüngste Studien zeigen, dass Neuronen in vivo resistent gegen Autophagiemangel sind, mit Ausnahme von Purkinjezellen im Kleinhirn, die im Vergleich zu GABAergen Neuronen im Vorderhirn selektiv anfällig für Autophagieverlust sind. Diese Studie versucht, die zelltypspezifische Anfälligkeit für Autophagieverlust in Purkinjezellen zu verstehen. Dabei wird gezeigt, dass das Kleinhirn von ATG5 cKO Mäusen stark glykolytisch ist, wohingegen diese Veränderungen im ATG5 cKO Kortex nicht beobachtet werden. Diese Veränderungen hängen vom Glukosetransporter 2 (GLUT2) ab, der in Purkinjezellen durch Autophagie abgebaut wird. Der Verlust von ATG5 führt zu erhöhten GLUT2-Leveln, was zu erhöhter Menge von Glykolyse-stammender Metabolite wie Laktat, Serin und ATP führt, ohne die Mitochondrienatmung zu beeinträchtigen. Die fortschreitende Degeneration von Purkinjezellen bei ATG5 cKO Tieren führt zu einer Beeinträchtigung der motorischen Koordination, wie des motorischen Gleichgewichts.

Der gleichzeitige Verlust von GLUT2 im ATG5 cKO Kleinhirn reduziert den glykolytischen Stoffwechsel. Darüber hinaus zeigen diese Mäuse weniger Verlust von Purkinjezellen und eine verbesserte motorische Koordination. Insgesamt weist diese Studie darauf hin, dass die Anfälligkeit der Purkinjezellen durch eine metabolische Umstellung auf Glykolyse verursacht wird, die durch erhöhte Level von GLUT2 unter autophagiedefizienten Bedingungen bedingt ist.

I. Introduction

1. Autophagy

1.1 Physiological role of autophagy

Autophagy is an evolutionary conserved catabolic process that provides nutrients to maintain cellular homeostasis. Under physiological and stress conditions, cytosolic components such as organelles or proteins are sequestered in autophagosomes and ultimately delivered to lysosomes for degradation. This cargo is then degraded into monomers, such as amino acids, that are then re-used to maintain cellular metabolism and cellular homeostasis (Lamb, Yoshimori, & Tooze 2013). Autophagy is essential for several physiological processes such as development, differentiation, tumorigenesis, immunity, and neurodegeneration (Perrotta et al. 2020; Mizushima and Levine 2010; Li et al. 2020; Levine et al. 2011; Frake et al. 2015).

Autophagy has been classified into two categories: basal and induced autophagy (Mizushima, 2005). Basal autophagy occurs constitutively, even under nutrient-rich conditions and it is described as an intracellular quality control by constant turnover of cytoplasmic material. Several studies described that loss of autophagy results in accumulation of ubiquitinated proteins (Mizushima et al., 2004; Komatsu et al., 2006; Hara et al., 2006; Nakai et al., 2007). Under nutrient-low conditions, such as starvation, autophagy is induced to maintain amino acid levels (Hara et al. 2006; Komatsu et al. 2006). This was shown in several studies where autophagy-deficient yeast cells displayed lower amino acid levels during starvation compared to wild type (WT) cells (Kuma et al., 2005). Moreover, autophagy-deficient newborn mice showed reduced levels of amino acids after birth compared to WT littermates (Kuma et al., 2004; Komatsu et al., 2005; Sou et al., 2008).

There are three different forms of autophagy namely macroautophagy, microautophagy, chaperone-mediated autophagy (CMA) that differ in their mode of cargo formation (Fig. 1). Chaperone-mediated autophagy involves targeting of proteins containing a particular KFERQ pentapeptide consensus motif by chaperones. The cargo is then imported into lysosomes for degradation (Majeski and Dice 2004; Aman et al. 2021; Yorimitsu and Klionsky 2005). Microautophagy describes the process of direct engulfment of cytoplasmic cargo by the endolysosomal membrane. Cargo for macroautophagic degradation can be cytoplasmic material and whole organelles (Yorimitsu and Klionsky 2005).

Macroautophagy is the major type of autophagy. It differs from CMA and microautophagy by the formation of a de-novo double membrane structure vesicle, the autophagosome, which then fuses with the lysosome to form an autolysosome for degradation. Substrates of macroautophagy can be either bulk cytosolic material or selective cargo. Selective targets can be mitochondria (mitophagy), lipids (lipophagy), endoplasmatic reticulum (ER-phagy), pathogens (xenophagy) and lysosomes (lysophagy) (Vargas et al., 2023).

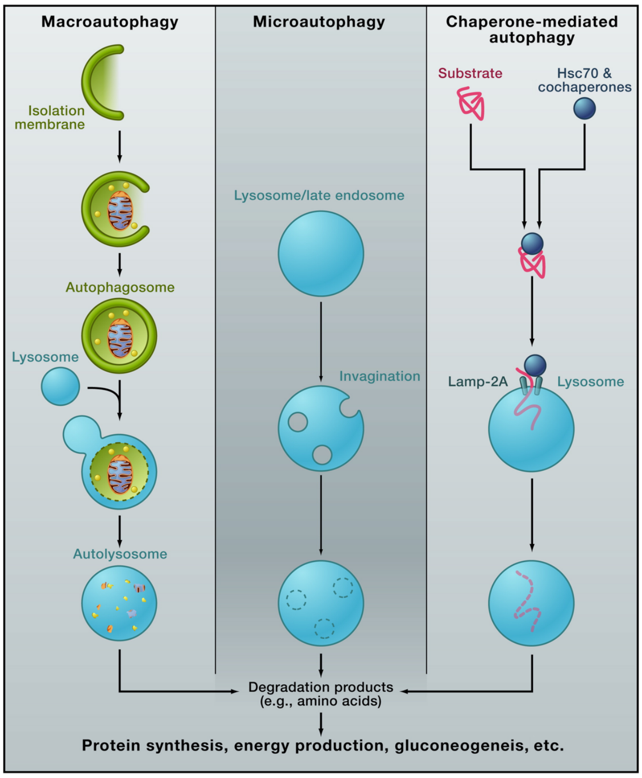

Figure 1: Overview of different types of autophagy. During macroautophagy, cytoplasm is engulfed by an isolation membrane, forming a double-membrane autophagosome which then fuses with the lysosome, forming an autolysosome for cargo degradation. During microautophagy cytoplasmic cargo is directly engulfed by endolysosomal membranes for degradation. During chaperone-mediated autophagy, cargo with a specific KFERQ pentapeptide motif is targeted via chaperones and then translocated into the lysosomal lumen for degradation. All three types of autophagy provide products such as amino acids after degradation to maintain cellular homeostasis (Mizushima and Komatsu, 2011).

1.2 The autophagic process

Autophagy is a dynamic process that can be subdivided into four major steps: 1) initiation of the phagophore formation, 2) nucleation, 3) expansion of the phagophore, and 4) fusion of the resulting autophagosome with a lysosome (Fig. 2). Each step requires orchestration of several autophagy genes (ATG) which were identified by studying the molecular basis of autophagy in yeast (Nakatogawa et al. 2009).

Proteins involved in the process can be grouped into several functional subunits, such as the ULK1 kinase complex for the induction of autophagy (ULK, ATG13, ATG101, and RB1CC1/FIP200), ATG9 for delivery of other ATG proteins and recycling of membranes, the class III phosphatidylinositol 3-kinase (PI3K) complex (VPS34-Beclin1-VPS15) for vesicle nucleation, and the ATG12-ATG5- ATG16L conjugation system for the microtubule-associated protein 1 light chain 3 (LC3, or LC3I) lipidation to phosphatidylethanolamine (LC3-PE or LC3II), which allows membrane expansion and enclosure of the autophagosome (Ariosa and Klionsky

2016; Hu et al. 2015). The closed autophagosome matures and then fuses with the lysosome, leading to the formation of an autolysosome.

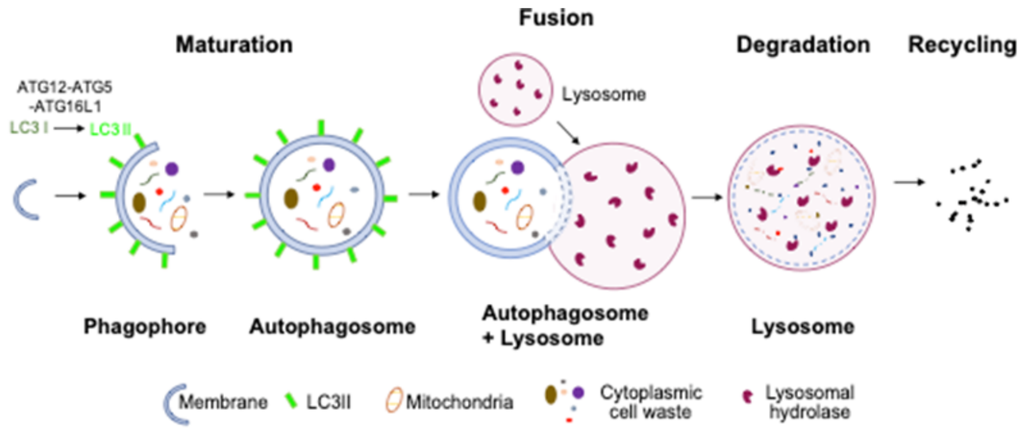

Figure 2: The autophagic process and its main regulatory machinery. After autophagy initiation, cytoplasmic material is engulfed by double-membrane structure and transported to the lysosome for degradation. This process can be divided into four major steps: 1) initiation, 2) nucleation, 3) expansion of the phagophore, and 4) the fusion with a lysosome. Degraded material is then released into the cytosol to maintain cellular homeostasis.

1.2.1 Initiation of the phagophore formation

Autophagy induction requires activation of serine/threonine kinase ATG1 (Unc-51- like kinase (ULK1) complex) and two accessory proteins, ATG13 and ATG17. The assembly of the ULK1 complex is controlled by the mammalian target of rapamycin complex 1 (mTORC1), a serine/threonine kinase that directly binds to ULK1/2 and promotes a phosphorylation-dependent inhibition of the autophagic process (Galluzzi et al., 2017). mTORC1 responds to amino acid and growth factor levels. Under nutrient rich conditions, mTORC1 is active, promoting protein biosynthesis and inhibiting autophagy (Liu and Sabatini 2020). Under nutrient deprivation and other stress conditions, mTORC1 is inhibited thereby inducing autophagy (Mizushima et al., 2004). After inactivation of mTORC1, ATG13 is rapidly and partially dephosphorylated, leading to a higher binding affinity for ATG1 and ATG17. The interaction of ATG1 with dephosphorylated ATG13 and ATG17 allows the activation of ATG1 kinase activity and promotes the activation of the ATG1-ATG13-ATG17 complex at phagophore assembly sites (PAS) (Hosokawa et al. 2009; Jung et al. 2009; Almeida et al. 2013). While mTORC1 is a negative regulator of autophagy, AMP-activated protein kinase (AMPK) is an activator of the autophagic process. AMPK responds to metabolic stress, such as low ATP levels, by inducing ULK1 activity via phosphorylation. Additionally, AMPK indirectly inhibits mTORC1 activity via phosphorylation of two components of the mTORC1 signaling pathway (TSC2 and raptor) (Sarkar, 2013). The activated ULK1 complex translocates from its former cytosolic localization to autophagy-specific exit sites of the endoplasmic reticulum (ER), which are specified by ATG9 vesicles, and with less extent to mitochondria, Golgi and plasma membrane to recruit membranes for autophagosome formation (Karanasios et al. 2013; Hamasaki et al. 2013; Mercer et al. 2018; Li et al., 2021).

1.2.2 Nucleation

Subsequently, the ULK1 complex directly activates the class III phosphatidylinositol 3-kinase (PI3K) complex, that includes the vacuolar protein sorting 34 (VPS34), 15 (VPS15), Beclin-1 (BECN1) and ATG14. Once activated, the PI3K complex is recruited to the phagophore initiation site. Here VPS34 generates phosphatidylinositol 3-phosphate (PI3P), a phospholipid found in cell membranes that helps to recruit proteins. This first membranous compartment is called the omegasome. PI3P additionally leads to the recruitment of tryptophan-aspartic acid (WD) repeat domain phosphoinositide-interacting (WIPI) proteins to the phagophore membrane that are important for the recruitment of downstream autophagic proteins (e.g., ATG16L1 recruited by WIPI2). This defines where the phagophore is formed (Menzies et al. 2017; Dooley et al. 2014).

1.2.3 Phagophore expansion and autophagosome maturation

The phagophore extension and elongation is mediated mainly by two ubiquitin-like conjugations systems: the ATG5-ATG12-ATG16L1 (E3) complex and microtubule associated protein 1 light chain 3 (LC3 - also known as ATG8).

LC3 can be subdivided into two forms, called LC3 I and LC3 II. LC3 I is cytosolic, whereas LC3 II is membrane-bound (Kabeya et al. 2000). The processing of LC3 I to LC3 II is mediated by the cysteine protease ATG4 that cleaves LC3 I, thereby exposing a glycine residue. The exposed glycine is subsequently activated by ATG7 in a reaction that requires ATP to form a thioester intermediate with the active cysteine residue of ATG7. The glycine residue of LC3 is then transferred to ATG3, which allows the conjugation of LC3 to phosphatidylethanolamine (PE), leading to the formation of LC3-PE (LC3 II). LC3 II is then recruited to both sides of the growing autophagophore membrane. Since LC3 II specifically associates with autophagosome membranes, its levels can be used as indication of autophagosome amount (Nakatogawa et al. 2009; Menzies et al. 2017; Mercer et al. 2018).

The last step in ATG3 conjugation of LC3 to PE requires the ATG12–ATG5–ATG16L1 complex (Hanada et al., 2007). ATG12 is activated via ATG7 and ATG10, thereby promoting covalent conjugation to ATG5. ATG16L1 directly interacts with ATG5, forming the ATG12-ATG5-ATG16L1 complex. Recruitment of ATG12–ATG5–ATG16L1 to the phagophore requires WIPI2 to link LC3 conjugation with PI3P at the site of autophagosome formation (Dooley et al. 2014). ATG12–ATG5–ATG16L1 is exclusively located at the outer membrane of the growing phagophore, recruiting LC3 II for phagophore elongation (Mizushima et al., 2001; Mizushima et al., 2003; Saitsu et al., 2013). LC3 interacts with cargo receptors that contain LC3-interacting motifs (LIR) for cargo delivery into autophagosomes.

Membranes for phagophore expansion are mostly delivered by ATG9-containing vesicles transmembrane. ATG9 is the protein that localizes to the trans-Golgi network and the endocytic compartment to facilitate the supply of lipid bilayers (Bento et al. 2016).

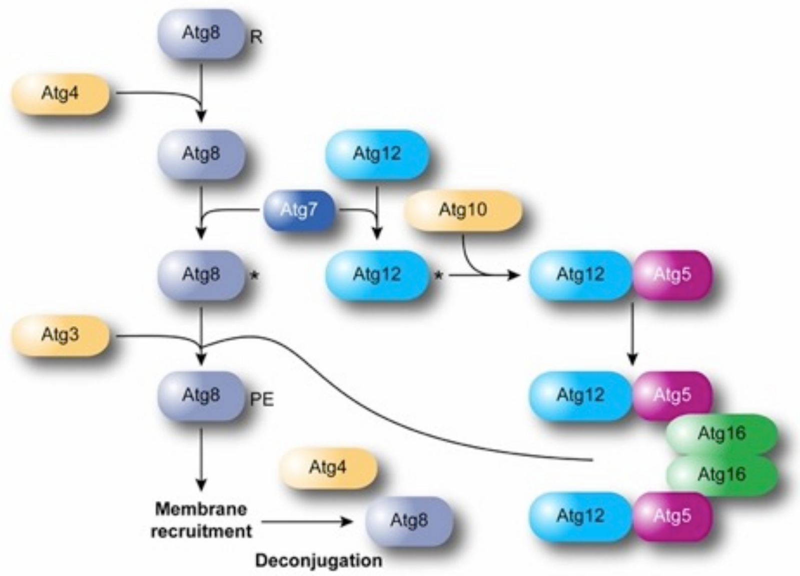

Figure 3: Schematic of the two ubiquitin-like conjugation systems involved in phagophore formation and expansion. ATG1212 is covalently conjugated to ATG5 through the activity of ATG7 and ATG10. ATG12-ATG5 complex associates with ATG16L1. LC3 (ATG8) is cleaved by the cysteine protease ATG4, exposing a glycine residue. Through ATG7 and ATG3, LC3 I is then conjugated to PE. ATG12-ATG5-ATG16L1 mediates LC3 II conjugation with PI3P at the site of autophagosome formation (Reggiori et al., 2013).

1.2.4 Fusion of the autophagosome with the lysosome

In neurons, once the autophagosome is mature and closed, it is transported to the cell soma where it fuses with a lysosome, resulting in an autolysosome. The autophagosome can also fuse with early endosomes, resulting in an amphisome which then ultimately fuses with lysosomes in the cell soma (Gordon and Seglen, 1988; Stromhaug et al., 1998). The fusion of amphisomes/ autophagosomes with lysosomes requires non-ATG components, such as small GTPases, tethering proteins and SNARE complex proteins (Lőrincz and Juhász, 2020). The growing phagophore acquires GTPase proteins RAB2 and RAB7 and RF-like GTPase ARL8, which bind to the HOPS tethering complex, bringing autophagosomes and lysosomes closely together and thus promoting the autophagosome- lysosome fusion (Boda et al., 2019; Lőrincz and Juhász, 2020; Langemeyer et al., 2018). In the last fusion step, the mechanical force for the fusion event is applied by components of the SNARE machinery, such as VAMP7 and VAMP9 (Fader et al., 2009; Furuta et al., 2010), Syntaxin 17, SNAP29 and VAMP8 (Itakura et al., 2012). Successful fusion also requires inositol polyphosphate-5 phosphatase converting lysosomal membrane phospholipid PI(3,5)P2 back to the PI3P, and phosphatidylinositol 4- kinase IIα (PI4K-IIα) generating the PI4P (Hasegawa et al., 2016; Wang, et al., 2015).

While lysosomes are usually located in the cell soma, the autophagomes /amphisomes are generated elsewhere in the cell. Multiple motor proteins, including kinesins and cytoplasmic dynein serve as the principal carriers for autophagosome and lysosome microtubule- dependent movement toward each other (Kimura et al., 2008; Lie & Nixon, 2019; Pu et al., 2016). Autophagosomes and amphisomes are usually transported along microtubules using the dynein-dynactin complex (Ravikumar et al., 2005; Fass et al., 2006; Monastyrska et al., 2009). Dynein and kinesins link autophagosomes/amphisomes to small GTPases, RAB7 and ARL8, supporting the fusion event (Guardia et al., 2016; Jia et al., 2017; Langemeyer & Ungermann, 2015; Pankiv et al., 2010). As the final step, cytoplasmic cargo is degraded by hydrolases in autolysosomes. Activity and acidification of lysosomes are necessary for degradation. The loss of catalytically active forms of lysosomal enzymes such as Cathepsin B and D results in a blockage of degradation in the autophagic pathway (Renna et al., 2011).

1.3 Autophagy in the central nervous system

Many studies could show that autophagy is important during neurodevelopment, in the maintenance of the physiological status and it is involved in ageing processes (Kulkarni et al., 2018; Azarnia Tehran et al., 2018; Liang and Sigrist, 2018; Stavoe and Holzbaur, 2019). Brain-confined loss of ATG genes in all neuronal precursor cells (Cre recombinase expression under Nestin promotor) resulted in growth retardation and behavioral deficits. Those animals displayed degeneration of neurons in several brain areas, accompanied by axonal degeneration and accumulation of intracellular proteins aggregates (Hara et al., 2006; Komatsu et al., 2006; Komatsu et al., 2007b; Liang et al., 2010; Zhao et al., 2015; Joo et al., 2016; Yamaguchi et al., 2018).

Since all of these knock-out (KO) mouse models were generated using the Nestin promoter to drive the expression of Cre recombinase, therefore leading to ATG genes KO in all neural progenitors, the neurodegeneration observed in these models can be caused by defects of autophagy in both neurons and glial cells.

Neurons are specialized postmitotic cells with a unique morphology characterized by elaborated dendritic trees and long axons. Their complex morphology makes neurons extremely dependent on a well-working clearance process and transport system to remove harmful material and constantly reorganize themselves to maintain cellular homeostasis. In contrast, mouse lines with neuron-specific ablation of ATG proteins in excitatory forebrain neurons (McMahon et al., 2012), dopaminergic neurons (Hernandez et al., 2012), and striatal spiny projection neurons (Lieberman et al., 2020), as well as mice deficient for ATG5 in excitatory forebrain neurons (Negrete-Hurtado et al., 2020; Overhoff et al., 2022) do not display neuronal cell loss.

Interestingly, not all neurons are resistant to autophagy-deficiency. Specific loss of ATG5 or ATG7 in Purkinje cells result in axonal dystrophy and accumulation of abnormal organelles, followed by age-dependent Purkinje cell death and mouse behavioral deficits (Komatsu et al., 2007; Nishiyama et al., 2007). Molecular and cellular mechanisms underlying the selective vulnerability or resistance of different neuronal subtypes to autophagy dysfunctions are currently unknown.

1.4 Selective autophagy

Autophagic cargo can be either bulk cytosolic material or selective targets, such as mitochondria (mitophagy), lipids (lipophagy), endoplasmatic reticulum (ER-phagy), pathogens (xenophagy), lysosomes (lysophagy) and aggregates (aggrephagy) (Vargas et al., 2023).

While selective and bulk autophagy share most molecular machinery, selective autophagy is characterized by receptor-mediated cargo recruitment to the growing autophagosome (Stavoe and Holzbaur, 2019) (Fig. 4). Recognition of selective cargo is regulated in most cases via cargo ubiquitination (Gubas and Dikic, 2022). Several autophagy receptor proteins have been already identified, such as p62/ Sequestosome 1 (SQSTM1) (Bjørkøy et al. 2005), NBR1 (neighbour of BRCA1 gene) (Kirkin et al. 2009), optineurin (OPTN) (Wild et al. 2011), Tax1 binding protein 1 (TAX1BP1) (Newman et al. 2012), nuclear dot protein 52 (NDP52)/CALCOCO2, TOLL-interacting protein (TOLLIP) (Baines et al. 2014) and 26S proteasome regulatory subunit (RPN10) (Stolz et al. 2014; Menzies et al. 2017). All receptors contain a LC3-interacting region (LIR) and a ubiquitin-binding domain, allowing the delivery of ubiquitinated cargo to lipidated LC3 on the growing autophagosome (Kirkin and Rogov, 2019; Johansen and Lamark, 2020).

Selective autophagy is important for cellular quality control. Hence, not surprisingly, aberrant selective autophagy has been associated with various human pathologies such as neurodegenerative diseases.

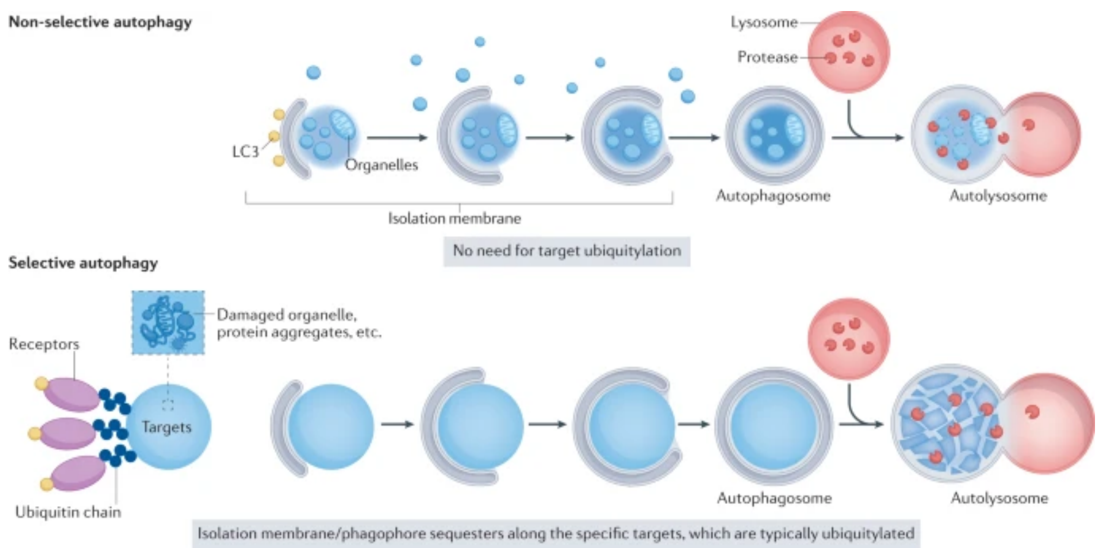

Figure 4: Comparison of bulk and selective autophagy. In both non-selective (bulk) and selective autophagy, cytoplasmic components are collected in autophagosomes and degraded in autolysosomes. Bulk autophagy engulfs bulk cytoplasmic cargo, including organelles or macromolecules. Selective autophagy targets specific cargo, mostly upon ubiquitination, via autophagy receptor proteins to the

growing autophagosome. Receptor proteins recognize LC3 (via their LIF motif), thereby creating a bridge between ubiquitinated cargo and autophagosomes (Vargas et al., 2023).

1.4.1 Mitophagy

Mitophagy is crucial to maintain healthy mitochondrial network and cellular energy homeostasis. Defects in mitophagy lead to accumulation of impaired mitochondria, possibly leading to release of harmful substrates, such as reactive oxygen species and mitochondrial DNA (mtDNA) or leading to insufficient energy supply (Pickles, Vigié and Youle, 2018; Borsche et al., 2020).

Especially in neurons, mitophagy is a challenging event that needs to be tightly controlled. In fact, mitochondria can be localized at distal neuronal compartments with high-energy demands far away from the cell body, like synapses and growth cones (Doxaki and Palikaras 2020).

PTEN-induced putative kinase 1 (PINK1) and parkin are the best described receptors for mitophagy. In healthy mitochondria, PINK1 is imported into mitochondria and subsequently degraded via the proteasome (Jin et al.,2010; Sekine and Youle, 2018). Upon loss of mitochondrial membrane potential, PINK1 import is impaired leading to the accumulation of damaged mitochondria on the outer membrane (Narendra et al., 2008). Within the outer membrane, PINK1 phosphorylates serine 65 of ubiquitin chains of outer membrane proteins, including parkin (Narendra et al., 2010; Kondapalli et al., 2012). Upon phosphorylation, parkin is activated and ubiquitinates outer membrane proteins (Sarraf et al., 2013; Ordureau et al., 2014; Ordureau et al., 2018). PINK1 and Parkin interact and facilitate a feed-forward mechanism generating poly-ubiquitin chains, amplifying mitophagy signals (Pickles et al. 2018). These poly-ubiquitin chains are then recognized via autophagy receptors with optineurin (OPTN) and nuclear dot protein 52 (NDP52)/CALCOCO2 as the main receptors (Lazarou et al., 2015; Heo et al., 2015; Moore and Holzbaur, 2016). However, SQSTM1/ p62, Tax1 binding protein 1 (TAX1BP1) and nuclear dot protein TOLL-interacting protein (TOLLIP) are also shown to be involved in mitophagy (Evans and Holzbaur, 2020).

Additionally, mitophagy can be initiated in an ubiquitin-independent manner via NIX (19 kDa-interacting protein-3 (NIP3)-like protein X), BNIP3 (BCL2/adenovirus E1B 19 kDa protein-interacting protein 3) or FUNDC1. These proteins localize to the outer mitochondrial membrane and interact directly with LC3, targeting mitochondria to autophagosomes (Zhang et al., 2009; Palikaras et al. 2018; Terešak et al., 2022).

Dysregulated mitophagy is associated with various neurodegenerative diseases such as Parkinson’s disease (PD) and amyotrophic lateral sclerosis (ALS). Mutations in genes encoding for PINK1 and parkin result in familial PD (Kitada et al., 1998; Valente et al., 2004) and OPTN and TBK1 are implicated in ALS pathogenesis (Evan and Holzbaur, 2019).

1.4.2 ER-phagy

ER-phagy is crucial to maintain cellular homeostasis by endoplasmatic reticulum (ER) quality control. The ER forms a complex network comprised of structures, such as sheets and tubules that span throughout the cell. Especially in neurons, ER-phagy is a challenging event that needs to be tightly controlled since the ER network extends throughout all neuronal compartments.

The ER undergoes a permanent remodeling, restructuring and turn-over during regular homeostasis, which is increased in the presence of cellular stress (Grumati et al. 2018; Wu et al. 2017b). Several ER-phagy receptor proteins have been identified, such as FAM134B (Khaminets et al., 2015), RTN3 (Grumati et al., 2017), SEC62 (Fumagalli et al., 2017), TEX264 (An et al., 2019; Chino et al., 2019), atlastin3 (Chen et al., 2019), CCGP1 (Smith et al., 2018) and CALCOCO1 (Nthiga et al., 2020). Additionally, p62 was shown to facilitate ER removal under proteotoxic stress (Ji et al., 2019). All receptors are localized at specific ER sites and do not require ubiquitination for ER-phagy induction. Moreover, most of the receptors contain a LIR motif, enabling them to interact with LC3 to mediate ER fragment degradation. Nevertheless, the crosstalk of the ER-luminal cargo and the transmembrane localized receptors is still enigmatic (Grumati et al. 2018).

1.4.3 Aggrephagy

Cargo for aggrephagy are proteins which are misfolded due to mutations, incomplete translation, misfolding after translation, aberrant protein modifications, oxidative damage or failed assembly of protein complexes (Lamark and Johansen, 2012). Misfolded proteins exist as soluble monomers, small aggregates or large, insoluble aggregates. The latter are believed to be cytotoxic by interfering with degradation systems or interaction with membranes or other proteins. The aggregate size is defining whether aggregates are degraded via the ubiquitin-proteasome-system (UPS), chaperone-mediated autophagy or aggrephagy. Especially, large insoluble aggregates are believed to be the main target of aggrephagy (Scotter et al., 2014; Dikic, 2017).

The main aggrephagy receptors are p62, autophagy-linked FYVE protein (ALFY) and NBR1 that mediate the engulfment of aggregates proteins (Bjørkøy et al., 2005; Pankiv et al., 2007; Clausen et al., 2010; Johansen and Lamark 2011; Savova et al., 2020).

Accumulation of protein aggregates in specific neuronal subtypes is a hallmark of several neurodegenerative diseases. Some examples are accumulation of hyperphosphorylated tau fibrils and amyloid-β in Alzheimer's disease (Pickford et al., 2008; Jo et al., 2014), α-synuclein in Parkinson's disease (Winslow et al., 2010), poly-glutamine huntingtin in Huntington´s disease (Ravikumar et al., 2004) and TDP43 and FUS in amyotrophic lateral sclerosis (Buchan et al., 2013). All proteins have been shown to be aggrephagy substrates.

Proteins aggregation is believed to be a critical pathomechanism and the main cause of neurodegeneration. Additionally, mutations in autophagy receptors result in impaired clearance of neurotoxic aggregates (Maruyama and Kawakami, 2013; Rea et al., 2014). In contrast, it was described that p62-positive inclusion bodies are beneficial for cell survival and neurons with p62-inclusion bodies were protected from neurodegeneration (Komatsu et al., 2007a).

1.5 Autophagy and neurodegeneration

Defects in autophagy are associated with the pathophysiology of several neurodegenerative diseases (Azarnia Tehran et al., 2018; Menzies et al., 2015; Schreij et al., 2016; Ventruti and Cuervo, 2007; Wong and Holzbaur, 2015). Current data suggest that autophagy dysfunctions underlie the earliest events in neurodegeneration (Cataldo et al., 2000; Wang et al., 2013). For instance, accumulation of autophagosomes is a hallmark of Huntington disease and ALS (Martinez-Vicente et al., 2010; Nguyen et al., 2019) as well as accumulation of aggrephagy substrates. Some mutations in ATG proteins directly cause neurodegenerative diseases.

A recessive missense mutation in Atg5 in two siblings causes congenital ataxia, mental retardation and developmental delay. Patient cells displayed decreased autophagic flux and defects in the conjugation of ATG12 to ATG5 (Kim et al., 2016).

Mutations in Wdr45, a PIP3 sensor involved in the recruitment of autophagy proteins during autophagophore expansion, was found to cause static encephalopathy in childhood with neurodegeneration in adulthood. Those patients display childhood psychomotor retardation that remains static until adulthood, with a sudden onset of progressive dystonia-parkinsonism and dementia in the twenties to early thirties (Kingwell, 2013). Impairment in the process of autophagy was characterized by impaired autophagy flux and accumulation of lipidated LC3-positive membranes (Saitsu et al., 2013).

1.5.1 Alzheimer's disease (AD)

AD is the most common neurodegenerative disorder with progressive cognitive decline as the primary symptom. Progressive degeneration of neurons is observed in several brain regions. Neuronal death is thought to be caused by intracellular aggregated tau protein and extracellular accumulation of amyloid-β (Aβ) plaques, generated by the cleavage of amyloid precursor protein (APP) by β- and γ-secretase (Vassar et al. 1999).

There are no mutations known that directly link autophagy and AD, however accumulation of hyperphosphorylated tau fibrils and amyloid-β in AD indicate defective autophagic clearance in AD patients (Pickford et al., 2008; Jo et al., 2014). Additionally, accumulation of unprocessed autophagosomes can be detected in induced pluripotent stem cell-derived neurons and post-mortem brains of AD patients. Accumulation of unprocessed autophagosomes were identified in PS-1/APP double transgenic mice prior to appearance of Aβ plaques (Yu et al., 2005; Nixon, 2007; Nixon & Yang, 2011). AD brains display reduced levels of Beclin-1, an initiation protein of autophagy (Pickford et al. 2008; Small et al. 2005). Reduction of Beclin-1 in mice resulted in decreased level of autophagy and the accumulation of Aβ peptides leading to neurodegeneration, while increased levels of Beclin-1 resulted in reduced cellular Aβ peptide levels (Jaeger et al., 2010; Rocchi et al., 2017). These studies highlight Beclin-1 as a promising therapeutic target for AD patients.

1.5.2 Parkinson's disease (PD)

PD is the second most common neurodegenerative disease. PD patients display motor symptoms such as tremor, rigidity, akinesia, bradykinesia, and postural instability and progressive degeneration of dopaminergic neurons of the substantia nigra pars compacta.

The main pathological hallmark of Parkinson's disease is the accumulation of α-Synuclein, which was shown to be degraded via autophagy and several mutations in genes coding for autophagic proteins have been found in PD cases (Webb et al., 2003).

Mutations in the Vacuolar Protein Sorting-Associated Protein 35 (VPS35), leading to ATG9 delocalization, results in impaired autophagy, causing an autosomal-dominant form of PD (Zavodszky et al., 2014). Autosomal-recessive forms of PD are caused by mutations in ATPase type 13A2 (ATP13A2 / PARK9), which is a lysosomal membrane protein involved in lysosomal acidification. PD-derived fibroblasts with ATP13A2 mutation displayed impaired lysosomal acidification and accumulation of autophagosomes. Additionally, PD brain tissue displayed decreased levels of ATG13A2 protein in dopaminergic neurons (Dehay et al., 2012). Mutations in genes encoding for PINK1 and parkin cause autosomal- recessive and sporadic juvenile-onset PD resulting in impaired mitophagy and accumulation of damaged mitochondria (Kitada et al., 1998; Valente et al., 2004). Increased levels of fragmented mitochondria are observed in aged mice (Noda et al., 2019), resulting in increased vulnerability to oxidative stress (Kand et al., 2019). Loss-of- function studies revealed that loss of parkin does not cause neuronal loss but a reduction in synaptic excitability (Goldberg et al., 2003) as well as a shift in dopamine receptor levels and localization (Itier et al., 2003).

A heterozygous variant in the promoter region of ATG5 was identified in one patient with sporadic PD (Chen et al., 2013) but whether this mutation affects autophagy is currently unknown.

1.5.3 Amyotrophic lateral sclerosis (ALS)

ALS is a motor neuron disease characterized by degeneration of motor neurons of the spinal cord, brain stem and motor cortex. The most prominent symptoms of ALS patients are muscle weakness, muscle wasting and paralysis (Salameh et al., 2015).

The main neuropathological hallmark of ALS is the presence of inclusion bodies of TDP43 and FUS in motor neurons (Buchan et al., 2013). Several genes associated with ALS pathophysiology are coding for proteins, which either directly or indirectly function in the autophagy pathway such as p62, optineurin, TBK1 and VCP.

Mutations in p62 result in impaired binding affinity, thereby negatively affecting autophagy or in aggregation of p62 in ubiquitin-positive inclusion bodies (Chen et al., 2014; Goode et al., 2016). Mutations in TBK1 and optineurin perturb enhanced affinity for ubiquitinated mitochondria, thereby leading to failed mitochondrial clearance and accumulation of dysfunctional mitochondria (Cirulli et al., 2015; Freischmidt et al., 2015; Pottier et al., 2015).

1.5.4 Huntington's disease (HD)

Patients suffering from HD show cognitive dysfunction, psychiatric disturbances and severe motor dysfunction caused by the neurodegeneration of medium spiny neurons of the caudate-putamen (Thu et al., 2010). This disease is caused by a trinucleotide repeat expansion (>35 repeats) mutation of cysteine, adenine, and guanine (CAG) in the coding region of the ubiquitously expressed huntingtin (mHTT) gene (Nørremølle et al., 1993; La Spada & Taylor, 2010). The long tract of polyglutamine of mHTT facilitates its aggregation and sequestration into inclusion bodies (Sieradzan et al., 1999; Waelter et al., 2001). Autophagy has been proposed to modify course and age of onset of HD. mTOR can be sequestered into mHTT inclusion bodies, which impairs its kinase activity and thus activates autophagy (Ravikumar et al., 2004; Heng et al., 2010). In contrast, mHTT aggregates can sequester Beclin-1 and thereby inhibit autophagy (Shibata et al., 2006). A V471A polymorphism in the Atg7 gene has been shown to be associated with the age at onset of HD patients (Metzger et al., 2013). How this mutation affects ATG7 function in neurons is still unknown.

2. Metabolism

2.1 Brain energy metabolism

Regulation of metabolite supply and cellular energy metabolism is essential to maintain healthy cellular and systemic function. This regulation is especially critical to the central nervous system (CNS) where energy consumption is highly dynamic. Within the brain, increased neuronal activity drives increased energy consumption (Roy and Sherrington, 1890). Normal brain function therefore requires metabolism to be tightly regulated within brain regions down to the level of a single synapse.

The energy demand of the brain accounts for 20% of the total body's consumption with glucose being the major energy source. Approximately 80% of the energy produced in the brain is consumed by neurons (Hyder et al., 2013). Neurons require high metabolic rate to maintain crucial neuronal functions such as vesicle recycling, neurotransmitter release, resting potential, action potentials, protein turnover, axonal transport, mitochondrial proton leak and actin cytoskeleton remodeling (Attwell and Laughlin, 2001; Harris et al., 2012; Rangaraju et al., 2014; Pathak et al., 2015). Therefore, it is not surprising that energy requirements are not uniform but rather highly localized. The brain relies on oxidative metabolism of glucose via glycolytic pathway and the tricarboxylic acid (TCA) cycle for ATP production.

Metabolic pathways of the brain differ in their importance during development. During development, aerobic glycolysis accounts for up to 30% of brain glucose metabolism while in the adult brain, aerobic glycolysis is believed to be restricted to specific regions. Positron emission tomography (PET) imaging in humans identified that brain regions differ in their glucose metabolism capacity. Cerebellum and temporal regions such as amygdala, hippocampus, entorhinal cortex and temporal lobe were shown to use low levels of glucose. Other cortical and subcortical regions were shown to use high levels of glucose (Tomasi et al., 2017; Blazey et al., 2018). Another PET study showed that in resting brains, cortical regions display highest levels of glucose metabolism, while cerebellum and temporal lobes have the lowest (Vaishnavi et al., 2010). During childhood, aerobic glycolysis peaks around the age of 5 years and then gradually declines while aging (Bauernfeind et al., 2014; Goyal et al., 2014).

2.2 Blood brain barrier and metabolite transporters

In order to maintain cellular energy metabolism, the brain depends on continuous supply of substrates from the blood which is regulated via the blood-brain-barrier (BBB). The BBB separates the brain interstitial fluid from the blood and it is formed by capillary endothelial cells interconnected by tight junctions, their underlying basement membrane, pericytes, and the “end feet” of astrocytes. Its main function is to limit free diffusion and selectively transport essential molecules such as nutrients, ions and signaling molecules.

The BBB mediates influx of metabolites such as glucose, amino acids and ketone bodies from the blood into the brain via specialized transporters (Fig. 5). Passive diffusion through the BBB is limited to small nonpolar lipids and gases such as oxygen and carbon dioxide. Large molecules such as hormones and growth factors are transferred via receptor-mediated transport (Zlokovic et al., 1995; Zlookovic et al., 2008). Two major families of transporters in the BBB are: ATP-binding cassette (ABC) proteins and solute carriers (SLC) proteins. ABC transporters work as efflux pumps to move lipid-soluble molecules against their concentration gradient upon ATP hydrolysis (Begley, 2004). Solute carrier proteins are a large superfamily of more than 300 members that are crucial for constant supply of carbohydrates, amino acids, monocarboxylic acids, nucleotides and fatty acids (Abbott et al., 2010). Especially monocarboxylic acid transporters (MCTs) and glucose transporters (GLUTs) are crucial for brain metabolism. Glucose transport across the BBB is mainly driven by the concentration gradient of glucose between blood and brain interstitium. Glucose concentration in the blood is 4-6 mM between meals, whereas the concentration in the brain interstitium is 1-2 mM. The gradient is maintained by constant glucose-uptake into astrocytes and neurons (Patching, 2017).

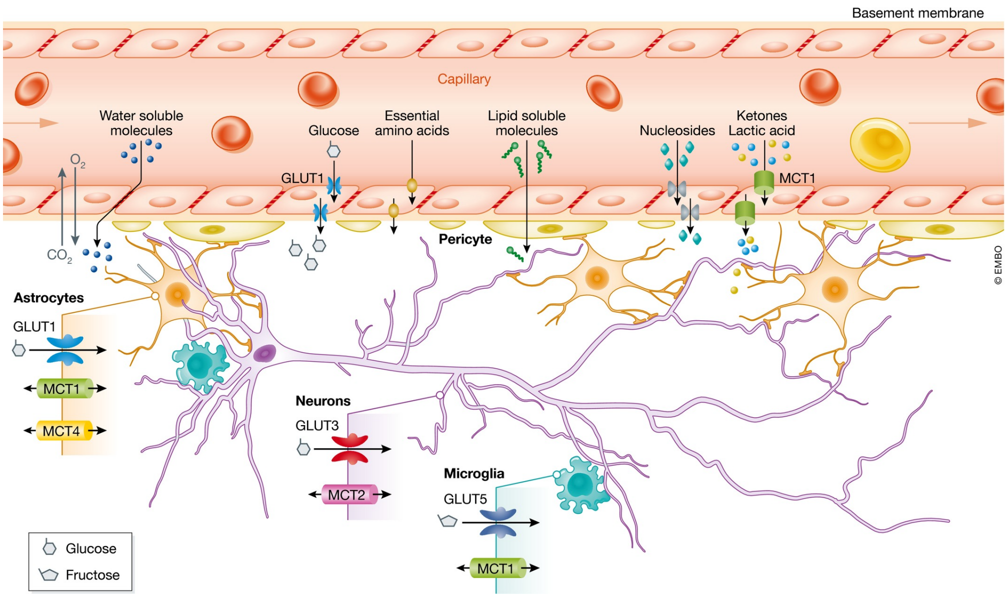

Figure 5: Nutrient transport across the blood-brain barrier. The BBB is formed by capillary endothelial cells interconnected by tight junctions, their underlying basement membrane, pericytes, and “end feet” of astrocytes. Passive diffusion is limited to gases and small nonpolar lipids. Other molecules are actively transported via specialized transporters such as GLUT1 (glucose transporter 1) for glucose transport, MCT1 (monocarboxylic acid transporters 1) for ketone bodies and lactate (Camandola, 2017).

2.3 Glucose transporters (*SLC2*) in the brain

There are currently 14 known members of the SLC2 family of GLUTs. Here only the four main glucose transporters of the central nervous system will be described (GLUT1-GLUT4).

2.3.1 GLUT1 (*SLC2A1*)

GLUT1 is highly expressed in endothelial cells of the BBB and glial cells in the brain (Bondy et al., 1992) and it is crucial for the import of hexose and pentose sugars into the brain. Additionally, GLUT1 was also described to be expressed in oligodendrocytes, microglia, neurons, ependymal cells and tanycytes (Garcia et al., 2001; Maher et al., 1994; Wang et al., 2019). Dysfunction of GLUT1 causes infantile epilepsy, also called GLUT1 deficiency syndrome (GLUT1DS). GLUT1DS patients develop pediatric-onset epileptic encephalopathy, mental retardation and movement disorders including dystonia, ataxia and spasticity (De Vivo et al, 1991). Additionally, GLUT1 deficiency has been described in patients with epilepsy, movement disorders and cognitive impairment (Pearson et al., 2013).

Heterozygous GLUT1-deficient mice showed epileptiform discharges, impairment in motor activity, incoordination, microencephaly and decrease in glucose uptake and GLUT1 expression in the brain (Wang et al, 2006). Additionally, those animals developed postnatal weight loss, reactive gliosis and decreased hippocampal volume (Ullner et al., 2009).

Cell-specific GLUT1 deletions from endothelium and astrocytes resulted in loss of BBB integrity and additionally accelerated Aβ accumulation in APPSw/0 mice leading to progressive neuronal dysfunction, behavioral deficits, neuronal loss and neurodegeneration that developed after initial cerebrovascular changes (Winkler et al., 2015).

2.3.2 GLUT2 (*SLC2A2*)

GLUT2 is a low-affinity glucose transporter that is mostly expressed in intestine, endocrine pancreas, kidney, and liver (Mueckler and Thorens, 2013). GLUT2 participates in the intestinal and renal absorption of glucose, the stimulation of insulin secretion by glucose in β-pancreatic cells and the entry and output of glucose by the liver. Mutations in the GLUT2 gene cause hepatorenal glycogen accumulation, nephropathy, and defects in glucose homeostasis in humans (Santer et al., 2002).
In the brain, GLUT2 is expressed in neurons, astrocytes, oligodendrocytes, ependymal cells, and tanycytes, primarily detected in thalamic nuclei, hypothalamic nuclei, nuclei of the brain stem, and hippocampus (Leloup et al., 1994; Garcia et al., 2003; Arluison et al., 2004a; Arluison et al., 2004b; Barahona et al., 2018).
GLUT2 is involved in the regulation of glucose homeostasis and food intake (Marty et al., 2007). In glial cells, GLUT2 is involved in the detection of hypoglycemia and mediates the regulatory responses to glucose deficits (Marty et al., 2005). A study with two Canadian populations suggests that also in humans GLUT2 is involved in the control of glucose uptake by the central nervous system. Individuals harboring a single-nucleotide polymorphism in the GLUT2 gene (Thr110Ile) show abnormal sugar intake (Eny et al., 2008). Additionally, abnormal feeding behavior could be observed in rats after GLUT2 knockdown in the hypothalamus (Barahona et al., 2018). Food intake was reduced after reduction of cerebral expression of GLUT2, in GLUT2-null mice, and in GLUT2-loop transgenic mice (Wan et al., 1998; Bady et al., 2006; Stolarczyk et al., 2010). Loss of GLUT2 in the hypothalamus indicated that GLUT2 plays a role in brain-dependent central regulation of insulin and glucagon (Leloup et al., 1998). In humans, mutations in Glut2 causes Fanconi-Bickel syndrome associated with defective kidney and impaired insulin secretion (Santer et al., 1998). Additionally, Glut2 variants are associated with increased risk of fasting hyperglycemia (Gaulton et al., 2008; Dupuis et al., 2010), type 2 diabetes (Kilpelainen et al., 2007), hypercholesteremia (Igl et al., 2010) and, cardivascular diseases (Borglykke et al., 2012). However, the role of GLUT2 in neurons other than hypothalamic nuclei is still elusive.

2.3.3 GLUT3 (*SLC2A3*)

GLUT3 is ubiquitously expressed in the brain (Nagamatsu et al., 1993; McCall et al., 1994; Moroo et al., 1994). It has a higher glucose affinity and transport capacity compared to other transporters, thereby ensuring constant neuronal glucose uptake. GLUT3 is predominantly expressed in neurons, mainly concentrated in axons and dendrites but also detectable in plasma membrane of cell bodies (Gerhart et al., 1992; Simpson et al., 2008). GLUT3 and GLUT1 have been shown to increase their expression with cerebral maturation (Nehling and Pereira de Vasconcelos, 1993; Nehling, 1996). Especially GLUT3 expression coincides with maturation of synaptic connectivity (Vannucci et al., 1998). Neuronal GLUT3 levels are adapting to glucose levels via the increase of mRNA during period of hypoglycemia and the decrease of mRNA levels in response to hyperglycemia (Uehara et al., 1997; Duelli et al., 1999; Lee et al., 2000; Hou et al., 2007; Stuart et al., 2011). Deficiency in GLUT3 during brain development results in reduced embryo size and increased cellular apoptosis in the CNS. Homozygous deletion of GLUT3 results in embryonic lethality (Ganguly et al., 2007; Carayannopoulos et al., 1014). Mice with neural-specific GLUT3 deletions display dendritic spine reduction, increase in neuronal excitability and reduced life span. Neural specific- deletion of GLUT3 restricted to the limbic system results in reduced inhibitory post-synaptic currents in cortical pyramidal neurons with changes in spatial exploration and social interactions of these animals (Shin et al., 2018). Heterozygous GLUT3 KO mice show impairments in spatial learning, social behavior and working memory (Birnbaum, 1989). Recent study showed that postnatal deletion of GLUT3 in hippocampal neurons results in decreased cytosolic glucose and ATP levels as well as reduced body weight and age-dependent memory deficits (Li et al., 2023). GLUT3 level are reported to decrease with ageing especially in hippocampus and cerebellum but also in the spinal cord (Fattoretti et al., 2001; Fattoretti et al., 2002; Fattoretti et al., 2003; Hu et al., 2010; von Leden et al., 2019). Interestingly, overexpression of GLUT3 can ameliorate aging-related declines in ATP and energy deficiency in flies (Oka et al., 2021).

2.3.4 GLUT4 (*SLC2A4*)

GLUT4 is an insulin-sensitive glucose transporter. In fact, it has been shown that in cultured neurons is transferred from intracellular compartments into the plasma membrane in response to extracellular insulin GLUT4 (Benomar et al., 2006; Huang, 2007; Grillo et al., 2009). In the brain, low expression levels can be detected in a subset of neurons, including Purkinje cells and granule cells in cerebellum, neurons in the hippocampus, cortex, hypothalamus, basal ganglia, and nuclei of medulla oblongata and spinal cord. GLUT4 is often coexpressed with GLUT3, with high expression in somatodendritic compartment but also detectable in neurites (Kobayashi et al., 1996; Leloup et al., 1996; El Messari et al., 1998; Vannucci et al., 1998; Choeiri et al., 2002; El Messari et al., 2002; Sankar et al., 2002). In addition to neurons, GLUT4 is also expressed in endothelial cells and ependymal cells in the brain (Kobayashi et al., 1996; Vannucci et al., 2000). GLUT4 does not only colocalize with GLUT3 but also with the insulin receptor (Kang et al., 2004; Grillo et al., 2009).

Its main role is in the central nervous regulation of body glucose homeostasis, but it is also involved in the regulation of active neuronal circuits. Increased energy demand promotes insertion of GLUT4 into the axonal plasma membrane under the control of AMP activated protein kinase (AMPK) (Rangaraju et al., 2014; Ashrafi et al., 2017). GLUT4 was also shown to be involved in hypothalamic regulation of food intake and energy expenditure (Ren et al., 2015; Reno et al., 2017). Heterozygous GLUT4 KO mice display insulin resistance and propensity toward diabetes (Rosetti et al., 1997).

2.4 Glucose metabolic pathways

Metabolic fate of glucose in the brain depends on the cell-type and their selective expression of metabolic enzymes. Neurons predominantly use oxidative phosphorylation (OXPHOS) to produce adenosine-5′-triphosphate (ATP) while astrocytes primarily use glycolysis (Belanger et al., 2011a; Hyder et al., 2006; Zhang et al., 2014). So far there is little evidence that neurons metabolize glucose via the glycolysis pathway. Glucose is not only used to generate ATP but also to provide intermediates for synthesis of fatty acids, amino acids and 5-carbon sugars (Gaitonde and Richter, 1966; Ramsey et al., 1971; Jones et al., 1975; Gaitonde et al., 1983). In general, glucose is oxidized via glycolysis, pentose phosphate pathway (PPP), tricarboxylic acid (TCA) cycle and oxidative phosphorylation (Fig. 6).

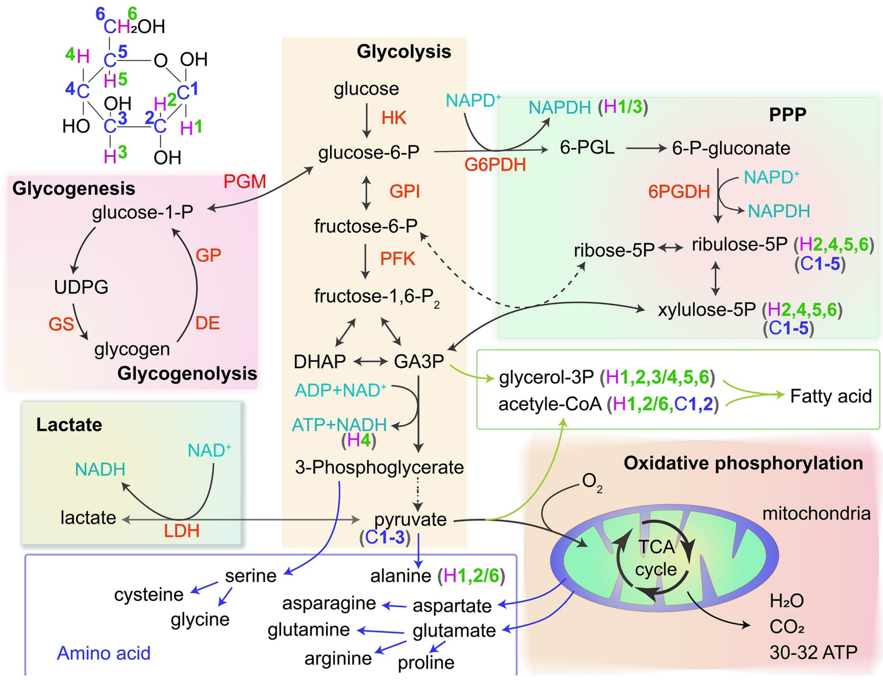

Figure 6: Major pathways of glucose metabolism in the brain. Glycolysis, TCA cycle and OXPHOS contribute to ATP production. Glycolytic intermediate glucose-6-phpshate can enter pentose-phosphate pathway for redox regulation and providing nucleotide. Pyruvate and 3-phosphoglycerate can be used for amino acid synthesis. In astrocytes, glucose can be stored as glycogen. Glyceraldehyde-3- phosphate can be used for fatty acid synthesis (Zhang et al., 2021).

2.4.1 Glycolysis

Glycolysis takes place in the cytosol and involves 10 reactions to convert glucose into pyruvate, thereby generating two ATP molecules. Pyruvate can then be actively transported into the mitochondria where it is converted to acetyl coenzyme A (acetyl-CoA). Under anaerobic conditions (no oxygen) pyruvate is converted into lactate instead of being imported into mitochondria (Chandel, 2020a).

Glucose phosphorylation via hexokinase (HK) is the first irreversible step of the glycolytic pathway. Glucose-6-phosphate (G6P) can have different fates: it either continues the glycolytic pathway, entering the pentose phosphate pathway or it is stored as glycogen. Storage in glycogen is believed to happen primarily in astrocytes because in neurons the enzyme glycogen synthase (GS) is constitutively inactive due to hyperphosphorylation (Magistretti et al, 1993).

The balance between glycolysis and PPP rates in neurons was shown to be very important, since excessive glycolysis can result in decreased availability of NADPH, increased oxidative stress and cell death (Herrero-Mendez et al, 2009). Neurons generally prefer the usage of G6P in the PPP. Additionally, studies demonstrated that neurons cannot up-regulate glycolysis, due to selective expression of enzymes. In addition to the HK step, glycolytic flux is regulated by phosphofructokinase 1 (PKF1) and pyruvate kinase (PK) (Lowry & Passonneau, 1964).

PKF1 catalyzes the phosphorylation of fructose-6-phosphate (F6P) to fructose-1,6-bisphosphate (F1,6P). Its activity is inhibited by metabolites associated with a high energy state (i.e., ATP, citrate, Acetyl-CoA) and enhanced by metabolites associated with high metabolic activity (i.e., ADP, AMP, phosphate). Neurons express pyruvate kinase M1 (PKM1), a constitutively active enzyme with high affinity for phosphoenolpyruvate (PEP), thereby favoring the generation of high levels of pyruvate. In contrast, low levels of the low-pyruvate- affinity isoform of lactate dehydrogenase (LDH1) can be found in neurons, thereby preventing pyruvate conversion to lactate and favoring conversion into acetyl-CoA (Zhang et al, 2014). PKM1 activity is inhibited by metabolites associated with a high energy state (i.e., ATP, citrate, Acetyl-CoA). Interestingly, postnatal deletion of PKM1 or GLUT3 in hippocampal neurons results in decreased glycolysis and memory deficits of those animals (Li et a., 2023), indicating that neurons use glycolysis to maintain neuronal function.

Many glycolytic metabolites can enter anabolic pathways that are involved in the generation of NADPH, glycogen, lipids, nucleotides and protein synthesis (Fig. 7). Additionally, some metabolites can fuel into hexosamine, serine or glycerol biosynthesis pathway (Locosale and Cantley, 2011; Chandel NS. 2020b).

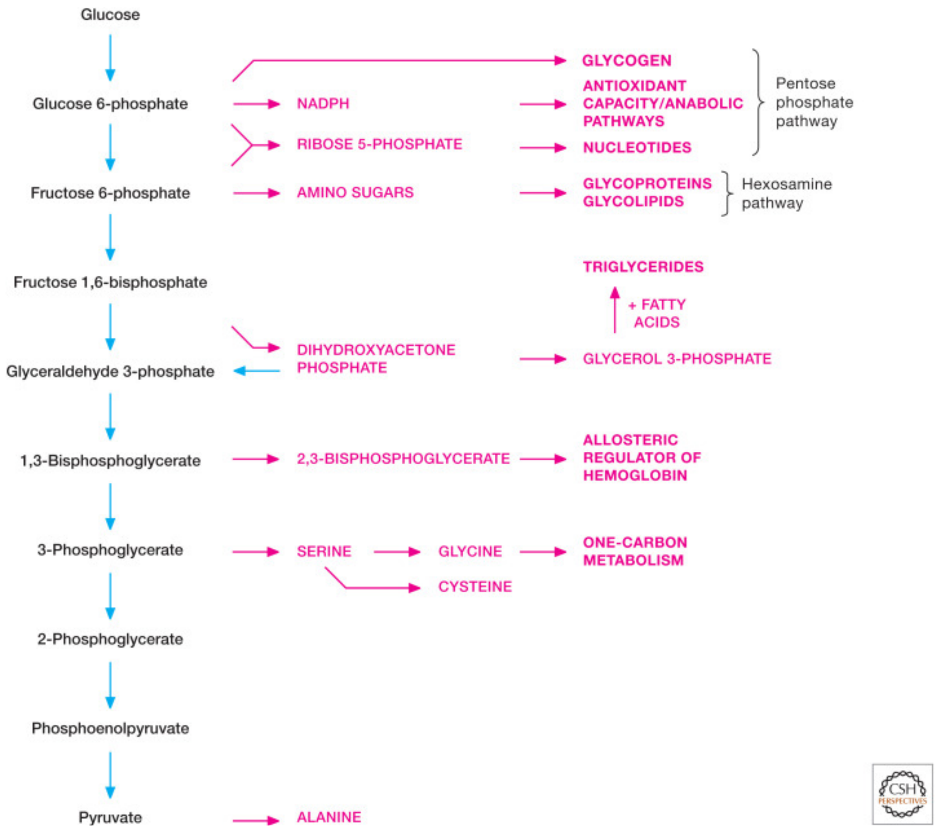

Figure 7: Glycolysis intermediates are involved in biosynthetic pathways. Glucose-6-phosphate can enter the pentose phosphate pathway generating NADPH for antioxidant pathways or ribose for nucleotide synthesis. Fructose-6-phosphate can enter the hexosamine pathway to generate amino sugars for glycoproteins or glycolipids. Fructose-1,6-phosphate can be used as a precursor for fatty acid synthesis. In red blood cells, 1,3-bisphosphoglycerate is used for regulation of hemoglobin. 3-phosphoglycerate can be converted into serine, glycine and cysteine and pyruvate can be converted into alanine (Chandel, 2021).

Another difference between astrocytes and neurons in respect to glycolysis is a biproduct methylglyoxal (MG). MG is a highly reactive dicarbonyl compound that promotes the formation of advanced glycation endproducts (AGEs), which are associated with several neurodegenerative disorders (Münch et al., 2012). MG is detoxified via the glyoxalase system (glyoxalase 1 (Glo-1) and Glo-2). Both enzymes are expressed in higher levels in astrocytes compared to neurons, resulting in increased resistance to MG toxicity. This allows astrocytes to sustain high levels of glycolysis, as they can detoxify MG. In neurons, upregulation of glycolysis (i.e. by increasing the activity of PFKFB3) results in increased MG levels and MG- modified proteins (Bélanger et al., 2011b). This suggests that the limited capacity of neurons (unlike astrocytes) to upregulate their glycolytic flux may be related to their weaker ability to detoxify MG.

2.4.1.1 Excurse: Warburg effect

The Warburg effect describes a process of metabolic reprogramming, where even in the presence of oxygen high rates of lactate are produced. Usually, cancer cells switch to increased glycolytic flux without mitochondrial dysfunction (Koppenol et al. 2011). Studies showed that highly proliferating cells, such as cancer cells or neuronal precursor cells, increase activity and expression of enzymes that are involved in glycolysis such as glucose transporter 1, monocarboxylate transporter 4, hexokinase 2, phosphofructokinase 1, enolase1, low-activity pyruvate kinase and lactate dehydrogenase A (Mazurek et al., 2002; Vaupel and Multhoff, 2020). Increased levels of glycolytic intermediates are used to fuel into biosynthetic pathways to generate increased levels of lipids, proteins and nucleotides to sustain proliferation and unlimited growth (Hay, 2016). Under normal oxygen conditions, some cancer cells can use lactate as a source for oxidative phosphorylation by importing lactate via MCT1 into mitochondria (Semenza, 2008; Sonveaux et al., 2008).

2.4.2 Tricarboxylic acid (TCA) cycle

The TCA cycle, also known as citric acid or Krebs cycle, describes a series of regenerative enzymatic reactions within mitochondria that produce reduced nicotinamide adenine dinucleotide (NADH) and flavin adenine dinucleotide (FADH2). Mitochondria take up cytosolic pyruvate via mitochondrial pyruvate carries (MPC1 and MPC2), which is then decarboxylated to form acetyl Coenzyme A (acetyl CoA). The TCA cycle begins with the reaction combining acetyl-CoA (coming from fatty acids, amino acids or pyruvate oxidation) with oxaloacetate (OAA) to generate citrate. Citrate is then converted into its isomer, isocitrate, which is then converted into α-ketoglutarate (α-KG). α-KG is subsequently converted into succinyl-CoA,
thereby releasing two molecules of CO2 and generating two NADH molecules. Next, succinyl-CoA is converted into succinate, which is coupled to the generation of GTP, which can be converted into ATP. Succinate is oxidized to fumarate, thereby transferring two hydrogen atoms to FAD, producing 2FADH. The enzyme that performs this step, succinate dehydrogenase (SDH), is also part of the electron transport chain (ETC). Fumarate gets converted into malate and further into OAA, that in combination with acetyl-CoA molecule can start another TCA cycle (Fig. 8).

The TCA cycle is involved in both anabolic and catabolic processes. TCA cycle intermediates such as citrate are exported into the cytosol and provide building blocks for macromolecule synthesis. To provide inputs into the TCA cycle two anaplerotic mechanism are necessary: the conversion of pyruvate into OAA and of glutamine into α-KG via glutaminolysis (De Berardinis and Chandel, 2016). One TCA cycle generates GTP, 3 NADH and 1 FADH2 that transfer their electrons into the electron transport chain (ETC) where they are oxidized back to FAD and NAD+ to keep the TCA cycle functioning. This shows that the TCA cycle and OXPHOS tightly work together to efficiently cover cells energy demands (Martínez-Reyes & Chandel, 2020).

2.4.3 Oxidative phosphorylation (OXPHOS)

OXPHOS describes a system coupling the electron transport chain (ETC) respiration with ATP production that is performed by 5 multi-subunit complexes and 2 electron carriers located in the cristae of the inner mitochondrial matrix (IMM) (Fig. 8). During respiration, NADH provides electrons to complex I (NADH-ubiquinone reductase) whereas FADH2 does it to complex II (succinate-ubiquinone reductase). Electrons are then transferred to complex III (cytochrome c oxidoreductase) and complex IV (cytochrome c oxidase) via two diffusible small components: a lipid-soluble ubiquinone (CoQ, from I to II) and a water-soluble cytochrome c (cyt c, from II to IV). While cytochrome c receives electrons, it produces water from oxygen. Complexes I, III and IV translocate protons (hydrogen ions) across the IMM creating a membrane potential used by the F1-F0-ATP synthase (complex V) to produce ATP. This protonmotive force is also utilized by many transporters to translocate mitochondrial proteins, metabolites and positive charged ions, such as calcium, into the mitochondrial matrix (Papa et al., 2012). Additionally, OXPHOS provides the main source of ROS in form of hydrogen peroxide and superoxide which are tightly controlled by antioxidant systems (Barnham et al., 2004; Lupoli et al., 2018).

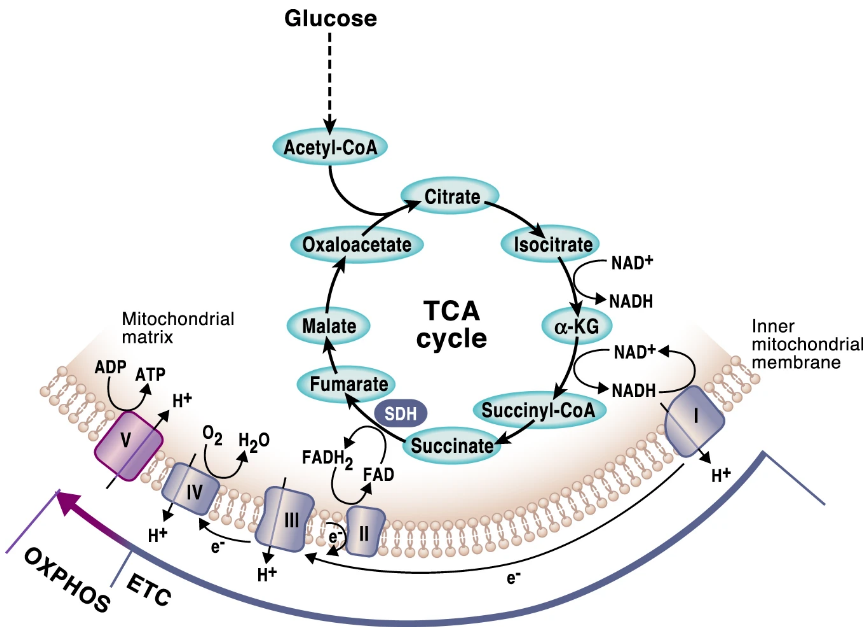

Figure 8: TCA cycle and OXPHOS are tightly regulated. TCA cycle is a series of enzymatic reactions within the mitochondrial matrix that produce reduced nicotinamide adenine dinucleotide (NADH) and flavin adenine dinucleotide (FADH2), which are required for electron transfer of mitochondrial chain complexes I-IV. As the electrons are transferred though the complexes in the inner mitochondrial membrane, a membrane potential is generated that is used to produce ATP. ATP production requires oxygen and takes places at complex V. This process is also called oxidative phosphorylation (OXPHOS) (Martinez-Reyes and Chandel, 2020).

2.5 Mitochondria

Mitochondria are not only essential for functional TCA cycle and OXPHOS for ATP production, as they also regulate several catabolic processes such as amino acid synthesis, Ca2+ and redox homeostasis, and apoptotic cell death.

Due to their large and highly specialized morphology, neurons depend on tight regulation of mitochondrial bioenergetics and mitochondrial transport. Correct position and a healthy proteome are crucial for maintaining a functional organelle that supports neuronal viability (Li et al., 2004; Courchet et al., 2013).

Mitochondria are endosymbiotic organelles containing a double membrane consisting of outer (OMM) and inner mitochondrial membrane (IMM), which forms specialized invaginations named cristae, an intermembrane space, and mitochondrial matrix. During evolution, most mitochondrial genes were transferred to the nuclear genome. In humans only 37 genes remain mitochondrial, encoding for 13 respiratory chain complex subunits, 22 transfer RNAs and 2 ribosomal RNAs. In mouse, a similar sequence and gene organization was observed (Maureen et al., 1981). All other mitochondrial proteins are synthesized in the cytoplasm and then imported into mitochondria (Zahedi et al., 2006; Schmidt et al., 2010; Rath et al., 2021).

Since neuronal structures as well as energy demands are constantly changing, the mitochondrial network needs to adapt constantly. Therefore, mitochondria have to redistribute constantly to regions with increased energy requirements such as sites of action potential generation and synapses, where mitochondria are strategically located to provide localized ATP efficiently (Devine and Kittler, 2018). In neurons, a tubular mitochondrial network is present in the cell body and dendrites but axonal mitochondrial display a unique morphology, with uniform and dispersed single mitochondria still forming and interconnected network (Collins et al., 2002; Rangaraju et al., 2019). Mitochondrial network dynamics is sustained via balanced fusion and fission events. Proteins driving fusion and fission belong to a large family of GTPases such as dynamin-related protein 1 (DRP1) for fission and optic atrophy 1 (OPA1) and Mitofusin 1/2 for inner and outer membrane fusion. Multiple signaling pathways converge on fusion and fission proteins to maintain mitochondrial network to support energetic requirements (Smirnova et al., 2001; Giacomello et al., 2020; Kraus et al., 2021).

Impairment in fusion results in fragmented mitochondrial network, whereas impaired fission results in hyperfused mitochondrial ultimately affecting mitochondrial bioenergetics (Burté et al., 2015). Mitochondrial associate with microtubular network for anterograde transport (kinesin) and retrograde transport (dynein) via interaction of OMM proteins (Morris and Hollenbeck, 1993; Sheng and Cai, 2012). Generally, mitochondrial motility is higher in cultured neurons but also higher in axonal shaft compared to terminal branches (Lewis et al., 2016). Studies showed that 50% of synapses are occupied by resident mitochondria and that those synapses contain more docked synaptic vesicles (Kwon et al., 2016; Smith et al., 2016).

2.6 Metabolic regulation

Multiple signaling pathways are involved in the regulation of brain glucose metabolism. Active Wnt3a-mediated Wnt signaling increases hexokinase activity thereby enhancing glucose uptake and glycolytic rate in neurons. Active Wnt signaling activates glycogen synthase kinase 3β (GSK-3β) which phosphorylates several downstream targets such as mTORC1 (Ma et al., 2011; Cisternas et al., 2016). Additionally, Wnt signaling supposedly has indirect effects on AKT and AMPK signaling pathway (Perry et al., 2011; von Maltzahn et al., 2012; Godoy et al., 2014). Insulin signaling is also involved in the regulation of glucose metabolism. Insulin binds to insulin receptors and modulates phosphoinositide 3-kinase (PI3K)
/AKT pathway, thereby controlling metabolism and mitogen-activated protein kinase pathway (MAPK), thereby regulating mitochondrial function (Kullmann et al., 2020). Increased PI3K/ AKT activity stimulates glucose uptake by increasing levels of glucose transporters, such as GLUT3 and GLUT4 (Liu et al., 2015; Gabbouj et al., 2019). In the hippocampus insulin signaling was shown to be important for spatial learning and memory by mediating GLUT4 levels (Mehran et al., 2012; Kleinridders et al., 2014; Soto et al., 2019).

Additionally, autophagy plays a major role in metabolic regulation mostly in response to starvation.

2.7 Autophagy and metabolism

ATG5-deficient mouse embryos die within a day of birth because of starvation due to hypoglycemia (Kuma et al., 2004). Re-expression of ATG5 in neurons could rescue ATG5-deficient animals from neonatal lethality (Yoshii et al., 2016).

Upon starvation, levels of glucose and amino acids decrease and therefore downstream metabolites such as TCA cycle intermediates. Starvation results in activation of AMPK, which in turn activates autophagic flux. AMPK mainly responds to energy levels of glucose and ATP. AMPK activates autophagic flux by inhibiting mTORC1 through direct phosphorylation and by phosphorylation of ULK1 (Inoki et al., 2006; Gwinn et al., 2008). mTORC1 pathway senses amino acid levels and in response to starvation mTORC1 activity is reduced, hence promoting autophagic flux (Li et al., 2017). Interestingly, mTORC1 is directly inhibited by hexokinase 2, the first irreversible enzyme of the glycolysis pathway, in the absence of glucose (Roberts et al., 2014).

Studies in cultured cells showed that bulk autophagy is induced upon serum or nutrient withdrawal, resulting in the release of many metabolites (Fig. 9.). Glycogen can be degraded into glucose to provide pyruvate and acetyl-CoA for TCA cycle and OXPHOS. Glucose-derived metabolites are used for anabolic processes such as synthesis of nucleotides and amino acids (Rabinowitz and White, 2010).

Autophagy controls metabolic states by removing damaged mitochondria via mitophagy. Dysfunctional mitochondria cannot maintain respirational capacity and release ROS that might result in apoptotic cell death (Wang and Youle, 2009). Especially, high metabolic organs such as the brain rely on high levels of mitophagy to sustain metabolic demands. Autophagy regulates metabolic states via degradation of metabolic enzymes. Especially CMA was shown to regulate cellular abundance of key metabolic enzymes. Liver-specific *lamp2a* knockout indicated that around 40% of CMA substrates are metabolic enzymes, such as glycolytic enzymes (Schneider et al., 2014). ER-stress induces metabolic alterations, such as altered glucose uptake and OXPHOS capacity (Wang et al., 2011). A major cause of ER-stress is the accumulation of protein aggregates within the ER caused by ineffective aggregate clearing by the autophagy pathway.

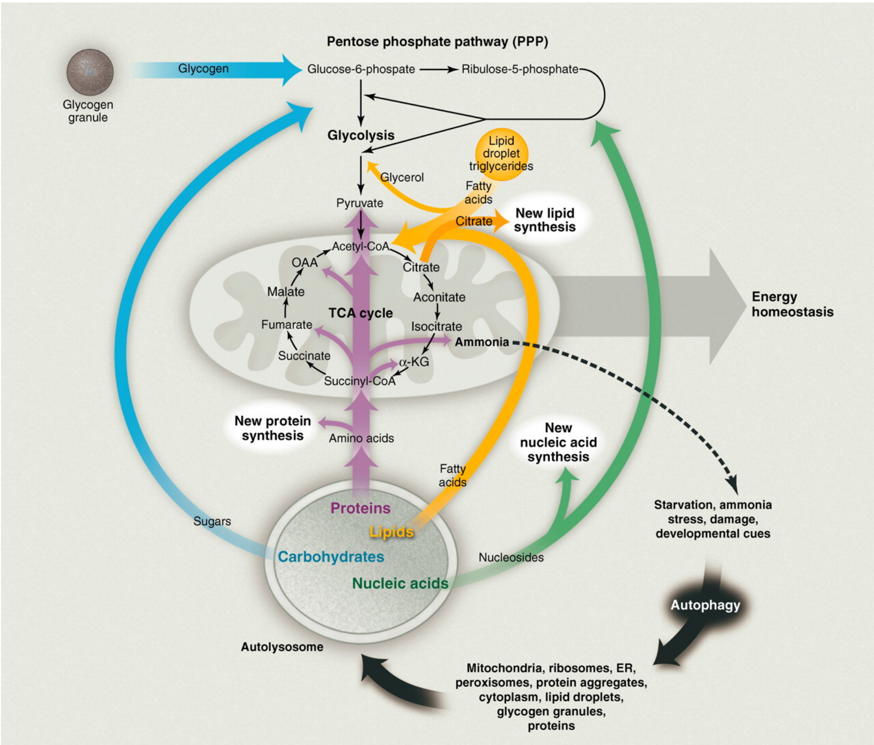

Figure 9: Autophagy provides nutrients in response to various stressors. Upon autophagy induction, the degradation of proteins, carbohydrates, nucleic acids and lipids provides substrates such as amino acids, sugars, fatty acids and nucleosides. Sugars such as glucose can be reused in glycolytic pathway or in the PPP. Nucleosides are used for nucleic acid synthesis mainly in PPP. Amino acids are used for protein synthesis, carbohydrate metabolism and TCA cycle. Fatty acids can be used for Acetyl-CoA and citrate synthesis (Rabinowitz and White, 2010).

2.8 Brain metabolism in diseases

Brain ageing and many degenerative diseases are characterized by altered brain metabolism. For example, loss of brain aerobic glycolysis is related to human aging and Alzheimer's disease as well as disruption of oxygen metabolism and mitochondrial function (Goyal et al., 2017; Vlassenko and Raichle, 2015).

2.8.1 Metabolism in aging

Healthy individuals from the age of 60 display progressive defects in working and spatial memory that correlate with neuroanatomical changes, such age-dependent decrease in gray matter volume in many cortical regions that are not related to pathological conditions (Resnick et al, 2003). The loss of grey matter is not caused by progressive degeneration but rather by the loss of dendritic arborization and synapse numbers (Page et al., 2002). Additionally, aerobic glycolysis gradually declines while aging (Goyal et al., 2014).

Functional neuroimaging studies have shown that glucose hypometabolism and mitochondrial dysfunction are early indicators of age-related functional changes (De Leon et al., 1983; Mosconi et al., 2008). PET imaging revealed age-related metabolic declines in temporal, parietal, and frontal cortex as well as cerebral cortex (Kuhl et al., 1984a). In rats, age-

dependent reduction in glucose metabolism in the hippocampus and prefrontal cortex is associated with impaired performance in learning and memory tests (Gage et al., 1984). When the neurons ability to generate sufficient ATP is compromised, synapses become vulnerable to dysfunction and degeneration (Harris et al., 2012). Many factors likely contribute to the age-dependent brain hypometabolism, such as increased permeability of the blood brain barrier that results in impaired import of nutrients (Rosenberg, 2012). Furthermore, expression levels of glucose transporters and metabolic enzymes of glycolysis and OXPHOS decrease with age, both in humans and animal models (Meier-Ruge et al., 1980; Ulfert, et al., 1982; Ding et al., 2013). In mice, ATP levels decline in white matter of aged animals associated with altered mitochondrial morphology and reduced mitochondria-ER contact sites (Stahon et al., 1016). Mice with reduced GLUT1 levels display an age-dependent reduced cerebral blood flow and glucose uptake that lead to dendritic spine loss in hippocampal neurons and impaired behavior (Winkler et al., 2015).

2.8.2 Metabolism in neurodegenerative diseases

Neurodegenerative diseases (NDDs) such as AD, PD and ALS are characterized by progressive region-specific neuronal loss, protein aggregation, impaired autophagic pathway, impaired axonal transport and mitochondrial dysfunction.

It is believed that metabolic alterations contribute to the initiation and progression of NDDs. PET imaging studies showed that patients with AD, PD, ALS, HD and ataxia display glycolytic hypometabolism in several brain regions which might result in increased neuronal vulnerability (Hoyer, 1982b).

AD patients and AD mouse models display increased oxidative stress, which impairs the function of glycolytic enzymes (Gordon et al., 2013; Butterfield and Hallowell, 2019). Levels of ROS are tightly controlled by antioxidant systems and their dysregulation has been linked to many neurodegenerative conditions including ALS, ataxia and AD (Barnham et al., 2004; Lupoli et al., 2018). Mitochondrial dysfunction can be observed in patients in early stages of AD (Terada et al., 2020). Pentatricopeptide repeat-containing protein 1 (PTCD1) is required for ATP production in mitochondria and gene variants leading to the disruption of neuronal energy homeostasis were identified in AD patients (Fleck et al., 2019).

AD mouse models show reduced hexokinase activity due to glucose-6-phosphate accumulation and mitochondrial complex I deficiency, especially in synapses, resulting in hypometabolism and energy failure (Demarest et al., 2020). Cortical regions of AD mice display reduced levels of GLUT1 and GLUT3 (Winkler et al., 2015; Szablewski, 2017). In drosophila AD-models, overexpression of glucose transporters or stimulation of increased glucose uptake results in increased survival rate (Niccoli et al., 2016). In AD mice, supplementation with ketone and nicotineamide improved behavioral deficits (Wang et al., 2022) A genetic risk factor for developing AD is ε4 allele of apolipoprotein E (APOE4), that affects insulin signaling and glucose metabolism. Mouse models with APOE4 mutations display deficits in glucose uptake, glucose metabolism and mitochondrial respiration (Keeney et al., 2015; Wu et al., 2018; Emrani et al., 2020). Dysfunctional glucose metabolism is also observed in early-stage AD patients. Moreover, AD mouse models show reduced glucose uptake in entorhinal cortex, hippocampus and amygdala prior to protein aggregation (Le Douce et al., 2020).

In PD hypometabolism in the caudate nucleus and inferior parietal lobe has been shown, as well as reduced glucose uptake in putamen after dopamine depletion (Meles et al., 2017; Ruppert et al., 2020). Familial PD is caused by mutations in *PARK6* (PINK1), *PARK2* (parkin), and *PARK7* (DJ-1) resulting in mitochondrial dysfunction (Pickrell and Youle, 2015). Parkin has been shown to regulate pyruvate kinase 2 activity and loss of parkin impairs glycolysis in neurons (Bogetofte et al., 2019).

In postmortem human PD brains, down-regulation of PPP enzymes and reduced NADPH are found in the putamen and cerebellum (Dunn et al., 2014). Decreased levels of the PPP key enzymes glucose-6-phosphate dehydrogenase and 6-phosphogluconate dehydrogenase occur at early stages in the putamen and cerebellum of PD patients (Dunn et al., 2014).

The glycolytic enzyme glucose-6-phosphate isomerase that catalyzes the conversion of G6P to F6P has been recently identified as a conserved modifier of dopamine metabolism, protein aggregation, and neurodegeneration in Caenorhabditis elegans, Drosophila melanogaster, and murine neurons (Knight et al, 2014).

In PD mouse models, activation of NADPH oxidase, a superoxide-producing enzyme, causes dopaminergic neurodegeneration and impairments of learning, memory, and motor functions. Blockage of NADPH oxidase resulted in neuroprotection (Hou et al., 2019). In addition, enhancing phosphoglycerate kinase 1 activity promotes glycolysis and ATP generation thereby slowing down neuronal loss and PD progression (Cai et al., 2019).

In HD patients, metabolic alterations in body weight and glucose homeostasis in pre-symptomatic and symptomatic disease stages. Especially, fluctuations in body weight of HD patients is used to predict the disease progression (van der Burg et al., 2009; Montojo et al., 2017). In HD patient brains, reduced glucose metabolism in striatum and cerebral cortex was shown prior to symptom onset (Kuhl et al., 1985; Antonini et al., 1996). Additionally, in post-mortem brain tissue of HD patients, reduced activity of OXPHOS complex II and III were detected in putamen and caudate nuclei (Gu et al., 1996; Browne et al., 1997). Additionally, increased levels of oxidative products such as protein carbonyls and lipofuscin indicate elevated levels of oxidative stress in HD brains (Browne and Beal, 2006). Proteomic analysis of brain tissue of R6/2 HD mouse model indicated alterations in proteins associated with branched chain amino acid metabolism, synaptic functions, glycolysis, TCA cycle and glutamate-GABA-glutamine metabolism (Skotte et al., 2018; Andersen et al., 2019).

Patients with cerebellar ataxia display a variety of metabolic alterations such as accumulation or deficiency of certain metabolites and dysfunctional energy metabolism. Many forms of cerebellar ataxia are caused by OXPHOS deficiencies (coenzyme Q10) or glucose metabolism deficiencies (GLUT1 or pyruvate dehydrogenase) (De Vivo et al., 1991; DeBrosse et al., 2012; Sofou et al., 2017). Other forms are cause by accumulation of lipids (Niemann-Pick type C, GM2 gangliosidosis) (Davidson et al., 2016; Schicks et al., 2012).

Interestingly, most metabolic disorders cause cerebellar dysfunction and atrophy (Poretti et al., 2016). Additionally, ataxia patients have an increased risk to develop diabetes mellitus and glucose intolerance (Kong et al., 2014; Garg et al., 2017).

3. Cerebellum

3.1 Anatomy

The cerebellum, which is the largest part of the hindbrain, is located in the posterior cranial fossa, behind the fourth ventricle, the pons, and the medulla oblongata. It is composed of two hemispheres and sub-divided into four lobes – anterior, posterior, central and flocculonodular (Fig. 10). The outermost part of the cerebellum is the cerebellar cortex composed of various folds, which are divided by fissures. In mammals up to ten lobes can be detected in the most central part (Delgado-García, 2002). The vestibulocerebellum, associated with the flocculonodular area (lobe X and cerebellar floccules and parafloccules), receives vestibular and visual inputs and sends projections to the vestibular nuclei, which are regulating balance, vestibular reflexes, and eye movements. The spinocerebellum, comprised of the vermis (lobes I–IX) and part of the hemisphere, receives somatosensory and proprioceptive inputs from the spinal cord, and projects towards descending pathways controlling the axial muscles. The cerebrocerebellum consists of the hemispheres and receives inputs from the cerebral cortex, and sends output to motor, premotor, and prefrontal areas of the cortex (Brooks and Thach, 1981).

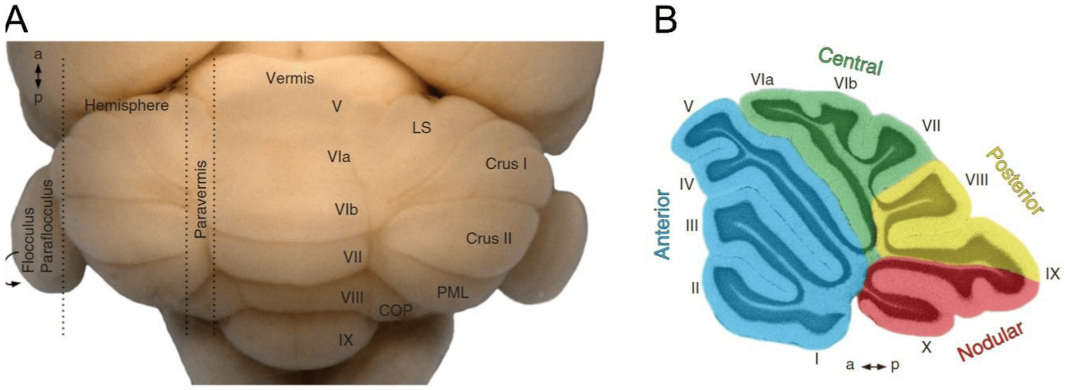

Figure 10: Cerebellum of an adult mouse. (A) Dorsal view of the whole cerebellum. The main regions that can be identified are vermis, paravermis and hemispheres. The cerebellum can be divided into ten lobes (I-X). (B) Sagittal section of cerebellar vermis showing the four main domains: anterior, central, posterior and nodular and the ten lobes (Hernández-Pérez et al., 2023).

The cerebellum contains 80% of the brain's neurons and it is highly organized way (van Essen et al., 2018). Its cerebellar cortex is divided into three layers: granular cell layer, Purkinje cell layer and molecular cell layer (Fig. 11). The granular cell layer contains mainly excitatory granular cells and unipolar brush cells, but also inhibitory Golgi cells (Sillitoe, and Joyner, 2007). The Purkinje cell layer contains mainly inhibitory Purkinje cell somata but also some Bergmann glia somata. The outermost layer is called molecular cell layer. It consists of Purkinje cell dendrites, inhibitory interneurons such as basket and stellate cells and parallel fibers, the axons of granular cells (Voogd and Glickstein, 1998; White and Sillitoe, 2012). Afferent input into the cerebellum comes from the spinal cord, brainstem, cerebral cortex and inferior olive via excitatory mossy or climbing fibers. Mossy fibers synapse onto granular cells and unipolar brush cells. Climbing fibers synapse onto Purkinje cells (Busch and Hansel, 2023). Parallel fibers are granular cell axons, that ascent to the molecular cell layer and synapse onto Purkinje cell dendrites, molecular cell layer interneurons and Golgi cells (Eccles, 1967; Ito, 1984). Climbing and parallel fibers give both excitatory input on Purkinje cell dendrites. However, climbing fibers primarily target primary Purkinje cell dendrites, whereas parallel fibers primarily target secondary and tertiary dendrites (Strata and Rossi, 1998).

Purkinje cells are the only efferent neurons of the cerebellar cortex and synapse onto excitatory deep cerebellar nuclei. Deep cerebellar nuclei receive excitatory input from mossy and climbing fibers and project onto nuclei of the brainstem and diencephalon such as thalamic nuclei. In the molecular cell layer, parallel fibers, stellate and basket cells synapse onto Purkinje cell dendrites (Barmack et al., 1992; Voogd and Glickstein, 1998; Miall, 2013; Beckinghausen and Sillitoe, 2018; Consalez et al., 2021).

Extensive mono- and poly-synaptic pathway analysis could show that the cerebellum is connected to various brain regions such as the cerebral cortex, hippocampus, amygdala, hypothalamus, periaqueductal gray, basal ganglia, thalamus, brain stem, and spinal cord

(Dietrichs and Haines, 1989; Middleton and Strick, 2001; Hoshi et al., 2005; Cerminara et al., 2009; Buckner et al., 2011; Dum and Strick, 2012).

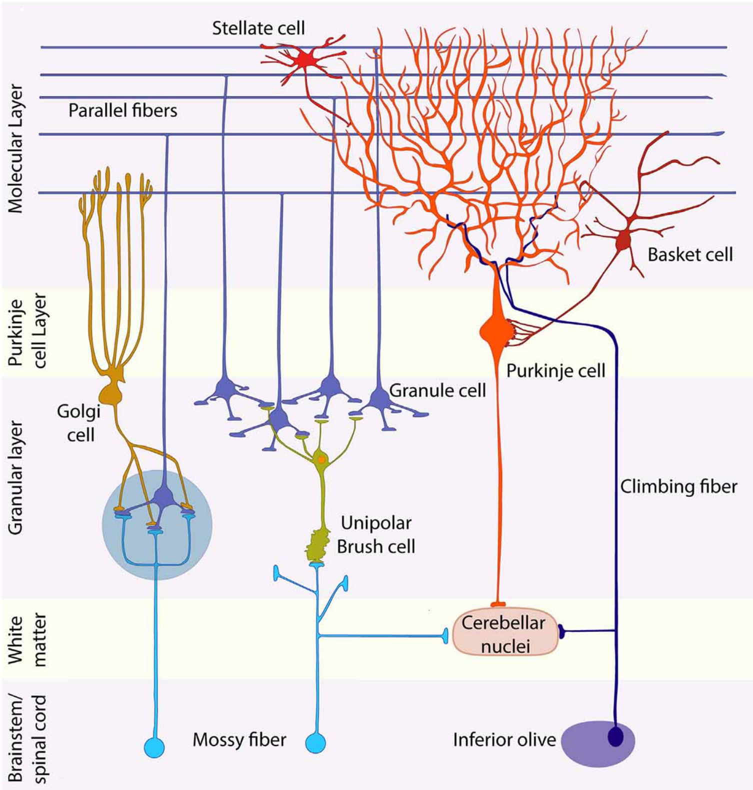

Figure 11: Structure of the cerebellar cortex. The cerebellar cortex is organized in three layers: molecular cell layer, Purkinje cell layer and granular cell layer. Purkinje, basket, stellate and Golgi cells are inhibitory neurons while unipolar brush and granular cells are excitatory neurons. Granular cells project their axons into molecular cell layer as parallel fibers, with synapses onto stellate, basket and Purkinje and Golgi cells. Excitatory input into cerebellar cortex come from brainstem nuclei (mossy fibers) and inferior olive (climbing fibers). Most mossy fibers synapse onto granular cells and a few onto unipolar brush cells. Each Purkinje cell receives input from a single climbing fiber and stellate and basket cells. Purkinje cells give inhibitory input onto deep cerebella nuclei, while mossy and climbing fibers give excitatory inputs. Cerebellar nuclei are excitatory neurons that project into nuclei of the brainstem and diencephalon such as thalamic nuclei (Consalez et al., 2021).

3.2 Cerebellar functions

The cerebellum plays a fundamental role in movement regulation and balance control. It coordinates gait and posture, it controls muscle tone and voluntary muscle activity. Dysfunctional cerebellum impairs the ability to control movements, posture and motor learning (Manto et al., 2012; Roostaei et al., 2014; Witter and Zeeuw, 2015). Although the cerebellum is linked to motor control, it is also involved in non-motor functions such as cognitive and emotional control and sleep (Galliano et al., 2013).

The best-known neocerebellar function is the planning and execution of fine and precise movements.

Several studies established a concept of three functional zones of the cerebellum: (I) the midline structures with the vermis and the flocculonodular lobes, (II) the intermediate zones and (III) the lateral zones of the cerebellar hemispheres.

Animal and human studies could show that functional zone (I) is important for balance regulation and regional dysfunctions result in gait disturbances, disturbed flexor/ extensor muscle activity and impaired sensorimotor processing. Flocculonodular lobe integrates vestibular information for motion feedback. Patients with floccular hypofunction exhibit aberrant walking pattern with increased walking irregularities during slow locomotion (Schniepp et al., 2014). The intermediate zones are involved in precise limb movements such as adjusting intra- and inter-limb coordination and the lateral zones are involved in complex walking paradigms such as visually guided locomotion and adjustment of locomotor patterns (Morton and Bastian, 2007; Ilg and Timmann, 2013).

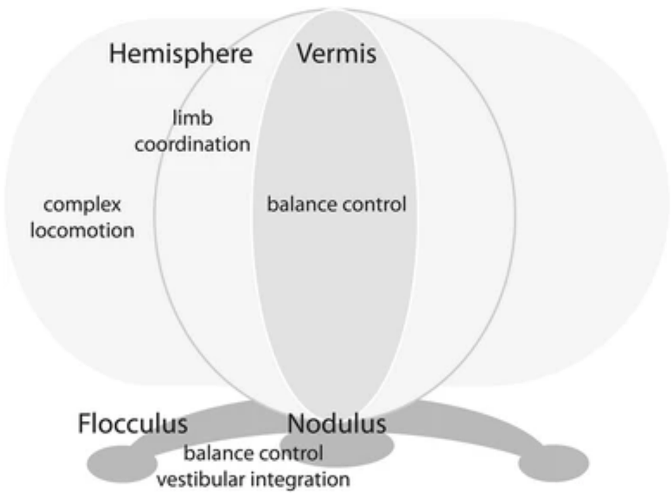

Figure 12: Scheme for different locomotor control regions within the cerebellum. Midline structures such as vermis, nodulus and flocculus are important for balance control during walking. The flocculus additionally integrates vestibular information. The intermediated zone of the cerebellar hemisphere controls multi-joint movements for limb coordination. Complex locomotor functions are controlled by lateral zones of the cerebellar hemispheres (Schniepp et al., 2017)

3.3 Cerebellar dysfunction

The cerebellum can be affected by direct mechanical trauma, vascular damage (stroke), degenerative diseases such as multiple sclerosis, and by long-term alcohol abuse. Cerebellar dysfunctions can be divided into motor and non-motor disease. Motor diseases include ataxia, dystonia, Huntington’s, Multiple sclerosis, Parkinson’s, Tremor and Tourette’s. Non-motor diseases include autism spectrum disorder, fetal alcohol syndrome, schizophrenia, vertigo and many more (Reeber et al., 2013).

3.3.1 Ataxia

Spinocerebellar ataxias (SCAs) are a genetically heterogeneous group of autosomal dominant inherited disorder. About 40 different types of ataxia have been identified, all characterized by uncoordinated movements (ataxic movements) such as cerebellar tremor and dyssynergia (the loss of simultaneous joint movements) (Vilis and Hore, 1980; Bastian et al., 1996).

Patients with cerebellar ataxia typically walk with increased step width, variable foot placement and irregular foot trajectories. This leads to an instable walk with high movement variability and high risk of falling (Diener and Dichgans, 1996; Morton and Bastian, 2004; Ilg et al., 2007; Fonteyn et al., 2012). Most SCA types cause Purkinje cell degeneration and cerebellar atrophy, but also spinal cord, basal ganglia and the brainstem can be affected (Klockgether et al., 2019). Recent findings indicated that mitochondrial dysfunction might precede disease onset in spinocerebellar ataxia (McBride et al., 2006; Pfeffer et al., 2012; Cornerlius et al., 2017).
Autophagy has been implicated in ataxia as well, since common forms of spinocerebellar ataxia (SCA1, SCA2, SCA3, SCA6) are characterized by intracellular accumulation of aberrantly folded polyglutamine-containing proteins. Upregulation of autophagic flux in a SCA3 mouse model resulted in improved clearance of proteins aggregates and improved motor behavior (Menzies et al., 2010). Two subjects with recessive ataxia were identified that displayed congenital ataxia, mental retardation and developmental delay in patients associated with a smaller cerebellum. The causative mutation is a E122D change in the *ATG5* gene causing an E/Glu to D/Asp change, which results in loss of function mutation. The E122D variant displayed reduced autophagic flux in yeast, mammalian cells and *Drosophila*. In addition, patient cells displayed decreased autophagic flux and defects in the conjugation of ATG12 to ATG5 (Kim et al., 2016).

II. Aims

Brain-confined loss of ATG proteins in all neuronal precursor cells (*Nestin*-Cre) results in growth retardation and behavioral deficits. Those animals displayed degeneration of neurons in several brain areas, accompanied by axonal degeneration and accumulation of intracellular proteins aggregates (Hara et al., 2006; Komatsu et al., 2006; Komatsu et al., 2007b; Liang et al., 2010; Zhao et al., 2015; Joo et al., 2016; Yamaguchi et al., 2018).
Neurons are specialized postmitotic cells with a unique morphology, composed of elaborated dendritic trees and long axons. Their complex morphology makes neurons extremely dependent on a well-working clearance process and transport system to remove harmful material and constantly reorganize to maintain cellular homeostasis. Mouse lines with neuron-specific ablation of ATG proteins in excitatory forebrain neurons (McMahon et al., 2012), dopaminergic neurons (Hernandez et al., 2012), and striatal spiny projection neurons (Lieberman et al., 2020), as well as mice deficient for ATG5 in excitatory and inhibitory forebrain neurons (Negrete-Hurtado et al., 2020; Overhoff et al., 2022) do not show any neuronal loss.
Interestingly, not all neurons are resistant to autophagy-deficiency. Specific loss of ATG5 or ATG7 in Purkinje cells result in axonal dystrophy and accumulation of abnormal organelles, followed by age-dependent Purkinje cell death and mouse behavioral deficits (Komatsu et al., 2007; Nishiyama et al., 2007).
Molecular and cellular mechanisms underlying selective vulnerability or resistance of different neuronal subtypes to autophagy dysfunctions are currently unknown, resulting in the two main questions of this study:

1. Why are Purkinje cells more vulnerable to autophagy loss compared to cortical inhibitory neurons?

2. How exactly is autophagy dysfunction linked to Purkinje cell degeneration?

To understand the selective vulnerability of Purkinje cells a neuronal-confined mouse model of ATG5 deficiency in inhibitory neurons of the brain was used, allowing to compare the effects of autophagy deficiency between cortical and cerebellar cells. Therefore, a combination of positron emission tomography (PET) imaging, quantitative proteomics, untargeted metabolomics, stable isotope-labeling studies and live-imaging approaches of *ex vivo* cerebellar slices was performed.

III. Material and Methods

1. Materials

Table 1: Instruments used for this study.

Instrument	Manufacturer	Catalogue number
bioRupter, Picorupter	Diagenode	B01060010
BioTek Cytation Hybrid Multimode Reader	AGILENT	
Cabinet, Horizontal laminar flow	Thermo Fisher Scientific	Heraguard ECO
Cabinet, vertical laminar flow (primary cells)	Thermo Fisher Scientific	Safe 2020
Cell culture inserts	Merck	PICM0RG50
Centrifuges	Eppendorf Hettich VWR	5702R 320R MicroSTAR 17R
Double Edge Coated Blades (Washed version)	Electron Mircoscopy Science	#72000-WA
EASY-nLCTM 1200 System	Thermo Scientific	LC140
Electrophoresis Power Source	VWR	300V
Electrophoresis chamber (PCR)	VWR	700-0569
Electrophoresis chamber (WB)	Bio-Rad	Mini-Protean Tetra Cell
VOSEP ONE	Evosep	EV-1000
Dissection tools Forceps Scissors Scalpel	FST	 11253-27 1 6020-14 11270-20 14090-09 13002-10 14002-13 10073-14
Feezer (-20°C)	LIEBHERR	9988187-12
Fridge (4°C)	LIEBHERR	9983491-10
Gel imager system (PCRs)	Bio-Rad	Gel DocTM XR+
Incubator CO2 (cell lines)	Binder	C170
Incubator Shaker	Eppendorf	Galaxy 1705
Incubator CO2 (primary neurons)	Eppendorf	M1335-0002
McIlwain Tissue Chopper	Cavey laboratory engineering Co. LTD	MTC/5E
Microscope, inverted (cell culture)	Leica	Leica DMi1
Microscope, inverted fluorescence Camera	Zeiss Hamamatsu	Axiovert 200M C11440
Temperature module LED Light source Software Objectives: 40x/1.4 oil DIC 63x/1.4 oil 10x/0.3	Zeiss CoolLED Micro-Manager Zeiss Zeiss Zeiss	TempMoudleS pE-4000 MicroManager1.4 420762-9900 420780-9900 420304-9901
Microtom	Thermo Fisher Scientific	Microm HM 430
Microwaver	Inverter	Sharp

Neubauer chamber	Marienfeld	0640110
Osmometer	Gonotec	Osmomat 3000
pH-meter	Mettler Toledo	Seven Easy
Perfusion pump	WPI	Peri-Star Pro
Photometer	Eppendorf	Bio Photomer plus
Real-time PCR Thermocyler	Applied Biosciences	7500 RealTimePCR System
SeahorseXF Pro M FluxPak Mini	Agilent	103777-100
Seahorse XFe96 Analyzer	Agilent	
Seahorse XF Calibrant solution	Agilent	100840-000
Seahorse XF Cell Mito Stress Test Kit	Agilent	103015-100
Seahorse XF Glycolysis Stress Test Kit	Agilent	103017-100
Sonicator	BRANSON	Sonifier 250
Scales	OHAUS VWR	EX225D T1502746
SpeedVac Eppendorf Concentrator plus	Eppendorf	5305000509
Thermocycler	VWR	peqSTAR
Thermoschaker	CellMedia	
Water bath	VWR	VWB6
Vortex	Scientific Industries	Vortex-Genie 2

Table 2: Chemicals used for solutions and buffers.

Chemical	Manufacturer	Identifier
2-NBDG	Biomol	ABD-36702
2-DG	Roth	CN96.3
2-ß-Mercaptoethanol	Roth	4227.1
2-Propanol	Roth	CP41.3
Acetic acid 100%	Roth	3738.4
Acetone	Roth	5052.1
Aceton (Proteomics)	Merck	1.00020.2500
Acetonitrile hypergrade for LC-MS LiChrosolv	Merck	1.00029.2500
Antimycin	Sigma	A8674
Ammonium chloride	Roth	K298.2
Ammonium peroxidisulfate (APS)	Merck	1.012.001.000
Ampicillin sodium salt	Roth	K029.2
AR-C155858 (MCT1 and MCT2 inhibitor)	Tocris	4960
Ascorbic acid	Roth	3525.1
Boric acid	VWR	J67202
Bovine Serum Albumin	Sigma	A7906
Bromophenol blue	Sigma	B5525
2-Chloracetamid (CAA)	Merck	CAS 79-07-2
Calcium chloride dihydrate	Roth	5239.2
Calcium chloride hexahydrate	Roth	T886.1
Chloroquine disphosphate salt	Sigma	C6628
Cresyl violet acetate	Sigma	C5042
1,4-Dithioerythritol (DTT)	Applichem	CAS 3483-12-3
D-(+)-Glucose	Sigma	G5767
D-mannitol	Roth	M4125

Dimethyl sulfoxide (DMSO)	Roth	A994.2
di-Potassium hydrogenphoshate	Roth	6875.1
di-Sodium hydrogen phosphate dihydrate	Roth	4984.1
di-Sodium hydrogen phosphate anhydrous	Merck	106559
EDTA	Applichem	A1104.1000
Entellan®	Merck	107960
Ethanol	Omnilabs	A1613.2500PE
EZ-Link™ Sulfo-NHS-SS-Biotin, No-Weigh-Format	Thermo Fisher Sci	A39258
FCCP	Sigma	SML2959-1ML
Formic Acid	Honeywell/FLUKA	607-001-00-0
Gelatin from porcine skin	Sigma	G2500
Glycerol	Roth	7530.1
Glycine	Roth	3908.3
HEPES	Sigma	H4034
Hydrochloric acide 32%	Roth	X896.2
IGEPAL	Sigma	I8896
Luminol	Roth	4203.1
Lysyl Endopeptidase (LysC)	WAKO	129-02541
Magnesium chloride hexahydrate	Roth	2189.1
Methanol	Roth	4627.5
Methanol LC-MS grade	VWR	83638.32
Milk powder	Roth	T145.2
Oligomycin	Sigma	495455
Paraformaldehyde (PFA)	Merck	104.005.100
p-coumaric acid	Sigma	C9008
Ponceau S	Roth	5938.1
Potassium chloride	Roth	6781.1
Potassium dihydrogen phosphate	Roth	3904.1
Potassium disulfite	Sigma	60508
Rotenone	Sigma	R8875
Sodium Chloride	Roth	3957.1
Sodium hydrogen carbonate	Roth	6885.1
Sodium dodecyl sulfate (SDS) ultra-pure	Roth	2326.2
Tetramethylenediamine (TEMED)	Applichem	A1148.0028
Tris (hydrogenmethyl) aminomethane (Tris- base)	VWR	28.808.294
Trizma hydrochloride (Tris-HCl)	Sigma	T3253
Trypan Blue	Roth	CN76.1
Tween 20	VWR	663684B
Urea	Sigma	U1250
Xylene	VWR	28975.291

Table 3: Reagents used in this study.

Reagent	**Manufacturer**	**Identifier**
Acryl/BisTM solution (30%) 37.5:1	VWR	E347
Bradford Reagent	Sigma	B6916
Bovine Serum Albumin	Sigma	A7906
Bovine Serum Albumin (fatty acid free)	Sigma	A6003
Complete Mini Protease Inhibitor	Roche	11836153001
DNA ladder (100 bp/ 1 kb)	Thermo Fisher Sci	SM0323/SM0311
DNA Gel Loading Dye (6X)	Thermo Fisher Sci	R0611
DreamTaq DNA polymerase	Thermo Fisher Sci	EP0703
DynabeadsTM Protein G	Invitrogen	10003D
ECLTM WB detection reagents	GE Healthcare	RPN2106
Isoflurane	Piramal	B73E16A

Ketamin hydrochloride	Sigma	K2753
Normal donkey serum	Merck	566460
LongAmp Taq DNA polymerase	BioLabs	M03235
Normal Goat Serum	Gibco	16210064
Nuclease-free water	Ambion	AM9938
PageRuler Plus Prestained Prot. Ladder	Thermo Fisher Sci	26619
Pierce™ High Capacity Streptavidin Agarose	Thermo Fisher Sci	20359
PierceTM Protease and phosphatase inhibitor mini tablets	Thermo Fisher Sci	A32959
Proteinase K	Sigma	AM2546
Rompun 2% (Xylazin)	Bayer	KP0BZPE
SuperSignalTM West Femto	Thermo Fisher Sci	34094

Table 4: Cell culture ingredients and reagents used for media preparation.

Reagent	**Manufacturer**	**Identifier**
B-27 Supplement (50X)	Thermo Fisher Sci	17504-044
Cytosine ß-D-arabinofuranpsode hydrochloride	Sigma	C6645
DMEM without glucose	Thermo Fisher Sci	A14430
Deoxyribonuclease I from bovine pancreas	Sigma	D5025
EBSS	Thermo Fisher Sci	14155-048
Fetal Bovine Serum	Merck	S0115
Fetal Bovine Serum	Sigma	F7524
GlutaMAXX^{TM}	Thermo Fisher Sci	35050-061
HBSS (1X) [-] $CaCl_2$, [-] $MgCl_2$	Thermo Fisher Sci	14175-053
HEPES (1M)	Thermo Fisher Sci	15630-080
Horse serum (heat-inactivated)	Gibco	26050088
Insulin, human recombinant zinc	Thermo Fisher Sci	12585-014
MEM	Sigma	7278
Penicillin/Streptomycin (P/S)	Thermo Fisher Sci	15140-122
Poly-D-lysine (1mg/mL)	Merck	A-003-E
Soybean Trypsin Inhibitor	Merck	10109886001
Sodium Pyruvate	Thermo Fisher Sci	11360-039
Transferrin, Holo, Bovine Plasma	Merck	616420
Trypsin from bovine pancreas	Sigma	T1005

Table 5: Data acquisition and analysis.

Computing	**Software**	**Manufacturer**
Image processing	Fiji version 1.53	Wayne Rasband, National Institute of Health
Image processing	Aperio Image Scope version 12.4.3.5008	Leica
Imaging processing	Vinci version 5.06	Max-Planck-Institute for Metbolism Research, Cologne
Statistical analysis	GraphPad Prism version 9.5.1	GraphPad Software
Image acquisition	LAS X	Leica

Table 6: Microsocpes.

Microscope	Manufacturer	Identifier
Transmission electron microscope	JEOL	JEOL JEM2100PLUSCameraGATAN
Slidescanner	Hamamatsu	S360
Confocal microscope Stellaris 20x objective 40x objective 63x objective	Leica Microsystems	Stellaris 5 HC PL APO 20x/0.75 CS2 HC PL APO 40x/0.95 CORR HC PL APO 63x/1.30 GLYC CORR CS2
Multiphoton confocal microscope 20x objective	Leica Microsystems	TCS SP8 MP-OPO PL Apo 20x/0.75 multi immersion
Confocal microscope SP8 10x objective 40x objective 63 x objective	Leica Microsystems	TCS SP8 PL Apo 10x/0.40 CS2 PL Apo 40x/0.85 CORR CS PL Apo 63x/1.40 Oil CS2

2. Methods

2.1 Animals

2.1.1 Mouse breeding and maintenance

All animal experiments were approved and performed according to the regulations of LANUV (Landesamt für Natur, Umwelt und Verbraucherschutz Nordrhein-Westfalen) guidelines. Mice were maintained in a pathogen-free environment in ventilated polycarbonate cages. Animals were housed in groups of five animals per cage with constant temperature and humidity at 12h/12h light/dark cycles. Food and water were provided *ad libitum*. Breedings were set up with males at least eight weeks old and females at least 6 weeks old. Pups were weaned at the age of 21 days.

2.1.2. Conditional gene activation of ATG5 and GLUT2 in GABAergic neurons

Animals used in this study are displayed in table 5. *Slc32a1*-Cre mice were created by driving Cre recombinase expression from the 3' untranslated region (3'UTR) of the endogenous vesicular GABA transporter (VGAT) gene (*Slc32a1*) (VGAT-Cre, #016962, The Jackson Laboratory). Exon 3 of the *Atg5* gene and exon 11 of the *Slc2a2* gene were flanked by loxP sites thereby creating *Atg5*^{flox} and *Slc2a2*^{flox} animals, respectively. *Slc2a2*^{flox} animals were generated via IVF (sperm was kindly provided by Bernhard Thorens, Lausanne, Switzerland).

To generate conditional ATG5 cKO animals *Slc32a1*-Cre mice were crossed with *Atg5*^{flox} animals. To generate ATG5 cKO:GLUT2 cKO animals, *Atg5*flox:*Slc32a1*-Cre animals were crossed with *Slc2a2*^{flox} animals.

Reporter lines were created by crossing both lines to Ai9(RCL-tdT) (tdTomato) line, kindly provided by Prof. Matteo Bergami (CECAD, Cologne, Germany).

Table 7: Mouse lines used in this study.

Mouse model	Manufacturer
*Atg5*flox:*Slc32a1*-Cre	Kononenko lab (Negrete-Hurtado et al., 2020; Overhoff et al., 2022)
*Atg5*flox:*Slc32a1*-Cre:tdTomato	Kononenko lab (Negrete-Hurtado et al., 2020; Overhoff et al., 2022)
*Atg5*flox:tdTomato	Kononenko lab (Negrete-Hurtado et al., 2020; Overhoff et al., 2022)
*Atg5*flox:*Glut2*flox:*Slc32a1*-Cre:tdTomato	Kononenko lab
*Atg5*flox:*Glut2*flox:tdTomato	Kononenko lab
*Atg5*flox	Kononenko lab (Negrete-Hurtado et al., 2020; Overhoff et al., 2022)

2.2 Genotyping

2.2.1 Tissue sample and DNA extraction

For genotyping, tissue probes were taken from newborn pups at postnatal day 1-3 (tail tip) or from 3 weeks old mice (ear punches). For DNA extraction, tissue samples were incubated in 300 µl of extraction solution (table 6) including proteinase K overnight at 55°C on a shaker. Afterwards samples were quickly spinned down, supernatant was transferred into fresh tubes and overlayed with 400 µl of isopropanol. After 15 minutes (min) incubation at room temperature samples were centrifuged at 13 000 rpm for 10 min. Supernatant was discarded and 300 µl of 70% ethanol was added before another 10 min centrifugation at 13 000 rpm. Afterwards supernatant was discarded and samples were dried for at least 30-45 min at 55°C on a shaker. The pellet was then dissolved in 75 µl of autoclaved water.

Table 8: Buffers used for genomic DNA extraction.

Buffers	Ingredients
Extraction solution	100 mM Tris-HCl pH 8.8 5 mM EDTA 0.2% SDS 200 mM NaCl 200 µg Proteinase K

2.2.2 PCR and gel electrophoresis

In order to determine allele inheritance, genotyping for single genes was performed by polymerase chain. Sample DNA and mastermix were mixed according to displayed protocols (table 7). PCR program specification are displayed in table 10.

Afterwards PCR samples were run on 2% agarose gels containing SYBR safe for 1h at constant voltage (120V). A 100 bp DNA ladder was used as a marker. Results were visualized via gel imaging system (BioRad).

Table 9: Primer sequences for genotyping.

Gene	Sequence (5' - 3')
Glut2	
7S	CCA ATC CCT TGG TTC ATG GTT GC
7AS	CGT AAG GCC CAA GGA AGT CCT GC
7AS Δ	CTG CTA AAG CGC ATG CTC CAG AC
Atg5	
forward1	GAA TAT GAA GCC ACA CCC CTG AAA TG
forward2	ACA ACG TCG AGC ACG CTG GCG AAG G
reverse	GTA CTG CAT AAT GGT TTA ACT CTT GC
Cre	
Cre_1	GAA CCT GAT GGA CAT GTT CAG G
Cre_2	AGT GCG TTC GAA CGC TAG AGC CTG T
Cre_3	TTA CGT CCA TCG TGG ACA
Cre_4	TGG GCT GGG TGT TAG CC
tdTomato	
tdTomato_1	AAG GGA GCT GCA GTG GAG TA
tdTomato_2	CCG AAA ATC TGT GGG AAG TC
tdTomato_4	GGC ATT AAA GCA GCG TAT CC
tdTomato_4	CTG TTC CTG TAC GGC ATG G

Table 10: PCR protocol for ATG5, GLUT2, tdTomato, Slc32a1-Cre.

Ingredient	Volume
Sample	2 µl
DreamTaq Buffer	2 µl
25 mM $MgCl_2$	2 µl
2 mM dNTPs	1.5 µl
Primer (10 mol/ µl)	0.75 µl
DreamTaq Polymerase	0.2 µl
Autoclaved water	12.55 µl

Table 11: Band size of PCR products.

Gene	Band size in basepairs (bp)	
	WT	KO
Atg5	350	700
Slc2a2	235	326
tdTomato	297	196
Slc32a1-Cre	250	320

Table 12: PCR Programs.

		ATG5		Slc2a2		tdTomato		Slc32a1-Cre	
Cycle number		36		28		10		35	
		T (°C)	Time (min)	T (°C)	Time (min)	T (°C)	Time (min)	T (°C)	Time (min)
Initial denaturation		94	4	95	1	94	2	95	5
Cycle	Denaturation	94	0.5	95	15s	94	2	95	0.5
	Annealing	63	0.5	60	15s	65	15	62	0.5
	Elongation	72	1s	72	0.5	68	10	72	0.5
Final extension		72	1s	72	5	72	120	72	5
Hold		4	∞	4	∞	4	∞	4	∞

Table 13: Solutions and buffers used for PCR and gel electrophoresis.

Buffers	**Ingredients**
2% SDS agarose gel	2% (w/v) agarose in 1x TBE
10x TBE	108g Tris-Base; 55g Boric acid; 7.4 g EDTA in 1l dH_2O

2.3 Primary cultures

2.3.1 PDL-coating

Coverslips for imaging, dishes and plates were coated with 0.1 M poly-D-lysine (PDL) diluted in PBS by covering surface with PDL solution for 4h at 37°C. Plates and dishes were then washed 3 times with autoclaved water and dried at 37°C until no solution was left.

2.3.2 Primary cortical culture

Postnatal pups (P1-3) were decapitated and brains were collected in Hank's + 20% fetal bovine serum (Hank's + FBS). Cortex was isolated, meninges were removed and then chopped into 700 µm small pieces (McIlwain tissue chopper, Cavey Laboratory Engineering Co. LTD). Brain tissue was washed twice with Hank's + FBS and then digested in digestion solution containing 10 mg trypsin and 1 µl DNase for 15 min at 37°C. Trypsinization was stopped by two washes with Hank's + FBS followed by two washed with Hank's. Tissue was then transferred into dissociation solution containing 10 µl DNase, mechanistically dissociated using fire-polished glass pipettes and centrifugated at 0.3 rcf for 8 min at 4°C. Supernatant was discarded, cells were dissolved in plating medium (500 µl per brain) and cell density was determined using Neubauer counting chamber. Cells were then plated at a concentration of 110000 cells per well. Cells were fed with plating medium after 1h, when cells were attached to PDL-coated surface. After 24 h half of the medium was replaced by growth medium containing 2 µM cytosine ß-D-arabinofuranoside hydrochloride (AraC) and after 48 h the same volume of growth medium containing 4 µM AraC was added to the wells. Cortical neurons were kept for 14-16 days (DIV14-16) under constant conditions at 37°C/5% CO_2.

Table 14: Solutions used for primary cortical culture.

Name	**Composition**
Basic media	1 l DMEM; 5 g glucose; 200 mg $NaHCO_3$; 100 mg transferrin
Digestion solution	dH_2O; 137 mM NaCl; 5 mM KCl; 7 mM Na_2HPO_4; 25 mM HEPES (pH=7.2)
Dissociation solution	Hank's; 12 mM $MgSO_4x7H_2O$
Growth medium	100 ml basic medium; 5 ml FBS; 10 mM glucose; 0.25 ml GlutaMAXX; 2 ml B27; 1 mM sodium pyruvate; 1 ml Penicillin/ Streptomycin (P/S)
Hank's	500 ml HBSS; 5 ml sodium pyruvate; 5ml HEPES; 5 ml P/S (pH=7.4)
Hank's + FBS	Hank's; 20% (v/v) fetal bovine serum (FBS)
Plating medium	100 ml basic medium; 10 ml FBS; 10 mM glucose; 1 ml GlutaMAXX; 625 µl insulin, 1.1 ml P/S

2.3.3 Primary cerebellar culture

Postnatal pups (P7-9) were decapitated and brains were collected in ice-cold solution B. Cerebellum was isolated and cut into 700 µm thick pieces (McIlwain tissue chopper, Cavey Laboratory Engineering Co. LTD). Pieces were incubated in solution B containing 0.25 mg trypsin for 15 min at 37°C. To stop trypsinization solution C containing trypsin inhibitor was added twice the volume as solution T and centrifuged at 1000 g for 1 min at 4°C. Afterwards supernatant was removed, cell suspension was dissolved in 1 ml growth medium and mechanistically dissociated using fire-polished glass pipettes. Dissociated cells were carefully layered on top of EBSS and centrifugated at 1500 g for 5 min at 4°C. Supernatant was discarded, cell pellets were dissolved in growth medium (600 µl per cerebellum) and cell density was determined using Neubauer counting chamber. Cells were then plated at a concentration of 750 000 per well and fed with growth medium after 1 h. After 24 h and 7 days half of the medium was replaced by fresh growth medium containing 4 µM AraC. Cerebellar neurons were kept for 17 days (DIV17) under constant conditions at 37°C/5% CO_2.

If necessary neurons were transduced with AAVs at DIV5 (0.2 µl per ml medium).

Table 15: Solutions used for primary cerebellar culture.

Name	**Composition**
EBSS	EBSS; 4% (w/v) bovine serum albumin (BSA); 3 mM 3.82% $MgSO_4$
Growth medium	50 ml stock medium; 5 ml FBS
Solution B	100 ml dPBS; 300 mg BSA (fatty acid free); 1 ml 3.82% $MgSO_4$
Soution C	10 ml solution B; 600U DNase; 0.5 mg Sobyean Trypsin Inhibitor (SBTI); 100 µl $MgSO_4$
Solution T	20 ml solution B; 5 mg trypsin
Stock medium	500 ml DMEM; 2 ml B-27; 0.74 g KCl; 10 mM glucose; 1 mM sodium pyruvate; 5 ml P/S

Table 16: Adeno-associated viruses used in cerebellar culture.

Identifier	Name	Titer [vg/ml]	Origin
GAD67-Cre	ssAAV-5/2-hGAD67-chI-iCre-SV40p(A)	5.6x10E12	Viral Vector Facility

2.5 Seahorse assay

2.5.1 Mito Stress test

Seahorse XF Cell Mito Stress Test was performed to assess mitochondrial function of cerebellar neurons. Cerebellar cells were prepared as described before and plated in 96-well Seahorse XF Cell Culture Microplates plates. The assay was performed on DIV17.

Cells were washed 1 h before the experiment and incubated with Seahorse XF Base Medium supplemented with 1 mM pyruvate, 2 mM glutamine and 10 mM glucose in a 37°C non-CO_2 incubator. As depicted in figure 13, oxygen consumption rate (OCR) was measured during the assay. The basal respiration capacity was measured within the first three rounds without the injection of inhibitors. Afterwards, 1.5 µM oligomycin (complex V inhibitor) was injected to measure ATP production, followed by 2 µM FCCP (uncoupling of oxygen consumption from ATP production) injection to measure maximal respiration capacity and 0.5 µM rotenone/antimycin A (inhibitors of complex I and III) combined with Hoechst was added at the end to measure non-mitochondrial respiration (Fig. 9). Afterwards, cell density was calculated based on Hoechst signal via a microplate reader and used for normalization of OCR values per cell density.

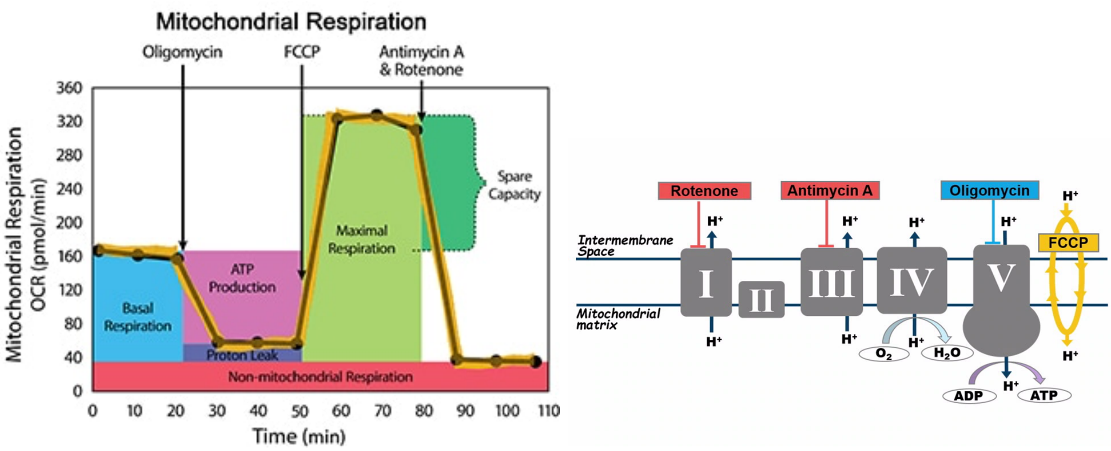

Figure 13: Agilent Seahorse XF Cell Mito Stress Test. (A) Schematic overview of the assay that was used to measure mitochondrial respiration of cerebellar neurons. Arrows indicate timepoint of injections and biological meaning of the injections. (B) Schematic overview showing how the injected compounds affect the electron transport chain (adopted from Agilent Seahorse XF Cell Mito Stress Test Kit User Guide).

2.5.2 Glycolysis Stress Test

The Seahorse XF Glycolysis Stress Test was performed to assess glycolytic function of cerebellar neurons by measuring the extracellular acidification rate (ECAR).

Cerebellar cells were prepared as described before and plated in 96-well Seahorse XF Cell Culture Microplates plates. The assay was performed on DIV17. Cells were washed and incubated with Seahorse XF Base Medium supplemented with 2 mM glutamine in a 37°C non-CO_2 incubator 1 h prior the experiment. As depicted in figure 14, during the assay the extracellular acidification rate (ECAR) of the cells is reported. The first set of measurements was performed without any injection and describes the non-glycolytic acidification caused by other processes than glycolysis. The first injection of 10 mM glucose indicates the rate of glycolysis under basal conditions. Afterwards, 1.5 µM oligomycin (complex V inhibitor) was injected to measure the maximum glycolytic capacity of the cells, followed by 50 mM 2-deoxy-glucose (2-DG, inhibitor of glycolysis by inhibiting hexokinase) combined with Hoechst injection to measure the glycolytic reserve of the cells. Afterwards, cell density was calculated based on Hoechst signal via a microplate reader and used for normalization of ECAR values per cell density.

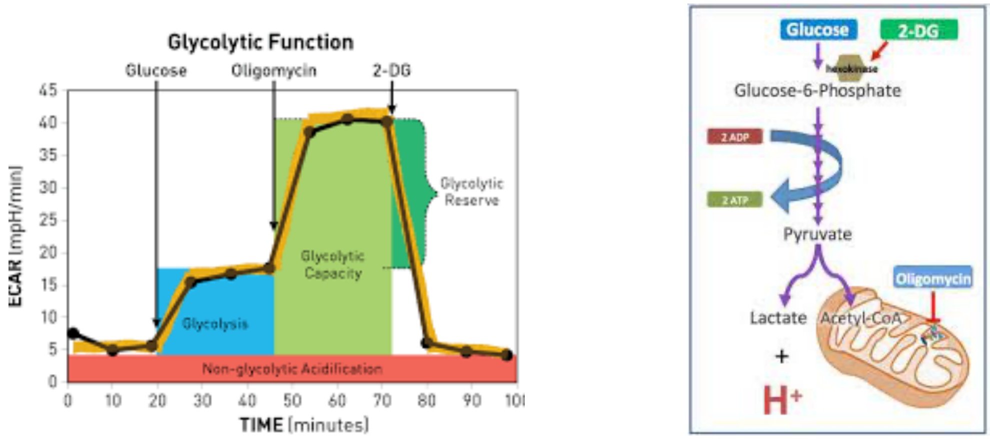

Figure 14: Agilent Seahorse XF Glycolysis Stress Test. (A) Schematic overview of the assay that was used to assess glycolytic function of cerebellar neurons. Arrows indicate timepoint of injections and biological meaning of the injections. (B) Schematic overview showing how the injected compounds affect glycolysis and mitochondrial respiration (adopted from Agilent Seahorse XF Glycolysis Stress Test Kit User Guide).

2.4 Cerebellar organotypic slice culture (OTC)

Postnatal pups (P6-9) were decapitated and brains were collected in ice-cold HBSS. Cerebellum was isolated and cut into 300 µm thick sagittal sections (McIlwain tissue chopper, Cavey Laboratory Engineering Co. LTD). Sections were separated and washed three times in pre-warmed (37°C) HBSS by carefully transferring slices with glass pipettes. Slices were then transferred onto membrane inserts with prewarmed OTC medium below. Medium was replaced every second day and OTCs were kept for 21 days (DIV21) under constant conditions at 37°C/5% CO_2.

Slices were either used for live imaging or for immune histochemistry and therefore fixed in 4% PFA for 30 min at RT.

Table 17: Culturing medium for cerebellar organotypic slices.

Name	Composition
OTC culturing medium	MEM; 0.00125% ascorbic acid; 10 mM D-glucose; 1 mM GlutaMAXX; 20% (v/v) horse serum; 0.01 mg/ml insulin; 14.4 mM NaCl; 1% P/S

2.4.1 Viral transduction and live imaging of OTCs

Viral transduction of OTCs was done on DIV1 by adding 1 µl of adeno-associated virus (AAV) on top of each single slice. Live-imaging was performed on DIV21 at the Multiphoton microscope SP8 (Leica) using a 20x/0.75 multi immersion objective. Single slices were recorded with constant perfusion of carbogenated OTC imaging medium at a 512x512 pixel resolution, bidirectional recording of 1 frame per second. Videos of 40 s length were recorded if not stated otherwise.

Table 18: Composition of OTC imaging medium.

Name	Composition
OTC imaging medium	dH_2O; 2 mM $CaCl_2$; 10 mM D-glucose; 3 mM KCl; 1 mM $MgCl_2$; 136 mM NaCl; 24 mM $NaHCO_3$; 1.25 mM NaH_2HPO_4

2.4.1.1 FRET-based imaging

For ATP and Lactate measurements FRET-based sensors were used. FRET works by excitation of a fluorescent molecule (donor) by a light of particular wavelength, which consequently transfers this energy to an adjacent fluorescent molecule (acceptor) that in-turn emits light. FRET-based sensor has two fluorophores: eCFP (donor) and mVenus (acceptor) (see figure 15). Only eCFP was excited at 448 nm, however emission of both eCFP and mVenus were captured by individual detectors. Recordings were then analyzed using ImageJ (Fiji) by measuring fluorescence intensity of eCFP and mVenus individually in the region of interest. Backgrounds were subtracted for each fluorophore and the ratio of mVenus/ eCFP was calculated and used as a readout of either ATP or lactate levels.

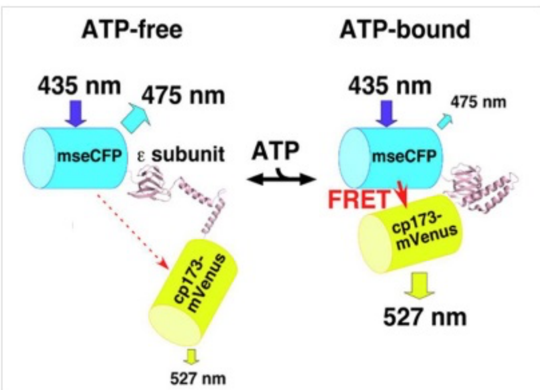

Figure 15: FRET-based sensor example based on Ateam. Ateam is a FRET-based ATP sensor consisting of eCFP with an ATP-sensing domain and mVenus. Upon ATP-binding eCFP undergoes a conformational change, decreasing the distance between eCFP and mVenus allowing fluorescence resonance energy transfer (FRET) from the donor to the acceptor. The mVenus/eCFP ratio gives indications about concentration of ATP (adopted from Imamura H, et al., 2009).

2.4.1.1.1 Laconic imaging

Lactate levels were measured in OTC imaging medium containing 1 µM MCT-inhibitor.

2.4.1.1.2 Ateam imaging

ATP levels were measured in OTC imaging medium containing either 10 mM or 30 mM glucose and in OTC imaging medium containing 10 mM glucose and 1.5 µM oligomycin.

2.4.1.2 GcamP7f$^{CamKII\alpha}$ imaging

For GCamP7f imaging recording with the length of 60 s were recorded (1 frame/s). After 20 s of baseline recordings, slices were stimulated once at 100 Hertz (Hz) using an RC-47FSLP stimulation chamber (Warner Instruments). Recordings were then analyzed using ImageJ (Fiji). First background was subtracted and then baseline fluorescence was measured by averaging fluorescence of the first 19 frames before stimulation. Fluorescent values of each frame were then normalized to baseline and plotted over time.

2.4.1.3 2-NBDG uptake

For 2-NBDG uptake cerebellar OTCs were incubated in OTC medium without glucose supplemented with 1 mM 2-NBDG for 30 min at 37°C in the dark. Slices were washed once with OTC medium and twice with OTC imaging medium before life image. Incubated slices were recorder for 40 s (1 frame/s). Fluorescence of each frame was analyzed after background subtraction (Fiji). Average fluorescence values over time were used for further analysis.

Table 19: Viruses used for OTCs.

Identifier	Name	Titer [vg/ml]	Origin
GAD67-Cre	ssAAV-5/2-hGAD67-chl-iCre-SV40p(A)	5.6x10E12	Viral Vector Facility (VVF)
Ateam	ssAAV-9/2-hSyn1-Ateam1.03YEMK-WPRE-hGHp(A)	8.1x10E12	Viral Vector Facility (VVF)
Laconic	ssAAV-9/2-hSyn1-Laconic-WPRE-hGHp(A)	6.9x10E12	Viral Vector Facility (VVF)
GCamP7f	ssAAV-9/2-mCaMKIIα-jGCaMP7f-WPRE-bGHp(A)	1.1x10E13	Viral Vector Facility (VVF)

2.5 Ex vivo acute slices

Mice were sacrificed at the age of three months via cervical dislocation and brains were isolated. Cortex and cerebellum were separated and cut with a vibratome (Leica) into 150 µm horizontal sections in ice-cold, carbogen-saturated (95% O_2 and 5% CO_2) low-Ca^{2+}artificial cerebrospinal fluid (ACSF).

Table 20: Composition of artificial cerebrospinal fluid (ACSF).

	Low-Ca^{2+} ACSF	**High-Ca^{2+} ACSF**
osmolarity adjusted between 310 and 330 milliosmoles, pH = 7,4		
NaCl (58,44 g/mol)	125 mM	125 mM
KCl (74,56 g/mol)	2.5 mM	2.5 mM
Sodium phosphate buffer (0,4 M)	1.25 mM	1.25 mM
$NaHCO_3$ (84,01 g/mol)	25 mM	25 Mm
Glucose (180,16 g/mol)	25 mM	25 mM
$CaCl_2$ (219,09 g/mol)	0.5 mM	1 mM
$MgCl_2$ (203,3 g/mol)	3.5 mM	2 mM

2.5.1 Starvation and chloroquine treatment

Cerebellar and cortical acute slices were incubated in control medium (OTC medium), control medium with 40 µM cloroquine, ACSF or ACSF with cloroquine for 6h at 37°C and 5% CO_2. Afterwards samples were shock frozen in liquid nitrogen and stored at -80°C until further processing via immunoblotting.

2.5.2 Surface biotinylation assay

Cerebellar acute slices were washed in 37°C pre-warmed ACSF for 30 min before incubation in biotinylation buffer for 1h at 4°C. Afterwards sections were incubated in stop reaction buffer to stop biotinylation reaction for 30 min at 4°C and washed three times with ice-cold ACSF. Sections were transferred into fresh tubes, lysed in lysis buffer, sonicated, incubated on ice for 45 min and centrifugated at 13 000 rpm for 15 min at 4°C. Supernatants were transferred into fresh tubes and proteins concentrations were assessed using Bradford assay (Sigma). Supernatant accounts for input fractions. 300 µg of protein of each sample were incubated with appropriate amount of prewashed Streptavidin beads over night at 4°C. The next day samples were centrifugated at 13 000 rpm for 30s at 4°C and the supernatant was transferred into fresh tubes. Samples account for unbiotinylated fraction and were stored at -80°C until further use for immunoblotting. Beads were washed three times with ice cold lysis buffer and once with 50 mM HCl. Samples were centrifugated at 13 000 rpm for 30s at 4°C and supernatant was discarded. For protein elution, 40µl of 2x SDS+ DTT were added and samples were incubated for 5 min at 95°C. After samples were equilibrated to RT, supernatant was collected and stored at -80°C until further use. Collected samples contained biotinylated proteins. Input and non-biotinylated fraction were equally mixed with 2x SDS+DTT according to their initial volume and incubated for 5min at 95°C. For immunoblotting the same amount of all samples were loaded (input, biotinylated, and non-biotinylated fraction).

Table 21: Solutions used for surface biotinylation assay.

Name	Composition
4x SDS	dH_2O; 250 mM Tris-HCL; 1% (w/v) SDS; 40% (v/v) Glycerol; 4% (v/v) ß- mercaptoethanol; 0.03% Bromophenol
2x SDS + DTT	dH_2O; 50% 4x SDS; 50 mM DTT
Biotinylation buffer	ACSF; 1 mg/ml EZ-Link™ Sulfo-NHS-SS-Biotin
Lysis buffer	dH_2O; 1% Igepal; 150 nM NaCl; 0.1% SDS; 0.5% SOD; 50 mM Tris
Stop reaction buffer	ACSF; 100 mM glycine

2.5.3 Isotope labeling (In collaboration with Patrick Giavalisco, MPI Cologne)

Cerebellar and cortical acute slices were incubated in ACSF containing 25 mM $^{12}C_6$ glucose (unlabeled) or $^{13}C_6$-labeled glucose for 1h at 37°C and 5% CO_2. Slices were then washed once in 75 mM ammonium carbonate (in water, pH=7.4) before fresh weight of samples was determined. Samples were snap-frozen in liquid nitrogen and stored in -80°C until further use. Further processing of samples was done in collaboration with Patrick Giavalisco (MPI of Ageing, Cologne).

2.5.3.1 Semi-targeted liquid chromatography-high-resolution mass spectrometry-based (LC-HRS-MS) analysis of amine-containing metabolites

The LC-HRMS analysis of amine-containing compounds was performed using a QE-Plus high-resolution mass spectrometer coupled to a Vanquish UHPLC chromatography system (Thermo Fisher Scientific). In brief: 50 µL of the available 150 µL of the above mentioned (AEX-MS method) polar phase was mixed with 25 µl of 100 mM sodium carbonate (Sigma), followed by the addition of 25 µl 2% [v/v] benzoylchloride (Sigma) in acetonitrile (UPC/MS-grade, Biosove, Valkenswaard, Netherlands). The derivatized samples were thoroughly mixed and kept at a temperature of 20°C until analysis.

For the LC-HRMS analysis, 1 µl of the derivatized sample was injected onto a 100 x 2.1 mm HSS T3 UPLC column (Waters). The flow rate was set to 400 µl/min using a binary buffer system consisting of buffer A (10 mM ammonium formate (Sigma), 0.15% [v/v] formic acid (Sigma) in UPC-MS-grade water (Biosove, Valkenswaard, Netherlands). Buffer B consisted of acetonitrile (IPC-MS grade, Biosove, Valkenswaard, Netherlands) 0.1% [v/v] formic acid (Sigma). The column temperature was set to 40°C, while the LC gradient was: 0% B at 0 min, 0-15% B 0-4.1min; 15-17% B 4.1 – 4.5 min; 17-55% B 4.5-11 min; 55-70% B 11 – 11.5 min, 70-100% B 11.5 - 13 min; B 100% 13 - 14 min; 100-0% B 14 -14.1 min; 0% B 14.1-19 min; 0% B. The mass spectrometer (Q-Exactive Plus) was operating in positive ionization mode recording the mass range m/z 100-1000. The heated ESI source settings of the mass spectrometer were: Spray voltage 3.5 kV, capillary temperature 300°C, sheath gas flow 60 AU, aux gas flow 20 AU at 330°C and the sweep gas was set to 2 AU. The RF-lens was set to a value of 60.

The LC-MS data analysis was performed using the TraceFinder software (Version 5.1, Thermo Fisher Scientific). The identity of each compound was validated by authentic reference compounds, which were measured at the beginning and the end of the sequence. For data analysis the area of the protonated $[M + nBz + H]^+$ (nBz stands for the number of benzoyl moieties attached to each compound) isotopologue mass peaks of every required compound were extracted and integrated using a mass accuracy <3 ppm and a retention time (RT) tolerance of <0.05 min as compared to the independently measured reference compounds. If no independent ^{12}C experiments were carried out, where the pool size is determined from the obtained peak area of the ^{12}C monoisotopologue, the pool size determination was carried out by summing up the peak areas of all detectable isotopologues per compound. These areas were then normalized, as performed for un-traced ^{12}C experiments, to the internal standards, which were added to the extraction buffer, followed by a normalization to the protein content or the cell number of the analyzed samples. The relative isotope distribution of each isotopologue was calculated from the proportion of the peak area of each isotopologue towards the sum of all detectable isotopologues. The ^{13}C enrichment, namely the area attributed to ^{13}C molecules traced in the detected isotopologues, was calculated by multiplying the peak area of each isotopologue with the proportion of the ^{13}C and the ^{12}C carbon number for the corresponding isotopologue (the ^{12}C and ^{13}C monoisotopologue areas were multiplied with 0 and 1 respectively). The obtained ^{13}C area of each isotopologue are summed up, providing the peak area fraction associated to ^{13}C atoms in the compound. Dividing this absolute ^{13}C area by the summed area of all isotopologues provides the relative ^{13}C enrichment factor.

2.5.3.2 Anion-Exchange Chromatography Mass Spectrometry (AEX-MS) for the analysis of anionic metabolites

Extracted metabolites were re-suspended in 150 µl of UPLC/MS grade water (Biosolve), of which 100 µl were transferred to p*olypropylene* autosampler vials (Chromatography Accessories Trott, Germany) before AEX-MS analysis.

The samples were analysed using a Dionex ionchromatography system (Integrion Thermo Fisher Scientific) as described previously. In brief, 5 µL of the resuspended polar metabolite extract were injected in push-partial mode, using an overfill factor of 1, onto a Dionex IonPac AS11-HC column (2 mm × 250 mm, 4 µm particle size, Thermo Fisher Scientific) equipped with a Dionex IonPac AG11-HC guard column (2 mm × 50 mm, 4 µm, Thermo Fisher Scientific). The column temperature was held at 30°C, while the auto sampler temperature was set to 6°C. A potassium hydroxide gradient was generated using a potassium hydroxide cartridge (Eluent Generator, Thermo Scientific), which was supplied with deionized water (Milli-Q IQ 7000, Millipore). The metabolite separation was carried at a flow rate of 380 µL/min, applying the following gradient conditions: 0-3 min, 10 mM KOH; 3-12 min, 10−50 mM KOH; 12-19 min, 50-

100 mM KOH; 19-22 min, 100 mM KOH, 22-23 min, 100-10 mM KOH. The column was re-equilibrated at 10 mM for 3 min.

For the analysis of metabolic pool sizes the eluting compounds were detected in negative ion mode using full scan measurements in the mass range m/z 77 – 770 on a Q-Exactive HF high resolution MS (Thermo Fisher Scientific). The heated electrospray ionization (ESI) source settings of the mass spectrometer were: Spray voltage 3.2 kV, capillary temperature was set to 300°C, sheath gas flow 50 AU, aux gas flow 20 AU at a temperature of 330°C and a sweep gas glow of 2 AU. The S-lens was set to a value of 60.

The LC-MS data analysis was performed using the TraceFinder software (Version 5.1, Thermo Fisher Scientific). The identity of each compound was validated by authentic reference compounds, which were measured at the beginning and the end of the sequence. For data analysis the area of the deprotonated $[M\text{-}H^{+}]^{-1}$ or doubly deprotonated $[M\text{-}2H]^{-2}$ isotopologues mass peaks of every required compound were extracted and integrated using a mass accuracy <3 ppm and a retention time (RT) tolerance of <0.05 min as compared to the independently measured reference compounds. If no independent ^{12}C experiments were carried out, where the pool size is determined from the obtained peak area of the ^{12}C monoisotopologue, the pool size determination was carried out by summing up the peak areas of all detectable isotopologues per compound. These areas were then normalized, as performed for un-traced ^{12}C experiments, to the internal standards, which were added to the extraction buffer, followed by a normalization to the protein content or the cell number of the analyzed samples. The relative isotope distribution of each isotopologue was calculated from the proportion of the peak area of each isotopologue towards the sum of all detectable isotopologues. The ^{13}C enrichment, namely the area attributed to ^{13}C molecules traced in the detected isotopologues, was calculated by multiplying the peak area of each isotopologue with the proportion of the ^{13}C and the ^{12}C carbon number for the corresponding isotopologue (the ^{12}C and ^{13}C monoisotopologue areas were multiplied with 0 and 1 respectively). The obtained ^{13}C area of each isotopologue are summed up, providing the peak area fraction associated to ^{13}C atoms in the compound. Dividing this absolute ^{13}C area by the summed area of all isotopologues provides the relative ^{13}C enrichment factor.

2.6 Animal behavior

2.6.1 SIMI Motion

To assess motor coordination and balance alterations animals were subjected to beams of different widths to determine how limbs are coordinated during self-paced locomotion in 1) unperturbed (25 mm beam), 2) mildly challenging (12 mm beam) and 3) stability-perturbed (5 mm beam) conditions. In three consecutive days animals were subjected to one of the beams starting with the widest one at 25 mm. Animals were instructed to cross each beam three times and their performance was recorded. The number of slips per run for each beam was quantified.

To gain more insight on why mice become less able to walk in perturbed conditions, the kinematics of limb movements within each step cycle were reconstructed in-depth. Joints were tracked using DeepLabCut and step cycles were defined as initiation of swing to end of stance, and manually annotated. The limb kinematics of individual step cycles were normalized to account for difference in the duration of stance and swing, and averaged for each mouse.

2.6.2 Rotarod

In order to analyze motor coordination animals were subjected to the Rotarod test. First animals were acclimated to the behavioral room for some minutes prior to the test. The first two consecutive days animals were trained to balance themselves on top of the rotating rod (TSE system) for 5 minutes at a constant speed of 4 rpm. The actual experiment was performed on day three. Animals had to walk on the rod with a starting speed of 4 rpm and a constant acceleration up 40 rpm to a maximum of 300 seconds. Three individual runs per mouse were performed. For each mouse and run, the latency to fall from the rod was recorded and used as a readout.

2.7 Histology methods

2.7.1 Perfusion

Adult mice were anesthetized (i.p., 10 µl per 10 g body weight) before transcardial perfusion with prewarmed Ringer to 37°C, followed by fixative of choice. Brains were isolated and post-fixed in the same fixative solution for 24 hours at 4°C. For long-term storage brains were stored in a mixture of 20% (v/v) glycerol and 2% (v/v) dimethylsulfoxide (DMSO) in 0.4 M PB phosphate buffer for cryoprotection. Horizontal sections (40 µm) were obtained at a microtome and stored at -80°C until further use. For stainings corresponding sections from littermates were used.

Table 22: Solutions and reagents used for perfusion.

Buffer	Ingredients
Anesthetic	PBS; 100 mg/ml Ketamine hydrochloride; 20 mg/ml Rompun (Xylazin)
DMSO for brain	46.75 ml H2O; 2 ml DMSO; 25.5 ml glycerol; 31.25 ml 0.4M PB
PFA	PBS; 4% (w/v) PFA; pH=7.4
Glutaraldehyde/ PFA	0.1M Cacodylate buffer; 2.5% (w/v) Glutaraldehyde; 2% (w/v) PFA

2.7.2 Immunohistochemistry

For immunohistochemistry (IHC) 1-, 3- and 12-months old animals were perfused and brains were post-fixed in ice-cold freshly depolymerized 4% (w/v) PFA in PBS. 40 µm horizontal free-floating sections were used for this purpose. All the following steps were performed with constant shaking. Sections were rinsed twice in PBS for 5 min and afterwards permeabilized and blocked in 10% normal goat serum (NGS) or 10% normal donkey serum (NDS) in 0.5 % Triton-X in PBS (PB-T) for 1 h at room temperature (RT). Primary antibodies were incubated in 3 % NGS or NDS in 0.3% PB-T for 48 hours at 4°C followed by three washes in 0.3% PB-T for 10 min at RT. Secondary fluorescently labeled antibodies and DAPI were incubated in 3% NGS or NDS in 0.3% PB-T for 2h at RT protected from light. Sections were then washed twice in PBS and mounted on gelatin-coated glass slides.

Images were acquired at the Leica SP8 and Leica Stellaris 5 confocal at a resolution of 1024x1024 pixels and visualized using Fiji (ImageJ). Mean gray values were used as fluorescence readout of protein levels after background subtraction. If otherwise stated, fluorescence levels were normalized to WT levels and used for statistical analysis.

Table 23: Primary antibodies used for immunohistochemistry.

Antibody target	**Concentration**	**Manufacturer**	**Catalog number**
AKT	1:500	Cell Signalling	46855
Calbindin	1.500	Novus Biologicals	NBP2-50028
Cleaved Caspase-3	1:5000	Cell Signalling	9661S
Extracellular GLUT2	1:300	Merck	07-1402-I
GFAP	1:500	Sigma	G3893
GFP	1:1000	Abcam	ab13970
GLUT1	1:300	Novus Biologicals	NB110-39113SS
GLUT2	1:300	Novus Biologicals	NBP2-22218SS
GLUT3	1:300	Invitrogen	OSG00012w
GLUT4	1:300	Novus Biologicals	NBP1-4953355
Hexokinase II	1:500	Abcam	ab227198
LC3	1:500	Biozol	M152-3
mCathepsin D	1:300	R&D systems	AF1029
mt-Cytb	1:300	Invitrogen	PA5-100740
Methylglyoxal	1.300	Novus Biologicals	NBP2-59368
NBR1	1:300	Santa Cruz Biotechnology	sc-130380
Parvalbumin	1:500	SySy	195002
p62	1:1000	Progen	GP62-C
pAKT (phospho Ser473)	1:500	Cell Signalling	4060
pS6 Ribosomal Protein (phosho Ser235/236)	1:300	Cell Signalling	2211
Ubiquitin	1:300	Sigma	U5379

Table 24: Secondary antibodies used for immunohistochemistry.

Antibody target	**Dilution**	**Manufacturer**	**Catalog number**
Alexa Fluor 488 Goat Anti-Chicken IgG	1:500	Life Technologies GmbH	A11039
Alexa Fluor 488 Goat Anti-Rabbit IgG	1:500	Life Technologies GmbH	A11034
Alexa Fluor 488 Goat Anti-Guinea Pig IgG	1:500	Life Technologies GmbH	A11073

Alexa Fluor 488 Goat Anti-Mouse IgG	1:500	Life Technologies GmbH	A11029
Alexa Fluor™ 488 Donkey Anti-Mouse	1:500	Life Technologies GmbH	A32766
Alexa Fluor 568 donkey anti-goat IgG Life	1:500	Life Technologies GmbH	A10057
Alexa Fluor 568 goat anti-rabbit IgG	1:500	Life Technologies GmbH	A11011
Alexa Fluor 647 Donkey Anti-Rabbit IgG	1:500	Life Technologies GmbH	A31573
Alexa Fluor 647 Goat Anti-Guinea Pig IgG	1:500	Life Technologies GmbH	A21450
Alexa Fluor 647 Goat Anti-Rabbit IgG	1:500	Life Technologies GmbH	A21245
Alexa Fluor 647 Goat Anti-Mouse IgG	1:500	Life Technologies GmbH	A21236

2.7.2.1 Reconstruction and colocalization analysis

For colocalization analysis, samples were scanned using Plan-Apochromat 63×/1.30 GLYC objective at a resolution of 1,024 × 1,024 pixels. Stacks of 20-30 optical sections were taken with a fixed sections size of 0.33 µm. Reconstructions and colocalization analysis were performed with Amira Software 2020.2 (Thermo Fisher Scientific). For each channel isosurfaces were extracted and positive colocalizations were defined when distance between voxels were smaller then 10 nm. Surface of distant voxels were mapped using surface distance tool and plotted as histogram and as a color-coded image.

2.7.3 Cresyl-violet (Nissl) staining

For cresyl-violet staining 40 µm horizontal sections were mounted on gelatin-coated “super-frost plus” glass slides and dried over night. Sections were hydrophylized in water for 1 min before incubation in cresyl-violet solution for 7 min. Sections were then washed three times in water for 2 min before being dehydrated in ascending ethanol solutions (70%, 80%, 90%, 96%, 100%) for 2 min in each solution. Afterwards, sections were incubated in xylene for at least 2 min and then covered with mounting solution Entellan ® (Merck). Images were acquired at a S360 Hamamatsu slide scanner using a 40x objective. Aperio Scope image viewing software was used to analyze number of Purkinje cell somata for individual cerebellar lobes.

2.7.4 Electron microscopy

For electron microcopy (EM) animals at the age of 3 months were perfusion fixed using 2% Formaldehyde (Science Services, München, Germany) and 2.5% Glutaraldehyde (Merck, Darmstadt, Germany) in 0.1M Cacodylate buffer, brain was removed and fixed overnight in the same fixative. 40 µm horizontal vibratome sections were prepared and region of interest was extracted using a biopsy punch. Postfixation was applied using 1% Osmiumtetroxid (Science Services, München, Germany) and 1% Potassium hexacyanoferrat (Merck, Darmstadt,

Germany) for 30 min at 4°C. After 3x5min wash with ddH2O, samples were dehydrated using ascending ethanol series (50%, 70%, 90%, 100%) for 10 min each. Infiltration was carried out with a mixture of 50% Epon/ethanol for 1h, 70% Epon/ethanol for 2h and overnight with pure Epon (Merck, Darmstadt, Germany). After fresh Epon for 4h, vibratome sections were mounted onto empty epon blocks and covered with Aclar foil. After 48h hardening at 60°C, Aclar foil was removed and samples were trimmed to the region of interest. Ultrathin sections (70nm) were cut using a diamond knife (Science Service, München, Germany) on an UC6 ultramicrotome (Leica, Wetzlar, Germany) and collected onto pioloform coated slot grids. Poststaining was performed with 1.5 % uranyl acetate (Agar Scientific, Stansted, United Kingdom) for 15 min and Reynolds lead citrate (Roth, Karlsruhe, Germany) solution for 3 min.
Images were acquired using a JEM-2100 Plus Transmission Electron Microscope (JEOL, Tokio, Japan) operating at 80kV equipped with a OneView 4K camera (Gatan, Pleasanton, USA). EM quantifications were carried out manually on acquired images (10 000K) of Purkinje cell somata. Number of mitochondria were counted and normalized to the total area of the cell. The total area of single mitochondria and the total length (perimeter) of the corresponding cristae was analyzed. Cristae length was then normalized to total area of mitochondria.

2.8 Immunoblot

2.8.1 Tissue preparation and lysis

Mice were sacrificed at the age of one, three and 12 months via cervical dislocation. Brains were isolated, individual brain regions were separated, shock frozen in liquid nitrogen and stored at -80°C until further use.
Samples were homogenized in RIPA buffer containing protease inhibitor (Roche) and phosphatase inhibitor (ThermoScientific) using a Wheaton otter-Elvehjem Tissue Grinder. Afterwards samples were sonicated (10 pulses), incubated on ice for 45 min and centrifugated at 13 000 rpm for 15 min at 4°C. Supernatants were transferred into fresh tubes and proteins concentrations were assessed using Bradford assay (Sigma). Sample were then mixed with Lämmli buffer and boiled for 95°C for 5 min.

Table 25: Reagents used for protein extraction.

Buffer	Ingredients
4x SDS	dH_2O; 250 mM Tris-HCL; 1% (w/v) SDS; 40% (v/v) Glycerol; 4% (v/v) ß- mercaptoethanol; 0.03% Bromophenol
RIPA/ Lysis buffer	dH_2O; 1% Igepal; 150 nM NaCl; 0.1% SDS; 0.5% SOD; 50 mM Tris;

2.8.2 SDS-PAGE and western blot

Depending on the assay, 10-20 µg protein per sample were loaded onto SDS-page gels for protein separation and then transferred onto nitrocellulose or methanol-activated PVDF membranes via full-wet transfer assay (BioRad) or semi-wet transfer. Protein transfer was confirmed by Ponceau S staining. Membranes were blocked in 5% milk or bovine serum albumin (BSA) in TBS containing 1% Tween (TBS-T) for 1h at RT followed by primary antibody incubation in TBS over night at 4°C. Afterwards, membranes were washed three times with TBS-T for 10 min and then incubated with HRP-tagged secondary antibodies for 1h at RT followed by three washes in TBS-T for 10 min at RT. Protein levels were visualized using ECL-based autoradiography film system (Super RX-N, Fujifilm) and analyzed using Gel Analyzer plugin from ImageJ (Fiji). Protein levels were always first normalized to loading control and the to WT control.

Table 26: Settings for protein transfer onto membranes.

	Full-wet transfer	**Semi-wet transfer**
Constant Current	75 V	280 mA
Time for run	90 min	35 min

Table 27: List of buffers used in SDS-PAGE and western blot analysis.

Buffer	**Ingredients**
1.5 M Tris pH=8.8	181.65g Tris Base; 0.4% (w/v) SDS; 1L ddH2O
0.5 M Tris pH=6..8	6g Tris Base; 0.4% (w/v) SDS; 100 mL ddH2O; pH 6.8
Ponceau S	200 ml dH_2O; 0.6 g Ponceau S; 6 ml acetic acid
Resolving gel	dH_2O; 1.5 M Tris; 30% Acrylamide; 10% APS; TEMED
Running buffer	H_2O; 192mM Glycine ; 25mM Tris-Base; 0.1% (w/v) SDS
Stacking gel	dH_2O; 0.5 M Tris; 30% Acrylamide; 10% APS; TEMED
TBS 10x	1l dH_2O; 88g NaCl; 24 g Tris Base
Transfer buffer	H_2O; 192mM Glycine ; 25mM Tris-Base; 0.025% (w/v) SDS

Table 28: List of antibodies used for western blot analysis.

Antibody target	**Dilution**	**Manufacturer**	**Catalog number**
ATG5	1:1000	Abcam	ab108327
α-Tubulin	1:5000	Synaptic Systems	302 211
β-Actin	1:3000	Sigma	A-5441
Calbindin	1:1000	Novus Biologicals	NBP2-50028
Cleaved-Caspase 3	1:500	Cell Signalling	9661S
GFAP	1:1000	Sigma	G3893
GLUT1	1:1000	Novus Biologicals	NB110-39113SS
GLUT2	1:500	Novus Biologicals	NBP2-22218SS
GLUT2	1:500	Proteintech	20436-1-AP
GLUT3	1:500	Invitrogen	OSG00012w
GLUT4	1:500	Novus Biologicals	NBP1-4953355
LC3B	1:1000	Novus Biologicals	NB600-1384
Methylglyoxal	1:1000	Novus Biologicals	NBP2-59368
NBR1	1:500	Santa Cruz Biotechnology	sc-130380
p62	1:1000	Progen	GP62-C

Vinculin	1:5000	Abcam	ab129002

Table 29: Secondary antibodies used for western blot analysis.

Antibody target	Dilution	Manufacturer	Catalog number
Rabbit anti-Mouse IgG (H+L) peroxidase-conjugated	1:10 000	Sigma	A9044
Goat anti-Rabbit IgG (H+L) peroxidase-conjugated	1:10 000	Sigma	A0545
Goat anti-Guinea Pig IgG (H+L) peroxidase-conjugated	1:5 000	Jackson Immuno Research	106-035-003
Rabbit anti-Chicken IgG (H+L) peroxidase-conjugated	1:5 000	Millipore	AP162P

2.9 Multi-omics analysis

2.9.1 Metabolomics analysis

2.9.1.1 Untargeted metabolomics (in collaboration with AG Frezza, CECAD, Cologne)

Untargeted metabolomics was performed on 10-20 mg of fresh-frozen cortex and cerebellum from one and three months-old animals. For metabolite extraction 25 µl of metabolite extraction solution was added per mg tissue and tissue was lysed in a homogenizer (2x 30s cycle at 6 000 rpm at 4°C. Tissue extracts were transferred into fresh tubes, shaked in a thermomix (Eppendorf) at full speed for 15 min at 4°C and centrifugated at full speed for 20 min at 4°C. Equal amounts of each sample were used for further analysis.

Metabolites were separated chromatographically utilizing a Millipore SeQuant ZIC-pHILIC analytical column (5 µm, 2.1 × 150 mm), complemented with a 2.1 × 20 mm guard column (both with 5 mm particle size), and a binary solvent system was employed. Solvent A consisted of 20 mM ammonium carbonate and 0.05% ammonium hydroxide, while Solvent B was pure acetonitrile. The column oven was maintained at 40 °C and the autosampler tray at 4 °C. The chromatographic gradient flowed at a rate of 0.200 mL/min and was programmed as follows: 0–2 min at 80% B, a linear gradient from 80% B to 20% B between 2-17 min, a swift change from 20% B to 80% B between 17-17.1 min, and a hold at 80% B from 17.1-23 min. Samples were injected in a randomized order with a volume of 5 µl each. A pooled quality control (QC) sample, created by mixing equal parts of all individual samples, was analyzed at regular intervals in between the test samples.

Metabolites were quantified using a Vanquish Horizon UHPLC connected to an Orbitrap Exploris 240 mass spectrometer (both provided by Thermo Fisher Scientific), with measurements facilitated by a heated electrospray ionization source. Spray voltages were configured at +3.5kV/-2.8kV, the RF lens value at 70, the heated capillary temperature at 320 °C, and the auxiliary gas heater at 280 °C. Sheath, aux, and sweep gas flow rates were set at 40, 15, and 0, respectively. For MS1 scans, the mass range was m/z=70-900, with a standard AGC target and auto-set maximum injection time. Experimental samples' data acquisition employed full scan mode with polarity switching, at an Orbitrap resolution of 120,000. The AcquireX Deep Scan workflow was used for untargeted metabolite identification, applying an iterative data-dependent acquisition strategy with multiple pooled sample injections. The setup included a full scan resolution of 60,000, fragmentation resolution of 30,000, and a fragmentation intensity threshold of 5.0e3. Dynamic exclusion was activated after one occurrence, with a 10s exclusion duration and a 5ppm mass tolerance. The isolation window was 1.2 m/z, with normalized HCD collision energies in stepped mode at 30, 50, 150. Mild trapping was enabled.

Metabolite identification was conducted using the Compound Discoverer software (v 3.2, Thermo Fisher Scientific), with criteria including a precursor ion m/z within 5 ppm of the predicted theoretical mass according to the chemical formula, fragment ions within 5 ppm to an internal spectral library of authentic compound standards (analyzed with the same ddMS2 method) with a minimum match score of 70, and retention time within 5% of a purified standard under the same chromatographic conditions. Peak area integration and chromatogram review were performed using Tracefinder software (v 5.0, Thermo Fisher Scientific). Each detected metabolite's peak area was normalized against the total ion count (TIC) of the respective sample to account for variations from sample handling to analysis, serving as variables for in-depth statistical analysis.

Pathway analysis of untargeted metabolomics was performed using MetaboAnalyst 5.0 (https://www.metaboanalyst.ca/home.xhtml).

Table 30: Metabolite extraction solutions.

Solution	
LC-MS grade methanol	50%
LC-MS grade methanol	30%
Ultrapure water	20%
Valine-d8	Final concentration 5 µM

2.9.1.2 Targeted metabolomics (performed by Susanne Brodesser)

Levels of amino acids, GABA, glycolysis intermediates, TCA cycle intermediates and pentose phosphate pathway intermediates were analyzed in fresh-frozen cortex and cerebellum from one and three months old mice.

2.9.1.2.1 Intermediates of glycolysis and tricarboxylic acid (TCA) cycle

Intermediates (organic acids, sugar phosphates) of the glycolysis and the TCA cycle in mouse cortex and cerebellum tissue were determined by Anion-Exchange Chromatography coupled to Electrospray Ionization High-Resolution Mass Spectrometry (IC-ESI-HRMS) using a procedure previously described (Schwaiger et al., 2017; Aravamudha et al., 2021). Approximately 50 mg of snap-frozen mouse tissue were homogenized in ice-cold acetonitrile/methanol/water 2:2:1 (v/v/v) (1 mg / 10 µl) using the Precellys 24 Homogenisator (Peqlab) at 6,400 rpm for two times 10 seconds with a 5-second pause. 100 µl of homogenate were mixed with further 225 µl of acetonitrile/methanol/water 2:2:1 (v/v/v) and 25 µl of a mixture of isotope-labeled internal standards in Milli-Q water (5 µM 13C6-D-glucose-6-phosphate (13C6-G6P) and 5 µM D4-succinic acid (D4-SUC), both Eurisotop). After thorough mixing and centrifugation (16,100 RCF, 5 min, 4 °C), 300 µl of supernatant were dried under reduced pressure. The residue was resolved in 100 µl of Milli-Q water, transferred to autoinjector vials and immediately measured. IC-HRMS analysis was performed using a Dionex Integrion RFIC system (Thermo Scientific) coupled to a Q Exactive HF quadrupole-orbitrap mass spectrometer (Thermo Scientific) as previously described (Schwaiger et al., 2017; Aravamudha et al., 2021). The exact m/z traces of the internal standards and endogenous metabolites were extracted and integrated using Skyline 21.2.0.369 (open-source). Endogenous metabolites were quantified by normalizing their peak areas to those of the internal standards: D4-SUC was used for organic acids, and 13C6-G6P for sugar phosphates.

2.9.1.2.2 Amino acids and γ- Aminobutyric acid (GABA)

Amino acids and GABA of mouse cortex and cerebellum tissue were derivatized with benzoyl chloride and quantified by Liquid Chromatography coupled to Electrospray Ionization Tandem Mass Spectrometry (LC-ESI-MS/MS) using a procedure previously described (Wrong et al., 2016; Aravamudha et al., 2021). The homogenates prepared for the analysis of sugar phosphates and organic acids (see above) were centrifuged (16,100 RCF, 5 min, 4 °C). 20 µl of the supernatant were mixed with 10 µl of the MassChrom Internal Standard Mixture Amino acids and Acylcarnitines from Dried Blood (Chromsystems), reconstituted in 5 ml water/methanol 2:1 (v/v), and 10 µl of a 10 µM solution of d6-GABA (Sigma-Aldrich) in Milli-Q water. Endogenous and isotope-labeled amino acids and GABA were derivatized by adding 10 µl of freshly prepared 2 % benzoyl chloride in acetonitrile and 10 µl of 100 mM sodium carbonate in water and thorough mixing (Wrong et al., 2016). After addition of 40 µl of Milli-Q water and centrifugation (16,100 RCF, 5 min, 4 °C), 80 µl of the supernatant were transferred to autoinjector vials and immediately measured. LC-MS/MS analysis was performed using a Nexera X2 UHPLC System (Shimadzu) coupled to a QTRAP 6500 triple quadrupole/linear ion trap mass spectrometer (SCIEX) as previously described (Ref. 2,3). The LC chromatogram peaks of benzoylated endogenous amino acids and GABA, and internal standards were integrated using the MultiQuant 3.0.2 software (SCIEX). The peak areas of the benzoylated metabolites were normalized to those of the internal standards.

2.9.2 Proteomics

2.9.2.1 Protein extraction

Total proteome analysis was performed on fresh frozen cerebellum from one and three months-old animals. Samples were prepared by in-solution digestion and all solution were provided by the proteomics facility. Samples were lysed in Urea lysis buffer, centrifugated for 15 min at 20 000 g and protein concentration was assessed using Bradford assay (Sigma). 50 µg of protein for each sample was transferred in fresh tubes, incubated with 5 mM DTT for 1h at 25°C and then incubated with 40 mM CAA for 30 min in the dark. Afterwards samples were incubated with LysC at an enzyme:substrate ratio of 1:75 for 4h at 25°C. Samples were then diluted with 50 mM TEAB to achive a final concentrate of 2 M Urea before overnight incubation in Trypsin (1:75 ratio) at 25°C. The next day samples were acidified with formic acid (final concentration 1%). Peptides were extracted and purified using Stagetips. First StageTips were equilibrated with washes once in methanol, buffer B and twice buffer A, each time followed by centrifugations at 2 600 rpm for 1-2 min. For peptide purification, samples were centrifugated at 13 000 rpm for 5 min and the loaded onto StageTips. Samples were centrifugated at 2 600 rpm for 5 min, StageTips were washed with buffer A and centrifugated at 2 600 for 3 min. Then StageTips were washed twice with buffer B and each time centrifugated at 2 600 for 3 min.

Eluted peptides were dried in vacuo, stored at 4°C and provided to proteomics facility for further processing.

Pathway analysis of proteomic approaches was performed using ShinyGO (South Dakota State University; Ge, Jung and Yao, 2020). Venn diagram analysis was done using Venny2.1 (Oliveros, J.C. (2007-2015) Venny. An interactive tool for comparing lists with Venn's diagrams. https://bioinfogp.cnb.csic.es/tools/venny/index.html).

Table 31: Reagents and solutions used for protein extraction for proteomics analysis.

Buffer	Ingredients
Buffer A	dH_2O; 0.1% (v/v) formic acid
Buffer B	80% acetonitril; 0.1% (v/v) formic acid
Chloroacetamide (CAA)	550 mM stock CAA
Dithiothreitol (DTT)	100 mM DTT stock
Formic acid	dH_2O; 10%; (v/v) formic acid
Lysyl Endopeptidase (LysC)	0.5 µg/µl LysC
Methanol	100%
Triethylammoniumbicarbonate	50 mM TEAB
Trypsin protease	1 µg/µl Trypsin
Urea buffer	50 mM TEAB; 8M Urea; 50x Protease inhibitor

2.9.2.2 Data Acquisition

Samples were analyzed by the CECAD Proteomics Facility on an Orbitrap Exploris 480 (Thermo Scientific, granted by the German Research Foundation under INST 1856/71-1 FUGG) mass spectrometer equipped with a FAIMSpro differential ion mobility device that was coupled to an UltiMate 3000 (Thermo Scientific). Samples were loaded onto a precolumn (Acclaim 5µm PepMap 300 µ Cartridge) for 2 min at 15 ul flow before reverse-flushed onto an in-house packed analytical column (30 cm length, 75 µm inner diameter, filled with 2.7 µm Poroshell EC120 C18, Agilent). Peptides were chromatographically separated at a constant flow rate of 300 nL/min and the following gradient: initial 6% B (0.1% formic acid in 80 % acetonitrile), up to 32% B in 72 min, up to 55% B within 7.0 min and up to 95% solvent B within 2.0 min, followed by column wash with 95% solvent B and re-equilibration to initial condition. The FAIMS pro was operated at -50V compensation voltage and electrode temperatures of 99.5 °C for the inner and 85 °C for the outer electrode.

For the Gas-phase fractionated library, a pool generated from all samples was analyzed in six individual runs covering the range from 400 m/z to 1000 m/z in 100 m/z increments. For each run, MS1 was acquired at 60k resolution with a maximum injection time of 98 ms and an AGC target of 100%. MS2 spectra were acquired at 30k resolution with a maximum injection time of 60 ms. Spectra were acquired in staggered 4 m/z windows, resulting in nominal 2 m/z windows after deconvolution using ProteoWizard (Chambers, 2012).

For the samples, MS1 scans were acquired from 399 m/z to 1001 m/z at 15k resolution. Maximum injection time was set to 22 ms and the AGC target to 100%. MS2 scans ranged from 400 m/z to 1000 m/z and were acquired at 15 k resolution with a maximum injection time of 22 ms and an AGC target of 100%. DIA scans covering the precursor range from 400 - 1000 m/z and were acquired in 60 x 10 m/z windows with an overlap of 1 m/z. All scans were stored as centroid.

2.9.2.3 Sample Processing in DIA-NN

The gas-phase fractionated library was built in DIA-NN 1.8.1 (Demichev 2020) using A Swissprot mouse canonical database (UP589, downloaded 04/01/22) with settings matching acquisition parameters.

Samples were analyzed in DIA-NN 1.8.1 as well using the previously generated library and identical database. DIA-NN was run with the additional command line prompts "—report-lib-info" and "—relaxed-prot-inf". Further output settings were: filtered at 0.01 FDR, N-terminal methionine excision enabled, maximum number of missed cleavages set to 1, min peptide length set to 7, max peptide length set to 30, min precursor m/z set to 400, max precursor m/z set to 1000, cysteine carbamidomethylation enabled as a fixed modification. Afterwards, DIA-NN output was further filtered on library q-value and global q-value <= 0.01 and at least two unique peptides per protein using R (4.1.3). Finally, LFQ values calculated using the DIA-NN R-package. Afterwards, analysis of results was performed in Perseus 1.6.15 (Tyanova 2016).

2.10 PET imaging

2.10.1 [18F]UCB-H-/[18F]MNI1126-PET

Animals were anesthetized with isoflurane in O2/air 3:7 (induction 5 %, maintenance 1.5–2.0 %), and a catheter for tracer injection was inserted into the lateral tail vein. To this end, the tail was slightly warmed and a torniquet was applied with low pressure to the base of the tail. The catheters were home-made from a 30G tip broken off from a regular 30G needle and inserted into a flexible polyethylene tube with 0.28 mm inner diameter (Smiths Medical, Minneapolis, USA). After placement in the tail vein, the needle tip was secured with adhesive tape, and the syringe with the tracer solution was attached to the other end of the tube. Mice were placed on an animal holder (medres® GmbH, Cologne, Germany) and fixed with a tooth bar in a respiratory mask. Body temperature was maintained at 37 °C using a feedback-controlled warming system. Eyes were protected from drying out by application of eye and nose ointment (Bepanthen, Bayer). A PET scan in list mode was conducted using a Focus 220 micro PET scanner (CTI-Siemens, Erlangen, Germany) with a resolution at the center of field of view of 1.4 mm. Data acquisition started with intravenous tracer injection (activity: 6–12 MBq in 125 µl) and lasted for 40 min. This was followed by a 10 min transmission scan using a 57Co point source for attenuation correction. After the scan was finished, the catheter was removed and the mice were returned to their home cage.

2.10.2 [18F]FDG-PET

For [18F]FDG-PET, animals were briefly anesthetized (see above) and 9-12 MBq [18F]FDG in 125 µl was injected intraperitoneally. The mice were then placed in a solitary cage where they spent the following 35 min awake. Subsequently, they were anesthetized again and scanned as described above for 30 min. This protocol takes advantage of metabolic trapping of [18F]FDG (Pauwels et al., 1998), which allows awake tracer uptake and subsequent scanning under anesthesia.

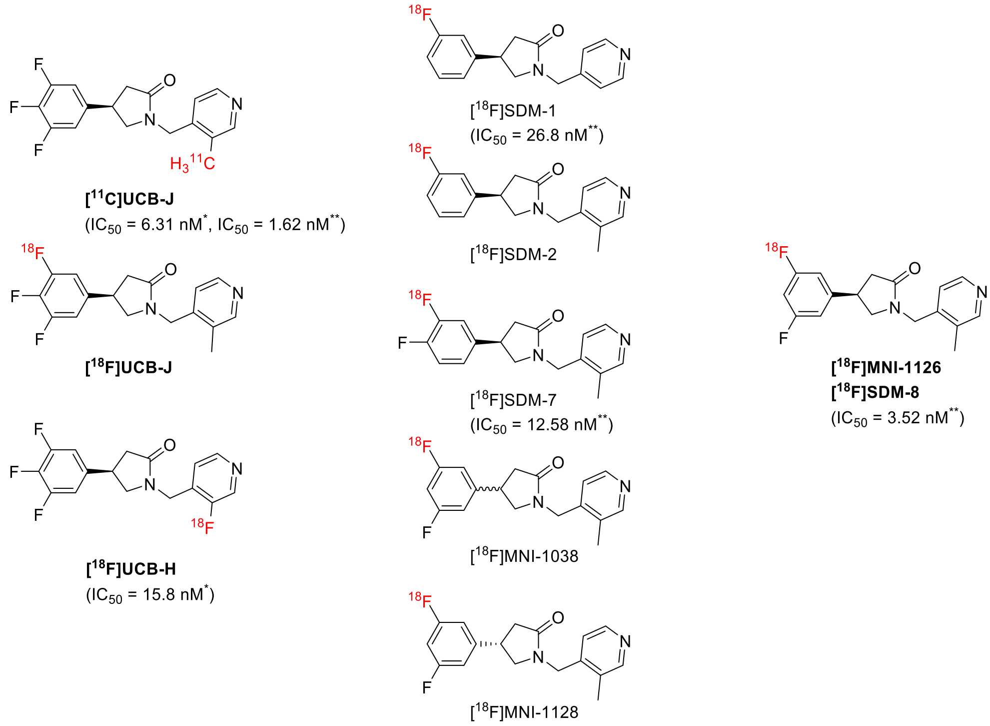

Figure 16: Chemical structures of tracers used in this study.

2.10.3 Image reconstruction

After full 3D rebinning, summed images were reconstructed using an iterative OSEM3D/MAP procedure (Qi et al., 1998), resulting in voxel sizes of 0.47 × 0.47 × 0.80 mm. For all further processing of the images including statistics, the software VINCI 5.21 for MacOS X (Max Planck Institute for Metabolism Research, Cologne, Germany) was used. Images were co-registered and intensity-normalized to thalamus. To this end, an elliptical volume of interest (VOI) of 7.2 mm3 (40 voxels) was placed inside the thalamus. Each image was divided by the mean value of the thalamus VOI, resulting in the "standardized uptake value ratio" (SUVRThal). No further postprocessing (e.g. Gauss filtering or spatial morphing) was done.

2.10.4 Image statistics

For comparison of ATG5 cKO versus controls, a voxel-wise t-test was performed for each tracer using VINCI 5.21 for MacOS X. The equation for the unpaired t-test (i.e. difference between the two group means divided by the pooled standard error of both groups) was executed manually in VINCI. The resulting t-maps were corrected for multiple comparisons using a threshold-free cluster enhancement (TFCE) procedure described in detail in the work of Smith and Nichols (2009). The TFCE procedure was implemented as a Python script in VINCI. For final thresholding at $p<0.05$, a permutation test with 10,000 permutations was performed in RStudio 1.0 for MaxOS X using the SUVRThal values of the voxel with the highest TFCE value. The 95% quantile was calculated, and the corresponding TFCE level was used as the lower threshold of the tTFCE-map. The resulting tTFCE-maps were displayed in voxel view in shades of red (ATG5 cKO>controls) or blue (ATG5 cKO<controls) and projected onto an C57BL/6 T2-weighted MRI template.

2.11 Stereotactic surgeries into cerebellar lobes IV/V

Mice were anesthetized by intraperitoneal injection of a ketamine/xylazine mixture. Upon the absence of reflexes, the surgery was carried on. The fur was removed, animal was given carprofen (5 mg/kg) subcutaneously and fixed in a stereotactic frame provided with a heating pad (David Kopf Instruments). An eye creme was applied on the eyes in order to prevent drying of the corneas. Local pain killer bucain was administered subcutaneously. The scalp was removed and the underlying connective tissue was cleared from the skull. A microinjection syringe (WPI) equipped with a 34g bevelled needle (WPI) was filled with virus solution (table 33) and placed into the stereotactic apparatus.
The stereotactic landmark bregma was identified in order to centre the tip of the needle directly on Bregma. The needle was then moved to the specific target region using predetermined anterior/posterior (AP) and medial/lateral (ML) coordinates (cerebellar lobes IV/V from Bregma: AP, -5.61 mm; ML, 0 mm). Subsequently, a circular craniotomy was performed with a micro drill and the needle was lowered to the surface of the brain to calculate the dorsal/ventral coordinates (DV: -1 mm and -0.75 mm).
The needle was slowly inserted in the brain to the desired depth and the viral injection started. 300 nL of virus solution was injected at a speed of 100 nL/min using a microsiringe pump controller (WPI). After the injection was complete, the needle was kept in place for 3 min and slowly retracted over 1 min. The incision was closed with sutures (Ethicon). During and after the surgery the mice body temperature was kept at 37°C via a heating pad. Mice were injected with 5% glucose-saline solution (100 µL/10g) after the surgery and with carprofen (5 mg/kg) 24 h and 48 h after the surgery.
Physical conditions of the animals were monitored daily to improve their welfare.
Three weeks after virus injection, animals were perfused with Ringer and 4% PFA (see section above for IHC).

Table 32: Reagents used for stereotactic surgeries.

Buffer	Ingredients
Anesthetic	0.9% NaCl; 100 mg/ml Ketamine hydrochloride; 20 mg/ml Rompun (Xylazin)
Analgesic	0.9 % NaCl; Carprofen 5 mg/kg
Local painkiller	0.9 % NaCl; 1:5 (v/v) bucain

Table 33: Adeno-associated viruses used for stereotactic surgeries.

Identifier	Name	Titer [vg/ml]	Origin
MitoTimer	ssAAV-5/2-mTH-dlox-MitoTimer(rev)-dlox-WPRE-bGHp(A)	6.2 x 10E12	Viral Vector Facility VVF
EGFP-ATG5	pAAV2/RH10-mDLX-EGFP-ATG5	4.78 x 10E12	AG Schwartz
EGFP	pAAV2/RH10-mDLX-EGFP	1.31 x 10E12	AG Schwartz

2.12 Statistical analysis

Statistical analysis was carried out using GraphPad Prism (9.5.1). Unpaired Student's t-test analysis was performed for two group comparisons. One-tailed Student's t-test analysis was performed for two group comparison, after values were normalized to WT levels.

For comparisons with more than two groups, one-way ANOVA followed by a Holm-Sidak post hoc test was applied. Two-way ANOVA was used for comparison of two groups and two independent variables followed by Holm-Sidak post hoc test for multiple comparisons.

P values of less than 0.05 were considered statistically significant. Data are reported as mean values ± standard error of the mean (SEM).

IV. Results

1. Region-specific vulnerability to autophagy loss

1.1 PET imaging reveals region-specific vulnerability to autophagy loss

In order to assess whether ATG5 deficiency results in cell loss, cerebral glucose metabolism was measured using a [^{18}F] FDG-PET tracer and synapse density was measured using [^{18}F] UCB-H/[^{18}F] MIN1126 tracers. Longitudinal PET study of 3 and 12 months-old animals was performed in collaboration with Dr. Heike Endepols (Uniklinik Köln).

[^{18}F] FDG uptake was significantly lower in the cerebellum of both 3 and 12 months-old ATG5 cKO animals, while those animals display increased [^{18}F] FDG uptake in cortical and subcortical regions. This implicates that the loss of ATG5 results in neurodegeneration in the cerebellum, indicated by hypometabolism and therefore reduced activity. On the contrary, autophagy deficiency in cortical regions does not lead to cell loss but results in hypermetabolism and increased activity (Fig. 13A). [^{18}F] UCB-H/[^{18}F] MIN1126 imaging indicated increased synaptic loss upon loss of ATG5. At the age of 3 and 12 months, consistently lower SV2A density was observed in the cerebellum and in several cortical regions (Fig. 13B).

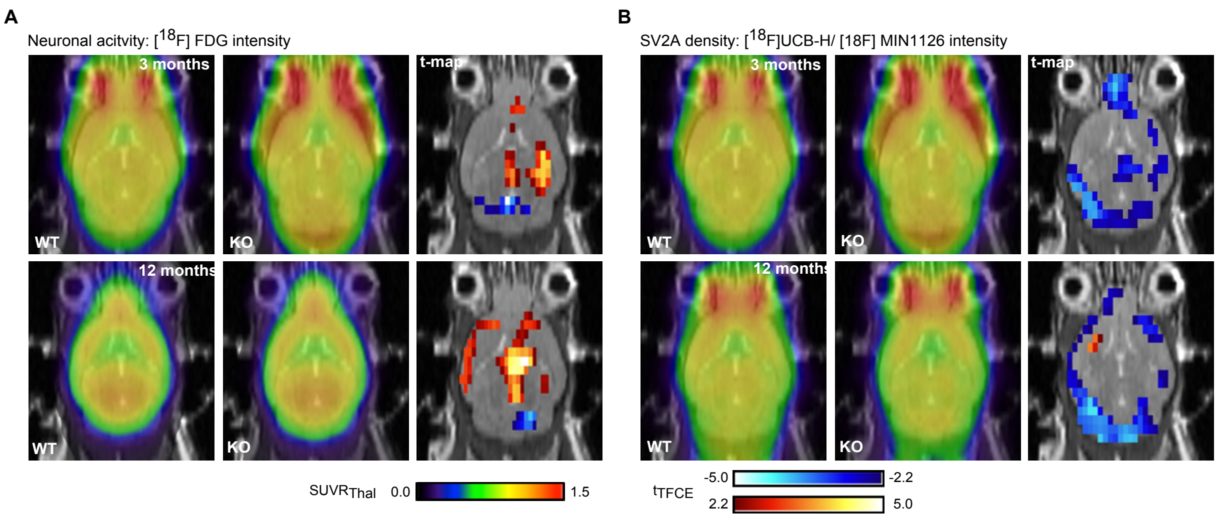

Figure 13: PET imaging reveals region-specific vulnerability to autophagy loss. (A) [^{18}F] FDG-imaging. Upper and lower row representative images of 3 months-old and 12 months-old animals, respectively. The first column shows mean images of WT controls (N=7 for 3-month old animals and N=6 for 12-month old animals) and the second row shows mean images of ATG5 cKO mice (N=6 per age). The third column shows t-map with voxel-wise comparison between ATG5 cKO and WT (t-test, corrected for multiple testing). Red and blue voxels indicate significantly ($p<0.05$) higher and lower tracer uptake in ATG5 cKO mice. (B) SV2A density: Upper row represents imaging of three months old animals using the tracer [^{18}F] UCB-H and second row displays 12 months-old animals using the tracer [^{18}F] MIN1126. The first column shows mean images of WT controls (N=7 for 3-month old animals and N=6 for 12-month old animals) and the second column shows mean images of ATG5 cKO mice (N=6 per age). The third column shows t-map with voxel-wise comparison between ATG5 cKO and WT mice (t-test, corrected for multiple testing). Red and blue voxels indicate significantly ($p<0.05$) higher and lower tracer uptake in ATG5 cKO mice.

1.2 Cell type-specific vulnerability of Purkinje cells to autophagy loss

In order to confirm that ATG5 cKO mice show resistance to cell loss in the cortex but selective vulnerability in the cerebellum as indicated in the PET imaging scans, targeted metabolomics analysis of GABA content was performed. GABA content can be used as a readout of the amount of GABAergic neurons. No differences were observed in GABA content in the cortex at the age of 1 and 3 months. At 1 month of age no difference was observed in the cerebellum, however at the age of 3 months a decrease in GABA levels was detected between WT and ATG5 cKO cerebellum (Fig. 14A). This further indicates that loss of ATG5 does not result in cell loss in the cortex, whereas in the cerebellum first indications for degeneration appear at the age of 3 months. Additionally, levels of ATG5 were analyzed via immunoblot of whole cerebellar lysates which revealed a 20% decrease in ATG5 cKO mice compared to WT at both ages (Fig. 14B). Reduction in cortical ATG5 levels in ATG5 cKO mice has been previously described (Negrete-Hurtado et al., 2020, Overhoff et al., 2022). In order to assess the degree of degeneration in the cerebellum immunofluorescence staining and Cresyl-violet staining was performed. Immunostaining against calbindin, a common marker for Purkinje cells, revealed reduced Purkinje cell number starting at the age of 3 months and even further decreased at the age of 12 months (Fig. 14C and D). The loss of calbindin was already detectable via immunoblotting of whole cerebellar lysates at the age of three months (Fig. 14E and F). To evaluate whether Purkinje cell loss is lobe-specific, cresyl-violet staining was performed on cerebellar sections and the number of Purkinje cells was quantified for each cerebellar lobe. The analysis revealed that at the age of 3 months, Purkinje cell loss appears to be with approximately 50% reduction in Purkinje cell number per lobe compared to WT (Fig. 14G and H). Since *Slc32a1*-Cre (VGAT-Cre) promoter does not only target Purkinje cells but also other GABAergic neurons in the cerebellum, cell density of GABAergic interneurons in the molecular cell layer was analyzed. Immunofluorescent staining for parvalbumin (main marker of those interneurons) indicated that molecular cell layer interneurons do not show signs of degeneration at the age of 1, 3 and 12 months. Instead, an increased cell density was observed starting at the age of 3 months and even more prominent at the age of 12 months (Fig. 14I and J). In order to test whether loss of Purkinje cells affects the motor behavior of ATG5 cKO mice, animals at the age of 12 months were tested for motor coordination (in collaboration with Prof. Gatto, Uniklinik Köln). Animals performed active locomotion while crossing beams of different widths (25 mm and 12 mm) (Fig.14K and L). WT mice were able to smoothly cross the 25 and 12 mm beams, whereas ATG5 cKO mice had already difficulties on the widest beam, indicated by increased number of slips. The number of slips further increased when challenging them with a narrower beam (12 mm) (Fig. 14M).

This indicates that loss of ATG5 in GABAergic neurons results in cell-type specific vulnerability of cerebellar Purkinje cells starting at 3 months of age, followed by the development of an ataxic motor phenotype at the age of 12 months.

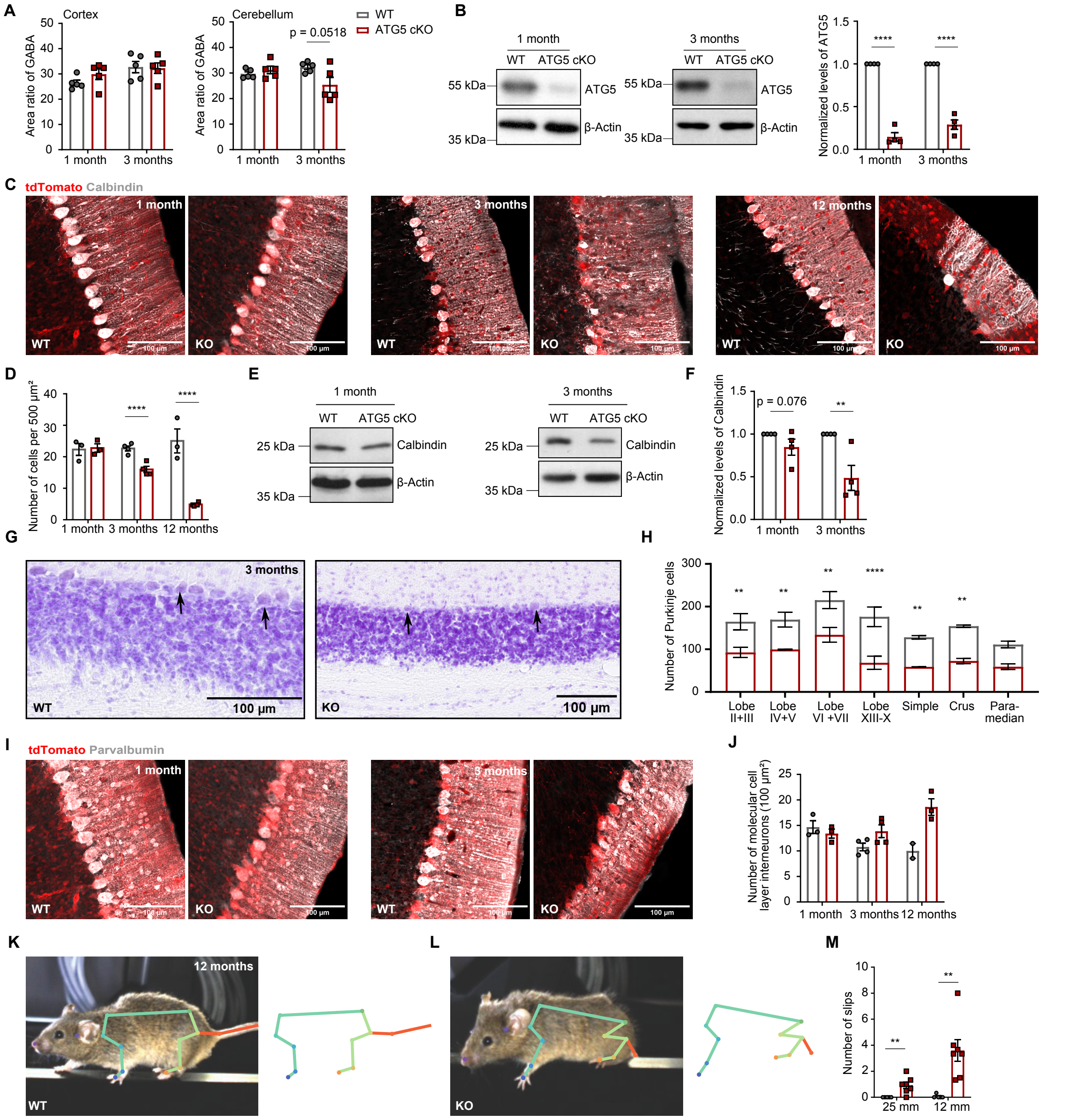

Figure 14: Cell type-specific vulnerability to autophagy loss. (A) Metabolomics analysis of GABA content in cortex and cerebellum of WT and ATG5 cKO mice. Each dot represents one animal (N=5 per genotype). One-tailed t-test was performed between WT and ATG5 cKO for each age. (B) Immunoblot analysis of ATG5 levels in 1- and 3-month-old cerebellum of WT and ATG5 cKO animals. β-actin was used as a loading control and for normalization of protein levels. Each dot represents one animal (N=4 per genotype). One-tailed unpaired t-test was performed for each age. (C) Representative images of cerebellar brain sections of from WT and ATG5 cKO mice at the age of 1,3 and 12 months immunostained for calbindin. Scale bar: 100 µm. (D) Purkinje cell number analysis based on Calbindin-positive cells from WT and ATG5 cKO mice at the age of 1,3 and 12 months. Each dot represents one animal (N=3 per genotype for 1 and 12-months old animals and N=4 per genotype for 3 months-old animals). Two-tailed t-test was performed for each age. (E) Representative immunoblots for Calbindin in WT and ATG5 cKO cerebellum at the age of 1 and 3 months. β-Actin was used as a loading control. (F) Immunoblot analysis of Calbindin levels in 1- and 3-month-old cerebellum of WT and ATG5 cKO animals. β-Actin was used for normalization of protein levels. Each dot represents one animal (N=4 per genotype). One-tailed unpaired t-test was performed for each age. (G) Representative cerebellar sections of WT and ATG5 cKO mice at the age of 3 months stained with Cresyl-violet. Arrows indicate Purkinje cell somata. Scale bar: 100 µm. (H) Purkinje cell number analysis per lobe based on Cresyl-violet staining of WT and ATG5 cKO animals at the age of 3 months (N=3 per genotype). Two-Way ANOVA with Holm-Sidak's multiple comparison test

was performed. (I) Representative images of molecular cell layer interneuron density of WT and ATG5 cKO mice at the age of 3 and 12 months immunostained for parvalbumin. Scale bar: 100 µm. (J). Molecular cell layer interneurons density analysis based on parvalbumin immunostaining of WT and ATG5 cKO animals at the age of 1, 3 and 12 months. Each dot represents one animal (N=3 per genotype for 1 and 12-months old animals, N=4 per genotype for 3 months-old animals and N=2 for WT at the age of 12 months). Two-tailed t-test was performed for each age. (K)/(L) Representative image of a 12-months old WT (K) and ATG5 cKO mouse (L) on a 25 mm beam during SIMI motion assay with tracked joints indicated in different colors. (M) SIMI motion analysis of the average number of slips per beam of WT and ATG5 cKO animals at the age of 12 months. Each dot represents one animal (N=5 for WT and N=7 for ATG5 cKO). Two-Way ANOVA with Holm-Sidak's multiple comparison test was performed. All Data are shown as mean ± SEM. Significant differences are indicated by asterisks (* $p<0.05$; ** $p<0.01$; *** $p<0.001$; ****$p<0.0001$).

1.3 Loss of autophagy results in region-specific astrogliosis

To assess whether the loss of ATG5 results in astrogliosis, immunohistochemistry and western blotting was performed for GFAP, a marker for reactive astrocytes. In the cerebellum of ATG5 cKO animals, increased immunofluorescent GFAP signal was observed at the age of 3 months (Fig. 15A). Increased GFAP signal was also observed in whole cerebellar lysates from ATG5 cKO mice at the age of 1 and 3 months (Fig. 15B and C). In contrast, cortical sections and cortical lysates did not indicate changes in GFAP signal (Fig. 15D, E and F). This indicates that loss of ATG5 results in region-specific astrogliosis in the cerebellum. Additionally, immunohistochemistry and western blotting was performed for cleaved Caspase-3, the main marker for apoptotic cell death. Immunoblotting of whole cerebellar and cortical tissue showed no indication of apoptosis at the age of 1 and 3 months (Fig. 15G and H). Furthermore, stained sections at the age of 3 months showed no sign of increased cleaved Caspase-3 signal (Fig. 15I).

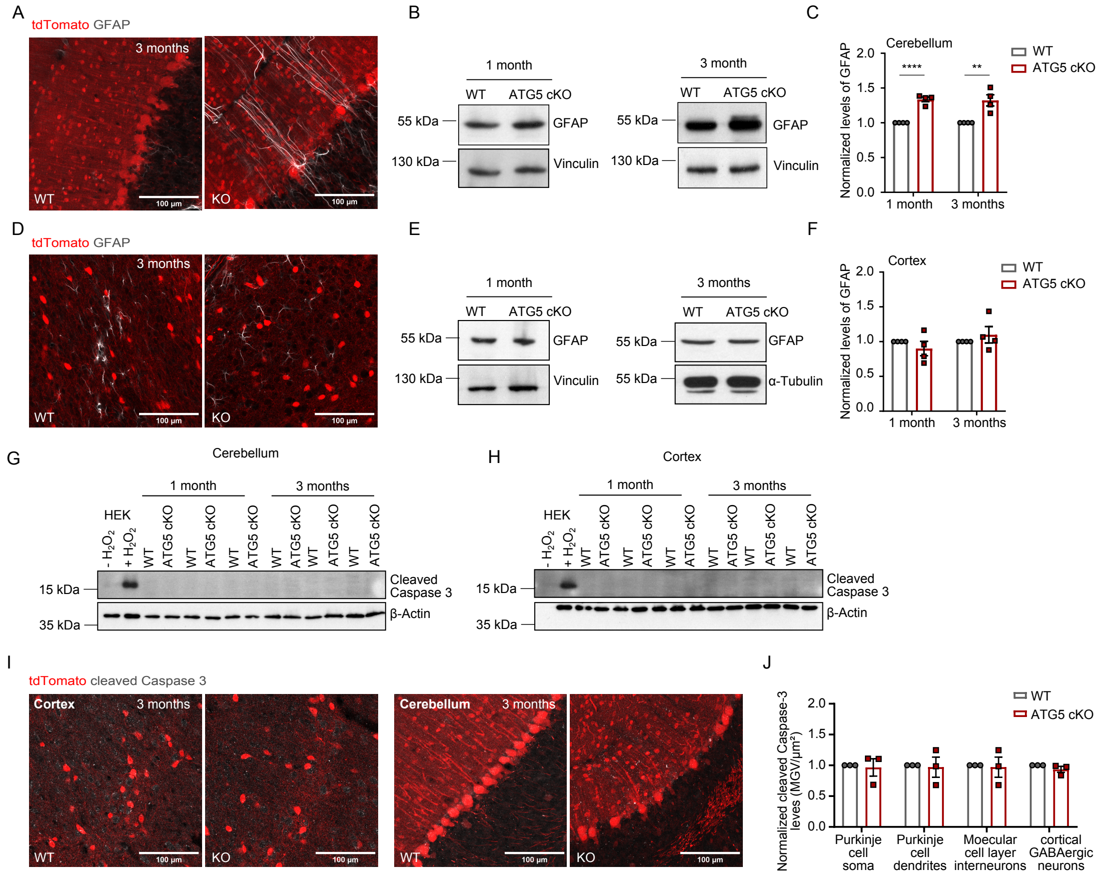

Figure 15: Region-specific astrogliosis upon loss of ATG5 in GABAergic neurons. (A)/(D) Representative images of cerebellar (A) and cortical (D) brain sections from WT and ATG5 cKO mice at the age of 3 months immunostained for GFAP. Scale bar: 100 µm. (B) Representative immunoblot of GFAP in 1- and 3-month-old cerebellum. Vinculin was used as a loading control. (C) Immunoblot analysis of GFAP levels in 1- and 3-month-old cerebellum of WT and ATG5 cKO animals. Vinculin was used normalization of protein levels. Each dot represents one animal (N=4 per genotype). One-tailed unpaired t-test was performed for each age. (E) Representative immunoblot of GFAP in 1- and 3-month-old cortex. Vinculin and α-Tubulin were used as a loading control. (F) Immunoblot analysis of GFAP levels in 1- and 3-month-old cortex of WT and ATG5 cKO animals. Vinculin and α-Tubulin were used for normalization of protein levels. Each dot represents one animal (N=4 per genotype). One-tailed unpaired t-test was performed for each age. (G)/(H) Representative immunoblot of cleaved Caspase-3 in 1- and 3-month-old cerebellum (G) and cortex (H). Untreated and H_2O_2-treated HEK cells were used as negative and positive control. β-Actin was used as a loading control. (I) Representative images of cerebellar and cortical brain sections from WT and ATG5 cKO mice at the age of 3 months immunostained for cleaved Caspase-3. Scale bar: 100 µm. (J) Analysis of fluorescent based levels of cleaved caspase-3 in cerebellum and cortex of 3-months old WT and ATG5 cKO animals. Each dot represents one animal (N=3 per genotype). One-tailed unpaired t-test was performed for each brain region. All Data are shown as mean ± SEM. Significant differences are indicated by asterisks (* p<0.05; ** p<0.01; *** p<0.001; ****p<0.0001).

1.4 Loss of autophagy results in region specific changes in AKT/mTORC1 signaling

To assess whether the loss of ATG5 affects mTORC1 signaling, immunostaining for phosphorylated ribosomal protein S6 (pS6) was performed and used as a read out.

Immunofluorescence analysis of pS6 in the cerebellum of 1 and 3 month old animals did not reveal any differences between WT and ATG5 cKO in Purkinje cells, as well as in molecular cell layer interneuron somata (Fig. 16A,C,D and E). In the cortex, increased pS6 levels could be detected in ATG5 deficient GABAergic neurons at one and three months of age (Fig. 16B and F).

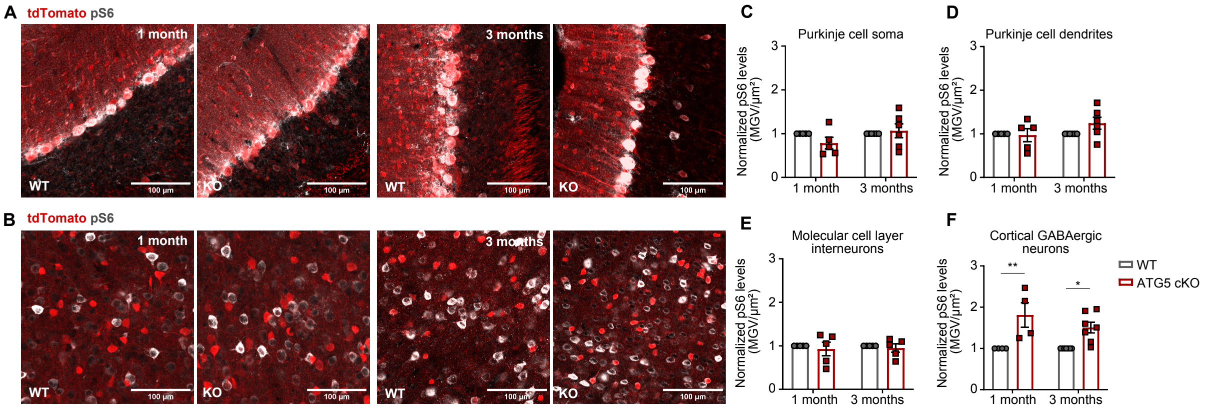

Figure 16: Region-specific changes in mTORC1 signaling upon loss of ATG5. (A)/(B) Representative images of cerebellar (A) and cortical (B) brain sections of 1- and 3-month-old WT and ATG5 cKO mice immunostained for pS6. Scale bar: 100 µm. (C) Fluorescent based analysis of pS6 in Purkinje cell soma of 1- and 3-month-old WT and ATG5 cKO animals. Each dot represents one animal (N=5 per genotype). One-tailed unpaired t-test was performed for each age. (D) Fluorescent based analysis of pS6 in Purkinje cell dendrites of 1- and 3-month-old WT and ATG5 cKO animals. Each dot represents one animal (N=5 per genotype. One-tailed unpaired t-test was performed for each age. (E) Fluorescent based analysis of pS6 in molecular cell layer interneurons of 1- and 3-month-old WT and ATG5 cKO animals. Each dot represents one animal (N=5 per genotype). One-tailed unpaired t-test performed for each age. (F) Fluorescent based analysis of pS6 in cortical GABAergic neurons of 1- and 3-month-old WT and ATG5 cKO animals. Each dot represents one animal (N=4 per genotype for 1-month old animals and N=7 for 3-month old animals). One-tailed unpaired t-test performed for each age. All Data are shown as mean ± SEM. Significant differences are indicated by asterisks (* $p<0.05$; ** $p<0.01$; *** $p<0.001$; **** $p<0.0001$).

To assess whether the loss of ATG5 affects AKT signaling, immunofluorescence analysis of AKT and phospho-AKT (pAKT) was performed. In the cerebellum, total AKT levels were decreased in ATG5 cKO Purkinje cell somata at 1 and 3 months of age (Fig. 17A and C). In Purkinje cell dendrites and molecular cell layer interneuron somata, decreased levels of AKT could be observed at the age of 1 month, while at 3 months of age no changes between ATG5 cKO and WT was observed (Fig. 17A,D and E). In cortical GABAergic somata no difference in AKT levels was observed in 1 and 3 months-old brain sections (Fig. 17B and F). pAKT levels were not changed upon loss of ATG5 in cerebellar and cortical GABAergic neurons at 1 and 3 months-of age (Fig. 17G and H). However, the ratio of pAKT levels to total AKT levels revealed increased ratio levels in ATG5 cKO cerebellum at 1 month of age and in ATG5 cKO Purkinje cell somata at the age of 3 months (Fig.17 I,j and K). In cortical ATG5 cKO GABAergic neurons no changes in pAKT/ AKT ratio could be detected (Fig.17 L).

These results outline that the loss of ATG5 results in region specific changes in AKT/mTORC1 signaling. In ATG5 cKO cortical GABAergic neurons AKT signaling is not changed while mTORC1 activity is increased, indicated by higher pS6 levels. In ATG5 cKO cerebellum, Purkinje cells display reduced levels of total AKT but no changes in pAKT, indicating increased AKT signaling. No changes in pS6 levels could be detected in ATG5 deficient cerebellum.

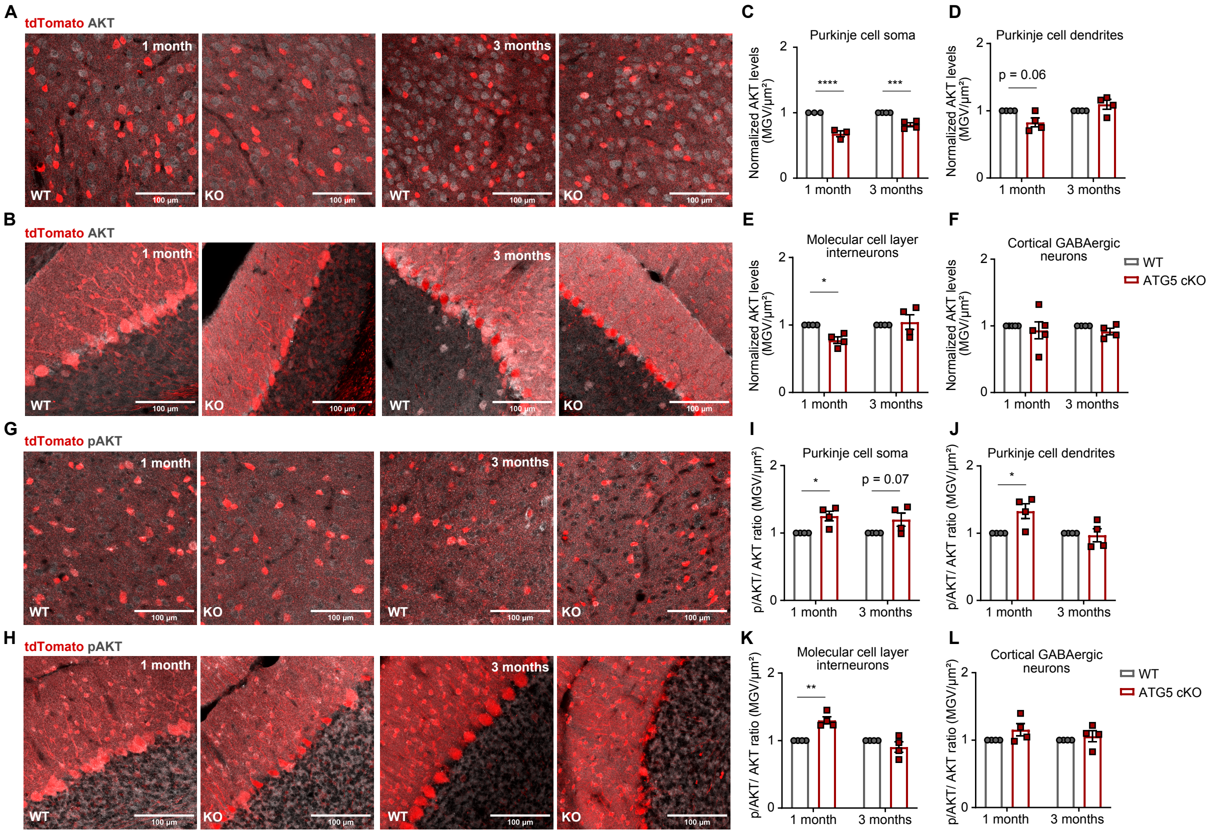

Figure 17: Region-specific changes in AKT levels upon loss of ATG5. (A)/(B) Representative images of cortical (A) and cerebellar (B) brain sections of 1- and 3-month old WT and ATG5 cKO mice immunostained for AKT. Scale bar: 100 µm. (C) Fluorescent based analysis of AKT in Purkinje cell soma of 1- and 3-month old WT and ATG5 cKO animals. Each dot represents one animal (N=4 per genotype). One-tailed unpaired t-test was performed for each age. (D) Fluorescent based analysis of AKT in Purkinje cell dendrites of 1- and 3-month old WT and ATG5 cKO animals. Each dot represents one animal (N=4 per genotype). One-tailed unpaired t-test was performed for each age. (E) Fluorescent based analysis of AKT in molecular cell layer interneurons of 1- and 3-month old WT and ATG5 cKO animals. Each dot represents one animal (N=4 per genotype). One-tailed unpaired t-test was performed for each age. (F) Fluorescent based analysis of AKT in cortical GABAergic neurons of 1- and 3-month old WT and ATG5 cKO animals. Each dot represents one animal (N=4 per genotype). One-tailed unpaired t-test was performed for each age. (G)/(H) Representative images of cortical (G) and cerebellar (H) brain sections of 1- and 3-month old WT and ATG5 cKO mice immunostained for pAKT. Scale bar: 100 µm. (I) Fluorescent based analysis of pAKT in Purkinje cell soma of 1- and 3-month old WT and ATG5 cKO animals. Each dot represents one animal (N=4 per genotype). One-tailed unpaired t-test was performed for each age. (J) Fluorescent based analysis of pAKT in Purkinje cell dendrites of 1- and 3-month old WT and ATG5 cKO animals. Each dot represents one animal (N=4 per genotype). One-tailed unpaired t-test was performed for each age. (K) Fluorescent based analysis of pAKT in molecular cell layer interneurons of 1- and 3-month old WT and ATG5 cKO animals. Each dot represents one animal (N=4 per genotype). One-tailed unpaired t-test was performed for each age. (L) Fluorescent based analysis of pAKT in cortical GABAergic neurons of 1- and 3-month old WT and ATG5 cKO animals. Each dot represents one animal (N=4 per genotype). One-tailed unpaired t-test was performed for each age.

All data shown as average ± SEM. Significant differences indicated by asterisks (* $p<0.05$; ** $p<0.01$; *** $p<0.001$; **** $p<0.0001$).

1.5 Loss of Purkinje cells does not correlate with accumulation of protein aggregates upon ATG5 deficiency

In order to assess whether loss of ATG5 afftects autophagic flux in cerebellum, levels of LC3 and p62 were analzed via immunoblotting. Based on previous publications, it is know that loss of ATG5 in GABAergic neurons results in elevated levels of p62 as well as decreased levels of LC3 II in the forebrain (Negrete-Hurtade et al., 2020; Overhoff et al., 2022). In the cerebellum, loss of ATG5 results in reduced levels of LC3 II and accumulation of LC3 I of 1 and 3 months-old animals, resulting in a decreased LC3 II vs I ratio compared to WT (Fig. 18A and B). Immunoblotting for p62 shows increased levels of p62 in 1 and 3 months-old cerebellum of ATG5 deficient mice (Fig.18C and D). Additionally, the number of mature and immature autophagosomes in WT and ATG5 cKO Purkinje cell somata at the age of three months was analyzed in electron microscopy images (Fig. 18E). WT Purkinje cell somata containined significantly more mature autophagosome and significantly less immature autophagsosomes compared to ATG5 cKO Purkinje cells (Fig.18F and G). This indicates that loss of ATG5 impairs cerebellar autophagic flux, resulting in increased levels of p62, decreased LC3 II/I ratio, and accumulation of immature autophagosomes.

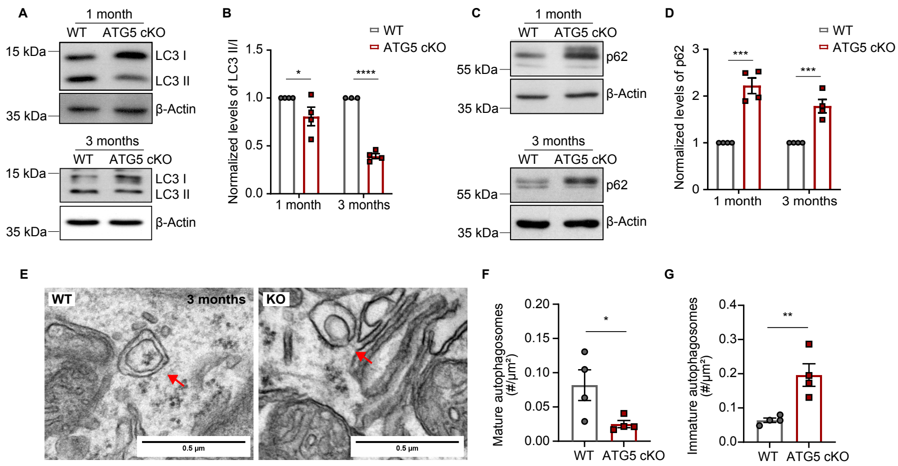

Figure 18: ATG5 deficient cerebellum displays defects in autophagic flux. (A) Representative immunoblot for LC3 in 1- and 3-month-old WT and ATG5 cKO cerebellum. β-Actin was used as a loading control. (B) Immunoblot analysis of LC3 in 1- and 3-month-old WT and ATG5 cKO cerebellum. Each dot represents one animal (N=4 per genotype). One-tailed unpaired t-test was performed between WT and ATG5 cKO for each age. (C) Representative immunoblot for p62 in 1- and 3-month-old WT and ATG5 cKO cerebellum. β-Actin was used as a loading control. (B) Immunoblot analysis of p62 in 1- and 3-month-old WT and ATG5 cKO cerebellum. Each dot represents one animal (N=4 per genotype). One-tailed unpaired t-test was performed between WT and ATG5 cKO for each age. (E) Representative electron microscopy (EM) image of WT and ATG5 cKO Purkinje cell somata at the age of 3 months. Arrows indicate mature (WT) and immature (KO) autophagosomes. Scale bar: 0.5 µm. (F) EM analysis of number of mature autophagosomes in WT and ATG5 cKO Purkinje cell somata at the age of 3 months. Each dot represents one animal (N=4 per genotype). Two-tailed unpaired t-test was performed. (G) EM analysis of number of immature autophagosomes in WT and ATG5 cKO Purkinje cell somata at the age of 3 months. Each dot represents one animal (N=4 per genotype). Two-tailed unpaired t-test was performed. All data shown as average ± SEM. Significant differences indicated by asterisks (* $p<0.05$; ** $p<0.01$; *** $p<0.001$; **** $p<0.0001$).

Autophagy deficiency is associated with accumulation of protein aggregates and inclusion bodies in several cell types and brain regions (Hara et al., 2006; Komatsu et al., 2006; Komatsu et al., 2007; Nishiyama et al., 2007; Liang et al., 2010; Zhao et al., 2015; Joo et al., 2016; Yamaguchi et al., 2018; Overhoff et al., 2022). To address whether Purkinje cell vulnerability is associated with accumulation of aggregates, immunofluorescence analysis of autophagic receptors NBR1 and p62 in cortical and cerebellar sections was performed.

Immunofluorescence staining revealed no accumulation of large aggregates in ATG5 cKO Purkinje cells (Fig. 19A and E). In contrast, accumulation of NBR1 and p62 positive aggregates was detected in cortical ATG5 deficient GABAergic neurons at the age of 1 and 3 months (Fig. 19C and G). The number of NBR1 and p62 puncta increases upon loss of ATG5 in both Purkinje cells and cortial GABAergic neurons (Fig. 19B,D,F and H). While ATG5 cKO Purkinje cells display signifiicantly higher numbers of NBR1 and p62 puncta (Fig. 19J and I) cortical ATG5 cKO GABAergic neuons show significantly bigger aggregates compared to ATG5 cKO Purkinje cells (Fig. 19I and K).

Thus, in agreement with previous findings, the lack of autophagy leads to an accumulation of structures that are positive for the autophagy receptors p62 and NBR1 in the cortex. In contrast, ATG5-deficient Purkinje cells show no signs of aggregates. Although they show a higher number of p62 and NBR1 puncta than WT cells, the size of the aggregates is significantly smaller compared to ATG5-deficient cortical GABAergic neurons.

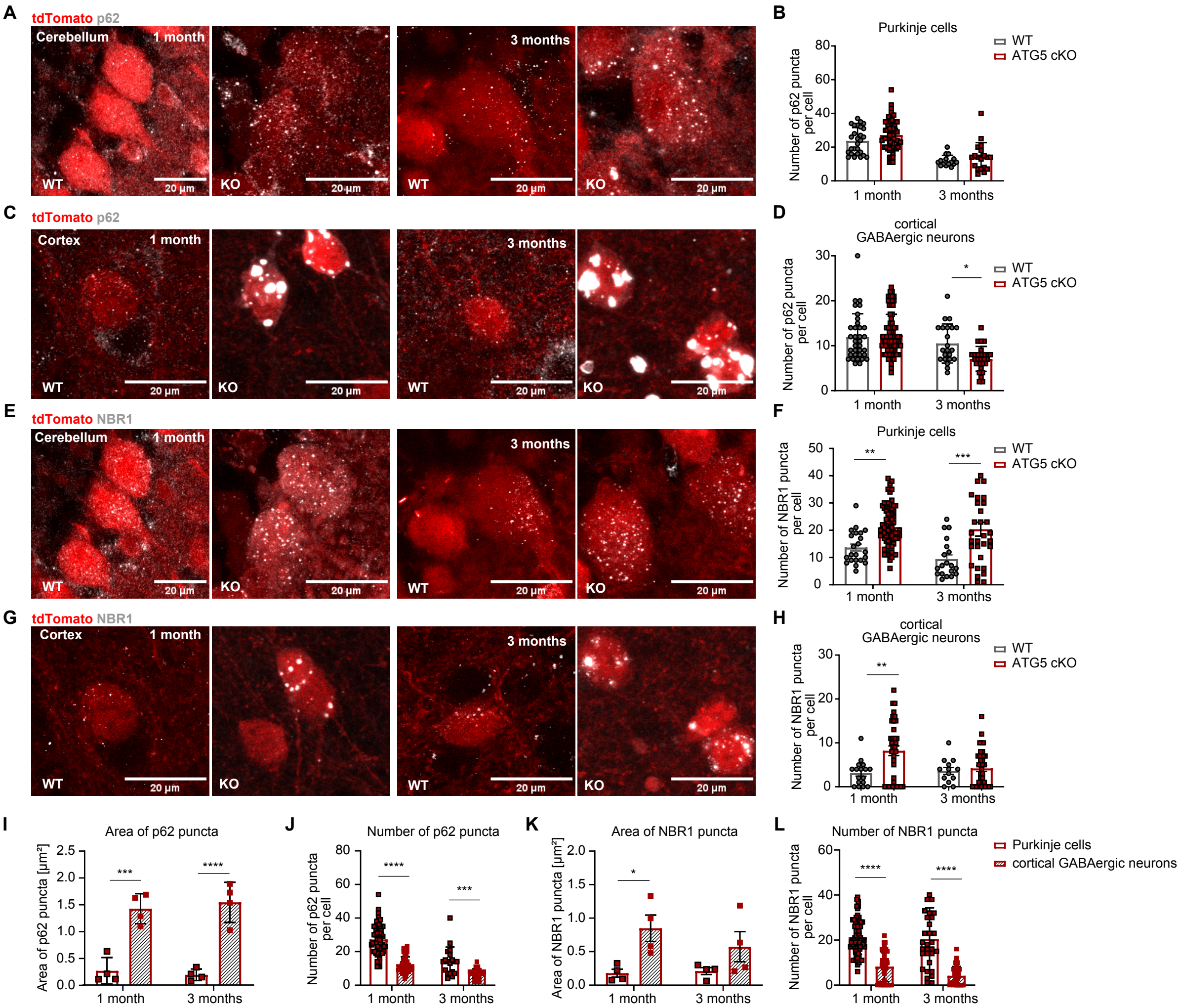

Figure 19: Purkinje cell loss upon autophagy dysfunction does not correlate with accumulation of protein aggregates. (A)/(C)Representative immunofluorescence images of p62 in cerebellar (A) and cortical (C) brain sections of 1- and 3-month old WT and ATG5 cKO. Scale bar: 20 µm. (B) Fluorescent based analysis of number of p62 puncta per Purkinje cell soma of 1- and 3-month old WT and ATG5 cKO animals. Each dot represents one cell (N=4 per genotype). Two-tailed unpaired t-test was performed for each age ((D) Fluorescent based analysis of number of p62 puncta per cortical GABAergic neuron soma of 1- and 3-month old WT and ATG5 cKO animals. Each dot represents one cell (N=4 per genotype). Two-tailed unpaired t-test was performed for each age. (E) /(G) Representative immunofluorescence images of NBR1 in cerebellar (E) and cortical (G) brain sections of 1- and 3-month old WT and ATG5 cKO. Scale bar: 20 µm. (F) Fluorescent based analysis of number of NBR1 puncta per Purkinje cell soma of 1- and 3-month old WT and ATG5 cKO animals. Each dot represents one cell (N=4 per genotype). Two-tailed unpaired t-test was performed for each age (H) Fluorescent based analysis of number of NBR1 puncta per cortical GABAergic neuron soma of 1- and 3-month old WT and ATG5 cKO animals. Each dot represents one cell (N=4 per genotype). Two-tailed unpaired t-test was performed for each age. (I) Fluorescent based analysis of the area of p62 puncta in Purkinje cell soma and cortical GABAergic neuron soma of 1- and 3-month old WT and ATG5 cKO animals. Each dot represents one animal (N=4 per genotype). Two-tailed unpaired t-test was performed for each age. (J) Fluorescent based analysis of number of p62 puncta per cell between Purkinje cell and cortical GABAergic neuron soma of ATG5 cKO animal at the age of one and three months. Each dot represents one cell (N=4 per genotype). Two-tailed unpaired t-test was performed for each age. (K) Fluorescent based analysis of the area of NBR1 puncta in Purkinje cell soma and cortical GABAergic neuron soma of 1- and 3-month old WT and ATG5 cKO animals. Each dot represents one animal (N=4 per genotype). Two-tailed unpaired t-test was performed. for each age. (L) Fluorescent based analysis of number of NBR1 puncta per cell between Purkinje cell and cortical GABAergic neuron soma of ATG5 cKO animal at the age of one and three months. Each dot

represents one cell (N=4 per genotype). Two-tailed unpaired t-test was performed for each age. All data shown as average ± SEM. Significant differences indicated by asterisks (* $p<0.05$; ** $p<0.01$; *** $p<0.001$; **** $p<0.0001$).

In order to assess whether the observed inclusion bodies are the result of defective aggrephagy, immunofluorescence staining for ubiquitin was performed. In the cortex of 3-month-old ATG5 cKO mice, some p62 and NBR1 positive aggregates colocalize with ubiquitin (Fig. 20A and C). However, in the cerebellum, no aggregates of ubiquitin were observed in Purkinje cell somata (Fig. 20B and D).

This data set indicates that the selective vulnerability of Purkinje cells to autophagy dysfunctions may not be due to the accumulation of protein aggregates.

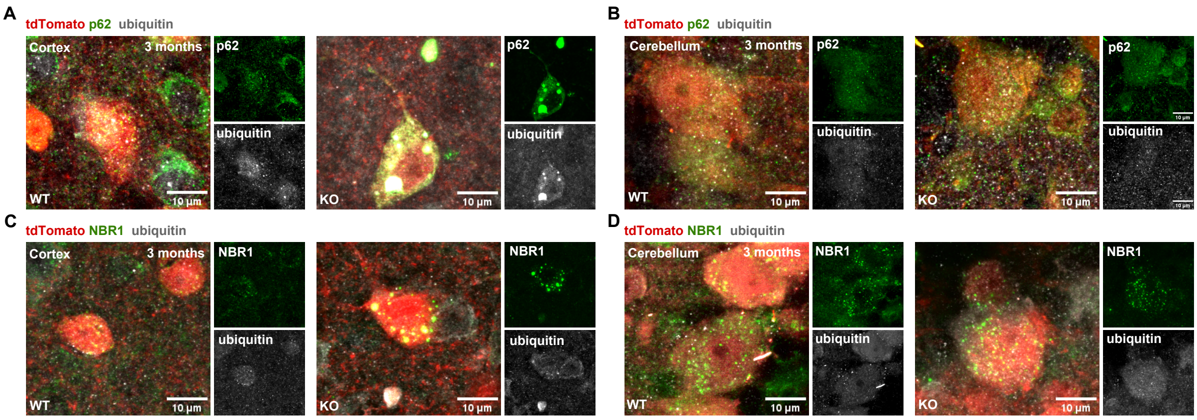

Figure 20: Purkinje cell loss upon autophagy deficiency does not correlate with accumulation of ubiquitin positive protein aggregates. (A)/(B) Representative immunofluorescent image of p62 and ubiquitin in cortical (A) and cerebellar (B) brain sections of 3-month-old WT and ATG5 cKO animals. Scale bar: 10 µm. (C)/(D) Representative immunofluorescent image of NBR1 and ubiquitin in cortical (C) and cerebellar (D) brain sections of 3-month-old WT and ATG5 cKO animals. Scale bar: 10 µm.

2. Proteomics analysis reveals metabolic changes in ATG5 deficient cerebellum prior to Purkinje cell loss

To understand what exactly causes the onset of Purkinje cell loss in ATG5 cKO cerebellum at the age of three months, total proteome analysis was performed on cerebellar tissue of 1- and 3- month- old WT and ATG5 cKO animals. A total of 609 and 853 significantly dysregulated proteins (p-value <0.05 and fold change > 0.25) was found in the cerebellum of ATG5 cKO mice at the age of 1 and 3 months, respectively. (Fig. 21A,B and C). KEGG pathway analysis of upregulated proteins revealed changes in metabolic pathways in both ages, while downregulated proteins cluster in pathways associated with neurodegenerative diseases (Fig. 21D and E). 32 proteins were commonly upregulated at 1 and 3 months in ATG5 cKO mice and cluster in KEGG pathway analysis such as metabolic pathways, mitophagy and ferroptosis (Fig. 21C and F). GO molecular function analysis of upregulated and downregulated proteins indicate changes in nucleotide binding and ubiquitin binding (Fig. 21G,H and I). GO biological process analysis of upregulated and downregulated proteins indicate alterations in protein transport and localization

(Fig. 21 J,K and L). GO cellular compartment analysis reveals alterations in mitochondria, synapses, vesicle and cytoskeleton (Fig. 21M, N and O).

Taken together, total proteome analysis of ATG5 cKO cerebellum indicates changes in metabolic processes prior to the onset of Purkinje cell loss. While some changes are specific to certain ages, metabolic alterations are detected at both ages and display most dysregulated proteins that are commonly upregulated at 1 month and 3 months of age.

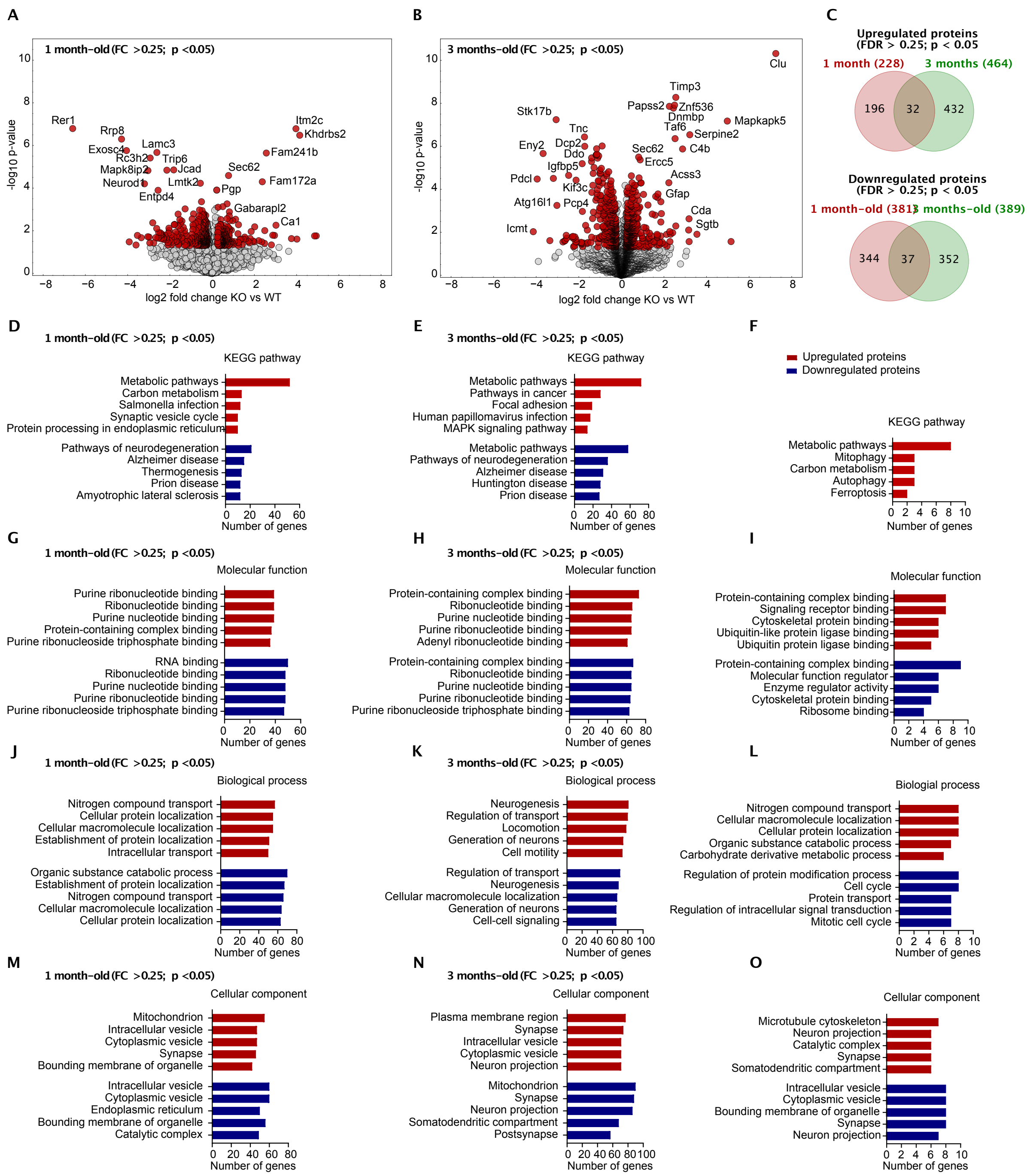

Figure 21: Proteomics analysis indicates metabolic changes in ATG5 cKO cerebellum prior to Purkinje cell loss. (A)/(B) Volcano plot of 1-month-old (A) and 3-months-old (B) cerebellum proteomics data with significantly changed proteins highlighted in red. N=5 per genotype. Log2 fold change > 0.25 and p-value < 0.05. (C) Venn diagram of common significantly upregulated and downregulated proteins in

ATG5 cKO cerebellum of 1 and 3 months of age. (D-F) GO KEGG pathway analysis of significantly changed proteins detected at 1 month of age (D), 3 months of age (E) and common changes at both ages (F). (G-I) GO molecular function analysis of significantly changed proteins detected at 1 month of age (G), 3 months of age (H) and common changes at both ages (I). (J-L) GO biological processes of significantly changed proteins detected at 1 month of age (J), 3 months of age (K) and common changes at both ages(L). (M-O) GO cellular component analysis of significantly changed proteins detected at 1 month of age (M), 3 months of age (N) and common changes at both ages (O).

3. Metabolomic analysis reveals increased glycolytic metabolism in ATG5 cKO cerebellum

3.1 Untargeted metabolomics reveals increased glycolysis upon loss of ATG5

The previously described proteomic data set indicates that the loss of ATG5 results in increased metabolic pathways starting at the age of 1 month. In order to confirm these changes, untargeted metabolomic analysis of cortex and cerebellum at the age of 1 and 3 months was performed in collaboration with Prof. Christian Frezza (CECAD, Universität zu Köln).

At 1 month of age only a few changes were detected in the cerebellum. More prominent changes were observed in ATG5 cKO cerebellum at the age of 3 months (Fig. 22A and B). Analysis of the upregulated metabolites revealed that they mainly clustered in metabolic pathways associated with glucose metabolism, such as Warburg effect, glycolysis, pentose phosphate pathway and pyruvate metabolism. Downregulated metabolites are associated with pyrimidine metabolism, mitochondrial metabolism and β-Oxidation (Fig. 22D). In the Cortex of ATG5 deficient mice, less changes could be observed compared to ATG5 cKO cerebellum (Fig. 22D and E). In the cortex of 1-month old ATG5 cKO animals only two metabolites were significantly increased, whereas several downregulated metabolites were detected (Fig. 22 D). In the cortex of ATG5 cKO animals, dysregulated metabolites barely clustered in pathway analysis.

The untargeted metabolomics data set shows significant changes in metabolic pathways in the cerebellum of ATG5 cKO animals, while the changes in the cortex are less pronounced

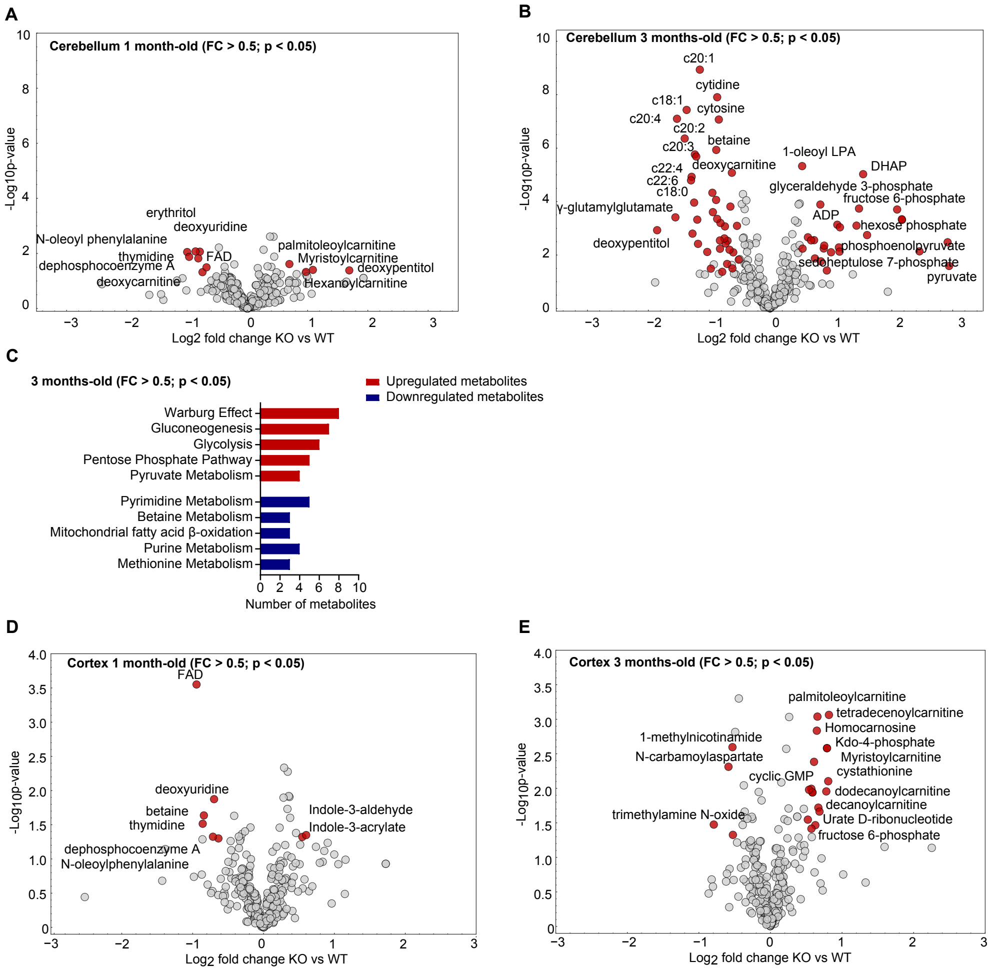

Figure 22: Untargeted metabolomics indicates increased glycolytic metabolism in ATG5 cKO cerebellum. (A)/(B) Volcano plot of 1-month (A) and 3-months-old (B) cerebellum metabolomic data set with significantly changed metabolites highlighted in red. N=5 per genotype. Log2 fold changes >0.5 and p-value <0.05. (C) Pathway analysis of significantly upregulated and downregulated metabolites in 3-months-old ATG5 cKO cerebellum. (D)/(E) Volcano plot of 1-month (D) and 3-months-old cortex (E) metabolomic data set with significantly changed metabolites highlighted in red. N=5 per genotype. Log2 fold changes > 0.5 and p-value <0.05.

3.2 Targeted metabolomics reveals global changes in amino acid metabolism in ATG5 cKO cerebellum

Since pyrimidine metabolism is reduced in both cortex and cerebellum, the amino acid content was analyzed in cortex and cerebellum at the age of 1 and 3 months using a targeted metabolomics approach.

Amino acid analysis of 1 and 3-month old cerebellum revealed global changes upon loss of ATG5. At the age of 1 month, significantly increased levels of several amino acids, such as histidine, cysteine, serine, phenylalanine, tyrosine, isoleucine, leucine, threonine, methionine and proline could be detected (Fig. 23A,G,K,L,M,O,P,Q,R,S and U). At the age of 3 months, significantly reduced levels of histidine, phenylalanine, valine threonine, asparagine, aspartate, proline, glutamate and glutamine were detected (Fig. 23B,E,F,H,I,K,P,Q,S and V). Interestingly, most changes are associated with the glycolytic pathway at 1 month, at 3 months changes are more associated with the TCA cycle pathway (Fig. 23A and B).

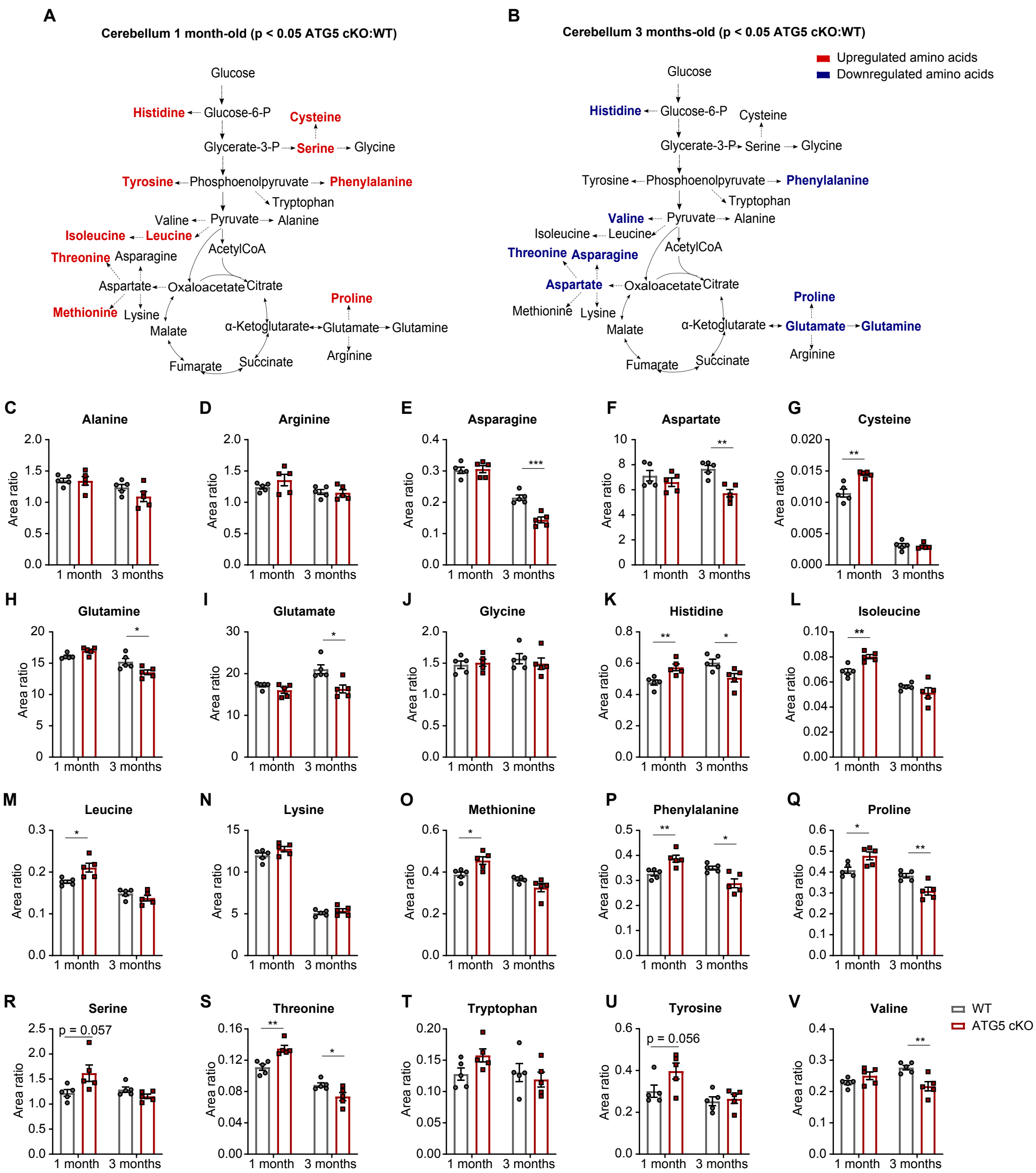

Figure 23: Global amino acid changes in ATG5 cKO cerebellum. (A-B) Schematic of amino acid metabolism in the cerebellum of 1-month-old (A) and 3-months-old (B) ATG5 cKO animals with significantly increased amino acids highlighted in red and significantly reduced amino acids highlighted in blue. (C) Alanine, (D) arginine, (E) asparagine, (F) aspartate, (G) cysteine, (H) glutamine, (I) glutamate, (J) glycine, (K) histidine, (L) isoleucine, (M) leucine, (N) lysine, (O) methionine, (P) phenylalanine, (Q) proline, (R) serine, (S) threonine, (T) tryptophan; (U) tyrosine, and (V) valine analysis in WT and ATG5 cKO cerebellum. Each dot represents one animal (N=5 per genotype). All data shown as average ± SEM. Two-tailed unpaired t-test was performed between WT and ATG5 cKO for each age. Significant differences indicated by asterisks (* p<0.05; ** p<0.01; *** p<0.001; ****p<0.0001).

Targeted metabolomics analysis of amino acids in the cortex of WT and ATG5 cKO mice displayed no changes in amino acid content at the age of 3 months (Fig. 24). At the age of 1 month, histidine, phenylalanine, threonine, and methionine are significantly increased in ATG5 cKO cortex (Fig. 24A,J,N and O).

These findings show that loss of ATG5 causes stronger changes in the cerebellum than in the cortex, in line with untargeted metabolomics analysis.

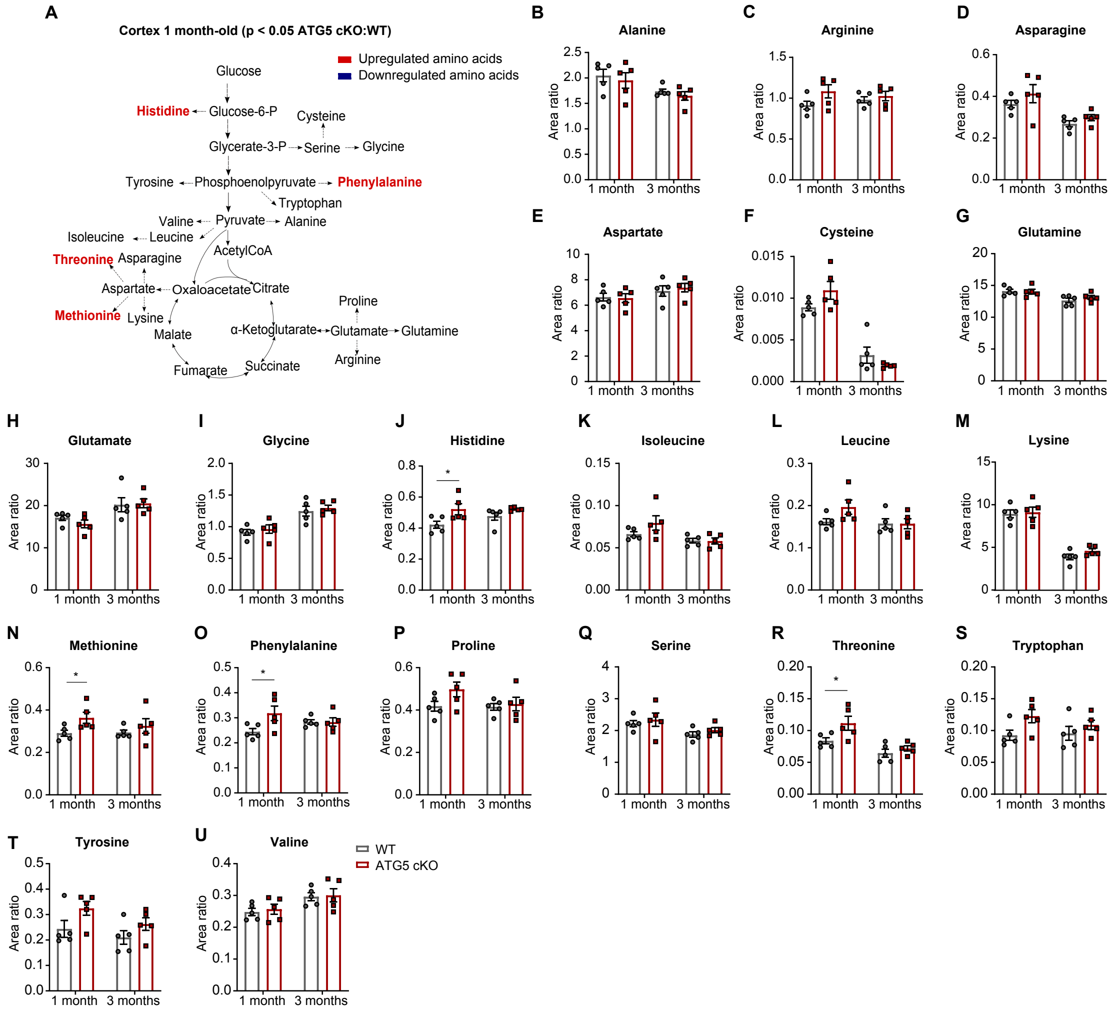

Figure 24: Minor amino acid changes in ATG5 cKO cortex. (A) Schematic of amino acid metabolism in the cortex of 1-month-old ATG5 cKO animals with significantly increased amino acids highlighted in red and significantly reduced amino acids highlighted in blue. (B) Alanine, (C) arginine, (D) asparagine, (E) aspartate, (F) cysteine, (G) glutamine, (H) glutamate, (I) glycine, (J) histidine, (K) isoleucine, (L) leucine, (M) lysine, (N) methionine, (O) phenylalanine, (P) proline, (Q) serine, (R) threonine, (S) tryptophan; (T) tyrosine, and (U) valine analysis in WT and ATG5 cKO cortex. Each dot represents one animal (N=5 per genotype). All data shown as average ± SEM. Two-tailed unpaired t-test was performed between WT and ATG5 cKO for each age. Significant differences indicated by asterisks (* p<0.05; ** p<0.01; *** p<0.001; ****p<0.0001).

3.3 Targeted metabolomics reveals increased glycolytic metabolites in ATG5 cKO cerebellum

The untargeted metabolomics approach indicates increased glucose metabolism in both cortex and cerebellum of ATG5-deficient animals. Therefore, a targeted metabolomic approach was used to specifically analyze metabolites of certain metabolic pathways. Glycolysis metabolites, pentose phosphate metabolites and TCA cycle metabolites were analyzed in cortex and cerebellum of 1-and 3-month old WT and ATG5 cKO animals.

Targeted metabolomic analysis of glycolysis metabolites displayed significantly increased levels of glucose-6-phosphate and fructose-6-phosphate in 1-month old ATG5 cKO cerebellum (Fig. 25A). Glucose-6-phosphate and fructose-1,6-phsphate are significantly increased in 3-months old ATG5 cKO cerebellum (Fig. 25B). No changes in lactate were observed, in both cerebellum and cortex of 1 and 3 months old ATG5 cKO animals (Fig.25C and F). However, lactate quickly diffuses out of the cell following the brain blood gradient and is therefore difficult to capture via metabolomics analysis (Dienel, 2012). In ATG5 cKO cortex, no changes in glycolysis metabolites were detected at both ages (Fig. 25D and E). This suggests that the loss of ATG5 results in increased metabolites of the glycolytic pathway, already detectable at the age of 1 month.

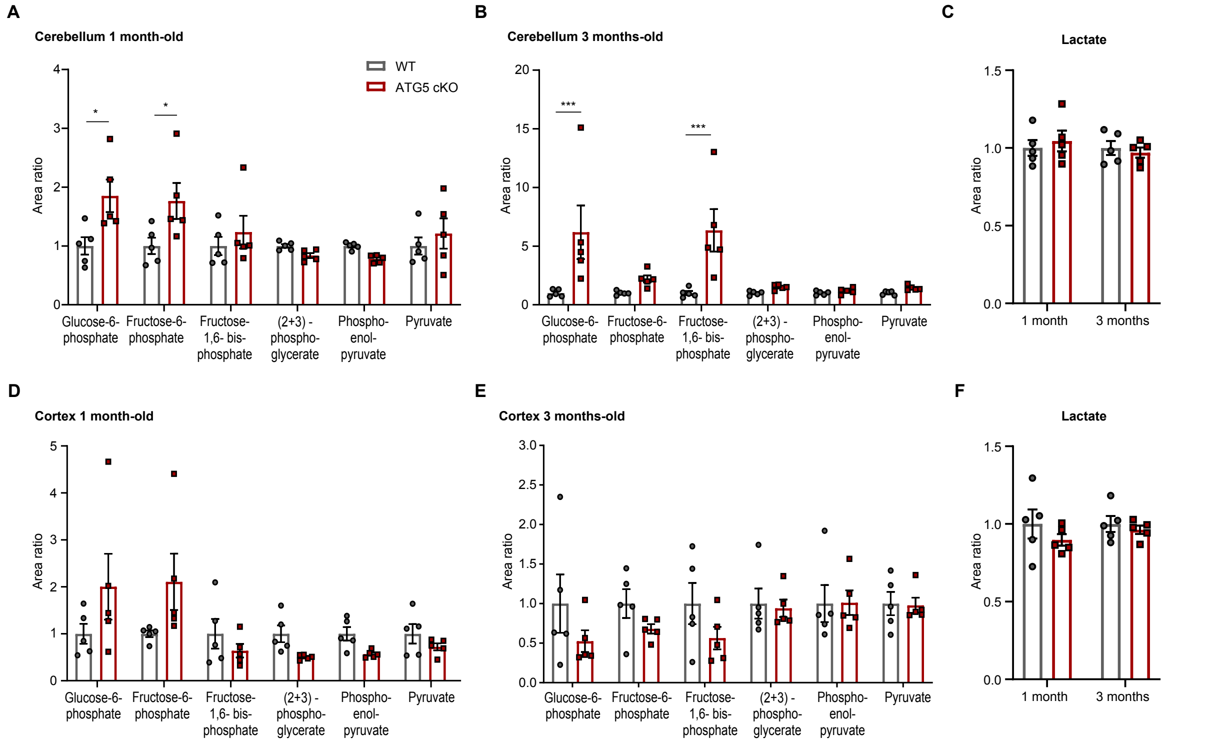

Figure 25: Increased levels of upper glycolysis intermediates in ATG5 cKO cerebellum. (A)/(B) Glycolysis metabolite analysis in 1-month (A) and 3-month s(B) old cerebellum of WT and ATG5 cKO mice. Each dot represents one animal (N=5 per genotype). Two-Way ANOVA with Holm-Sidak's multiple comparison test was performed. (C) Lactate analysis in one- and three-month old cerebellum of WT and ATG5 cKO cerebellum. Each dot represents one animal (N=5 per genotype). Two-tailed t-test between WT and ATG5 cKO for each age was performed. (D)/(E) Glycolysis metabolite analysis in 1-month (D) and 3-months (E) old cortex of WT and ATG5 cKO mice. Each dot represents one animal (N=5 per genotype). Two-Way ANOVA with Holm-Sidak's multiple comparison test was performed. (F) Lactate analysis in one- and three-month old cortex of WT and ATG5 cKO cerebellum. Each dot represents one animal (N=5 per genotype). Two-tailed t-test between WT and ATG5 cKO was performed for each age.
All data shown as average ± SEM. Significant differences indicated by asterisks (* p<0.05; ** p<0.01; *** p<0.001; ****p<0.0001).

In order to assess whether changes in metabolic pathways are affecting mitochondrial metabolism, TCA cycle metabolites were analyzed. No changes in TCA cycle intermediates were detected in 1-month old ATG5 cKO cerebellum (Fig. 26A). In 3-months old cerebellum, significantly decreased levels of citrate, succinate and fumarate were detected (Fig. 26B).

Significantly increased levels of aconitate and isocitrate were observed in 1-month old ATG5 cKO cortex, while no changes were detected in 3 months old ATG5 cKO cortex (Fig. 26C and D).

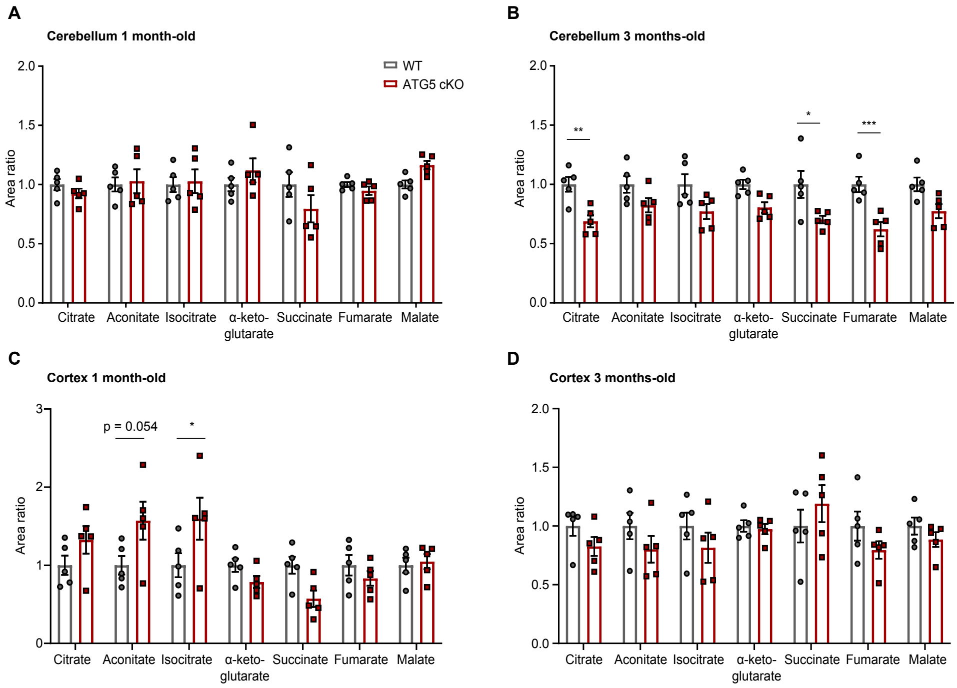

Figure 26: Targeted metabolomics analysis of amino acids in ATG5 deficient cortex and cerebellum. (A)/(B) TCA cycle metabolite analysis in 1-month (A) and 3-months (B) old cerebellum of WT and ATG5 cKO mice. Each dot represents one animal (N=5 per genotype). Two-Way ANOVA with Holm-Sidak's multiple comparison test was performed. (C)/(D) TCA cycle metabolite analysis in 1-month (C) and 3-months (D) old cortex of WT and ATG5 cKO mice. Each dot represents one animal (N=5 per genotype). Two-Way ANOVA with Holm-Sidak's multiple comparison test was performed. All data shown as average ± SEM. Significant differences indicated by asterisks (* $p<0.05$; ** $p<0.01$; *** $p<0.001$; **** $p<0.0001$).

Additionally, levels of pentose phosphate pathway metabolites were analyzed in cortex and cerebellum of ATG5 deficient mice. In 1-month old cerebellum, no changes in pentose phosphate pathway metabolites were detected, whereas 6-phosphogluconate was significantly increased in 3-months old ATG5 cKO cerebellum (Fig. 27A and B). In 1-month old ATG5 cKO cortex increased levels of sedulose-7-phosphate was observed, but no changes in 3-months old ATG5 cKO cortex (Fig. 27C and D).

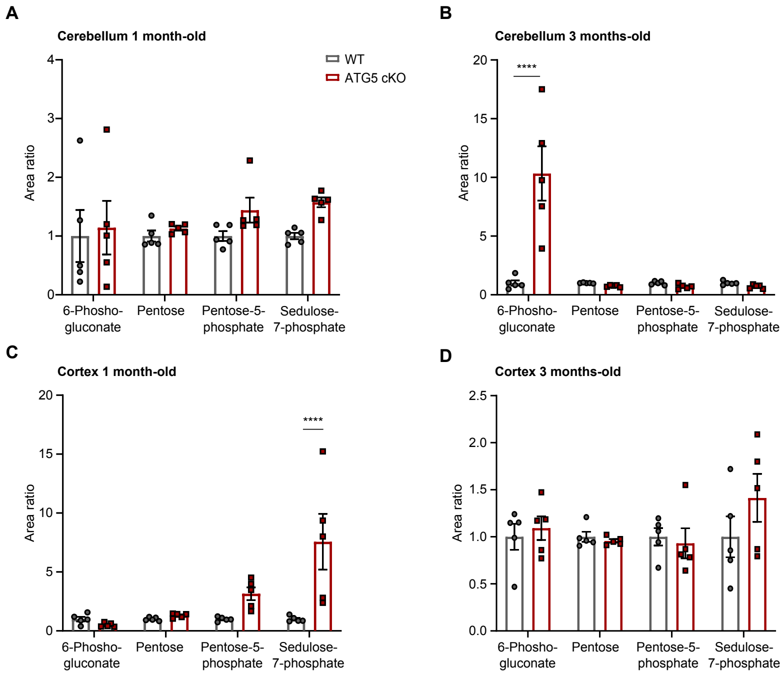

Figure 27: Targeted metabolomics analysis of pentose-phosphate pathway metabolites in ATG5 deficient cortex and cerebellum. (A)/(B) Pentose phosphate pathway metabolite analysis in 1-month (A) and 3-months (B) old cerebellum of WT and ATG5 cKO mice. Each dot represents one animal (N=5 per genotype). Two-Way ANOVA with Holm-Sidak's multiple comparison test was performed. (C)/(D) Pentose phosphate pathway metabolite analysis in 1-month (C) and 3-months (D) old cortex of WT and ATG5 cKO mice. Each dot represents one animal (N=5 per genotype). Two-Way ANOVA with Holm-Sidak's multiple comparison test was performed. All data shown as average ± SEM. Significant differences indicated by asterisks (* p<0.05; ** p<0.01; *** p<0.001; ****p<0.0001).

3.4 Isotope labeling reveals increased glycolytic flux in ATG5 cKO cerebellum

In order to assess whether the changes in glycolysis metabolites detected in targeted and untargeted metabolomics are due to increased glucose uptake and flux, isotope labeling of $^{13}C_6$ glucose in 3-month old acute brain sections was performed (in collaboration with Dr. Patrick Giavalisco, MPI of Ageing, Cologne).

Isotope labeling revealed that ATG5 deficient cerebellar slices display significantly increased glucose uptake compared to WT slices. Additionally, ATG5 cKO cerebellum displays increased glycolytic flux, indicated by increased carbogen flux into lactate as well as glycolytic derived metabolites such as serine, glycine and alanine. Increased glucose flux was also detected into pentose phosphate pathway metabolites such as pentose-5-phosphate and sedulose-7-phosphate. In addition, import and glucose flux into the TCA cycle is not altered in ATG5 cKO cerebellum (Fig. 28A).

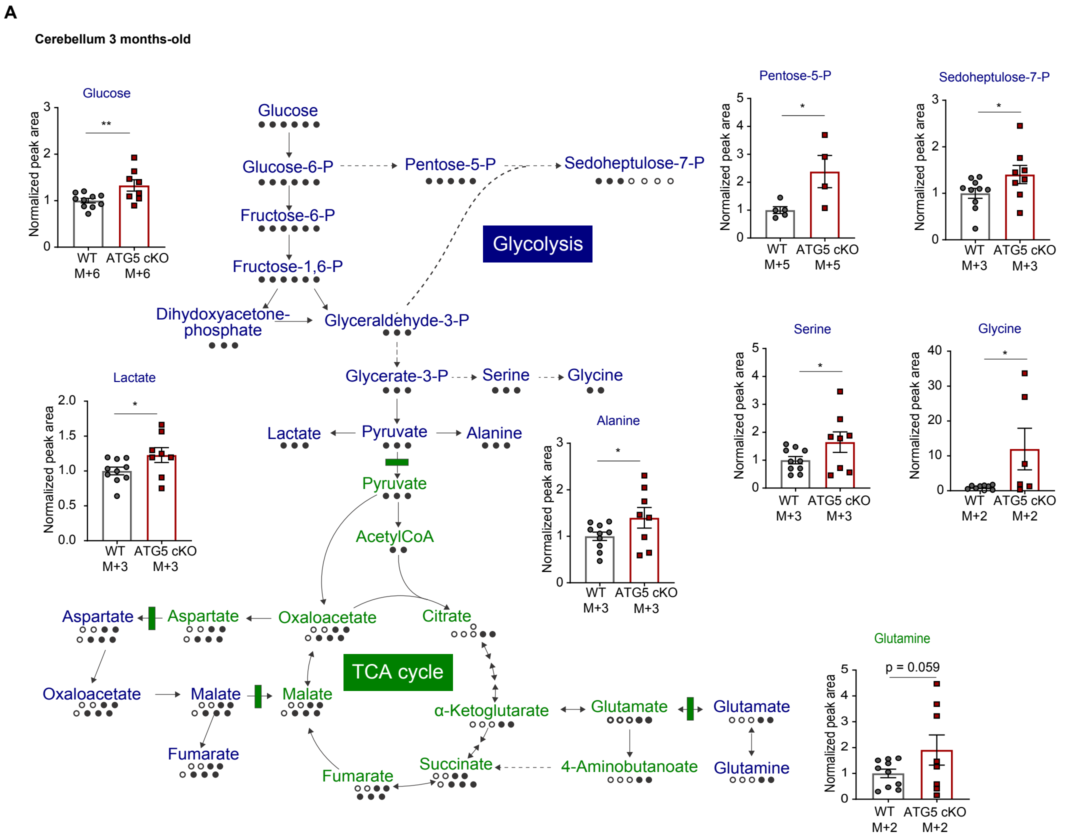

Figure 28: Isotope labeling reveals increased glycolytic flux in ATG5 cKO cerebellum. (A) Schematic of glucose metabolism with graphs of metabolites with significantly changed glucose flux. Each dot represents one animal (N=8 per genotype). Data represents average ± SEM. Two-tailed t-test was performed. All data shown as average ± SEM. Significant differences indicated by asterisks (* p<0.05; ** p<0.01; *** p<0.001; ****p<0.0001).

Additionally, isotope labeling of $^{13}C_6$ glucose in 3-months old cortical acute slices was performed. In contrast to ATG5 deficient cerebellum, no differences in glucose uptake was observed. Glucose enrichment into glycolytic metabolites and TCA cycle intermediates are also not changed. However, in ATG5 cKO cortex, significantly increased glucose-derived carbogen enrichment into pentose-5-phosphate and sedulose-7-phosphate was detected (Fig. 29A).

This indicates that loss of ATG5 results in region specific changes in glucose enrichment. In the cerebellum, loss of ATG5 results in increased glucose uptake and increased glucose oxidation via the glycolytic pathway and to some extend in the pentose phosphate pathway. In contrast, loss of ATG5 in the cortex results in increased glucose enrichment exclusively into pentose phosphate pathway metabolites.

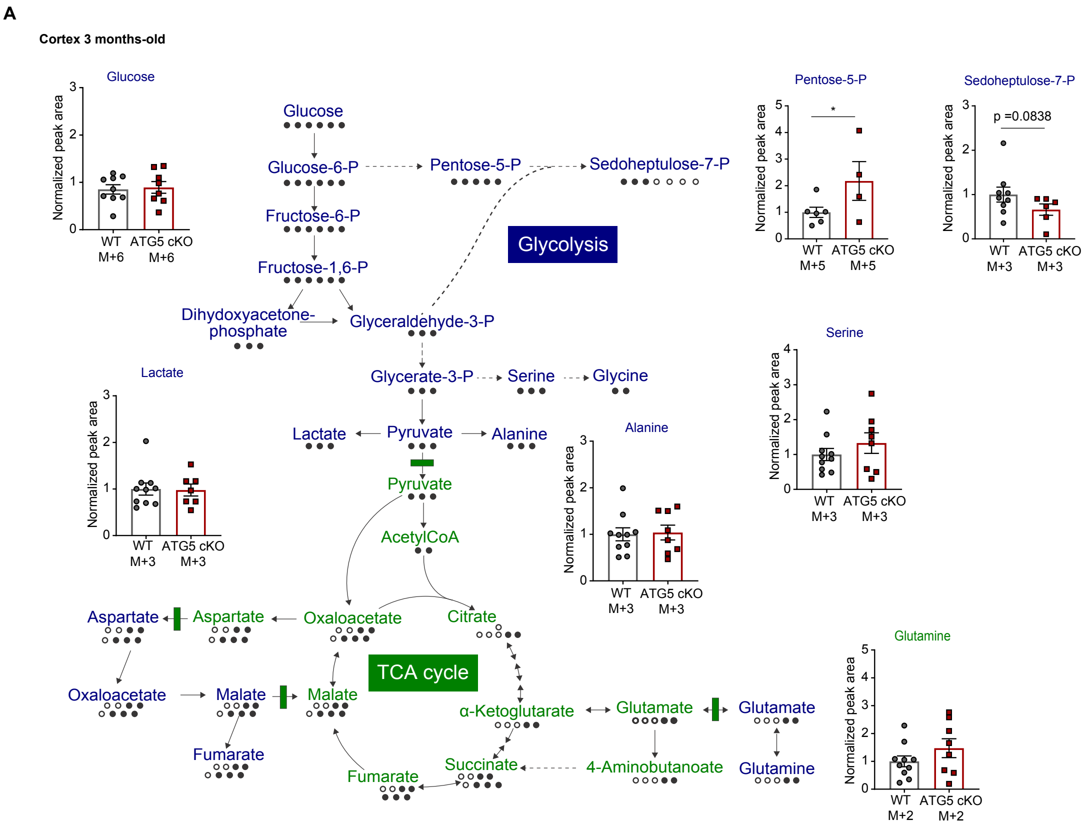

Figure 29: Isotope labeling reveals increased glycolytic flux into pentose phosphate pathway in ATG5 cKO cortex. (A) Schematic of glucose metabolism with representative graphs of cortical metabolites. Each dot represents one animal (N=8 per genotype). Data represents average ± SEM. Two-tailed t-test was performed. All data shown as average ± SEM. Significant differences indicated by asterisks (* p<0.05; ** p<0.01; *** p<0.001; ****p<0.0001).

4. Purkinje cell loss upon loss of autophagy dysfunction does not correlate with impaired mitochondrial function

Proteomics and metabolomics analysis of ATG5 cKO cerebellum did not indicated impaired mitochondrial function nor mitochondrial metabolism. However, targeted metabolomics revealed decreased levels of some TCA cycle derived amino acids and some TCA cycle metabolites at the age of 3 months. To address mitochondrial morphology in ATG5 cKO cerebellum, immunofluorescence analysis and electron microscopy was performed. For immunofluorescence analysis, a subunit of mitochondrial OXPHOS complex III, mitochondrial cytochrome B (MT-CYB), was used. In Purkinje cells and molecular cell layer interneurons, no difference was observed in 1- and 3-month- old ATG5 cKO cerebellum (Fig. 30A,C,D and E). In cortical GABAergic neurons, decreased levels of MT-CYB were detected at the age of 1 month, however at the age of 3 months no differences could be detected (Fig. 30B and F). Electron microscopy (EM) of Purkinje cell somata at the age of 3 months indicated not alterations in mitochondrial ultrastructure (Fig. 30G). Number of mitochondria and the area of mitochondria are not changed in ATG5 cKO Purkinje cell somata (Fig. 30H and I). However, the cristae length normalized by mitochondrial area indicated slight increase in cristae volume upon loss of ATG5 (Fig. 30J).

In order to assess whether loss of ATG5 results in accumulation of aged mitochondria, an adeno-associated virus (AAV) encoding for mitoTimer was injected into cerebellar lobes IV/V of WT and ATG5 cKO mice. MitoTimer fluorescence changes upon oxidative status of mitochondria, young mitochondria are labeled in green and older mitochondria are labeled in red. Immunofluorescence analysis of the ratio of red divided by green fluorescence gives an indication about the accumulation of older mitochondria. Immunofluorescent images show a trend of increased levels of older mitochondria in ATG5 cKO Purkinje cells (Fig.30K). However, immunofluorescent analysis did not show any differences between WT and ATG5 cKO Purkinje cell somata and dendrites (Fig. 30L). Lastly, mitochondrial function was assessed via MitoStress test in primary cerebellar cells. ATG5 cKO cells display slightly increased oxygen consumption rate after injection of oligomycin and FCCP (Fig. 30M). However, no differences were observed when analyzing single parameters of the assay (Fig. 30N).

In summary, this data set indicates that mitochondrial morphology is not altered in ATG5 cKO cerebellum. Mitochondrial ultrastructure is maintained in Purkinje cell somata and loss of ATG5 does not result in accumulation of damaged mitochondria. In addition, *in vitro* MitoStress test assay of primary cerebellar cells indicates that mitochondrial function in maintained.

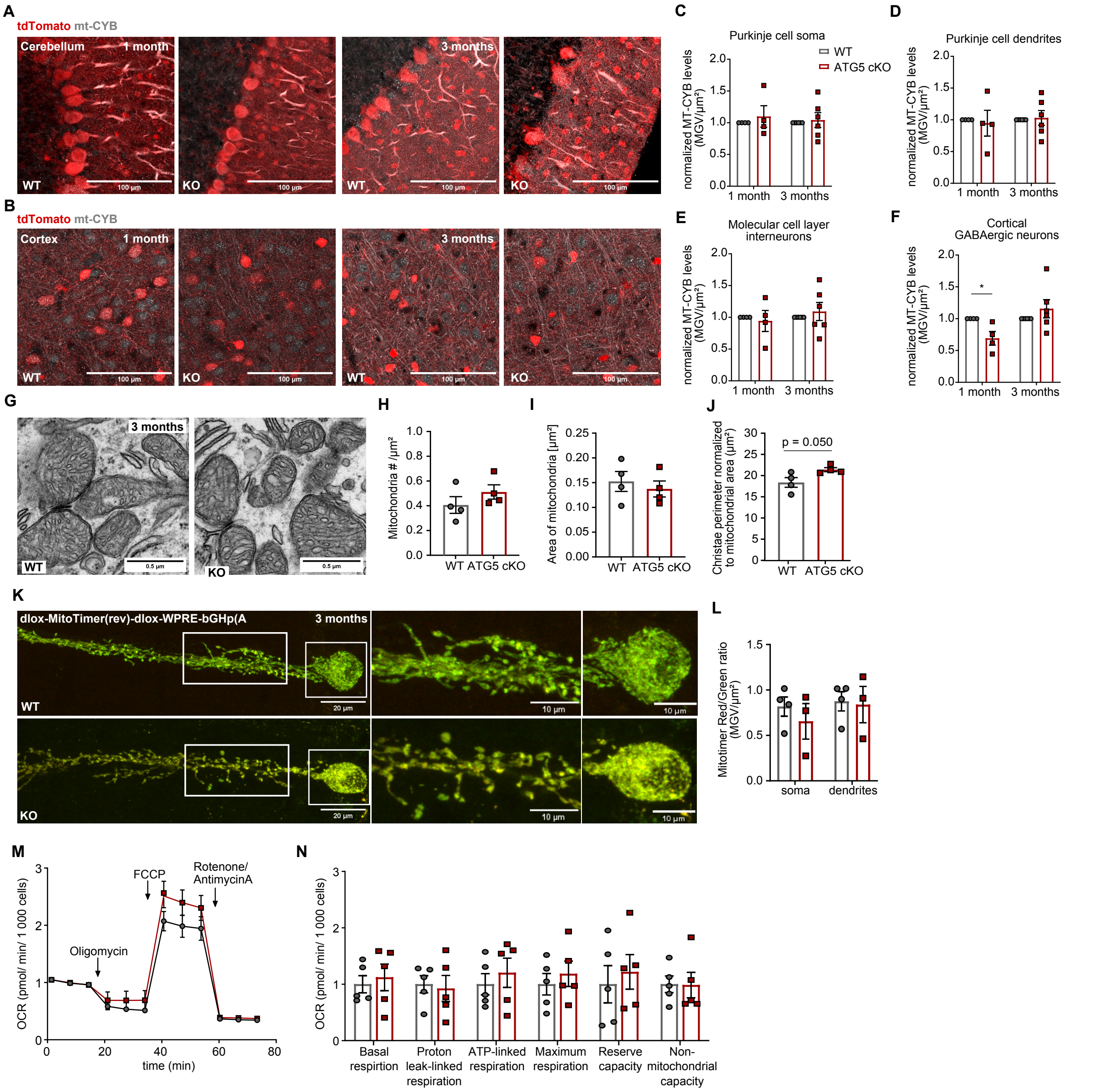

Figure 30: Loss of Purkinje cells upon autophagy dysfunction does not correlate with impaired mitochondrial function. (A)/(B) Representative immunofluorescence images of MT-CYB in WT and ATG cKO cerebellum (A) and cortex (B) at the age of 1 and 3 months. Scale bar: 100 µm. (C) Fluorescent based analysis of MT-CYB in Purkinje cell somata of 1- and 3-month old WT and ATG5 cKO mice. Each dot represents one animal (N=4 per genotype for 1-month old animals and N=5 per genotype for 3-month old animals). Two-tailed unpaired t-test between WT and ATG5 cKO was performed for each age. (D) Fluorescent based analysis of MT-CYB in Purkinje cell dendrites of 1- and 3-month old WT and ATG5 cKO mice. Each dot represents one animal (N=4 per genotype for 1-month old animals and N=5 per genotype for 3-month old animals). Two-tailed unpaired t-test between WT and ATG5 cKO was performed for each age. (E) Fluorescent based analysis of MT-CYB in molecular cell layer interneurons of 1- and 3-month old WT and ATG5 cKO mice. Each dot represents one animal (N=4 per genotype for 1-month old animals and N=5 per genotype for 3-month old animals). Two-tailed unpaired t-test between WT and ATG5 cKO was performed for each age. (F) Fluorescent based analysis of MT-CYB in cortical GABAergic neurons of 1- and 3-month old WT and ATG5 cKO mice. Each dot represents one animal (N=4 per genotype for 1-month old animals and N=5 per genotype for 3-month old animals). Two-tailed unpaired t-test between WT and ATG5 cKO was performed for each age. (G) Representative electron microscopy images of WT and ATG5 Purkinje cell somata at the age of 3 months. Scale bar: 0.5 µm. (H) EM based analysis of mitochondrial number per Purkinje cell soma of WT and ATG5 cKO mice at the age of 3 months. Each dot represents one animal (N=4 per genotype). Two-tailed unpaired t-test was performed. (I) EM

based analysis of mitochondrial area in WT and ATG5 cKO Purkinje cell somata at the age of 3 months. Each dot represents one animal (N=4 per genotype). Two-tailed unpaired t-test was performed. (J) EM based analysis of cristae length normalized to mitochondrial area in WT and ATG5 cKO Purkinje cell somata at the age of 3 months. Each dot represents one animal (N=4 per genotype). Two-tailed unpaired t-test was performed. (K) Representative images of mitoTimer injected Purkinje cells of WT and ATG5 cKO cerebellum at the age of 3 months. Scale bar: 20/10 µm. (L) MitoTimer based fluorescence image analysis of red fluorescence divided by green fluorescence in Purkinje cell somata and dendrites of WT and ATG5 cKO cerebellum at the age of 3 months. Each dot represents one animal with N=4/3 per genotype. Two-Way ANOVA with Holm-Sidak's multiple comparison test was performed. (M) Oxygen consumption rate during the assay of WT and ATG5 cKO primary cerebellar cells (DIV17) (N=5 per genotype). Two-Way ANOVA with Holm-Sidak's multiple comparison test was performed. (N) Mito Stress test assay parameter analysis of oxygen consumption rate during the assay of WT and ATG5 cKO primary cerebellar cells (DIV17). Each dot represents one animal (N=5 per genotype). Two-Way ANOVA with Holm-Sidak's multiple comparison test was performed. All data shown as average ± SEM. Significant differences indicated by asterisks (* p<0.05; ** p<0.01; *** p<0.001; ****p<0.0001).

5. ATG5 deficient Purkinje cells display increased glycolysis

5.1 *Ex vivo* ATG5 cKO Purkinje cells display increased glycolysis indicators

Metabolomic and proteomic approaches indicated increased glucose metabolism in ATG5 cKO cerebellum, therefore the Seahorse XF Glycolysis Stress Test was performed in primary cerebellar neurons. This assay assesses glycolytic function by measuring the extracellular acidification rate (ECAR) of WT and ATG5 cKO cerebellar cells at DIV17. ATG5 cKO cells displayed higher ECAR at baseline and after glucose and oligomycin injections, revealing increased ECAR rate upon loss of ATG5 (Fig. 31A). Analysis of single parameters of the assay did not indicate any significant differences however glycolytic rate and glycolytic capacity were slightly increased in ATG5 cKO cells compared to WT (Fig. 31B). Since this assay measures ECAR levels of mixed cerebellar cells, the glycolytic capacity of *ex vivo* Purkinje cells in WT and ATG5 cKO cerebellar organotypic slices (OTCs) was analyzed. In order to address changes in glucose uptake, WT and ATG5 cKO OTCs were incubated for 30 min with 1 mM 2-NBDG, a fluorescent D-glucose analog. 2-NBDG is taken up by the cell and phosphorylated via the first glycolytic enzyme hexokinase into 2-deoxy-d-glucose-6-phosphate, a metabolite that cannot be further metabolized and therefore stays unprocessed within the cell (Pajak et al., 2019). Live imaging of 2-NBDG displayed significantly increased glucose uptake in ATG5 cKO Purkinje cells (Fig. 31C and D). Additionally, cerebellar OTCs were transduced with an AAV expressing the FRET sensor Laconic to measure Lactate levels in WT and ATG5 cKO Purkinje cells. Lactate levels were significantly higher in ATG5 cKO Purkinje cells compared to WT levels (Fig. 31E,F and G). In order to measure ATP levels, cerebellar OTCs were transduced with an AAV expressing ATeam to measure ATP levels in Purkinje cells. ATeam signal indicated significantly increased ATP levels in ATG5 cKO Purkinje cells (Fig. 31H,I and J). To exclude the contribution of mitochondrial ATP, cerebellar OTCs expressing ATeam were incubated with oligomycin to block ATP synthesis of mitochondrial OXPHOS. In the presence of oligomycin, ATG5 deficient Purkinje cells displayed significantly higher ATP levels than WT Purkinje cells (Fig. 31K,L and

M). This indicates that *ex vivo* ATG5 cKO Purkinje cells display increased glycolytic flux, indicated by increased glucose uptake, increased lactate levels and increased non-mitochondrial derived ATP levels.

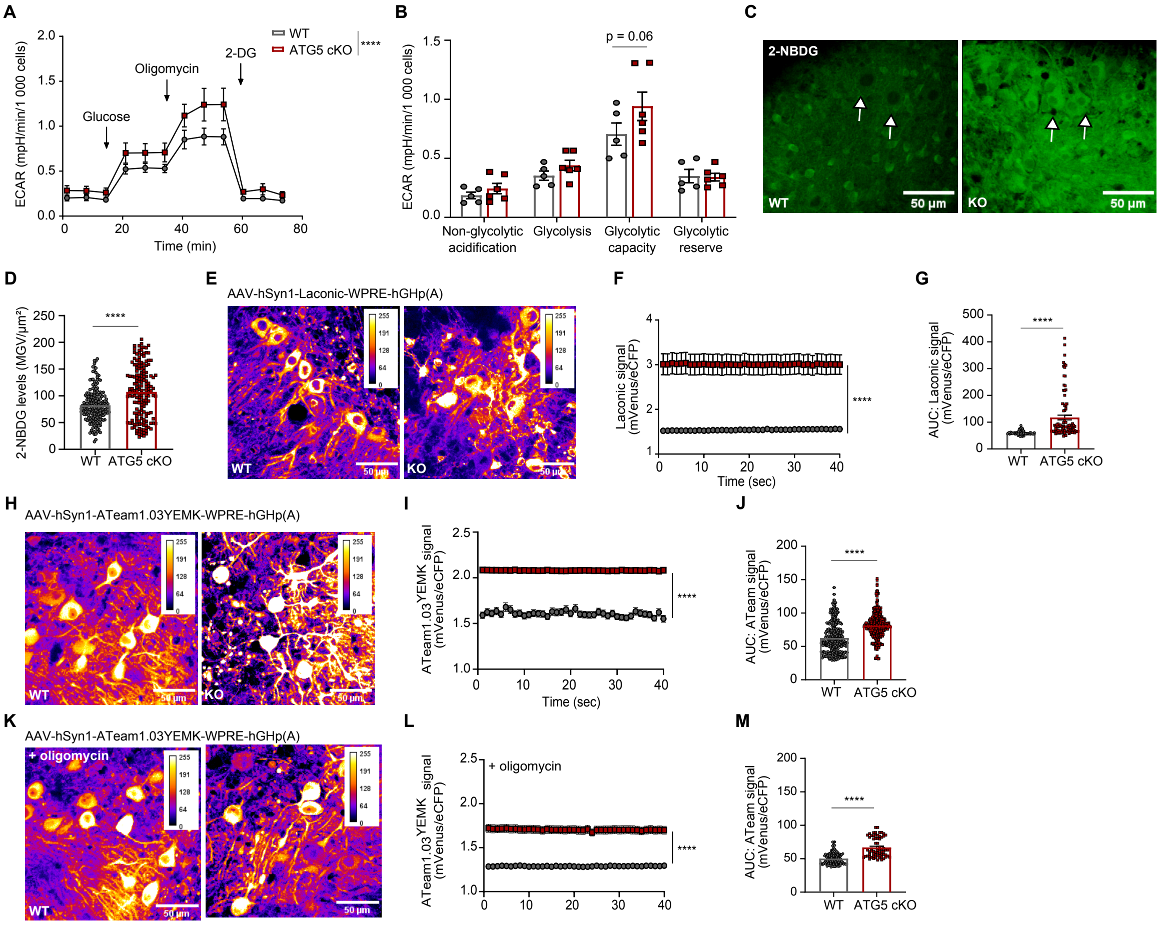

Figure 31: Excessive glycolysis in ATG5 cKO Purkinje cells *ex vivo*. (A) Extra acidification rate of primary cerebellar cells (DIV17) from WT (N=5) and ATG5 cKO (N=6) animals during glycolysis Stress test with injections of 10 mM glucose, 1.5 µM oligomycin and 50 nM 2-DG. Two-Way ANOVA with Holm-Sidak's multiple comparison test was performed. (B) Analysis of glycolysis Stress Test parameters of primary cerebellar cells from WT and ATG5 cKO animals. Each dot represents one animal (N=5 for WT and N=6 for ATG5 cKO). Two-Way ANOVA with Holm-Sidak's multiple comparison test was performed. (C) Representative image of 2-NBDG fluorescence in WT and ATG5 cKO cerebellar organotypic slices (OTCs). Scale bar: 50 µm. Arrows indicate Purkinje cell somata. (D) Fluorescence based analysis of 2-NBDG uptake in WT and ATG5 cKO Purkinje cells in OTCs. Each dot represents a single cell (for WT 190 cells from N=7 and for ATG5 cKO 168 cells from N=5). Two-tailed t-test was performed. (E) Representative ratiometric images of AAV-hSyn1-Laconic transduced WT and ATG5 cKO OTCs. Scalebar: 50 µm. (F) Ratiometric analysis of Laconic signal of WT (83 cells from N=6) and ATG5 cKO (95 cells from N=5) Purkinje cells. Two-Way ANOVA with Holm-Sidak's multiple comparison test was performed. (G) Area under the curve of Laconic signal over time in WT and ATG5 cKO Purkinje cells of OTCs. Each dot represents one cells (N=6 for WT and N=5 for ATG5 cKO). Two-Way ANOVA with Holm-Sidak's multiple comparison test was performed. (H) Representative ratiometric images of AAV-hSyn1-ATeam transduced WT and ATG5 cKO OTCs. Scalebar: 50 µm. (I) Ratiometric analysis of ATeam signal of WT (560 cells from N=6) and ATG5 cKO (317 cells from N=6) Purkinje cells. Two-Way ANOVA with Holm-Sidak's multiple comparison test was performed. (J) Area under the curve of ATeam signal over time in WT and ATG5 cKO Purkinje cells of OTCs. Each dot represents one cells (N=6 per genotype with 560 cells for WT and 317 ells for ATG5 cKO). Two-Way ANOVA with Holm-Sidak's multiple comparison test was performed.

(K) Representative ratiometric images of AAV-hSyn1-ATeam transduced WT and ATG5 cKO OTCs incubated with 1.5 µM oligomycin. Scalebar: 50 µm. (L) Ratiometric analysis of ATeam signal of WT (131 cells from N=3) and ATG5 cKO (66 cells from N=4) Purkinje cells incubated with 1.5 µM oligomycin. Two-Way ANOVA with Holm-Sidak's multiple comparison test was performed. (M) Area under the curve of ATeam signal over time in WT and ATG5 cKO Purkinje cells of OTCs incubated with 1.5 µM oligomycin. Each dot represents one cells (for WT 131 cell from N=3 and for ATG5 cKO 66 cells from N=4). Two-Way ANOVA with Holm-Sidak's multiple comparison test was performed. All data shown as average ± SEM. Significant differences indicated by asterisks (* p<0.05; ** p<0.01; *** p<0.001; ****p<0.0001).

5.2 Hexokinase II levels are increased in one-month old Purkinje cells

Ex vivo ATG5 deficient Purkinje cells in cerebellar OTCs display increased glycolytic flux (Fig. 31) and *ex vivo* ATG5 cKO acute cerebellar slices display increased glucose uptake and glycolytic flux (Fig. 28). To gain insights into whether ATG5 cKO Purkinje cell display increased glycolysis, immunohistochemistry for hexokinase II was performed. Hexokinase II (HK II) is the first enzyme of the glycolytic reaction that oxidizes glucose irreversibly to glucose-6-phopshate (and can be used as an indicator of glycolytic activity). In the cerebellum, increased levels of hexokinase II were observed in ATG5 cKO Purkinje cell somata at the age of 1 month (Fig. 32A and C). However, at the age of 3 months, decreased levels of hexokinase II were detected in ATG5 cKO Purkinje cell somata (Fig. 32B and C). No changes were observed in Purkinje cell dendrites and molecular cell layer interneurons at the age of 1 and 3 months of age (Fig. 32D and E). Interestingly, hexokinase levels decrease from 1 to 3 months in WT Purkinje cells and molecular cell layer interneurons (Fig. 32F). In cortical GABAergic neurons no changes were observed at the age of 1 month but significantly increased levels of hexokinase II could be detected in 3-month old ATG5 cKO cortical GABAergic neurons (Fig. 32G,H and I). In WT cortical GABAergic neurons, no difference between hexokinase II levels were observed between 1 and 3 months (Fig. 32J). This data indicates that at the age of 1 month, increased glycolytic enzyme hexokinase II is present in ATG5 cKO Purkinje cells. In the cortex, increased levels of hexokinase were detected at the age of 3 months. In WT conditions, hexokinase II levels do not differ between 1 and 3 months, whereas levels in the cerebellum decrease between 1 and 3 months.

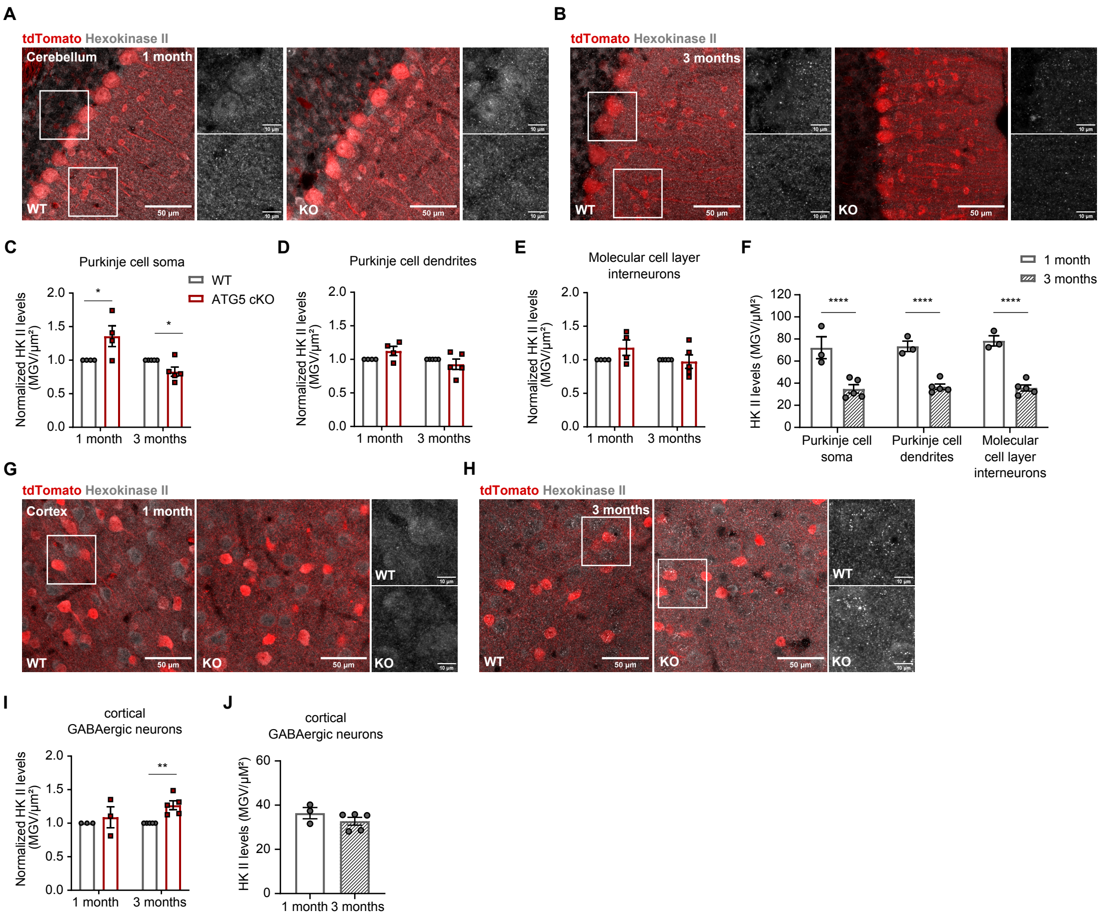

Figure 32: One-month old ATG5 cKO Purkinje cells display increased Hexokinase II levels. (A)/(B) Representative images of immunofluorescence images stained for hexokinase II (HK II) in WT and ATG5 cKO cerebellum at the age of 1 (A) and 3 (B) months. Scale bar: 50 µm. ((C) Fluorescent based analysis of HK II in Purkinje cell somata of 1- and 3-month old WT and ATG5 cKO mice. Each dot represents one animal (N=4 per genotype for 1-month old animals and N=5 per genotype for 3-month old animals). One-tailed unpaired t-test between WT and ATG5 cKO was performed for each age. (D) Fluorescent based analysis of HK II in Purkinje cell dendrites of 1- and 3-month old WT and ATG5 cKO mice. Each dot represents one animal (N=4 per genotype for 1-month old animals and N=5 per genotype for 3-month old animals). One-tailed unpaired t-test between WT and ATG5 cKO was performed for each age. (E) Fluorescent based analysis of HK II in molecular cell layer interneurons of 1- and 3-month old WT and ATG5 cKO mice. Each dot represents one animal (N=4 per genotype for 1-month old animals and N=5 per genotype for 3-month old animals). One-tailed unpaired t-test between WT and ATG5 cKO for each age was performed. (F) Fluorescent based analysis of HK II in Purkinje cell somata, Purkinje cell dendrites and molecular cell layer interneurons of 1- and 3-month old WT mice. Each dot represents one animal (N=4 per genotype for 1-month old animals and N=5 per genotype for 3-month old animals). Two-Way ANOVA with Holm-Sidak's multiple comparison test was performed. (G) /(H) Representative images of immunofluorescence images stained for HK II in WT and ATG5 cKO cortex at the age of 1 (G) and 3 (H) months. Scale bar: 50 µm. (I) Fluorescent based analysis of HK II in cortical GABAergic cell somata of 1- and 3-month old WT and ATG5 cKO mice. Each dot represents one animal (N=4 per genotype for 1-month old animals and N=5 per genotype for 3-month old animals). One-tailed unpaired t-test was performed. (J) Fluorescent based analysis of HK II in cortical GABAergic cell somata of 1- and 3-month old WT mice. Each dot represents one animal (N=4 per genotype for 1-month old animals and N=5 per genotype for 3-month old animals). Two-tailed unpaired t-test was performed. All data shown as average ± SEM. Significant differences indicated by asterisks (* p<0.05; ** p<0.01; *** p<0.001; ****p<0.0001).

6. Loss of ATG5 results in upregulation of GLUT2 in Purkinje cells

In order to assess whether the loss of ATG5 results in changes in glucose transporter (GLUT) expression linked to increased glucose uptake, immunofluorescence for the four main GLUTs (1-4) was performed in 1 and 3month old WT and ATG5 cKO brain sections.

6.1 GLUT1 expression is not altered upon the loss of ATG5 in GABAergic neurons

Immunofluorescence analysis of GLUT1 at the age of 1 and 3 months of age shows no changes between WT and ATG5 cKO cerebellum (Fig. 33A-E). In WT cerebellum, GLUT1 levels are slightly higher in Purkinje cells and molecular cell layer interneurons at the age of 3months compared to 1 month (Fig. 33F). No differences between WT and ATG5 cKO animals in 1 and 3 month old GABAergic neurons was observed (Fig. 33G-I). In WT cortical GABAergic neurons, GLUT1 level increases from 1 to 3 months of age, although these changes were not significant (Fig. 33J).

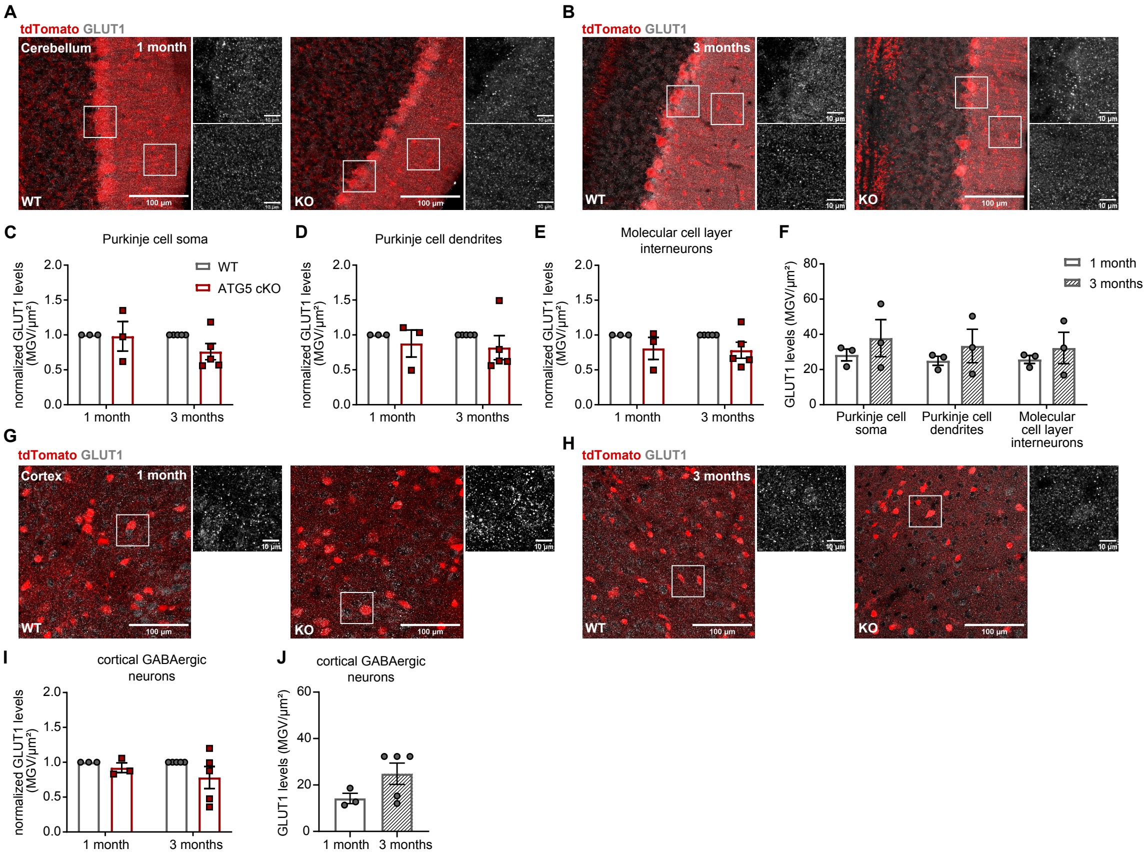

Figure 33: GLUT1 levels are not altered in ATG5 cKO brains. (A) /(B) Representative images of immunofluorescence images stained for GLUT1 in WT and ATG5 cKO cerebellum at the age of 1 (A) and 3 (B) months. Scale bar: 100 µm. (C) Fluorescent based analysis of GLUT1 in Purkinje cell somata of 1- and 3-month old WT and ATG5 cKO mice. Each dot represents one animal (N=3 per genotype). One-tailed unpaired t-test between WT and ATG5 cKO was performed for each age. (D) Fluorescent based analysis of GLUT1 in Purkinje cell dendrites of 1- and 3-month old WT and ATG5 cKO mice. Each dot represents one animal (N=3 per genotype). One-tailed unpaired t-test between WT and ATG5 cKO was performed for each age. (E) Fluorescent based analysis of GLUT1 in molecular cell layer interneurons of 1- and 3-month old WT and ATG5 cKO mice. Each dot represents one animal (N=3 per genotype). One-tailed unpaired t-test between WT and ATG5 cKO was performed for each age. (F) Fluorescent based

analysis of GLUT1 in Purkinje cell somata, Purkinje cell dendrites and molecular cell layer interneurons of 1- and 3-month old WT mice. Each dot represents one animal (N=3 per age). Two-Way ANOVA with Holm-Sidak's multiple comparison test was performed. (G)/(H) Representative images of immunofluorescence images stained for GLUT1 in WT and ATG5 cKO cortex at the age of 1 (G) and 3 (H) months. Scale bar: 100 µm. (I) Fluorescent based analysis of GLUT1 in cortical GABAergic neuron somata of 1- and 3-month old WT and ATG5 cKO mice. Each dot represents one animal (N=3 per genotype for 1-month old animals and N=5 per genotype for 3-month old animals)). One-tailed unpaired t-test between WT and ATG5 cKO was performed for each age. (J) Fluorescent based analysis of GLUT1 in cortical GABAergic cell somata of 1- and 3-month old WT mice. Each dot represents one animal (N=3 for 1-month old animals and N=5 for 3-month old animals). Two-tailed unpaired t-test. All data shown as average ± SEM. Significant differences indicated by asterisks (* $p<0.05$; ** $p<0.01$; *** $p<0.001$; **** $p<0.0001$).

6.2 Loss of ATG5 results in upregulation of GLUT2 in Purkinje cells

Immunofluorescence analysis revealed increased levels of GLUT2 in 1- and 3-month old Purkinje cells and molecular cell layer interneurons in 3-month old ATG5 cKO cerebellum (Fig. 34B-E). In WT cerebellum, GLUT2 generally decreases from 1 to 3 months, with the strongest decrease in Purkinje cell somata (Fig. 34F). GLUT2 is not changed in the cortex at the age of 1 and 3 months upon loss of ATG5 (Fig. 34G-I). Similar to the cerebellum, in WT cortical GABAergic neurons GLUT2 levels decrease from 1 to 3 months of age (Fig. 34J). This data shows, that generally GLUT2 levels decrease with age in the WT brain. However, upon loss of ATG5, GLUT2 is specifically increased in cerebellar GABAergic neurons with the strongest increase in Purkinje cells. This increase can be already observed at the age of one month.

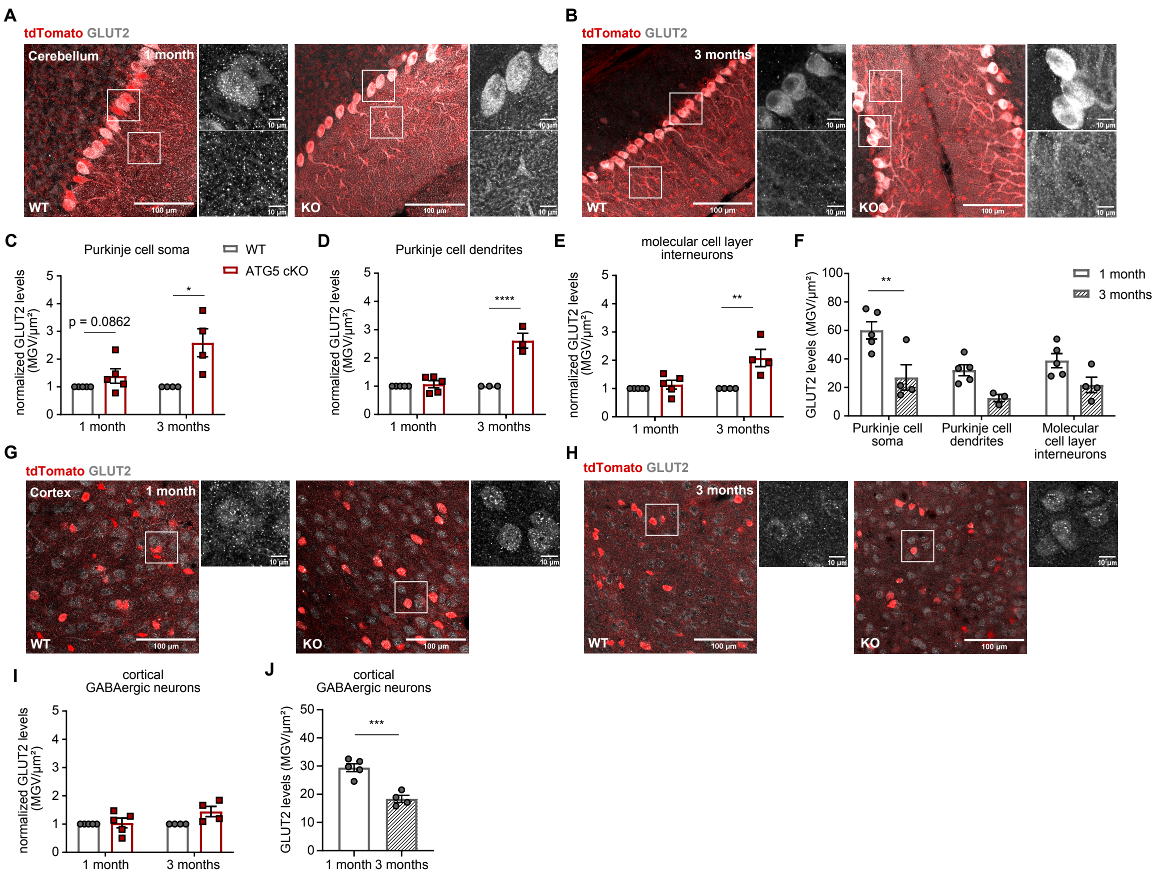

Figure 34: Loss of ATG5 results in increased GLUT2 levels in Purkinje cells. (A)/(B) Representative images of immunofluorescence images stained for GLUT2 in WT and ATG5 cKO cerebellum at the age of 1 (A) and 3 (B) months. Scale bar: 100 µm. (C) Fluorescent based analysis of GLUT2 in Purkinje cell somata of 1- and 3-month old WT and ATG5 cKO mice. Each dot represents one animal (N=5 per genotype for 1 month old animals and N=4 per genotype for 3-month old animals). One-tailed unpaired t-test between WT and ATG5 cKO was performed for each age. (D) Fluorescent based analysis of GLUT2 in Purkinje cell dendrites of 1- and 3-month old WT and ATG5 cKO mice. Each dot represents one animal (N=5 per genotype for 1 month old animals and N=4 per genotype for 3-month old animals). One-tailed unpaired t-test between WT and ATG5 cKO was performed for each age. (E) Fluorescent based analysis of GLUT2 in molecular cell layer interneurons of 1- and 3-month old WT and ATG5 cKO mice. Each dot represents one animal (N=5 per genotype for 1 month old animals and N=4 per genotype for 3-month old animals). One-tailed unpaired t-test between WT and ATG5 cKO was performed for each age. (F) Fluorescent based analysis of GLUT2 in Purkinje cell somata, Purkinje cell dendrites and molecular cell layer interneurons of 1- and 3-month old WT mice. Each dot represents one animal (N=5 per genotype for 1 month old animals and N=4 per genotype for 3-month old animals). Two-Way ANOVA with Holm-Sidak's multiple comparison test was performed. (G)/(H) Representative images of immunofluorescence images stained for GLUT2 in WT and ATG5 cKO cortex at the age of 1 (G) and 3 (H) months. Scale bar: 100 µm. (I) Fluorescent based analysis of GLUT2 in cortical GABAergic neuron somata of 1- and 3-month old WT and ATG5 cKO mice. Each dot represents one animal (N=5 per genotype for 1 month old animals and N=4 per genotype for 3-month old animals). One-tailed unpaired t-test between WT and ATG5 cKO was performed for each age. (J) Fluorescent based analysis of GLUT2 in cortical GABAergic cell somata of 1- and 3-month old WT mice. Each dot represents one animal (N=5 per genotype for 1 month old animals and N=4 per genotype for 3-month old animals). Two-tailed unpaired t-test was performed. All data shown as average ± SEM. Significant differences indicated by asterisks (* p<0.05; ** p<0.01; *** p<0.001; ****p<0.0001).

6.3 GLUT3 expression is not altered upon loss the of ATG5 in GABAergic neurons

Immunofluorescence analysis of GLUT3 at the age of 1 and 3 months of age shows no changes in cortex and cerebellum upon loss of ATG5 (Fig.35 A-E, G-I)). In both the cerebellum and the cortex of WT mice, GLUT3 levels remain mostly unaltered between 1 and 3 months of age (Fig. 35F and J).

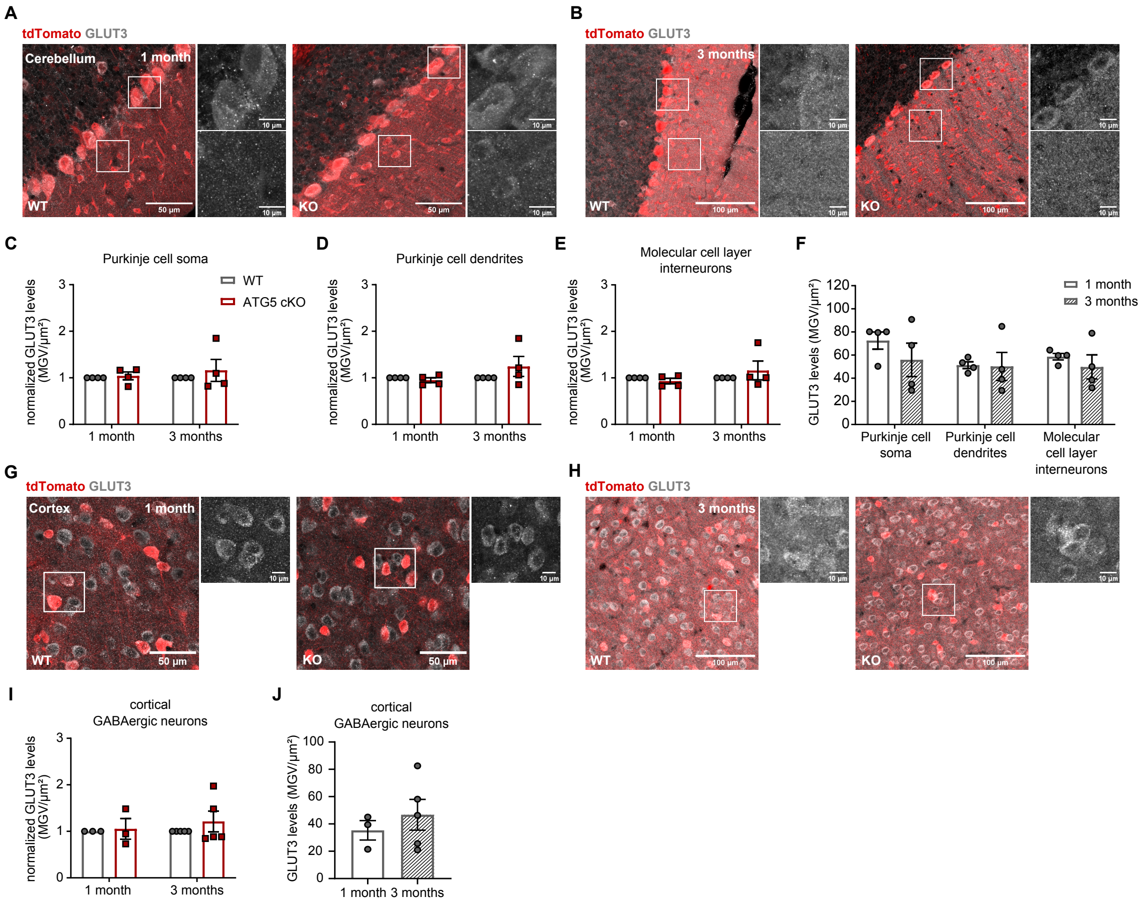

Figure 35: GLUT3 levels are not altered upon the loss of ATG5 in GABAergic neurons. (A)/(B) Representative images of immunofluorescence images stained for GLUT3 in WT and ATG5 cKO cerebellum at the age of 1 (A) and 3 (B) months. Scale bar: 100 µm. (C) Fluorescent based analysis of GLUT3 in Purkinje cell somata of 1- and 3-month old WT and ATG5 cKO mice. Each dot represents one animal (N=4 per genotype). One-tailed unpaired t-test between WT and ATG5 cKO was performed for each age. (D) Fluorescent based analysis of GLUT3 in Purkinje cell dendrites of 1- and 3-month old WT and ATG5 cKO mice. Each dot represents one animal (N=4 per genotype). One-tailed unpaired t-test between WT and ATG5 cKO was performed for each age. (E) Fluorescent based analysis of GLUT3 in molecular cell layer interneurons of 1- and 3-month old WT and ATG5 cKO mice. Each dot represents one animal (N=4 per genotype). One-tailed unpaired t-test between WT and ATG5 cKO was performed for each age. (F) Fluorescent based analysis of GLUT3 in Purkinje cell somata, Purkinje cell dendrites and molecular cell layer interneurons of 1- and 3-month old WT mice. Each dot represents one animal (N=4 per age). Two-Way ANOVA with Holm-Sidak's multiple comparison test was performed. (G)/(H) Representative images of immunofluorescence images stained for GLUT3 in WT and ATG5 cKO cortex at the age of 1 (G) and 3 (H) months. Scale bar: 100 µm. (I) Fluorescent based analysis of GLUT3 in cortical GABAergic neuron somata of 1- and 3-month old WT and ATG5 cKO mice. Each dot represents one animal (N=3 for 1 month old animals and N=5 for 3-month old animals). One-tailed unpaired t-test between WT and ATG5 cKO was performed for each age. (J) Fluorescent based analysis of GLUT3 in cortical GABAergic cell somata of 1- and 3-month old WT mice. Each dot represents one animal with N=3/5 per age. Two-tailed unpaired t-test was performed t. All data shown as average ± SEM. Significant differences indicated by asterisks (* $p<0.05$; ** $p<0.01$; *** $p<0.001$; **** $p<0.0001$).

6.4 GLUT4 expression is not altered upon the loss of ATG5 in GABAergic neurons

Immunofluorescence analysis of GLUT4 at the age of 1 and 3 months of age shows no changes in ATG5 cKO cortex and cerebellum compared to WT (Fig. 35A-E, G-I)). In WT GABAergic neurons of cerebellar and cortical brain regions, GLUT4 levels stay similar between 1 and 3 months (Fig. 35F and J).

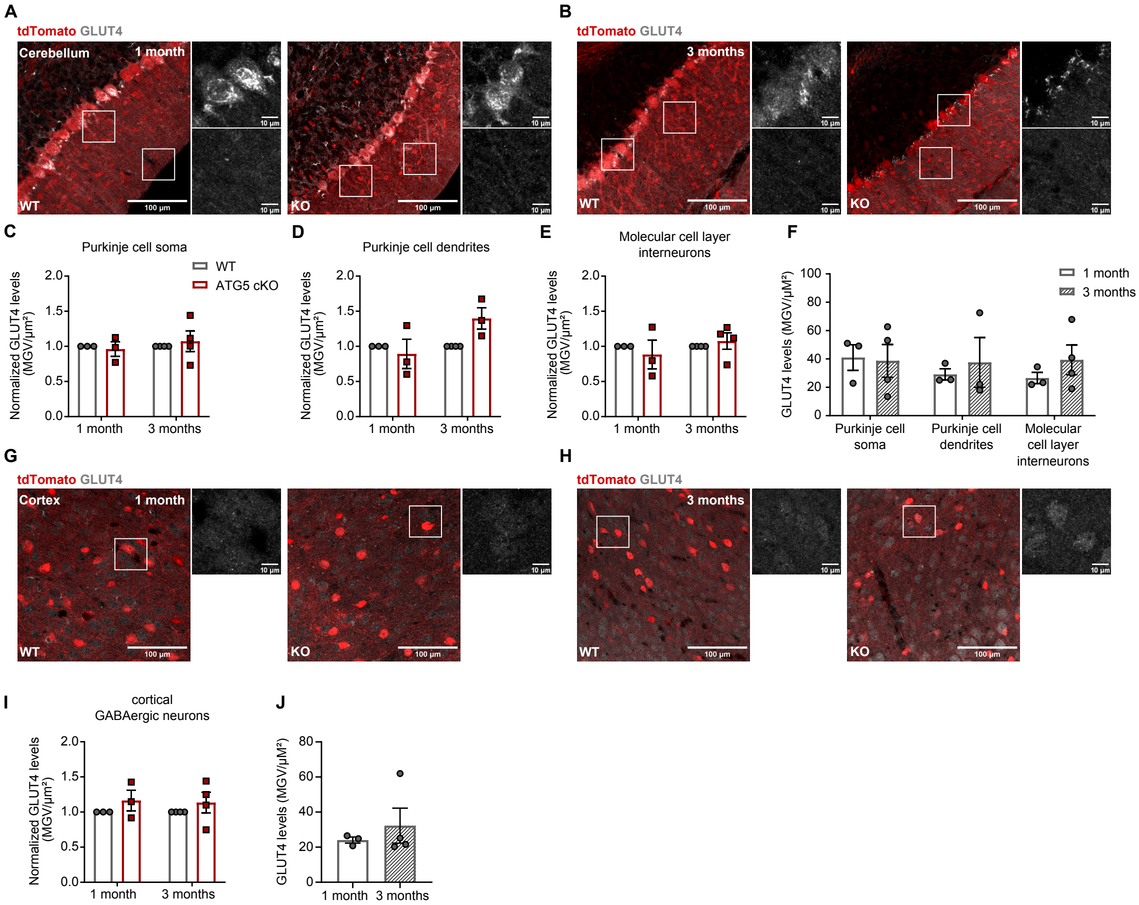

Figure 36: GLUT4 levels are not altered upon the loss of ATG5 in GABAergic neurons. (A)/(B) Representative images of immunofluorescence images stained for GLUT4 in WT and ATG5 cKO cerebellum at the age of 1 (A) and 3 (B) months. Scale bar: 100 µm. (C) Fluorescent based analysis of GLUT4 in Purkinje cell somata of 1- and 3-month old WT and ATG5 cKO mice. Each dot represents one animal (N=3 per genotype for 1 month old animals and N=4 per genotype for 3-month old animals). One-tailed unpaired t-test between WT and ATG5 cKO was performed for each age. (D) Fluorescent based analysis of GLUT4 in Purkinje cell dendrites of 1- and 3-month old WT and ATG5 cKO mice. Each dot represents one animal (N=3 per genotype for 1 month old animals and N=4 per genotype for 3-month old animals). One-tailed unpaired t-test between WT and ATG5 cKO was performed for each age. (E) Fluorescent based analysis of GLUT4 in molecular cell layer interneurons of 1- and 3-month old WT and ATG5 cKO mice. Each dot represents one animal (N=3 per genotype for 1 month old animals and N=4 per genotype for 3-month old animals). One-tailed unpaired t-test between WT and ATG5 cKO was performed for each age. (F) Fluorescent based analysis of GLUT4 in Purkinje cell somata, Purkinje cell dendrites and molecular cell layer interneurons of 1- and 3-month old WT mice. Each dot represents one animal (N=3 for 1 month old animals and N=4 for 3-month old animals). Two-Way ANOVA with Holm-Sidak's multiple comparison test was performed. (G)/(H) Representative images of immunofluorescence images stained for GLUT4 in WT and ATG5 cKO cortex at the age of 1 (G) and 3 (H) months. Scale bar: 100 µm. (I) Fluorescent based analysis of GLUT4 in cortical GABAergic neuron somata of 1- and 3-month old WT and ATG5 cKO mice. Each dot represents one animal (N=3 per genotype for 1 month old animals and N=4 per genotype for 3-month old animals). One-tailed unpaired t-test between WT and ATG5 cKO was performed for each age. (J) Fluorescent based analysis of GLUT4 in cortical GABAergic cell somata of 1- and 3-month old WT mice. Each dot represents one animal (N=3 for 1 month old animals and N=4 for 3-month old animals). Two-tailed unpaired t-test was performed. All data shown as average ± SEM. Significant differences indicated by asterisks (* $p<0.05$; ** $p<0.01$; *** $p<0.001$; **** $p<0.0001$).

6.5 Loss of ATG5 results in increased levels of GLUT2 in Purkinje cell plasma membrane

In order to analyze whether increased GLUT2 levels lead to GLUT2 accumulation at the plasma membrane, a surface biotinylation assay was performed in acute cerebellar slices of WT and ATG5 cKO animals at the age of 3 months. In short, acute slices were incubated with biotin, resulting in biotinylation of extracellular proteins. Afterwards biotinylated proteins were captured with beads and further processed for immunoblotting. Via immunoblotting total GLUT2 levels were detected in addition to the surface and cytoplasmic fraction. In ATG5 cKO cerebellar slices, increased levels of GLUT2 could be detected in the surface fraction although not significant (Fig. 37A and B). Additionally, immunofluorescence analysis for extracellular domain of GLUT2 was performed. In line with the surface biotinylation assay, immunofluorescence analysis shows increased levels of surface GLUT2 in 3 month-old ATG5 cKO Purkinje cells (Fig. 37C and D). This indicates that the ATG5 loss in Purkinje cells not only increases intracellular levels of GLUT2 but also results in increased GLUT2 levels at the plasma membrane.

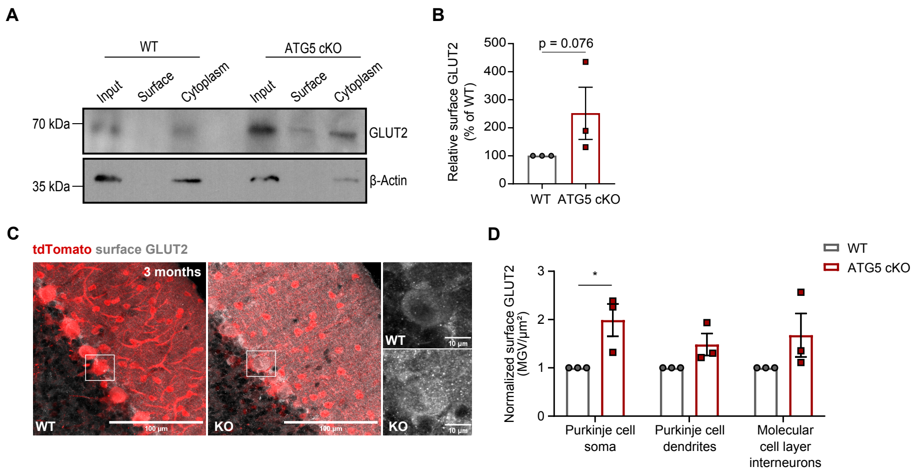

Figure 37: ATG5 deficient Purkinje cells display increased levels of surface GLUT2. (A) Representative immunoblot of surface biotinylation assay of cerebellar acute slice at the age of 3 months to detect total, surface and cytoplasmic GLUT2 levels in WT and ATG5 cKO animals. (B) Immunoblot analysis of surface GLUT2 levels in WT and ATG5 cKO cerebellar acute slices at the age of 3 months. Each dot represents one animal (N=3 per genotype). One-tailed unpaired t-test was performed. (C) Representative images of immunofluorescence staining for surface GLUT2 in WT and ATG5 cKO cerebellum at the age of 3 months. Scale bar: 100/10 µm. (D) Immunofluorescence image analysis of surface GLUT2 in Purkinje cells and molecular cell layer interneurons of WT and ATG5 cKO cerebellum at the age of 3 months. Each dot represents one animal (N=3 per genotype). Two-Way ANOVA with Holm-Sidak's multiple comparison test was performed. All data shown as average ± SEM. Significant differences indicated by asterisks (* $p<0.05$; ** $p<0.01$; *** $p<0.001$; **** $p<0.0001$).

7. Autophagy regulates cerebellar GLUT2 levels

The analysis of GLUT2 levels in WT Purkinje cells indicated that GLUT2 expression decreases from 1 to 3 months in the cerebellum. To test whether autophagy is responsible for downregulation of GLUT2 levels in the cerebellum, WT cerebellar and cortical acute slices at the age of 3 months were treated with chloroquine (CQ) that blocks fusion of autophagosomes with autolysosomes, thereby inhibiting autophagic flux (Mauthe et al., 2018). CQ treatment in cerebellar acute slices increased LC3 II to I ratio, indicating successful blockage autophagic flux. In cortical acute slices CQ treatment did not block the autophagic flux as successful as in cerebellar slices, indicating that the levels of constitute autophagy might differ between the cortex and cerebellum in WT mice (Fig. 38A and B). Additionally, in cerebellar slices CQ treatment results in increased GLUT2 levels, whereas GLUT2 levels in CQ treated cortical slices are unchanged (Fig. 38C and D). Next, GLUT2 was co-stained with autophagic markers such as NBR1 (autophagic receptor), LC3 (autophagosome marker) and Cathepsin D (lysosomal marker). Immunofluorescence images of LC3 and GLUT2 indicate colocalization of GLUT2 with autophagosomes in Purkinje cell somata (Fig. 38E and G). GLUT2 also colocalizes with the autophagic receptor protein NBR1 (Fig. 38F and G). Additionally, the colocalization of GLUT2 with the lysosomal markers Cathepsin D was significantly reduced in ATG5 cKO Purkinje cells (Fig. 38H, I and J).

This shows that GLUT2 colocalizes with autophagic markers and that block of autophagy results in accumulation of GLUT2 in the cerebellum, indicating that GLUT2 is degraded via autophagy.

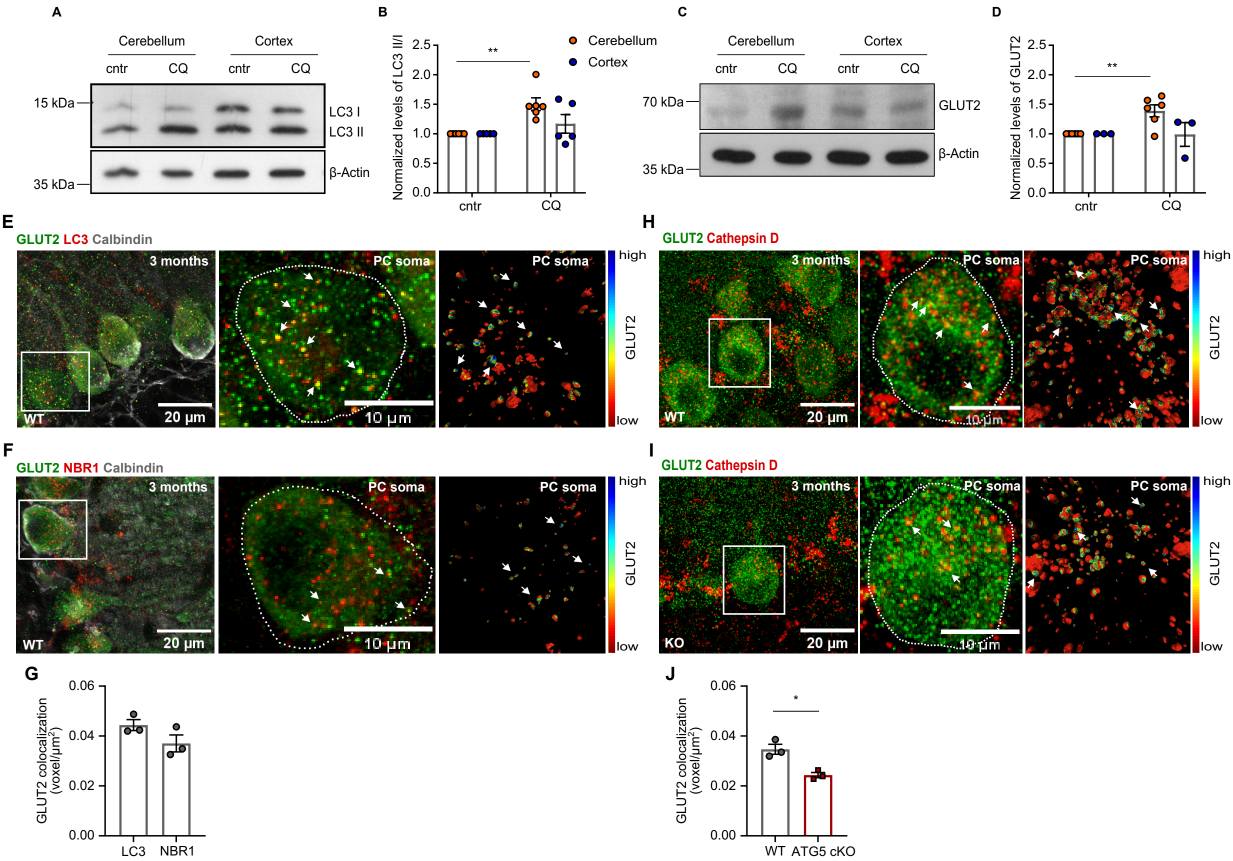

Figure 38: Autophagy regulates cerebellar GLUT2 levels. (A) Representative immunoblot for LC3 of control and CQ-treated cerebellar and cortical acute slices of 3-month old WT animals. β-Actin was used as a loading control. (B) Immunoblot analysis of LC3 II vs I ratio in WT cerebellar and cortical acute slices at the age of 3 months. β-Actin was used for protein normalization. Each dot represents one animal (N=5). Two-Way ANOVA with Holm-Sidak's multiple comparison test was performed. (C) Representative immunoblot for GLUT2 of control and CQ-treated cerebellar and cortical acute slices of 3-month old WT animals. β-Actin was used as a loading control. (D) Immunoblot analysis of GLUT2 in WT cerebellar and cortical acute slices at the age of 3 months. β-Actin was used for protein normalization. Each dot

represents one animal (N=5 for cerebellum and N=3 for cortex). Two-Way ANOVA with Holm-Sidak's multiple comparison test was performed. (E) Representative immunofluorescence image of GLUT2 and LC3 in WT cerebellum at the age of 3 months and AMIRA based reconstruction of GLUT2 and LC3 colocalization. Calbindin was used as a marker of Purkinje cells. Arrows indicate colocalization. Scale bar: 20/10 µm. (F) Representative immunofluorescence image of GLUT2 and NBR1 in WT cerebellum at the age of 3 months and AMIRA based reconstruction of GLUT2 and NBR1 colocalization. Calbindin was used as a marker for Purkinje cells. Arrows indicate colocalization. Scale bar: 20/10 µm. (G) AMIRA-based colocalization analysis of GLUT2 with LC3 and NBR1 in WT Purkinje cell somata at the age of 3 months. Each dot represents one animal (N=3). (H)/(I) Representative immunofluorescence image of GLUT2 and Cathepsin D in WT (H) and ATG5 cKO (I) cerebellum at the age of 3 months and AMIRA based reconstruction of GLUT2 and Cathepsin D colocalization. Scale bar: 20/10 µm. (J) AMIRA-based colocalization analysis of GLUT2 with Cathepsin D in WT and ATG5 cKO Purkinje cell somata at the age of 3 months. Each dot represents one animal (N=3). Two-tailed unpaired t-test was performed. All data shown as average ± SEM. Significant differences indicated by asterisks (* p<0.05; ** p<0.01; *** p<0.001; ****p<0.0001).

To further understand whether ATG5 regulates GLUT2 levels in Purkinje cells *in vivo*, an AAV expressing ATG5-EGFP or EGFP as a control under the control of the mDLX promotor was injected into the cerebellar lobes IV/V of eight weeks old WT and ATG5 cKO animals. The DLX genes were shown to be expressed in several GABAergic neurons of the murine brain, including Purkinje cells (Aouci et al., 2022). Injection of pAAV2/RH20-mDLX-EGFP and pAAV2/RH20-mDLX-EGFP-ATG5 resulted in Purkinje cell transduction, even though transduction efficiency was relatively low (Fig. 39A). GLUT2 levels of ATG5 cKO Purkinje cells were significantly higher than WT levels after injection with the control virus. Overexpression of ATG5 in ATG5 cKO cerebellum resulted in reduced levels of GLUT2 that were comparable to control WT levels. Overexpression of ATG5 in WT cerebellum resulted in significantly reduced levels of GLUT2 in Purkinje cells (Fig. 29B). This shows that autophagy regulates GLUT2 levels in cerebellar Purkinje cells.

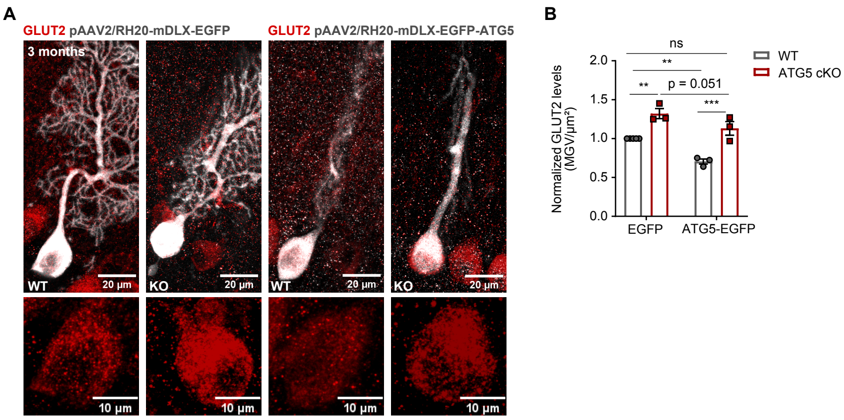

Figure 39: Overexpression of ATG5 reduces GLUT2 levels in Purkinje cells *in vivo*. (A) Representative immunofluorescence images of GLUT2 and EGFP in pAAV2/RH20-mDLX-EGFP or pAAV2/RH20-mDLX-EGFP-ATG5 transduced WT and ATG5 cKO cerebellum at the age of 3 months. Scale bar: 20/10 µm. (B) Immunofluorescence analysis of GLUT2 levels in pAAV2/RH20-mDLX-EGFP (EGFP) or pAAV2/RH20-mDLX-EGFP-ATG5 (EGFP-ATG5) Purkinje cell somata of WT and ATG5 cKO animals at the age of 3 months. Each dot represents one animal (N=3 per genotype). Data shown as average ± SEM. Two-Way ANOVA with Holm-Sidak's multiple comparison test was performed. Significant differences indicated by asterisks (* p<0.05; ** p<0.01; *** p<0.001; ****p<0.0001).

8. Increased cerebellar glycolytic metabolism causes Purkinje cell loss

Proteomics and metabolomics analysis indicated increased glycolytic metabolism starting at the age of 1 month in ATG5 cKO cerebellum (see Fig. 21-28) coinciding with the onset of Purkinje cell loss (Fig. 2). Several direct and indirect metabolites were tested in their contribution to Purkinje cell death.kupkups

Methylglyoxal is a constant glycolytic byproduct that derives from the glycolysis metabolite fructose-1,6-biphosphate which is converted into dihydroxyacetone phosphate (DHAP) which is then further converted into methylglyoxal. Increased levels of methylglyoxal induce cellular damage and are thus toxic for neurons (Igor et al., 2015). Since DHAP was found to be upregulated in ATG5 cKO cerebellum at the age of three months (Fig. 22), levels of methylglyoxal levels were assed via immunoblotting and immunofluorescence using an antibody targeting methylglyoxal-modified proteins. Levels of methylglyoxal-modified proteins were significantly higher in ATG5 cKO cerebellum compared to WT levels at the age of three months (Fig. 40A and B). Purkinje cell somata and dendrites revealed increased levels of methylglyoxal-modified proteins but not molecular cell layer interneurons of 3-months old ATG5 cKO cerebellum compared to WT (Fig. 40C and D).

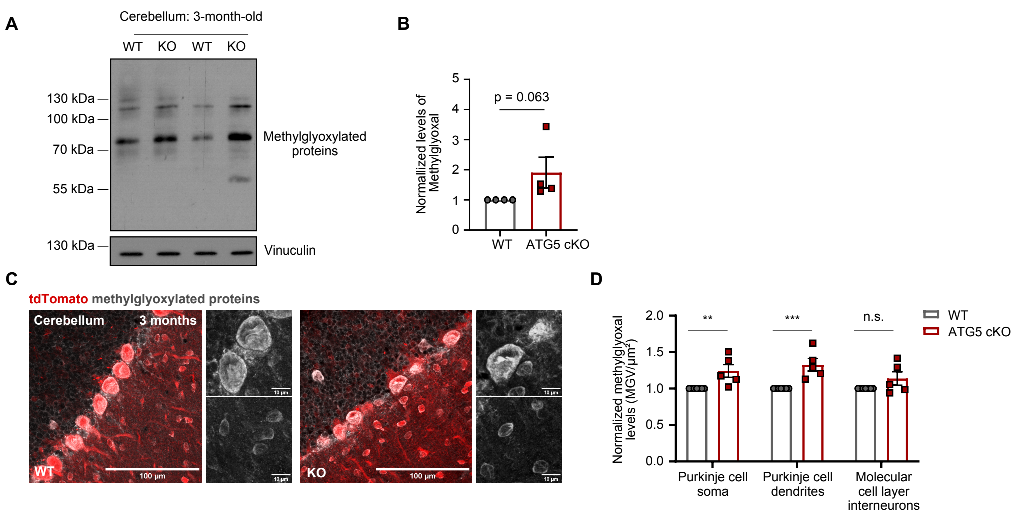

Figure 40: Loss of ATG5 results in increased levels of methylglyoxal-modified proteins in the cerebellum. (A) Immunoblot for methylglyoxal-modified proteins of WT and ATG5 cKO cerebellum at the age of 3 months. Vinculin was used as a loading control. (B) Immunoblot analysis of methylglyoxal-modified proteins in WT and ATG5 cKO cerebellum at the age of 3 months. Vinculin was used for protein normalization. Each dot represents one animal (N=4 per genotype). One-tailed t-test was performed. (C) Representative immunofluorescence images of methylglyoxal-modified proteins in WT and ATG5 cKO cerebellum at the age of 3 months. Scale bar: 100 µm. (D) Immunofluorescence analysis of methylglyoxal-modified protein level in WT and ATG5 cKO Purkinje cell somata, dendrites and molecular cell layer interneurons at the age of 3 months. Each dot represents one animal (N=5). Two-Way ANOVA with Holm-

Sidak's multiple comparison test was performed. All data shown as average ± SEM. Significant differences indicated by asterisks (* $p<0.05$; ** $p<0.01$; *** $p<0.001$; **** $p<0.0001$).

Serine is another metabolite that was significantly upregulated in 1 month-old cerebellum (Fig. 23). Moreover, isotope labeling revealed increased glucose flux into serine at the age of 3 months (Fig. 28). Serine is present in the brain in two isoforms: L-serine as an amino acid and its D-isomer D-serine. D-serine is an agonist of the N-methyl-D-aspartate (NMDA) receptor and elevated levels were shown to be toxic for neurons due to excitotoxicity (Meftah et al., 2021). In order to assess whether increased D-serine levels cause Purkinje cell loss, cerebellar organotypic slices (OTCs) from WT mice were incubated in medium supplemented with 5 µM D-serine for three weeks (Fig. 41A). Purkinje cell density was used as a readout. Immunofluorescence analysis of calbindin-positive Purkinje cells indicated that D-serine treatment results in decreased Purkinje cell density compared to control slices (Fig. 41B).
Another possible cell death cause was indicated in KEGG pathway analysis of commonly upregulated proteins in one- and three-month old cerebellum, that indicated increased ferroptosis upon loss of ATG5 (see Fig. 21). In order to test whether ferroptosis can cause Purkinje cell loss, WT cerebellar OTCs were treated either with a ferroptosis inducing drug RAS-selective lethal (RSL3) or with RSL3 and an ferroptosis inhibitor ferrostatin-1 (Fer1) (Miotto et al., 2020; Dorian et al., 2023). Purkinje cell density was used as a readout. Immunofluorescence analysis of calbindin-positive Purkinje cells indicated that RSL3 treatment induces Purkinje cell loss which can be partially rescued by co-treatment with Fer-1 (Fig. 41C and D).

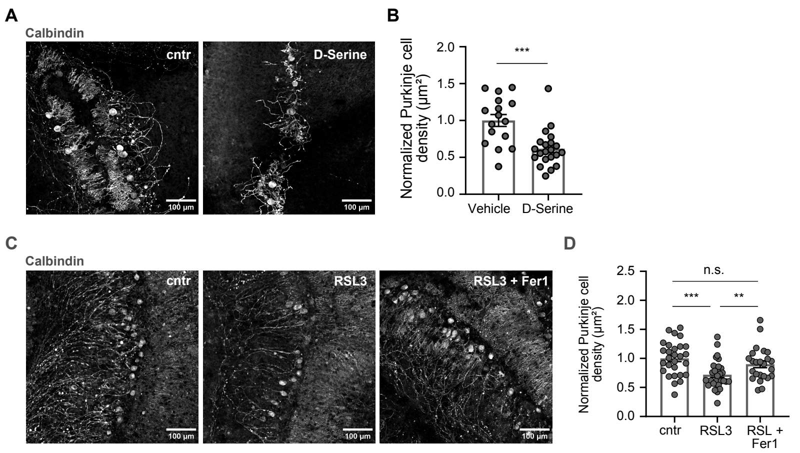

Figure 41: Treatment with D-Serine and ferroptosis-inducer RSL3 leads to Purkinje cell loss in cerebellar organotypic slices (OTCs). (A) Representative immunofluorescence image of Calbindin in WT cerebellar OTCs. Slices were either cultured in control or in D-serine (5 µM) containing medium for three weeks. Scale bar: 100 µm. (B) Immunofluorescence based analysis of Purkinje cell density in control or D-serine treated WT cerebellar OTCs. Each dot represents a single image (N=3 per genotype with 18 images for control and 21 images for D-serine treated). Two-tailed t-test was performed (C)Representative immunofluorescence image of Calbindin in WT cerebellar OTCs. Slices were either treated with vehicle, 1 µM RSL3 or 10 µM Fer-1 for 24h. Scaler bar: 100 µm. (D) Immunofluorescence based analysis of Purkinje cell density in control, RSL3, and RSL3+Fer1 treated WT cerebellar OTCs. Each dot represents a single image (N=4 per genotype with 28 images for control, 30 images for RSL3 and 25 images for RSL3+Fer1 treated). One-Way ANOVA with Holm-Sidak's multiple comparison test was performed. All

data shown as average ± SEM. Significant differences indicated by asterisks (* p<0.05; ** p<0.01; *** p<0.001; ****p<0.0001).

Another metabolite that can be derived from DHAP is lysophosphatic acid (LPA), that is upregulated in 3 month-old ATG5 cKO cerebellum (Fig. 22). LPA is a bioactive lipid and increased LPA levels were shown to cause cortical network hyperexcitability and subsequently excitotoxicity (Thalman et al., 2018). WT OTCs were treated with 100 nM LPA for one week to assess whether LPA increases Purkinje cell excitability and whether LPA might cause Purkinje cell loss. To analyze Purkinje cell excitability, WT and ATG5 cKO cerebellar OTCs were transduced with an AAV encoding for GCamP7f, which is a calcium sensor coupled to GFP. Live imaging was performed and slices were stimulated with 100 action potentials (APs) at 100 Hz stimulation after 20 seconds of recording. Changes in GCaMP fluorescence were used as a readout of Purkinje cell activity (Fig. 42A). ATG5 cKO Purkinje cells showed a stronger response to the stimulus than WT Purkinje cells (Fig. 42B and D). LPA-treated WT Purkinje cells showed increased response to the stimulus when compared to control WT Purkinje cells (Fig. 42C and D). Analysis of the area under the curve of GCaMP7 fluorescence indicated that ATG5 cKO and LPA-treated WT Purkinje cells are hyperexcitable compared to control Purkinje cells (Fig. 42D). Immunofluorescence analysis of WT cerebellar OTCs was performed to assess Purkinje cell density. Immunofluorescence analysis revealed that LPA treatment of WT cerebellar OTCs results in decreased Purkinje cell density compared to control slices (Fig. 42E and F).
Several glycolysis byproducts are known to be neurotoxic. This data set shows that several of these neurotoxic glycolysis byproducts demonstrated to be increased in ATG5 cKO cerebellum such as methylglyoxal, serine and LPA, as well as the ferroptosis pathway, can cause Purkinje cell loss in WT cerebellar OTCs.

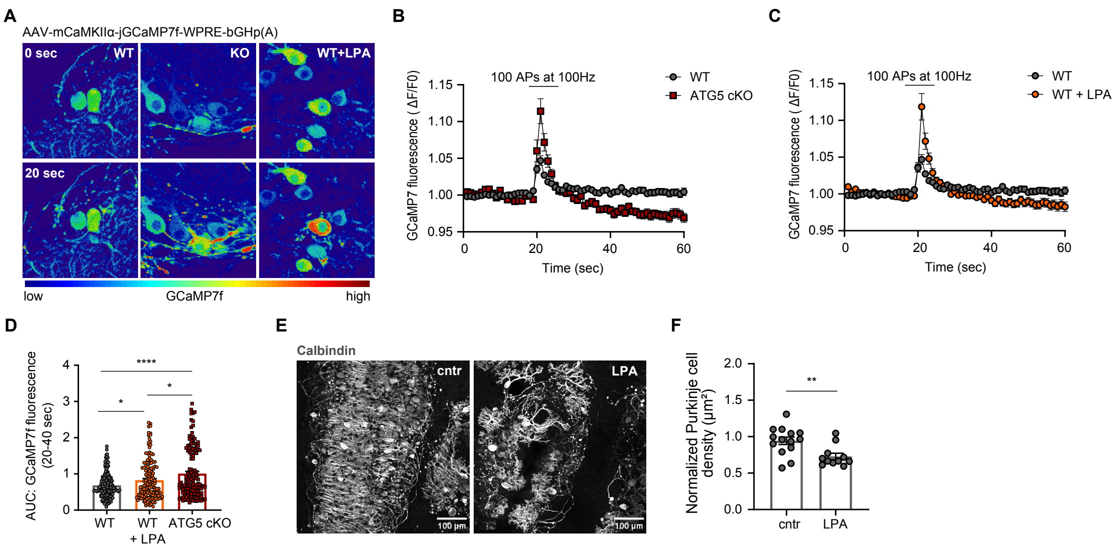

Figure 42: LPA increases Purkinje cell excitability and induces Purkinje cell loss. (A) Representative heatmap of GCaMP7f fluorescence at baseline (0 sec) and after stimulation (20 sec) with 100 action potentials (APs) at 100 Hz of WT, untreated and LPA-treated, and ATG5 cKO cerebellar organotypic slices (OTCs) at DIV21. WT slices were treated with 100 nM LPA for one week. (B) GCaMP7f fluorescence normalized to baseline levels (0-19 sec) of WT and ATG5 cKO Purkinje cells of cerebellar OTCs at DIV

21. N=2 per genotype (163 cells for WT and 142 cells for ATG5 cKO). (C) GCaMP7f fluorescence normalized to baseline levels (0-19 sec) of untreated and LPA-treated WT Purkinje cells of cerebellar OTCs at DIV 21. N=2 per genotype (163 cells for WT and 166 cells for WT + LPA). (D) Analysis of area under the curve of GCaMP7f fluorescence after the stimulus (20-40 sec) of WT, untreated and LPA-treated, and ATG5 cKO cerebellar organotypic slices (OTCs) at DIV21. Each dot represents a single Purkinje cell (N=2 per genotype with 163 cells for WT, 166 cells for WT+LPA and 142 cells for ATG5 cKO). One-Way ANOVA with Holm-Sidak's multiple comparison test was performed. (E) Representative immunofluorescence image of Calbindin of untreated and LPA treated WT cerebellar OTCs. Scaler bar: 100 µm (F) Immunofluorescence based analysis of Purkinje cell density in control or LPA treated WT cerebellar OTCs. Each dot represents a single image (N=3 per genotype with 14 images for control and 12 images for LPA treated WT). Two-tailed t-test was performed. All data shown as average ± SEM. Significant differences indicated by asterisks (* p<0.05; ** p<0.01; *** p<0.001; ****p<0.0001).

9. Loss of GLUT2 ameliorates ATG5 - deficient caused Purkinje cell loss

9.1 Loss of GLUT2 reduced glycolytic capacity of ATG5 cKO Purkinje cells

In order to investigate whether upregulated GLUT2 levels in ATG5 cKO Purkinje cells are causative for increased glycolytic metabolism, *Glut2*^{flox} animals (kindly provided by Prof. Bernhard Thorens, University of Lausanne) were crossed into the *Atg5*flox:*Slc32a1*-Cre mouse line to generate a double knockout mouse line for ATG5 and GLUT2 in GABergic neurons (Fig. 43A). For the rest of the thesis, ATG5 cKO animals are herein reffered to as KO and ATG5 cKO;GLUT2 cKO animals are reffered to as DKO for simplicity purposes.

To test whether loss of GLUT2 reduces ATG5 cKO-driven increased glycolytic capacity, cerebellar OTCs of WT, KO and DKO animals were used for 2-NBDG uptake and lactate measurement. 2-NBDG is significantly increased in KO Purkinje cells compared to WT. However, uptake in DKO is significantly reduced compared to KO Purkinje cells and similar to WT levels (Fig. 43B and C). The lactate levels of DKO Purkinje cells were not completely rescued, but they were significantly lower than those of KO Purkinje cells (Fig. 43D-F). Immunofluorescence analysis of methylglyoxylated proteins of WT, KO and DKO animals at the age of 3 months indicate a global reduction in methylglyoxal-modified proteins in DKO cerebellum (Fig. 43G and H). This indicates that loss of GLUT2 can ameliorate increased glycolytic capacity in the cerebellum upon loss of ATG5.

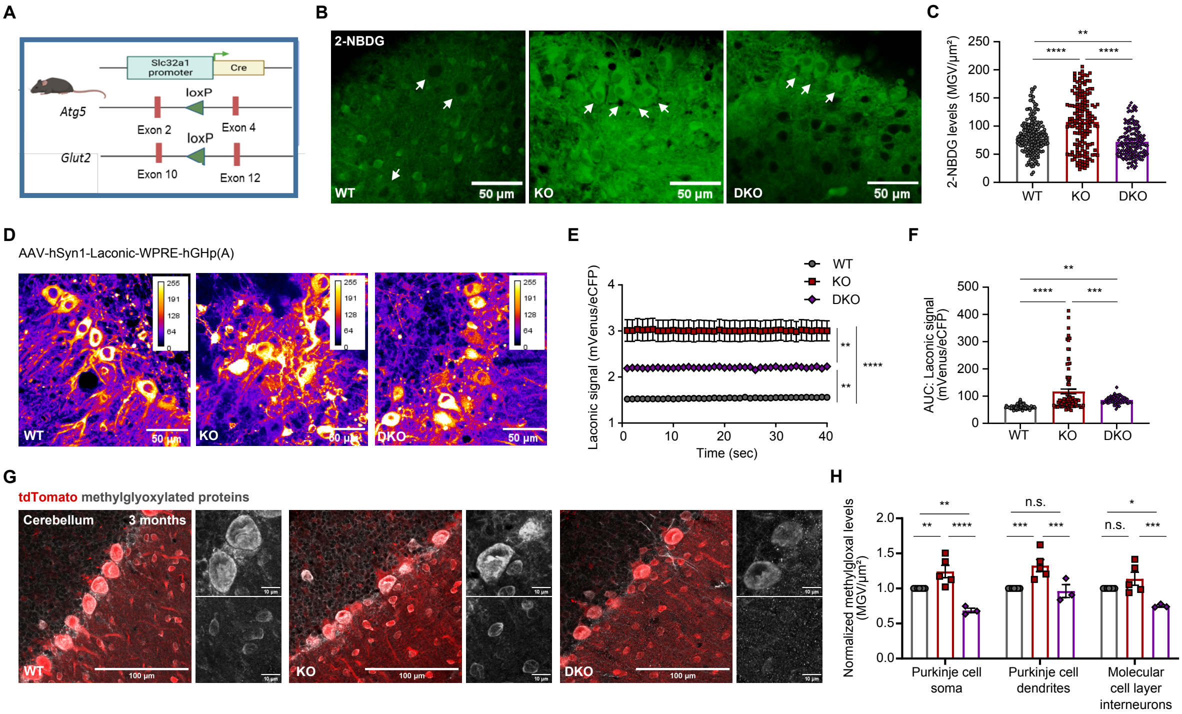

Figure 43: Loss of GLUT2 reduced glycolytic capacity of ATG5 cKO Purkinje cells. (A) Schematic of *Atg5*flox:*Glut2*flox:*Slc32a1*-Cre mouse with Slc32a1-dependent Cre expression in GABAergic neurons and floxed exon 3 of the *Atg5* gene and floxed exon 11 of the *Glut2* gene, resulting in DKO mutant in GABAergic neurons of the brain. (B) Representative images of 2-NBDG uptake in WT, KO and DKO cerebellar OTCs at DIV21. Scale bar: 50 µm. (C) Fluorescence based analysis of 2-NBDG uptake in WT, KO and DKO cerebellar OTCs at DIV21. Each dot represents a single Purkinje cell (for WT 190 cells from N=7, for KO 168 cells from N=5 and for DKO 175 cells from N=5). One-Way ANOVA with Holm-Sidak's multiple comparison test was performed. (D) Representative ratiometric images of AAV-hSyn1-Laconic transduced WT, KO and DKO cerebellar OTCs. Scalebar: 50 µm. (E) Ratiometric analysis of Laconic signal of WT (83 cells N=6), KO (96 cells from N=5) and DKO (70 cells from N=3) Purkinje cells. Two-Way ANOVA with Holm-Sidak's multiple comparison test was performed. (F) Area under the curve of Laconic signal over time in WT, KO and DKO Purkinje cells of cerebellar OTCs. Each dot represents a single Purkinje cells (for WT 83 cells from N=6, for KO 96 cells from N=5 and for DKO 70 cells from N=3). One-Way ANOVA with Holm-Sidak's multiple comparison test was performed. (G) Representative immunofluorescence image of methylglyoxylated proteins in WT, KO and DKO cerebellum at the age of 3 months. Scale bar: 100/10 µm. (H) Immunofluorescence based analysis of methylglyoxylated levels in Purkinje cell somata, Purkinje cell dendrites and molecular cell layer interneurons of WT, KO and DKO cerebellum at the age of 3 months. Each dot represents one animal (N=7 for WT, N=5 for KO and N=3 for DKO).Two-Way ANOVA with Holm-Sidak's multiple comparison test was performed. All data shown as average ± SEM. Significant differences indicated by asterisks (* p<0.05; ** p<0.01; *** p<0.001; ****p<0.0001).

9.2 Loss of GLUT2 ameliorates ataxic phenotype of ATG5 cKO animals

To test whether the loss of GLUT2 can rescue the ataxic phenotype of ATG5 cKO, the motor coordination of WT, KO and DKO animals was tested at the age of 3 months while crossing beams of different widths (using 3D SIMI-DeepLabCut analysis together with Prof. G. Gatto).

All animals were able to smoothly cross the 25 and 12 mm beams. However, ATG5 cKO mice displayed a significant increase in slips compared to littermate controls when crossing the narrowest beam (5 mm width) while DKO mice showed similar number of slips compared to WT controls (Fig. 44A and B). This shows that ATG5 cKO mice have reduced ability to perform motor coordination under perturbed (5 mm) conditions at 3 months of age, and that this phenotype can be rescued by concomitant deletion of GLUT2.

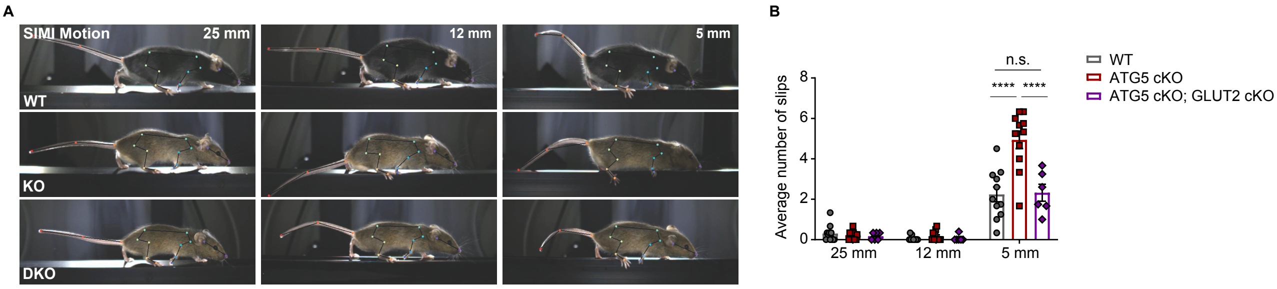

Figure 44: Loss of GLUT2 ameliorates ataxic phenotype of ATG5 cKO animals. (A) Representative image of WT, KO and DKO animals crossing beams at different widths (25, 12 and 5 mm). (B) Average number of slips of WT, KO and DKO animals at the age of 3 months per beams. Each dot represents one animal (N=11 for WT, N=11 for KO and N=6 for DKO). Data represents average ± SEM. Two-Way ANOVA with Holm-Sidak's multiple comparison test was performed. Significant differences indicated by asterisks (* $p<0.05$; ** $p<0.01$; *** $p<0.001$; ****$p<0.0001$).

9.3 Loss of GLUT2 rescues Purkinje cell loss in cerebellar lobes VIII-X

In order to assess whether improved motor coordination is caused by ameliorated Purkinje cell degeneration in DKO animals, Purkinje cell number in WT, KO and DKO cerebellum was determined by cresyl-violet staining (Fig. 45A). Cresyl-violet based analysis of Purkinje cell somata per lobe indicated partial rescue in DKO cerebellum compared to KO cerebellum. In Lobes IV+V, VI+VII and the lateral lobes (simple, crus and paramedian lobes) the number of Purkinje cells was similar or lower in DKO compared to KO cerebellum. However, in cerebellar lobes II+III and VIII-X the number of Purkinje cells per lobe is higher in DKO than in KO cerebellum (Fig. 45B). To confirm that in lobes VIII-X Purkinje cell number is higher in DKO cerebellum than in the KO, immunofluorescence staining for Purkinje cell marker Calbindin was performed and number of Purkinje cells specifically in those lobes was determined. Calbindin based analysis of Purkinje cell number confirmed the results of cresyl-violet staining. Purkinje cell number is still lower compared to WT levels, however significantly higher than KO levels (Fig. 45C and D). This indicates that loss of GLUT2 ameliorates Purkinje cell loss in certain cerebellar lobes such as VIII, XI and X.

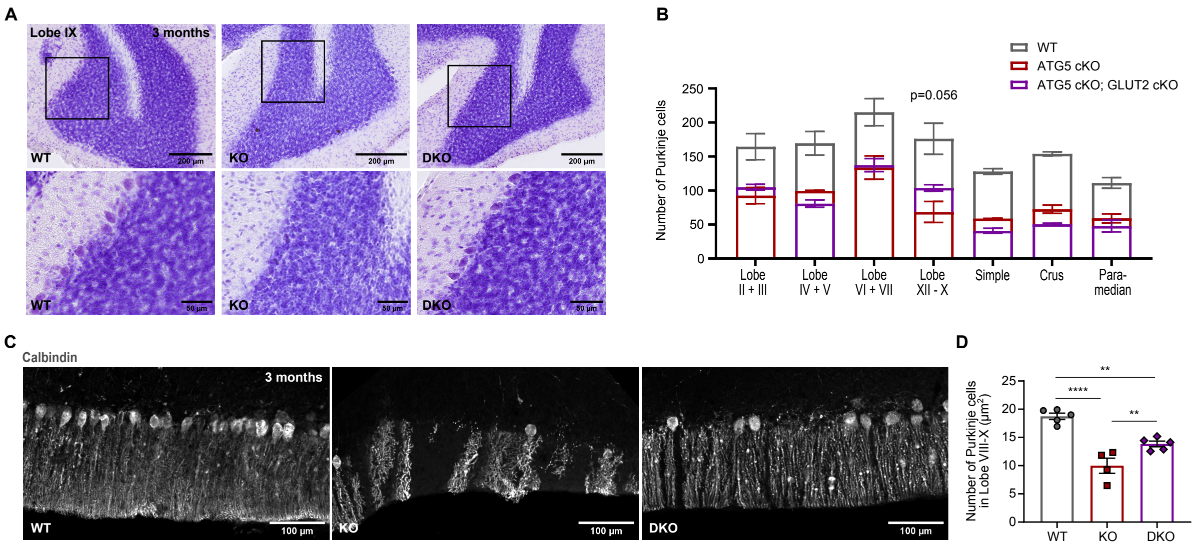

Figure 45: Loss of GLUT2 rescues Purkinje cell loss in cerebellar lobes VIII-X. (A) Representative cresyl-violet images of WT, KO and DKO cerebellum at the age of 3 months. Scale bar: 200/ 50 µm. (B) Cresyl-violet based analysis of Purkinje cell number per cerebellar lobes in WT, KO and DKO cerebellum of 3-months old animals (N=3 per genotype). Two-Way ANOVA with Holm-Sidak's multiple comparison test was performed and significance is only indicated between KO and DKO. (C) Representative immunofluorescence image of Calbindin of WT, KO and DKO cerebellum at the age of 3 months. Scale bar: 100 µm. (D) Immunofluorescence based analysis of Purkinje cell number in cerebellar lobes VIII-X of WT, KO and DKO cerebellum at the age of 3 months. Each dot represents one animal (N=5 for WT, N=4 for KO and N=5 for DKO). One-Way ANOVA with Holm-Sidak's multiple comparison test was performed. All data shown as average ± SEM. Significant differences indicated by asterisks (* p<0.05; ** p<0.01; *** p<0.001; ****p<0.0001).

V. Discussion

1. Region-specific vulnerability to autophagy loss

Brain-confined loss of ATG genes in neuronal precursor cells (*Nestin*-Cre) resulted in degeneration of neurons in several brain areas, accompanied by axonal degeneration and accumulation of intracellular proteins aggregates (Hara et al., 2006; Komatsu et al., 2006; Komatsu et al., 2007b; Liang et al., 2010; Zhao et al., 2015; Joo et al., 2016; Yamaguchi et al., 2018). However, because the *Nestin*-Cre promoter drives Cre recombinase expression in all neuronal progenitors the neurodegeneration observed in these mouse models can be due to defects of autophagy in both neurons and glial cells. In contrast, mouse lines with neuron-specific ablation of ATG proteins in excitatory forebrain neurons (McMahon et al., 2012), dopaminergic neurons (Hernandez et al., 2012), and striatal spiny projection neurons (Lieberman et al., 2020), as well as mice deficient for ATG5 in excitatory or inhibitory forebrain neurons (Negrete-Hurtado et al., 2020; Overhoff et al., 2022) show no neuronal cell loss.

Interestingly, loss of ATG5 or ATG7 in Purkinje cells results in age-dependent Purkinje cell death and mouse behavioral deficits (Komatsu et al., 2007; Nishiyama et al., 2007). In order to understand cellular mechanisms underlying selective vulnerability or resistance of different neuronal subtypes to autophagy the *Atg5*flox:*Slc32a1*-Cre mouse line was used in this study. In this mouse line all GABAergic neurons lack ATG5, thereby allowing the direct comparison of autophagy deficient cortical and cerebellar GABAergic neurons. This study shows that ablation of ATG5 in GABAergic neurons of the brain results in region- and cell type-specific vulnerability. Longitudinal PET imaging revealed hypometabolism in ATG5 cKO cerebellum and hypermetabolism in ATG5 cKO cortical and subcortical regions. Interestingly, synapse density was decreased in both cortex and cerebellum of ATG5 cKO animals. While cortical GABAergic forebrain neurons (Overhoff et al., 2022) and cerebellar molecular cell layer interneurons were shown to be resistant to autophagy loss, Purkinje cells display progressive degeneration starting at the age of three months. Purkinje cell vulnerability to autophagy impairment was already shown in other studies with Purkinje cell specific ATG5 and ATG7 ablation (Komatsu et al., 2007; Nishiyama et al., 2007) and β-Cathepsin D deficiency (Koike et al., 2017) leading to ataxic motor impairment and Purkinje cell degeneration. Cathepsin D deficient Purkinje cells start to degenerate after one month of age and show ataxic phenotype around two months of age, whereas mice with Purkinje cell specific ATG5 and ATG7 ablation show Purkinje cell loss starting at the age of two months and ataxic behavior at the age of 10 months (Komatsu et al., 2007; Nishiyama et al., 2007). The *Atg5*flox:*Slc32a1*-Cre mouse line shows similar onset of Purkinje cell degeneration, since the number of Purkinje cells was already significantly reduced compared to WT littermates at the age of three months. Interestingly, these animals show ataxic phenotype with impaired motor coordination and

balance at the age of three months when subjected to beams of different widths. Accumulation of intracellular proteins aggregates is a hallmarks of autophagy deficiency (Hara et al., 2006; Komatsu et al., 2006; Komatsu et al., 2007b; Liang et al., 2010; Zhao et al., 2015; Joo et al., 2016; Yamaguchi et al., 2018). In line with that, ATG5-deficient cortical GABAergic neurons show accumulation of large cytosolic aggregates containing p62 and NBR1.Some aggregates were even positive for ubiquitin. However, ATG5-deficient Purkinje cells do not show accumulation of p62 or NBR1$^+$ cytosolic aggregates nor accumulation of cytosolic ubiquitin. The number of puncta increase compared to WT littermates, however the size is not comparable to inclusion bodies in ATG5 deficient cortex. Purkinje cell-specific ATG7 loss resulted in similar phenotype, with increased number of small inclusions positive for p62 (Koike et al., 2017). Whether accumulation of cytosolic aggregates might be beneficial for cell survival is currently unknown.
Degenerating ATG5 cKO Purkinje cells do not show signs of apoptotic cell death. Purkinje cell specific β-Cathepsin D and ATG7 ablation does not result in ultrastructural indications of apoptosis (Koike et al., 2017). This indicates the contribution of alternative cell death pathways. In line with that, deregulation of ferroptosis was detected in the proteomics data and the pharmacological treatment with ferroptosis inducer RSL3 lead to Purkinje cell degeneration.

2. Metabolic alterations precede Purkinje cell loss in ATG5 cKO cerebellum

Total proteome analysis of 1- and 3- months old cerebellum revealed alterations in metabolic pathways upon loss of ATG5. Upregulated proteins of both ages indicated changes in metabolic pathways and thus a common change upon autophagy deficiency. While some changes are specific to certain ages, metabolic alterations are detected at both ages and display most dysregulated proteins that are commonly upregulated at one month and three months of age. Additionally, the few commonly upregulated proteins between one and three months of age indicated changes in pathways such as mitophagy and ferroptosis. Untargeted and targeted metabolomics analysis revealed increased glucose metabolism in ATG5 cKO cerebellum, starting already at the age of 1 month. ATG5 cKO cortex displayed mild changes in glucose metabolism as well. Changes in metabolism upon loss autophagy deficiency has been described in several studies. Especially, cancer cells use the interplay of autophagy and metabolism to promote their proliferation and survival by supplying nutrients and energy precursors (Kocaturk et al., 2019).
This study indicates that loss of autophagy results in cell-type specific metabolic alterations. While ATG5 cKO cortex displays mild changes in glucose metabolism, with increased flux into the pentose phosphate pathway, ATG5 cKO cerebellum shows increased glucose metabolism similar to cancer cells using the Warburg effect. However, loss of ATG5 does not result in changes in flux into the TCA cycle and OXPHOS. ATG5 cKO cerebellum shows increased glycolysis metabolites, increased flux into pentose-phosphate pathway and increased levels of

several glycolytic side products such as serine, DHAP and alanine. At the age of 1 month, ATG5 cKO deficient Purkinje cells already show increased glucose uptake, lactate and ATP levels. Additionally, ATG5 cKO cerebellum shows increased amino acid levels of which the homeostasis is interconnected with glycolytic intermediates. Interestingly, cancer cells use increased glycolysis to produce lipids, nucleotides, and amino acids (Lunt et al., 2011). However, three-month old ATG5 cKO cerebellum shows decreased amino acid levels, possibly due to the loss of Purkinje cells at that age.

Especially upper glycolysis metabolites such as glucose-6-phosphate (G-6-P), fructose-1,6-phosphate (F-1,6-P) and fructose-6-phosphate (F-6-P) were increased upon loss of ATG5. At the age of 1 month, Purkinje cells displayed increased levels of hexokinase 2 (HK II), which is the first enzyme of the glycolytic pathway that irreversibly phosphorylates glucose to G-6-P (Magistretti et al, 1993). In liver cancer cells, HK II was shown to be degraded through p62-mediated autophagy (Jiao et al., 2018). However, at the age of three months, when ATG5 cKO cerebellum displays further increased glycolytic metabolism, HK II levels were significantly reduced in Purkinje cells. This indicates that defective degradation of HK II might be not the cause of increased glycolytic metabolism in ATG5 cKO Purkinje cells. HK II levels possibly decrease due to a feedback inhibition mechanism mediated by elevated G-6-P levels (Ardehali et al., 1999). Interestingly, increased levels of HK II were detected in ATG5 deficient cortical GABAergic neurons at the age of three months. Even though no alterations in glycolysis metabolites were present, increased glucose flux and increased levels of pentose-phosphate metabolites were detected. This is not surprising, since neurons are believed to favor G-6-P flux into the pentose phosphate pathway (Herrero-Mendez et al, 2009). Thus, increased HK II levels might be a result of increased demand of pentose phosphate metabolites.

Autophagy was shown to regulate metabolic states via degradation of metabolic enzymes, especially chaperone-mediated autophagy (CMA) was shown to regulate cellular abundance of key metabolic enzymes. Liver-specific *lamp2a* knockout indicated that around 40% of CMA substrates are metabolic enzymes such as glycolytic enzymes (Schneider et al., 2014). However, no evidence was found in this study that key metabolic enzymes were increased upon loss of ATG5, indicating that increased glycolysis is primarily caused by GLUT2 accumulation.

Several studies indicated that loss of autophagy results in impaired mitochondrial clearance, resulting in accumulation of damaged mitochondria. Dysfunctional mitochondria cannot maintain respirational capacity and release ROS that might result cell death (Wang and Youle, 2009). Upon dysfunctional OXPHOS, increased glycolysis is believed to be a compensatory mechanism to maintain cellular homeostasis (Allen et al., 2014; Valbuena et al., 2016). However, ATG5 cKO Purkinje cells do not present signs of defective mitochondria. Upon loss of ATG5, mitochondrial respiration is not impaired in cerebellar cells and Purkinje cell somata do not contain damaged mitochondria. Initial characterization of mitochondrial cytochrome B does not indicate changes in complex II of the OXPHOs machinery. The *pcd* mouse, a model of Purkinje cell degeneration is caused by a spontaneous autosomal recessive mutation in the *agtpb1 (*ATP/GTP binding carboxylase) gene (Wang and Morgan, 2007). These mice show early onset of Purkinje cell degeneration after three weeks, display increased autophagic flux and increased levels of mitophagy. Most likely dysfunctional mitophagy might cause non-apoptotic Purkinje cell death (Chakrabarti et al., 2009). To understand whether impaired mitophagy contributes to Purkinje cell degeneration in ATG5 cKO animals, further studies are needed to further analyze mitochondria of ATG5 cKO Purkinje cells to rule out that the degeneration could be caused by energy failure of distal compartments such as axons and synapses.

Several neurodegenerative diseases (NDDs) such as AD, PD and ALS are associated with metabolic alterations. Those metabolic alterations are believed to contribute to the initiation and progression of NDDs. PET imaging studies showed that patients with AD, PD, ALS, HD and ataxia display glycolytic hypometabolism in several brain regions which might result in increased neuronal vulnerability (Hoyer, 1982b). Levels of ROS are tightly controlled by antioxidant systems and their dysregulation has been linked to many neurodegenerative conditions including ALS, ataxia and AD (Barnham et al., 2004; Lupoli et al., 2018). Mitochondrial dysfunction can be observed in patients in early stages of AD (Terada et al., 2020) AD mouse models show reduced hexokinase activity due to G-6-P accumulation (Demarest et al., 2020). Cortical regions of AD mice display reduced levels of GLUT1 and GLUT3 (Winkler et al., 2015; Szablewski, 2017). In drosophila AD-models, overexpression of glucose transporters or stimulation of increased glucose uptake results in increased survival rate (Niccoli et al., 2016). Dysfunctional glucose metabolism is also observed in early-stage AD patients and AD mouse models show reduced glucose uptake in entorhinal cortex, hippocampus and amygdala prior to protein aggregation (Le Douce et al., 2020).

In postmortem human PD brains, down-regulation of PPP enzymes and reduced NADPH are found in the putamen and cerebellum (Dunn et al., 2014). Decreased levels of the PPP key enzymes glucose-6-phosphate dehydrogenase and 6-phosphogluconate dehydrogenase occur at early stages in the putamen and cerebellum of PD patients (Dunn et al., 2014).

In PD mouse models, activation of NADPH oxidase, a superoxide-producing enzyme, causes dopaminergic neurodegeneration and impairments of learning, memory, and motor functions. Blockage of NADPH oxidase resulted in neuroprotection (Hou et al., 2019). In addition, enhancing phosphoglycerate kinase 1 activity promotes glycolysis and ATP generation thereby slowing down neuronal loss and PD progression (Cai et al., 2019). The cell death cause of ATG5 cKO Purkinje cells is still not clear. However, several glycolytic metabolites are known to cause cell death. Some of them such as DHAP, LPA, serine and methylglyoxal were increased in ATG5 cKO cerebellum.

Methylglyoxal is a constant glycolytic byproduct that derives from the glycolysis metabolite F-1,6-P, which is converted into dihydroxyacetone phosphate (DHAP), which is then further converted into methylglyoxal. Increased levels of MG-modified proteins were detected in ATG5 cKO Purkinje cells at the age of three months, and this increase could be reversed in DKO cerebellum upon concomitant loss of GLUT2. MG is a highly reactive dicarbonyl compound that promotes the formation of advanced glycation endproducts (AGEs), which are associated with several neurodegenerative disorders (Münch et al., 2012). MG reacts with phospholipids, nucleotides, and amino acid residues of proteins thereby generating AGEs (Rabbani et al., 2016). Those AGEs cause cellular damage, neuronal dysfunction and subsequently neuronal loss (Igor et al., 2015; Schmitz et al., 2017; Szczepanik et al., 2020). MG is detoxified via the glyoxalase (Glo) system (Glo-1 and Glo-2). Both enzymes are expressed in higher levels in astrocytes compared to neurons, indicating increased resistance to MG toxicity. This might allow astrocytes to sustain high levels of glycolysis, as they can better detoxify MG. Upregulation of glycolysis results in increased MG levels and MG- modified proteins as well as neuronal loss. Additionally, exogenous application of MG to neuronal cultures from hippocampus and cortex resulted in decreased neuronal viability, whereas astrocytes were not affected by MG treatment of even higher concentrations (de Arriba et al., 2007; Bélanger et al., 2011). Although this indicates that neurons are more vulnerable to MG toxicity, Purkinje cell vulnerability to MG toxicity was not described before. This study shows that loss of ATG5 cKO Purkinje cells can be caused by increased glycolytic metabolism, implicating Purkinje cell vulnerability to increased MG concentrations. However, how exactly MG leads to the death pf Purkinje cells needs to be investigated further.

Another metabolite that was shown to cause excitotoxicity is D-serine. Serine is significantly upregulated in 1-month old cerebellum and increased glucose flux into serine at the age of 3 months could be observed. Serine is present in the brain in two isoforms: L-serine as an amino acid and its D-isomer D-serine. Although it is believed that D-serine is mainly present in astrocytes, higher levels of serine racemace (SR) were found in neurons. SR is an enzyme that synthesized L-serine to D-serine (Benneyworth et al., 2012). D-serine is an agonist of the N-methyl-D-aspartate (NMDA) receptor and elevated levels were to be toxic for neurons due to excitotoxicity (Meftah et al., 2021). Several neurodegenerative diseases are associated with increased D-serine release and excitotoxicity. In AD, amyloid-β accumulation induces increased D-serine release and this is believed to contribute to the pathogenesis of neuronal cell death in AD (WU et al., 2004). Excitotoxicity is believed to be the major cause of motorneuron cell death in ALS (Bruijn et al., 2004). Transgenic mouse models for ALS have higher D-serine levels in the spinal cord than control animals (Sasabe et al., 2007). Additionally, rat hippocampal organotypic slices (OTCs) were shown to be susceptible to D-serine induced NMDAR-mediated excitotoxicity, which could be abolished by addition of a D-serine deaminase (Shelper et al., 2005). In line with these finding, increased D-serine levels caused Purkinje cell loss in cerebellar OTCs from WT mice. D-serine also binds to glutamate-like receptor δ2 (GluRδ2), which is highly expressed in Purkinje cell dendrites and is believed to mediate neuron-glia communication

(Kashiwabuchi et al., 1995). This indicates that Purkinje cell might be highly vulnerable to intrinsic and extrinsic elevated D-serine levels.

Lysophosphatic acid (LPA) is an abundant bioactive phospholipid which can be generated from membrane phospholipids or from the glycolytic metabolite DHAP (Yung et al., 2014). LPA can be present intra- and extracellularly at physiological and pathophysiological conditions (van Meer et al., 2008). LPA signals through different LPA receptors, inducing a wide range of different cellular responses (Yung et al., 2014). During brain development, LPA is required for cell proliferation, cell survival, differentiation and morphology (Ye et al., 2002; Sheng et al., 2015; Spohr et al., 2019). Even though LPA exerts several functions in neurons such as synapse formation, synaptic transmission and survival, its signaling is associated with a variety of NDDs such as AD (Noguchi et al., 2009; Spohr et al., 2019; Xiang et al., 2020). In AD patients increased lipid peroxidation was observed (Casado et al., 2008). Additionally, AD patients have increased iron levels in hippocampus, cortex and basal ganglia (Masaldan et al., 2019), indicating a possible trigger for ferroptosis. LPA is thought to be the main bioactive component for lipid peroxidation, thereby disrupting membranous structures such as the blood brain barrier in AD patients (Frisardi et al., 2011). Additionally, increased LPA levels are believed to be a risk factor for developing AD. Increased LPA levels cause pathological processes such as neurite retraction, reactive gliosis and cell death (McDonald et al., 2018). Increase in LPA causes cortical network hyperexcitability because of increased presynaptic glutamate release and subsequent excitotoxicity (Thalman et al., 2018). In line with that, WT Purkinje cells treated with LPA display increased excitability similar to ATG5 cKO Purkinje cells Additionally, LPA treatment results in Purkinje cell degeneration, indicating a possible contribution of LPA to Purkinje cell degeneration in ATG5 cKO animals. Many studies have shown that ferroptosis is a contributor to cell death in several diseases, such as NDDs and metabolic diseases (Ren et al., 2020; Le et al., 2021). KEGG pathway analysis of commonly upregulated proteins in 1- and 3-month old cerebellum indicated increased ferroptosis upon loss of ATG5. Ferroptosis is an iron-dependent form of cell death that is characterized by the accumulation of ROS and lipid peroxidation (Dixon et al., 2012). Ferroptosis is regulated by multiple pathways such as XC-/GSH/GPX4, GCH1/DHFR/BH4, FSP1/CoQ10 y, DHODH/CoQ, and p62/Keap1/Nrf2 pathway. If anti-ferroptosis pathways fail, free lipid radicals are generated in the presence of iron resulting in increased lipid peroxidation, oxidative damage and cell death (Guichardant et al., 2011). XC-/GSH/GPX4 is best studied anti-ferroptosis pathway. The XC-system consists of two solute carriers that exchanges glutamate and cystine along membranes. After import, cystine is converted into cysteine that is required for glutathione (GSH) synthesis. GSH is then used as a cofactor for Glutathione peroxidase 4 (GPX4) that reduces lipid hyperoxides to lipid alcohols, thereby reducing the amount of lipid peroxidation (Seibt et al., 2019; Lin et al., 2020; Chen et al., 2021). Increasing glutamate or decreasing cystine concentrations therefore favor ferroptotic cell death (Hambright et al., 2017). Ferroptosis inducing drugs such as RL3 block GPX4, thereby promoting ROS accumulation and lipid peroxidation. On the other side, ferroptosis inhibitor ferrostatin-1 (Fer1) acts as an iron chelator, thereby reducing the amount of free iron (Miotto et al., 2020; Dorian et al., 2023). Ferroptosis can also be modulated via p62/Keap1/Nrf2 pathway where p62 has a protective role. Nrf2 is a key transcriptional regulator, which is indirectly activated by p62. Activated pathway controls iron metabolism and increases antioxidant capacity of cells by promoting increased expression of glutathione synthase or glucose-6-phosphate dehydrogenase (G-6-PD) thereby increasing the production of antioxidants such as NADPH and GSH (Sun et al., 2016; Dodson et al.,2019; Sun et al., 2020). Additionally, Nrf2 can upregulate autophagy-related genes such as ATG5 (Sun et al., 2020). In this study, the degeneration of WT Purkinje cells could be induced by RSL3 treatment and ameliorated by concomitant Fer1 incubation, which indicates the role of ferroptosis in selective vulnerability of Purkinje cells to autophagy dysfunction.

Upon ATG5 deficiency, increased glucose flux could be observed into the pentose phosphate pathway in both cortex and cerebellum, which might be a protective compensatory mechanism against ferroptosis. However, in ATG5 cKO cerebellum only a minority of G-6-P ends up in PPP via G-6-PD, while most of it is used to produce lactate and pyruvate. A possible explanation for Purkinje cell vulnerability compared to cortical neurons might be different levels of PPP flux, since increased PPP flux was shown to have neuroprotective roles. G-6-PD is the first PPP enzyme that irreversibly catalyzes the conversion of G-6-P to 6-phosphoglucono-δ-lactone thereby producing NAPDH. Thus, the PPP is the major cellular source of NADPH (Kletzien et al., 1994). In cortical neurons, excitotoxicity was shown to result in elevated glycolytic flux and reduced PPP flux and NADPH levels. This promoted oxidative stress and cell death which could be prevented by overexpression of G-6-PD (Rodriguez-Rodriguez et al., 2012). TP53-induced glycolysis and apoptosis regulators (TIGAR) are shown to inhibit glycolysis and promote increased PPP flux (Geng et al., 2018). TIGARs are highly expressed in neurons and can be further upregulated upon stress (Li et al., 2014). Not only TIGARs but also heat shock protein 27 (HSP27) was shown to be able to upregulate G-6-PD activity in response to neuronal stressors (Yamamoto et al., 2018). G-6-PD alterations are implicated in many NDDs. Increased G-6-PD levels but decreased activity were observed in human AD brains (Bigl et al., 1999; Russel et al., 1999). However, in human studies there is limited evidence of a direct causality between G-6-PD alterations and disease pathology. In an AD rat mouse model, overexpression of G-6-PD was shown to have beneficial effects in decreasing tau and amyloid-β levels (Jovanović et al., 2014). In PD, levels of NADPH-producing enzymes G-6-PD and 6-phosphogluconate (6-PG) are reduced in putamen and cerebellum of presymtomatic patients (Dunn et al., 2014). Additionally, in an PD-mouse model, a neurotoxin 1-methyl-4-phenyl-1,2,3,6-tetrahydropyridine (MPTP) is used to induce mitochondrial induced- PD like cell loss. Overexpression of G-6-PD in the nigrostriatal pathway prevented MPTP-inducible toxic effects, even in aged mice (Mejías et al., 2006). Interestingly, overexpression of ferritin, an iron-binding protein in dopaminergic neurons

could prevent MPTP-inducible toxic effects as well (Kaur et al., 2003). This suggests, a possible contribution of ferroptosis in the pathogenesis of PD.
In the spinal cord of an ALS mouse model (hSOD1-G93A mutant), reduced PPP and G-6-PD activity was observed already at disease onset (Tefera et al., 2019). Those studies indicate a possible protective effect of PPP and G-6-PD activity. Whether this might cause selective vulnerability in autophagy-deficient mouse models is still elusive. The exact mechanism underlying differential glucose fates in cerebellar and cortical GABAergic neurons as well as in Purkinje cells needs to be determined. Furthermore, the molecular machinery of glycolysis and PPP machinery needs to be elucidated for individual cell types. Therefore, further analysis needs to be carried out whether PPP has a cell type specific role or whether molecular diversity determines glucose fate in different neuronal subtype and thereby resulting in cell-type specific vulnerability.

3. Autophagy regulates GLUT2 levels in Purkinje cell

Glucose transporters (GLUTs) are crucial for brain metabolism because of their role in regulating constantly glucose-uptake into astrocytes and neurons (Patching, 2017). This study could show that GLUT2 is expressed in cerebellar Purkinje cells and cortical neurons. Loss of ATG5 results in specific accumulation of GLUT2 in Purkinje cells but not in cortical GABAergic neurons. Increased levels of GLUT2 can be already observed at the age of one month in ATG5 cKO Purkinje cells. Since increased GLUT2 levels can be detected in the plasma membrane, this might be the cause of increased glycolytic flux. While GLUT1,3 and 4 levels increase with age or display similar expression levels in WT cerebellum and cortex between 1 and 3 months, GLUT2 levels decrease with age. GLUT3 expression was shown to coincide with maturation of synaptic connectivity (Vannucci et al., 1998). Additionally, GLUT3 levels are reported to decrease with ageing especially in hippocampus and cerebellum (Fattoretti et al., 2001; Fattoretti et al., 2002; Fattoretti et al., 2003; Hu et al., 2010; von Leden et al., 2019). Further analysis is required to assess whether GLUT3 might accumulate at later stages (e.g. at the age of one year) upon loss of ATG5.
However, if autophagy contributes to the degradation of GLUTs in the brain is currently still elusive. GLUT1 and GLUT3 were shown to be substrates of forebrain autophagosomes (Kallergi et al., 2023). Whether these are neuronal cargo is currently not known. Additionally, autophagic cargo of cerebellar cells has not been characterized yet. In cancer cells, autophagy is required for GLUT1 recycling from endosomes to the plasma membrane (Pei et al., 2022). Another study suggests that autophagy mediates GLUT4 translocation from intracellular compartments into the plasma membrane of adipocytes and skeletal muscles (Elhassan et al., 2018). This study provides the first evidence that autophagy is required for GLUT2 degradation in cerebellar Purkinje cells.

In order to prove whether upregulated GLUT2 levels in ATG5 cKO Purkinje cells are causative for increased glycolytic metabolism, a double knockout mouse for ATG5 and GLUT2 was generated as described above. Double cKO Purkinje cells displayed reduced glucose uptake and lactate levels. Additionally, DKO animals showed imporved motor coordination while crossing beam of different widths. Interestingly, Purkinje cell number could be partially rescued in specific cerebellar lobes, such as II+III and VIII-X in comparison to ATG5 cKO animals. Cerebellar Purkinje cells are believed to be highly heterogenous. Already during development, climbing and mossy fibers enter the cerebellum and contact specific Purkinje cell clusters (Arsenio Nunes and Sotelo, 1985; Chédotal et al., 1997). Some Purkinje cell markers are uniformly expressed, such as Calbindin, but other markers like Zebrin II are specifically expressed in certain Purkinje cell clusters (Wassef et al., 1990; Lannoo et al., 1991). During aging Purkinje cell death has been observed to similar extent throughout the cerebellar cortex (Sturrock 1989). Similar observations were made in humans. Starting at the age of 50 years, loss of vermis volume could be detected (Torvik et al., 1986; Luft et al., 1999).
Several studies showed that cerebellar morphology after Purkinje cell death depends on the timepoint of death and whether a selective subpopulation is affected. Non-selective Purkinje cell loss in the adult brain results in gaps within the molecular cell layer, which are often taken over by astrocytes. While the loss of a specific Purkinje cell subset results in a unique pattern of stripes and zones (Wassef et al., 1987, Sarna et al., 2001, Sarna et al., 2003). A mouse model of Niemann-Pick disease type C1, which is a autosomal recessive lipid-storage disorder, show progressive Purkinje cell loss at the age of one month (Tanaka et al., 1988). In this mouse model, HSP25 expressing Purkinje cells are resistant to cell death (Armstrong et al., 2000; Sarna et al., 2003). Around 2% of Purkinje cells express HSP25, confined to two cerebellar regions: lobes VI/VII and IX/X (Armstrong and Hawkes, 2000). This might be one of the explanations for why certain Purkinje cells are more vulnerable to degeneration. Loss of ATG5 results in a homogeneous loss of Purkinje cells throughout all cerebellar lobes, whereas GLUT2 loss rather affects specific Purkinje cells in certain brain regions. This might indicate that Purkinje cell death is dependent on the molecular phenotype.
Lobules V, VI, VIII, IX, and Crus were shown to be required for working memory and several motor tasks (Stoodley and Schmahmann, 2009; Ilg et al., 2019). Especially, lobes VIII,IX and X are important for the integrity of motor balance and higher cognitive functions (Grosse et al., 2021). Several studies show the involvement of the inferior vermis (lobes VII-X) in motor impairments such as ataxia (Puget et al., 2009; Küper et al., 2013; Albazron et al., 2019). Interestingly, spinocerebellar ataxia and sporadic adult late-onset ataxia patients showed specific cerebellar volume loss in cerebellar lobes V,VI,VII, IX and X (Conrad et al., 2023). Therefore, it is not surprising that DKO animals display improved motor coordination compared to ATG5 cKO animals, since DKO cerebellum shows increased Purkinje cells number in cerebellar lobes VIII-X. Further motor coordination analysis would be required to assess the full

range of possible rescues of motor coordination impairment in DKO animals. Additionally, reduced glycolytic flux in DKO animals highlights a possible therapeutic treatment for ataxia patients. One possible treatment would be a reduction in sugar-intake. Ketogenic diet is a low-carbohydrate high-fat diet that shifts metabolism from glycolysis and glucose metabolism towards β-oxidation, a pathway which was found to be decreased in ATG5 cKO cerebellum (Kossoff and Hartman, 2012). It is assumed that the ketogenic diet has beneficial effects on mitochondrial biogenesis and function, thereby reducing levels of oxidative stress. This diet is already used as a treatment for patients with epilepsy and mitochondrial diseases (Bough et al., 2006; Khang et al., 2007; Stafford et al., 2010). Ketogenic diet was also shown to improve myopathy progression in mice (Ahola-Erkkila et al., 2010). One study could also show that ketogenic diet ameliorates cerebellar atrophy in spinocerebellar ataxia. Patients with developmental delay associated with ataxia and progressive atrophy of both cerebellar hemispheres and cerebellar vermis were treated with ketogenic diet. The treatment caused a reduction in cerebellar atrophy progression and gradual enhancement of physical skills and vitality (Al Madhoun et al., 2019). Further studies are needed to test the effect of ketogenic diet on motor performance and Purkinje cells loss in ATG5 cKO mice.

Loss of GLUT2 in DKO animals reduces the levels of glycolytic flux and leads to lobe-specific rescue of Purkinje cell loss, indicating increased glycolysis a major contributor to Purkinje cell vulnerability. However, whether molecular differences between Purkinje cells and other GABAergic neurons in the brain are responsible for their selective susceptibility or whether these differences are due to different degradation and recycling of autophagic cargo requires further investigation.

VI. Conclusion

Autophagy is believed to contribute to neuronal health by eliminating defective proteins and organelles. However, recent studies show that neurons are resistant to autophagy-deficiency in-vivo, with an exception of cerebellar Purkinje cells, which are selectively vulnerable to autophagy loss, compared to forebrain GABAergic neurons.

This study shows that neurons are able to rewire the metabolism upon autophagy-deficient conditions. This might present the underlying mechanism of selective vulnerability of cerebellar Purkinje cells to autophagy deficits. Proteomics and metabolomics analysis indicated that loss of ATG5 results in increased glycolytic metabolism in cerebellum and increased PPP in the cortex. Several glycolytic metabolites such as methylglyoxal, LPA and serine are increased in cerebellum but not the cortex of ATG5 cKO animals. These metabolites cause Purkinje cell loss *ex vivo* and are predicted to be the cause of Purkinje cell degeneration *in vivo*. Increased glycolytic metabolism is triggered by specific upregulation of glucose transporter 2 (GLUT2) in Purkinje cells. In WT Purkinje cells, GLUT2 levels decrease during development from 1 to 3 months of age, while other GLUTs show similar expression levels. Under autophagy-deficient conditions GLUT2 accumulates in Purkinje cell plasma membrane resulting in increased glucose uptake. ATG5 cKO animals display ataxic motor coordination with impaired motor balance starting at the age of 3 months with progressive worsening until the age of one year. GLUT2 loss concomitant with ATG5 loss rescues motor impairment in 3-month old animals and improved Purkinje cell number in specific cerebellar lobes VIII-X. Additionally, loss of GLUT2 can rescue increased glycolytic metabolism in ATG5 cKO Purkinje cells.

In summary, this study shows that autophagy deficiency leads to an accumulation of GLUT2 in Purkinje cells, which in turn results in increased glycolysis and the accumulation of various neurotoxic metabolites that ultimately cause Purkinje cell degeneration. This suggests that diseases with Purkinje cell loss such as ataxia may benefit from dietary interventions and reduced glucose metabolism.

VII. Outlook

This study aimed to understand the selective vulnerability of Purkinje cell compared to cortical GABAergic neurons and was able to identify the specific upregulation of GLUT2 in Purkinje cells as the cause of their vulnerability. Other GLUTs were not altered upon loss of ATG5, however further time points during brain maturation and aging should be analyzed. GLUT1 and GLUT3 were described to show decreased expression levels while ageing, therefore the cortex and cerebellum of ATG5 cKO animals at the age of one year should be investigated. Additionally, different GLUTs should be analyzed upon blockage of autophagy to elucidatewhether autophagy is involved in the degradation of other GLUTs. The underlying mechanism of GLUT2 degradation is still elusive, thus further analysis should be carried out to identified autophagic receptors and autophagic modulators that regulate GLUT2 degradation. Additionally, profiling of cell-type specific autophagic cargo would help to understand cell-type specific vulnerability not only upon loss of autophagy but also in several diseases with impaired autophagic flux such as AD and PD.

A Purkinje cell specific ATG5 cKO mouse line should be created to investigate contributions of other cell types towards the phenotype. Since ATG5 cKO cerebellum displays astrogliosis upon loss of Purkinje cells, astrocytic contribution to glycolytic metabolism cannot be excluded. Molecular cell layer GABAergic interneurons are resistant to neuronal cell loss upon loss of ATG5, however further analysis is required to elucidate changes in their homeostasis or activity since some studies could show that alterations in the activity of molecular cell layer interneurons can contribute to Purkinje cell degeneration.

GLUT2 loss upon ATG5 deficiency was shown to have beneficial effects, however the effect of GLUT2 loss alone in cortical and cerebellar neurons has not yet been studied. Further studies should be carried out to investigate the consequences of GLUT2 loss in the brain and whether other GLUTs or glycolytic metabolic enzymes compensate for GLUT2 loss to maintain cellular glucose homeostasis.

The role of PPP should be investigated, since cortical GABAergic neurons are resistant to cell loss upon loss of ATG5, whereas Purkinje cells are more vulnerable. ATG5 cKO cortex displayed increased PPP flux compared to ATG5 cKO cerebellum, indicating beneficial effect of PPP. Further studies should focus on the role of PPP in cortical and Purkinje cells, and whether it is differentially regulated which might cause cell type-specific vulnerability.

Additionally, differences in autophagic flux of cerebellum and cortex should be analyzed. This might help to understand why the cortex is more resistant to autophagy loss.

Lastly, to further prove that Purkinje cell loss is caused by increased cerebellar glucose metabolism, ATG5 cKO animal should be treated with a ketogenic diet. This was shown to be beneficial for ataxia patients by improving motor behavior and slowing down cerebellar atrophy. This would further contribute to understand the selective vulnerability of Purkinje cell and additionally this would help understand why ketogenic diet has beneficial effects on ataxia patients.

VIII. References

Abbott NJ, Patabendige AAK, Dolma DEM, Yusof SR, Begley DJ (2010). Structure and function of the blood-brain barrier. Neurobiol Dis. 37**:13–25**

Ahola-Erkkilä S, Carroll CJ, Peltola-Mjösund K, Tulkki V, Mattila I, Seppänen-Laakso T, Oresic M, Tyynismaa H, Suomalainen A (2010). Ketogenic diet slows down mitochondrial myopathy progression in mice. Hum Mol Genet. 19(10):1974-1984

Al Madhoun A, Alnaser F, Melhem M, Nizam R, Al-Dabbous T, Al-Mulla F (2019). Ketogenic diet attenuates cerebellar atrophy progression in a subject with a biallelic variant at the ATAD3A locus. Appl Clin Genet. 12:79-86.

Albazron FM, Bruss J, Jones RM, Yock TI, Pulsifer MB, Cohen AL, Nopoulos PC, Abrams AN, Sato M, Boes AD (2019) Pediatric postoperative cerebellar cognitive affective syndrome follows outflow pathway lesions. Neurology 93:e1561–e1571

Allen SP, Rajan S, Duffy L, Mortiboys H, Higginbottom A, Grierson AJ, Shaw PJ (2014). Superoxide dismutase 1 mutation in a cellular model of amyotrophic lateral sclerosis shifts energy generation from oxidative phosphorylation to glycolysis. Neurobiol Aging. 35(6):1499-1509

Almeida S, Gascon E, Tran H, Chou HJ, Gendron TF, Degroot S, Tapper AR, Sellier C, Charlet-Berguerand N, Karydas A, Seeley WW, Boxer AL, Petrucelli L, Miller BL, Gao FB (2013). Modeling key pathological features of frontotemporal dementia with C9ORF72 repeat expansion in iPSC-derived human neurons. Acta Neuropathol. 126(3):385-399

Aman Y, Schmauck-Medina T, Hansen M, Morimoto RI, Simon AK, Bjedov I, Palikaras K, Simonsen A, Johansen T, Tavernarakis N, Rubinsztein DC, Partridge L, Kroemer G, Labbadia J, Fang EF (2021). Autophagy in healthy aging and disease. Nat Aging. 1(8):634-650

An H, Ordureau A, Paulo JA, Shoemaker CJ, Denic V, Harper JW (2019). TEX264 Is an Endoplasmic Reticulum-Resident ATG8-Interacting Protein Critical for ER Remodeling during Nutrient Stress. Mol Cell. 74(5):891-908.e10

Andersen JV, Skotte NH, Aldana BI, Nørremølle A, Waagepetersen HS (2019). Enhanced cerebral branched-chain amino acid metabolism in R6/2 mouse model of Huntington's disease. Cell Mol Life Sci. 76(12):2449-2461

Antonini A, Leenders KL, Spiegel R, Meier D, Vontobel P, Weigell-Weber M, Sanchez-Pernaute R, de Yébenez JG, Boesiger P, Weindl A, Maguire RP (1996). Striatal glucose metabolism and dopamine D2 receptor binding in asymptomatic gene carriers and patients with Huntington's disease. Brain. 119 (6):2085-2095

Aouci R, El Soudany M, Maakoul Z, Fontaine A, Kurihara H, Levi G, Narboux-Nême N. Dlx5/6 Expression Levels in Mouse GABAergic Neurons Regulate Adult Parvalbumin Neuronal Density and Anxiety/Compulsive Behaviours. Cells. 2022; 11(11):1739.

Apelt J, Mehlhorn G, Schliebs R (1999). Insulin-sensitive GLUT4 glucose transporters are colocalized with GLUT3-expressing cells and demonstrate a chemically distinct neuron-specific localization in rat brain. J Neurosci Res. 57:693–705

Aravamudhan S, Türk C, Bock T, Keufgens L, Nolte H, Lang F, Krishnan RK, König T, Hammerschmidt P, Schindler N, Brodesser S, Rozsivalova DH, Rugarli E, Trifunovic A, Brüning J, Langer T, Braun T, Krüger M. (2021) Phosphoproteomics of the developing heart identifies PERM1 - An outer mitochondrial membrane protein. J Mol Cell Cardiol 154:41–59

Ardehali H, Printz RL, Whitesell RR, May JM, Granner DK (1999). Functional interaction between the N- and C-terminal halves of human hexokinase II. J Biol Chem. 274:15986–15989

Ariosa AR, Klionsky DJ (2016). Autophagy core machinery: overcoming spatial barriers in neurons. J Mol Med (Berl). 94(11):1217-1227

Arluison M, Quignon M, Nguyen P, Thorens B, Leloup C, Penicaud L (2004a). Distribution and anatomical localization of the glucose transporter 2 (GLUT2) in the adult rat brain--an immunohistochemical study. J Chem Neuroanat. 28:117–136

Arluison M, Quignon M, Thorens B, Leloup C, Penicaud L (2004b). Immunocytochemical localization of the glucose transporter 2 (GLUT2) in the adult rat brain. II. Electron microscopic study. J Chem Neuroanat. 28:137–146

Armstrong CL, Hawkes R (2000). Pattern formation in the cerebellar cortex. Biochem Cell Biol. 78(5):551-62

Armstrong CL, Krueger-Naug AM, Currie RW, Hawkes R (2000). Constitutive expression of the 25-kDa heat shock protein Hsp25 reveals novel parasagittal bands of purkinje cells in the adult mouse cerebellar cortex. J Comp Neurol. 416(3):383-97.

Arsénio Nunes ML, Sotelo C (1985). Development of the spinocerebellar system in the postnatal rat. J Comp Neurol. 237(3):291-306

Ashrafi G, Wu Z, Farrell RJ, Ryan TA (2017). GLUT4 mobilization supports energetic demands of active synapses. Neuron. 93:606–615.e3

Attwell D, Laughlin SB (2001). An energy budget for signaling in the grey matter of the brain. J Cereb Blood Flow Metab. 21(10):1133-1145

Azarnia Tehran D, Kuijpers M, Haucke V (2018). Presynaptic endocytic factors in autophagy and neurodegeneration. Curr Opin Neurobiol. 48:153-159

Azarnia Tehran D, Kuijpers M, Haucke V (2018). Presynaptic endocytic factors in autophagy and neurodegeneration. Curr Opin Neurobiol. 48:153-159

Bady I, Marty N, Dallaporta M, Emery M, Gyger J, Tarussio D, Foretz M, Thorens B (2006). Evidence from glut2-null mice that glucose is a critical physiological regulator of feeding. Diabetes. 55(4):988-995

Barahona MJ, Llanos P, Recabal A, Escobar-Acuna K, Elizondo-Vega R, Salgado M, Ordenes P, Uribe E, Sepulveda FJ, Araneda RC, Garcia-Robles MA (2018). Glial hypothalamic inhibition of GLUT2 expression alters satiety, impacting eating behavior. Glia. 66:592–605

Barmack NH, Baughman RW, Eckenstein FP (1992). Cholinergic innervation of the cerebellum of rat, rabbit, cat, and monkey as revealed by choline acetyltransferase activity and immunohistochemistry. J Comp Neurol. 317(3):233-249

Barnham KJ, Masters CL, Bush AI (2004). Neurodegenerative diseases and oxidative stress. Nat Rev Drug Discov. 3(3):205-214

Bastian AJ, Martin TA, Keating JG, Thach WT (1996). Cerebellar ataxia: abnormal control of interaction torques across multiple joints. J Neurophysiol. 76:492–509

Bauernfeind AL, Barks SK, Duka T, Grossman LI, Hof PR, Sherwood CC (2014). Aerobic glycolysis in the primate brain: reconsidering the implications for growth and maintenance. Brain Struct Funct. 219(4):1149-1167

Beckinghausen J, Sillitoe RV (2019). Insights into cerebellar development and connectivity. Neurosci Lett. 688:2-13.

Begley DJ (2004). ABC transporters and the blood-brain barrier. **Curr Pharm Des. 10**:1295–1312

Bélanger M, Allaman I, Magistretti PJ (2011a). Brain energy metabolism: focus on astrocyte-neuron metabolic cooperation. Cell Metab. 14(6):724-738

Bélanger M, Yang J, Petit JM, Laroche T, Magistretti PJ, Allaman I (2011). Role of the glyoxalase system in astrocyte-mediated neuroprotection. J Neurosci. 31(50):18338-18352

Benneyworth MA, Li Y, Basu AC, Bolshakov VY, Coyle JT (2012). Cell selective conditional null mutations of serine racemase demonstrate a predominate localization in cortical glutamatergic neurons. Cell. Mol. Neurobiol. 32:613–624

Benomar Y, Naour N, Aubourg A, Bailleux V, Gertler A, Djiane J, Guerre-Millo M, Taouis M (2006). Insulin and leptin induce Glut4 plasma membrane translocation and glucose uptake in a human neuronal cell line by a phosphatidylinositol 3-kinase- dependent mechanism. Endocrinology. 147:2550–2556

Bibb MJ, Van Etten RA, Wright CT, Walberg MW, Clayton DA (1981). Sequence and gene organization of mouse mitochondrial DNA. Cell. 26(2 Pt 2):167-180

Bigl M, Brückner MK, Arendt T, Bigl V, Eschrich K (1999). Activities of key glycolytic enzymes in the brains of patients with Alzheimer's disease. J Neural Transm. 106: 499-511

Birnbaum MJ (1989). Identification of a novel gene encoding an insulin-responsive glucose transporter protein. Cell. 57(2):305-315

Bjørkøy G, Lamark T, Brech A, Outzen H, Perander M, Overvatn A, Stenmark H, Johansen T (2005). p62/SQSTM1 forms protein aggregates degraded by autophagy and has a protective effect on huntingtin-induced cell death. J Cell Biol. 171(4):603-614

Blazey T, Snyder AZ, Su Y, Goyal MS, Lee JJ, Vlassenko AG, Arbeláez AM, Raichle ME (2019). Quantitative positron emission tomography reveals regional differences in aerobic glycolysis within the human brain. J Cereb Blood Flow Metab. 39(10):2096-2102

Bogetofte H, Jensen P, Ryding M, Schmidt SI, Okarmus J, Ritter L, Worm CS, Hohnholt MC, Azevedo C, Roybon L, Bak LK, Waagepetersen H, Ryan BJ, Wade-Martins R, Larsen MR, Meyer M (2019). PARK2 Mutation Causes Metabolic Disturbances and Impaired Survival of Human iPSC-Derived Neurons. Front Cell Neurosci. 13:297

Bondy CA, Lee WH, Zhou J (1992). Ontogeny and cellular distribution of brain glucose transporter gene expression. Mol Cell Neurosci. 3:305–314

Borglykke A, Grarup N, Sparsø T, Linneberg A, Fenger M, Jeppesen J, Hansen T, Pedersen O, Jørgensen T. (2012). Genetic variant SLC2A2 [corrected] is associated with risk of cardiovascular disease - assessing the individual and cumulative effect of 46 type 2 diabetes related genetic variants. PLoS One. 7:e50418

Borsche M, König IR, Delcambre S, Petrucci S, Balck A, Brüggemann N, Zimprich A, Wasner K, Pereira SL, Avenali M, Deuschle C, Badanjak K, Ghelfi J, Gasser T, Kasten M, Rosenstiel P, Lohmann K, Brockmann K, Valente EM, Youle RJ, Grünewald A, Klein C (2020). Mitochondrial damage-associated inflammation highlights biomarkers in PRKN/PINK1 parkinsonism. Brain. 143(10):3041-3051

Bough KJ, Wetherington J, Hassel B, Pare JF, Gawryluk JW, Greene JG, Shaw R, Smith Y, Geiger JD, Dingledine RJ (2006). Mitochondrial biogenesis in the anticonvulsant mechanism of the ketogenic diet. Ann Neurol. 60(2):223-35

Brooks VB, Thach WT (2001). Cerebellar Control of Posture and Movement. Comprehensive Physiology:877-946

Browne SE, Bowling AC, MacGarvey U, Baik MJ, Berger SC, Muqit MM, Bird ED, Beal MF (1997). Oxidative damage and metabolic dysfunction in Huntington's disease: selective vulnerability of the basal ganglia. Ann Neurol. 41(5):646-653

Browne SE, Beal MF (2006) Oxidative damage in Huntington’s disease pathogenesis. Antioxid Redox Signal. 8:2061–2073

Bruijn LI, Miller TM, Cleveland DW (2004). Unraveling the mechanisms involved in motor neuron degeneration in ALS. Annu Rev Neurosci. 27:723-49

Buchan JR, Kolaitis RM, Taylor JP, Parker R (2013). Eukaryotic stress granules are cleared by autophagy and Cdc48/VCP function. Cell. 153(7):1461-1474

Buckner RL, Krienen FM, Castellanos A, Diaz JC, Yeo BTT (2011). The organization of the human cerebellum estimated by intrinsic functional connectivity. J Neurophysiol. 106:2322–2345

Burté F, Carelli V, Chinnery PF, Yu-Wai-Man P (2015). Disturbed mitochondrial dynamics and neurodegenerative disorders. Nat Rev Neurol. 11(1):11-24

Busch SE, Hansel C (2023). Climbing fiber multi-innervation of mouse Purkinje dendrites with arborization common to human. Science. 381(6656):420-427

Butterfield DA, Halliwell B (2019). Oxidative stress, dysfunctional glucose metabolism and Alzheimer disease. Nat Rev Neurosci. 20(3):148-160

Cai R, Zhang Y, Simmering JE, Schultz JL, Li Y, Fernandez-Carasa I, Consiglio A, Raya A, Polgreen PM, Narayanan NS, Yuan Y, Chen Z, Su W, Han Y, Zhao C, Gao L, Ji X, Welsh MJ, Liu L (2019). Enhancing glycolysis attenuates Parkinson's disease progression in models and clinical databases. J Clin Invest. 129(10):4539-4549

Camandola S, Mattson MP (2017). Brain metabolism in health, aging, and neurodegeneration. EMBO J. 36(11):1474-1492

Carayannopoulos MO, Xiong F, Jensen P, Rios-Galdamez Y, Huang H, Lin S, Devaskar SU (2014). GLUT3 gene expression is critical for embryonic growth, brain development and survival. Mol Genet Metab. 111(4):477-483

Casado A, Encarnación López-Fernández M, Concepción Casado M, de La Torre R (2008). Lipid peroxidation and antioxidant enzyme activities in vascular and Alzheimer dementias. Neurochem Res. 33(3):450-8

Cataldo AM, Peterhoff CM, Troncoso JC, Gomez-Isla T, Hyman BT, Nixon RA (2000). Endocytic pathway abnormalities precede amyloid beta deposition in sporadic Alzheimer's disease and Down syndrome: differential effects of APOE genotype and presenilin mutations. Am J Pathol. 157(1):277-86

Cerminara NL, Koutsikou S, Lumb BM, Apps R (2009). The periaqueductal grey modulates sensory input to the cerebellum: a role in coping behaviour? Eur J Neurosci. 29(11):2197-2206

Chakrabarti L, Eng J, Ivanov N, Garden GA, La Spada AR (2009). Autophagy activation and enhanced mitophagy characterize the Purkinje cells of pcd mice prior to neuronal death. Mol Brain. 29;2:24

Chandel NS (2020a). Mitochondria. Cold Spring Harb Perspect Biol. 13(3):a040543

Chandel NS (2020b). Signaling and metabolism. Cold Spring Harb Perspect Biol. 13(2):a040600

Chandel NS (2021). Glycolysis. Cold Spring Harb Perspect Biol. 13(5):a040535

Chédotal A, Bloch-Gallego E, Sotelo C (1997). The embryonic cerebellum contains topographic cues that guide developing inferior olivary axons. Development. 124(4):861-70

Cheff DM, Huang C, Scholzen KC, Gencheva R, Ronzetti MH, Cheng Q, Hall MD, Arnér ESJ (2023). The ferroptosis inducing compounds RSL3 and ML162 are not direct inhibitors of GPX4 but of TXNRD1. Redox Biology 62:102703

Chen Z, Fu Q, Shen B, Huang X, Wang K, He P, Li F, Zhang F, Shen H (2014). Enhanced p62 expression triggers concomitant autophagy and apoptosis in a rat chronic spinal cord compression model. Mol Med Rep. 9(6):2091-2096

Chen L, Na R, Danae McLane K, Thompson CS, Gao J, Wang X, Ran Q (2021). Overexpression of ferroptosis defense enzyme Gpx4 retards motor neuron disease of SOD1G93A mice. Sci Rep. 11(1):12890

Chen D, Zhu C, Wang X, Feng X, Pang S, Huang W, Hawley RG, Yan B (2013). A novel and functional variant within the ATG5 gene promoter in sporadic Parkinson's disease. Neurosci Lett. 538:49-53

Chen Q, Xiao Y, Chai P, Zheng P, Teng J, Chen J (2019). ATL3 Is a Tubular ER-Phagy Receptor for GABARAP-Mediated Selective Autophagy. Curr Biol. 29(5):846-855.e6

Chino H, Hatta T, Natsume T, Mizushima N (2019). Intrinsically Disordered Protein TEX264 Mediates ER-phagy. Mol Cell. 74(5):909-921.e6

Choeiri C, Staines W, Messier C (2002). Immunohistochemical localization and quantification of glucose transporters in the mouse brain. Neuroscience. 111:19–34

Cirulli ET, Lasseigne BN, Petrovski S, Sapp PC, Dion PA, Leblond CS, Couthouis J, Lu YF, Wang Q, Krueger BJ, Ren Z, Keebler J, Han Y, Levy SE, Boone BE, Wimbish JR, Waite LL, Jones AL, Carulli JP, Day-Williams AG, Staropoli JF, Xin WW, Chesi A, Raphael AR, McKenna-Yasek D, Cady J, Vianney de Jong JM, Kenna KP, Smith BN, Topp S, Miller J, Gkazi A; FALS Sequencing Consortium; Al-Chalabi A, van den Berg LH, Veldink J, Silani V, Ticozzi N, Shaw CE, Baloh RH, Appel S, Simpson E, Lagier-Tourenne C, Pulst SM, Gibson S, Trojanowski JQ, Elman L, McCluskey L, Grossman M, Shneider NA, Chung WK, Ravits JM, Glass JD, Sims KB, Van Deerlin VM, Maniatis T, Hayes SD, Ordureau A, Swarup S, Landers J, Baas F, Allen AS, Bedlack RS, Harper JW, Gitler AD, Rouleau GA, Brown R, Harms MB, Cooper GM, Harris T, Myers RM, Goldstein DB (2015). Exome sequencing in amyotrophic lateral sclerosis identifies risk genes and pathways. Science. 347(6229):1436-1441

Cisternas P, Inestrosa NC (2017). Brain glucose metabolism: Role of Wnt signaling in the metabolic impairment in Alzheimer's disease. Neurosci Biobehav Rev. 80:316-328

Cisternas P, Salazar P, Silva-Álvarez C, Barros LF, Inestrosa NC (2016). Activation of Wnt Signaling in Cortical Neurons Enhances Glucose Utilization through Glycolysis. J Biol Chem. 291(50):25950-25964

Clausen TH, Lamark T, Isakson P, Finley K, Larsen KB, Brech A, Øvervatn A, Stenmark H, Bjørkøy G, Simonsen A, Johansen T (2010). p62/SQSTM1 and ALFY interact to facilitate the formation of p62 bodies/ALIS and their degradation by autophagy. Autophagy. 6(3):330-344

Coccini T, Schicchi A, Locatelli CA, Caloni F, Negri S, Grignani E, De Simone U (2023). Methylglyoxal-induced neurotoxic effects in primary neuronal-like cells transdifferentiated from human mesenchymal stem cells: Impact of low concentrations. J Appl Toxicol. 43(12):1819-1839

Collins TJ, Berridge MJ, Lipp P, Bootman MD (2002). Mitochondria are morphologically and functionally heterogeneous within cells. EMBO J. 21(7):1616-1627.

Conrad J, Huppert A, Ruehl RM, Wuehr M, Schniepp R, Zu Eulenburg P (2023). Disability in cerebellar ataxia syndromes is linked to cortical degeneration. J Neurol. 270(11):5449-5460

Consalez GG, Goldowitz D, Casoni F, Hawkes R (2021). Origins, Development, and Compartmentation of the Granule Cells of the Cerebellum. Front Neural Circuits. 14:611841

Cornelius N, Wardman JH, Hargreaves IP, Neergheen V, Bie AS, Tumer Z et al (2017) Evidence of oxidative stress and mitochondrial dysfunction in spinocerebellar ataxia type 2 (SCA2) patient fibroblasts: effect of coenzyme Q10 supplementation on these parameters. Mitochondrion 34:103–114

Courchet J, Lewis TL Jr, Lee S, Courchet V, Liou DY, Aizawa S, Polleux F (2013). Terminal axon branching is regulated by the LKB1-NUAK1 kinase pathway via presynaptic mitochondrial capture. Cell. 153(7):1510-1525

Davidson CD, Fishman YI, Puskás I, Szemán J, Sohajda T, McCauliff LA, Sikora J, Storch J, Vanier MT, Szente L, Walkley SU, Dobrenis K (2016). Efficacy and ototoxicity of different cyclodextrins in Niemann-Pick C disease. Ann Clin Transl Neurol. 3(5):366–80

De Arriba SG, Stuchbury G, Yarin J, Burnell J, Loske C, Münch G (2007). Methylglyoxal impairs glucose metabolism and leads to energy depletion in neuronal cells-protection by carbonyl scavengers. Neurobiology of Aging. 28(7):1044–1050

DeBerardinis RJ, Chandel NS (2016). Fundamentals of cancer metabolism. Sci Adv. 2(5):e1600200

DeBrosse SD, Okajima K, Zhang S, Nakouzi G, Schmotzer CL, Lusk-Kopp M, Frohnapfel MB, Grahame G, Kerr DS (2012). Spectrum of neurological and survival outcomes in pyruvate dehydrogenase complex (PDC) deficiency: lack of correlation with genotype. Mol Genet Metab. 107(3):394–402

Dehay B, Ramirez A, Martinez-Vicente M, Perier C, Canron MH, Doudnikoff E, Vital A, Vila M, Klein C, Bezard E (2012). Loss of P-type ATPase ATP13A2/PARK9 function induces general lysosomal deficiency and leads to Parkinson disease neurodegeneration. Proc Natl Acad Sci U S A. 109(24):9611-9616

De Leon MJ, Ferris SH, George AE, Reisberg B, Christman DR, Kricheff II, Wolf AP (1983). Computed tomography and positron emission transaxial tomography evaluations of normal aging and Alzheimer's disease. J Cereb Blood Flow Metab. 3:391–394

Delgado-García JM (2001) Structure and function of the cerebellum. Rev Neurol. 33(7):635-42

Demarest TG, Varma VR, Estrada D, Babbar M, Basu S, Mahajan UV, Moaddel R, Croteau DL, Thambisetty M, Mattson MP, Bohr VA (2020). Biological sex and DNA repair deficiency drive Alzheimer's disease via systemic metabolic remodeling and brain mitochondrial dysfunction. Acta Neuropathol. 140(1):25-47

Devine MJ, Kittler JT (2018). Mitochondria at the neuronal presynapse in health and disease. Nat Rev Neurosci. 19(2):63-80

De Vivo DC, Trifiletti RR, Jacobson RI, Ronen GM, Behmand RA, Harik SI (1991). Defective glucose transport across the blood-brain barrier as a cause of persistent hypoglycorrhachia, seizures, and developmental delay. N Engl J Med. 325(10):703-709

Dienel GA (2012). Brain Lactate Metabolism: The Discoveries and the Controversies. Journal of Cerebral Blood Flow & Metabolism. 32(7):1107-1138

Dietrichs E, Haines DE (1989). Interconnections between hypothalamus and cerebellum. Anat Embryol (Berl). 179(3):207-220

Dikic I (2017). Proteasomal and Autophagic Degradation Systems. Annu Rev Biochem. 86:193-224

Dikic I, Elazar Z (2018). Mechanism and medical implications of mammalian autophagy. Nat Rev Mol Cell Biol.19(6):349-364

Ding F, Yao J, Rettberg JR, Chen S, Brinton RD (2013). Early decline in glucose transport and metabolism precedes shift to ketogenic system in female aging and Alzheimer's mouse brain: implication for bioenergetic intervention. PLoS ONE. 8:e79977

Dixon SJ, Lemberg KM, Lamprecht MR, Skouta R, Zaitsev EM, Gleason CE, Patel DN, Bauer AJ, Cantley AM, Yang WS, Morrison B 3rd, Stockwell BR (2012). Ferroptosis: an iron-dependent form of nonapoptotic cell death. Cell. 149(5):1060-1072

Dodson M, Castro-Portuguez R, Zhang DD (2019). NRF2 plays a critical role in mitigating lipid peroxidation and ferroptosis. Redox Biol. 23:101107

Dooley HC, Razi M, Polson HE, Girardin SE, Wilson MI, Tooze SA (2014). WIPI2 links LC3 conjugation with PI3P, autophagosome formation, and pathogen clearance by recruiting Atg12-5-16L1. Mol Cell. 55(2):238-52

Doxaki C, Palikaras K (2021). Neuronal Mitophagy: Friend or Foe? Front Cell Dev Biol. 8:611938

Duelli R, Staudt R, Duembgen L, Kuschinsky W (1999). Increase in glucose transporter densities of Glut3 and decrease of glucose utilization in rat brain after one week of hypoglycemia. Brain Res. 1999 Jun 12;831(1-2):254-262

Dum RP, Strick PL (2013). Transneuronal tracing with neurotropic viruses reveals network macroarchitecture. Curr Opin Neurobiol. 23(2):245-9

Dunn L, Allen GF, Mamais A, Ling H, Li A, Duberley KE, Hargreaves IP, Pope S, Holton JL, Lees A, Heales SJ, Bandopadhyay R (2014) Dysregulation of glucose metabolism is an early event in sporadic Parkinson's disease. Neurobiol Aging. 35:1111–1115

Dupuis J, Langenberg C, Prokopenko I, Saxena R, Soranzo N, Jackson AU, Wheeler E, Glazer NL, Bouatia-Naji N, Gloyn AL, Lindgren CM, Mägi R, Morris AP, Randall J, Johnson T, Elliott P, Rybin D, Thorleifsson G, Steinthorsdottir V, Henneman P, Grallert H, Dehghan A, Hottenga JJ, Franklin CS, Navarro P, Song K, Goel A, Perry JR, Egan JM, Lajunen T, Grarup N, Sparsø T, Doney A, Voight BF, Stringham HM, Li M, Kanoni S, Shrader P, Cavalcanti-Proença C, Kumari M, Qi L, Timpson NJ, Gieger C, Zabena C, Rocheleau G, Ingelsson E, An P, O'Connell J, Luan J, Elliott A, McCarroll SA, Payne F, Roccasecca RM, Pattou F, Sethupathy P, Ardlie K, Ariyurek Y, Balkau B, Barter P, Beilby JP, Ben-Shlomo Y, Benediktsson R, Bennett AJ, Bergmann S, Bochud M, Boerwinkle E, Bonnefond A, Bonnycastle LL, Borch-Johnsen K, Böttcher Y, Brunner E, Bumpstead SJ, Charpentier G, Chen YD, Chines P, Clarke R, Coin LJ, Cooper MN, Cornelis M, Crawford G, Crisponi L, Day IN, de Geus EJ, Delplanque J, Dina C, Erdos MR, Fedson AC, Fischer-Rosinsky A, Forouhi NG, Fox CS, Frants R, Franzosi MG, Galan P, Goodarzi MO, Graessler J, Groves CJ, Grundy S, Gwilliam R, Gyllensten U, Hadjadj S, Hallmans G, Hammond N, Han X, Hartikainen AL, Hassanali N, Hayward C, Heath SC, Hercberg S, Herder C, Hicks AA, Hillman DR, Hingorani AD, Hofman A, Hui J, Hung J, Isomaa B, Johnson PR, Jørgensen T, Jula A, Kaakinen M, Kaprio J, Kesaniemi YA, Kivimaki M, Knight B, Koskinen S, Kovacs P, Kyvik KO, Lathrop GM, Lawlor DA, Le Bacquer O, Lecoeur C, Li Y, Lyssenko V, Mahley R, Mangino M, Manning AK, Martínez-Larrad MT, McAteer JB, McCulloch LJ, McPherson R, Meisinger C, Melzer D, Meyre D, Mitchell BD, Morken MA, Mukherjee S, Naitza S, Narisu N, Neville MJ, Oostra BA, Orrù M, Pakyz R, Palmer CN, Paolisso G, Pattaro C, Pearson D, Peden JF, Pedersen NL, Perola M, Pfeiffer AF, Pichler I, Polasek O, Posthuma D, Potter SC, Pouta A, Province MA, Psaty BM, Rathmann W, Rayner NW, Rice K, Ripatti S, Rivadeneira F, Roden M, Rolandsson O, Sandbaek A, Sandhu M, Sanna S, Sayer AA, Scheet P, Scott LJ, Seedorf U, Sharp SJ, Shields B, Sigurethsson G, Sijbrands EJ, Silveira A, Simpson L, Singleton A, Smith NL, Sovio U, Swift A, Syddall H, Syvänen AC, Tanaka T, Thorand B, Tichet J, Tönjes A, Tuomi T, Uitterlinden AG, van Dijk KW, van Hoek M, Varma D, Visvikis-Siest S, Vitart V, Vogelzangs N, Waeber G, Wagner PJ, Walley A, Walters GB, Ward KL, Watkins H, Weedon MN, Wild SH, Willemsen G, Witteman JC, Yarnell JW, Zeggini E, Zelenika D, Zethelius B, Zhai G, Zhao JH, Zillikens MC; DIAGRAM Consortium; GIANT Consortium; Global BPgen Consortium; Borecki IB, Loos RJ, Meneton P, Magnusson PK, Nathan DM, Williams GH, Hattersley AT, Silander K, Salomaa V, Smith GD, Bornstein SR, Schwarz P, Spranger J, Karpe F, Shuldiner AR, Cooper C, Dedoussis GV, Serrano-Ríos M, Morris AD, Lind L, Palmer LJ, Hu FB, Franks PW, Ebrahim S, Marmot M, Kao WH, Pankow JS, Sampson MJ, Kuusisto J, Laakso M, Hansen T, Pedersen O, Pramstaller PP, Wichmann HE, Illig T, Rudan I, Wright AF, Stumvoll M, Campbell H, Wilson JF; Anders Hamsten on behalf of Procardis Consortium; MAGIC investigators; Bergman RN, Buchanan TA, Collins FS, Mohlke KL, Tuomilehto J, Valle TT, Altshuler D, Rotter JI, Siscovick DS, Penninx BW, Boomsma DI, Deloukas P, Spector TD, Frayling TM, Ferrucci L, Kong A, Thorsteinsdottir U, Stefansson K, van Duijn CM, Aulchenko YS, Cao A, Scuteri A, Schlessinger D, Uda M, Ruokonen A, Jarvelin MR, Waterworth DM, Vollenweider P, Peltonen L, Mooser V, Abecasis GR, Wareham NJ, Sladek R, Froguel P, Watanabe RM, Meigs JB, Groop L, Boehnke M, McCarthy MI, Florez JC, Barroso I (2010). New genetic loci implicated in fasting glucose homeostasis and their impact on type 2 diabetes risk. Nat Genet. 42(2):105-116

Eccles JC, Ito M, Szentágothai J (1967). The Cerebellum as a Neuronal Machine. Berlin: Springer-Verlag

El Messari S, Ait-Ikhlef A, Ambroise DH, Penicaud L, Arluison M (2002). Expression of insulin-responsive glucose transporter GLUT4 mRNA in the rat brain and spinal cord: an in situ hybridization study. J Chem Neuroanat. 24:225–242

El Messari S, Leloup C, Quignon M, Brisorgueil MJ, Penicaud L, Arluison M (1998). Immunocytochemical localization of the insulin-responsive glucose transporter 4 (Glut4) in the rat central nervous system. J Comp Neurol. 399:492–512

Elhassan SAM, Candasamy M, Chan EWL, Bhattamisra SK (2018). Autophagy and GLUT4: The missing pieces. Diabetes Metab Syndr. 12(6):1109-1116

Emrani S, Arain HA, DeMarshall C, Nuriel T (2020). APOE4 is associated with cognitive and pathological heterogeneity in patients with Alzheimer's disease: a systematic review. Alzheimers Res Ther. 12(1):141

Eny KM, Wolever TM, Fontaine-Bisson B, El-Sohemy A (2008). Genetic variant in the glucose transporter type 2 is associated with higher intakes of sugars in two distinct populations. Physiol Genomics. 33:355–360

Evans CS, Holzbaur EL (2020). Degradation of engulfed mitochondria is rate-limiting in Optineurin-mediated mitophagy in neurons. Elife. 9:e50260

Evans CS, Holzbaur ELF (2019). Autophagy and mitophagy in ALS. Neurobiol Dis. 122:35-40

Fattoretti P, Bertoni-Freddari C, Casoli T, Di Stefano G, Giorgetti G, Solazzi M (2003). Ethanol-induced decrease of the expression of glucose transport protein (Glut3) in the central nervous system as a predisposing condition to apoptosis: the effect of age. Ann N Y Acad Sci. 1010:500-503

Fattoretti P, Bertoni-Freddari C, Casoli T, Di Stefano G, Solazzi M, Giorgetti B (2002). Decreased expression of glucose transport protein (Glut3) in aging and vitamin E deficiency. Ann N Y Acad Sci. 973:293-296

Fattoretti P, Bertoni-Freddari C, Di Stefano G, Casoli T, Gracciotti N, Solazzi M, Pompei P (2001). Quantitative immunohistochemistry of glucose transport protein (Glut3) expression in the rat hippocampus during aging. J Histochem Cytochem. 49(5):671-672.

Fleck D, Phu L, Verschueren E, Hinkle T, Reichelt M, Bhangale T, Haley B, Wang Y, Graham R, Kirkpatrick DS, Sheng M, Bingol B (2019). PTCD1 Is Required for Mitochondrial Oxidative-Phosphorylation: Possible Genetic Association with Alzheimer's Disease. J Neurosci. 39(24):4636-4656

Fonteyn EM, Schmitz-Hübsch T, Verstappen CC, Baliko L, Bloem BR, Boesch S, Bunn L, Giunti P, Globas C, Klockgether T, Melegh B, Pandolfo M, Schöls L, Timmann D, van de Warrenburg BP (2013). Prospective analysis of falls in dominant ataxias. Eur Neurol. 69(1):53-57.

Freischmidt A, Wieland T, Richter B, Ruf W, Schaeffer V, Müller K, Marroquin N, Nordin F, Hübers A, Weydt P, Pinto S, Press R, Millecamps S, Molko N, Bernard E, Desnuelle C, Soriani MH, Dorst J, Graf E, Nordström U, Feiler MS, Putz S, Boeckers TM, Meyer T, Winkler AS, Winkelman J, de Carvalho M, Thal DR, Otto M, Brännström T, Volk AE, Kursula P, Danzer KM, Lichtner P, Dikic I, Meitinger T, Ludolph AC, Strom TM, Andersen PM, Weishaupt JH (2015). Haploinsufficiency of TBK1 causes familial ALS and fronto-temporal dementia. Nat Neurosci. 18(5):631-636

Frisardi V, Panza F, Seripa D, Farooqui T, Farooqui AA (2011). Glycerophospholipids and glycerophospholipid-derived lipid mediators: a complex meshwork in Alzheimer's disease pathology. Prog Lipid Res. 50(4):313-330

Fumagalli F, Noack J, Bergmann TJ, Cebollero E, Pisoni GB, Fasana E, Fregno I, Galli C, Loi M, Soldà T, D'Antuono R, Raimondi A, Jung M, Melnyk A, Schorr S, Schreiber A, Simonelli L, Varani L, Wilson-Zbinden C, Zerbe O, Hofmann K, Peter M, Quadroni M, Zimmermann R, Molinari M (2016). Translocon component Sec62 acts in endoplasmic reticulum turnover during stress recovery. Nat Cell Biol. 18(11):1173-1184

Gabbouj S, Ryhänen S, Marttinen M, Wittrahm R, Takalo M, Kemppainen S, Martiskainen H, Tanila H, Haapasalo A, Hiltunen M, Natunen T (2019). Altered Insulin Signaling in Alzheimer's Disease Brain - Special Emphasis on PI3K-Akt Pathway. Front Neurosci. 13:629

Gaitonde MK, Evison E, Evans GM (1983). The rate of utilization of glucose via hexose monophosphate shunt in brain. J Neurochem. 41:1253–1260

Gaitonde MK, Richter D (1966). Changes with age in the utilization of glucose carbon in liver and brain. J Neurochem. 13:1309–1316

Galliano E, Potters JW, Elgersma Y, Wisden W, Kushner SA, De Zeeuw CI, Hoebeek FE (2013). Synaptic transmission and plasticity at inputs to murine cerebellar Purkinje cells are largely dispensable for standard nonmotor tasks. J Neurosci. 33(31):12599-12618

Galluzzi L, Baehrecke EH, Ballabio A, Boya P, Bravo-San Pedro JM, Cecconi F, Choi AM, Chu CT, Codogno P, Colombo MI, Cuervo AM, Debnath J, Deretic V, Dikic I, Eskelinen EL, Fimia GM, Fulda S, Gewirtz DA, Green DR, Hansen M, Harper JW, Jäättelä M, Johansen T, Juhasz G, Kimmelman AC, Kraft C, Ktistakis NT, Kumar S, Levine B, Lopez-Otin C, Madeo F, Martens S, Martinez J, Melendez A, Mizushima N, Münz C, Murphy LO, Penninger JM, Piacentini M, Reggiori F, Rubinsztein DC, Ryan KM, Santambrogio L, Scorrano L, Simon AK, Simon HU, Simonsen A, Tavernarakis N, Tooze SA, Yoshimori T, Yuan J, Yue Z, Zhong Q, Kroemer G (2017). Molecular definitions of autophagy and related processes. EMBO J. 36(13):1811-1836

Ganguly A, McKnight RA, Raychaudhuri S, Shin BC, Ma Z, Moley K, Devaskar SU (2007). Glucose transporter isoform-3 mutations cause early pregnancy loss and fetal growth restriction. Am J Physiol Endocrinol Metab. 292(5):E1241-1255

Garcia M, Millan C, Balmaceda-Aguilera C, Castro T, Pastor P, Montecinos H, Reinicke K, Zuniga F, Vera JC, Onate SA, Nualart F (2003). Hypothalamic ependymal-glial cells express the glucose transporter GLUT2, a protein involved in glucose sensing. J Neurochem. 86:709–724

Garcia MA, Carrasco M, Godoy A, Reinicke K, Montecinos VP, Aguayo LG, Tapia JC, Vera JC, Nualart F (2001). Elevated expression of glucose transporter-1 in hypothalamic ependymal cells not involved in the formation of the brain-cerebrospinal fluid barrier. J Cell Biochem. 80:491–503

Garg M, Kulkarni SD, Shah KN, Hegde AU (2017). Diabetes Mellitus as the Presenting Feature of Friedreich's Ataxia. J Neurosci Rural Pract. 8(Suppl 1):S117-S119

Gaulton KJ, Willer CJ, Li Y, Scott LJ, Conneely KN, Jackson AU, Duren WL, Chines PS, Narisu N, Bonnycastle LL, Luo J, Tong M, Sprau AG, Pugh EW, Doheny KF, Valle TT, Abecasis GR, Tuomilehto J, Bergman RN, Collins FS, Boehnke M, Mohlke KL (2008). Comprehensive association study of type 2 diabetes and related quantitative traits with 222 candidate genes. Diabetes. 57(11):3136-3144

Ge SX, Jung D, Yao R (2020). ShinyGO: a graphical gene-set enrichment tool for animals and plants. Bioinformatics 36(8):2628-2629

Geng J, Yuan X, Wei M, Wu J, Qin ZH (2018). The diverse role of TIGAR in cellular homeostasis and cancer. Free Radic Res. 52: 1240-1249

Gerhart DZ, Broderius MA, Borson ND, Drewes LR (1992). Neurons and microvessels express the brain glucose transporter protein GLUT3. Proc Natl Acad Sci U S A. 89:733–737

Giacomello M, Pyakurel A, Glytsou C, Scorrano L (2020). The cell biology of mitochondrial membrane dynamics. Nat Rev Mol Cell Biol. 21(4):204-224

Godoy JA, Rios JA, Zolezzi JM, Braidy N, Inestrosa NC (2014). Signaling pathway cross talk in Alzheimer's disease. Cell Commun Signal. 12:23

Goldberg MS, Fleming SM, Palacino JJ, Cepeda C, Lam HA, Bhatnagar A, Meloni EG, Wu N, Ackerson LC, Klapstein GJ, Gajendiran M, Roth BL, Chesselet MF, Maidment NT, Levine MS, Shen J (2003). Parkin-deficient mice exhibit nigrostriatal deficits but not loss of dopaminergic neurons. J Biol Chem. 278(44):43628-43635

Gordon BA, Blazey TM, Su Y, Hari-Raj A, Dincer A, Flores S, Christensen J, McDade E, Wang G, Xiong C, Cairns NJ, Hassenstab J, Marcus DS, Fagan AM, Jack CR Jr, Hornbeck RC, Paumier KL, Ances BM, Berman SB, Brickman AM, Cash DM, Chhatwal JP, Correia S, Förster S, Fox NC, Graff-Radford NR, la Fougère C, Levin J, Masters CL, Rossor MN, Salloway S, Saykin AJ, Schofield PR, Thompson PM, Weiner MM, Holtzman DM, Raichle ME, Morris JC, Bateman RJ, Benzinger TLS (2018). Spatial patterns of neuroimaging biomarker change in individuals from families with autosomal dominant Alzheimer's disease: a longitudinal study. Lancet Neurol. 17(3):241-250

Gordon PB, Seglen PO (1988). Prelysosomal convergence of autophagic and endocytic pathways. Biochem Biophys Res Commun. 151:40–47

Goyal M, Singh S, Sibinga EM, Gould NF, Rowland-Seymour A, Sharma R, Berger Z, Sleicher D, Maron DD, Shihab HM, Ranasinghe PD, Linn S, Saha S, Bass EB, Haythornthwaite JA (2014). Meditation programs for psychological stress and well-being: a systematic review and meta-analysis. JAMA Intern Med. 174(3):357-368

Grillo CA, Piroli GG, Hendry RM, Reagan LP (2009). Insulin-stimulated translocation of GLUT4 to the plasma membrane in rat hippocampus is PI3-kinase dependent. Brain Res. 1296:35–45

Grosse F, Rueckriegel SM, Thomale UW, Hernáiz Driever P (2021). Mapping of long-term cognitive and motor deficits in pediatric cerebellar brain tumor survivors into a cerebellar white matter atlas. Childs Nerv Syst. 37(9):2787-2797

Grumati P, Dikic I, Stolz A (2018). ER-phagy at a glance. J Cell Sci. 131(17):jcs217364

Grumati P, Morozzi G, Hölper S, Mari M, Harwardt MI, Yan R, Müller S, Reggiori F, Heilemann M, Dikic I (2017). Full length RTN3 regulates turnover of tubular endoplasmic reticulum via selective autophagy. Elife. 6:e25555

Guardia CM, Farías GG, Jia R, Pu J, Bonifacino JS (2016). BORC Functions Upstream of Kinesins 1 and 3 to Coordinate Regional Movement of Lysosomes along Different Microtubule Tracks. Cell Rep. 17(8):1950-1961

Gubas A, Dikic I (2022). A guide to the regulation of selective autophagy receptors. FEBS J. 289(1):75-89

Guell X, Gabrieli JDE, Schmahmann JD (2018). Triple representation of language, working memory, social and emotion processing in the cerebellum: convergent evidence from task and seed-based resting-state fMRI analyses in a single large cohort. Neuroimage. 172:437–449

Guichardant M, Chen P, Liu M, Calzada C, Colas R, Véricel E, Lagarde M (2011). Functional lipidomics of oxidized products from polyunsaturated fatty acids. Chem Phys Lipids. 164(6):544-8

Guillemain G, Loizeau M, Pinçon-Raymond M, Girard J, Leturque A (2000). The large intracytoplasmic loop of the glucose transporter GLUT2 is involved in glucose signaling in hepatic cells. J Cell Sci. 113(Pt 5):841–847

Gwinn DM, Shackelford DB, Egan DF, Mihaylova MM, Mery A, Vasquez DS, Turk BE, Shaw RJ (2008). AMPK phosphorylation of raptor mediates a metabolic checkpoint. Mol Cell. 30(2):214-226

Hamasaki M, Furuta N, Matsuda A, Nezu A, Yamamoto A, Fujita N, Oomori H, Noda T, Haraguchi T, Hiraoka Y, Amano A, Yoshimori T (2013). Autophagosomes form at ER-mitochondria contact sites. Nature. 495(7441):389-393

Hambright WS, Fonseca RS, Chen L, Na R, Ran Q (2017). Ablation of ferroptosis regulator glutathione peroxidase 4 in forebrain neurons promotes cognitive impairment and neurodegeneration. Redox Biol. 12:8-17

Hanada T, Noda NN, Satomi Y, Ichimura Y, Fujioka Y, Takao T, Inagaki F, Ohsumi Y (2007). The Atg12-Atg5 conjugate has a novel E3-like activity for protein lipidation in autophagy. J Biol Chem. 282(52):37298-37302.

Hara T, Nakamura K, Matsui M, Yamamoto A, Nakahara Y, Suzuki-Migishima R, Yokoyama M, Mishima K, Saito I, Okano H, Mizushima N (2006). Suppression of basal autophagy in neural cells causes neurodegenerative disease in mice. Nature. 441(7095):885-889

Harris JJ, Jolivet R, Attwell D (2012). Synaptic energy use and supply. Neuron. 75:762–777

Harris JJ, Jolivet R, Attwell D (2021). Synaptic energy use and supply. Neuron. 75(5):762-777

Hay N (2016). Reprogramming glucose metabolism in cancer: can it be exploited for cancer therapy? Nat Rev Cancer. 16:635–649

Heo JM, Ordureau A, Paulo JA, Rinehart J, Harper JW (2015). The PINK1-PARKIN Mitochondrial Ubiquitylation Pathway Drives a Program of OPTN/NDP52 Recruitment and TBK1 Activation to Promote Mitophagy. Mol Cell. 60(1):7-20

Hernandez D, Torres CA, Setlik W, Cebrián C, Mosharov EV, Tang G, Cheng HC, Kholodilov N, Yarygina O, Burke RE, Gershon M, Sulzer D (2012). Regulation of presynaptic neurotransmission by macroautophagy. Neuron. 74(2):277-284

Hernández-Pérez C, Weruaga E, Díaz D (2023) Lobe X of the Cerebellum: A Natural Neuro-Resistant Region. Anatomia. 2(1):43-62

Herrero-Mendez A, Almeida A, Fernández E, Maestre C, Moncada S, Bolaños JP (2009). The bioenergetic and antioxidant status of neurons is controlled by continuous degradation of a key glycolytic enzyme by APC/C-Cdh1. Nat Cell Biol. 11:747–752

Hoshi E, Tremblay L, Féger J, Carras PL, Strick PL (2005). The cerebellum communicates with the basal ganglia. Nat Neurosci. 8(11):1491-1493

Hosokawa N, Hara T, Kaizuka T, Kishi C, Takamura A, Miura Y, Iemura S, Natsume T, Takehana K, Yamada N, Guan JL, Oshiro N, Mizushima N (2009). Nutrient-dependent mTORC1 association with the ULK1-Atg13-FIP200 complex required for autophagy. Mol Biol Cell. 20(7):1981-1991

Hou L, Sun F, Huang R, Sun W, Zhang D, Wang Q (2019). Inhibition of NADPH oxidase by apocynin prevents learning and memory deficits in a mouse Parkinson's disease model. Redox Biol. 22:101134

Hou WK, Xian YX, Zhang L, Lai H, Hou XG, Xu YX, Yu T, Xu FY, Song J, Fu CL, Zhang WW, Chen L (2007). Influence of blood glucose on the expression of glucose trans-porter proteins 1 and 3 in the brain of diabetic rats. Chin Med J (Engl). 120(19):1704-1709

Hoyer S (1982). The abnormally aged brain. Its blood flow and oxidative metabolism. A review-part II. Arch Gerontol Geriatr. 1:195–207

Hu Z, Yang B, Mo X, Xiao H (2015). Mechanism and Regulation of Autophagy and Its Role in Neuronal Diseases. Mol Neurobiol. 52(3):1190-1209

Huang S, Czech MP (2007). The GLUT4 glucose transporter. Cell Metab. 5:237–252

Hyder F, Patel AB, Gjedde A, Rothman DL, Behar KL, Shulman RG (2006). Neuronal-glial glucose oxidation and glutamatergic-GABAergic function. J Cereb Blood Flow Metab. 26(7):865-877

Hyder F, Rothman DL, Bennett MR (2013). Cortical energy demands of signaling and nonsignaling components in brain are conserved across mammalian species and activity levels. Proc Natl Acad Sci U S A. 110(9):3549-3554

Ilg W, Christensen A, Mueller OM, Goericke SL, Giese MA, Timmann D (2013) Effects of cerebellar lesions on working memory interacting with motor tasks of different complexities. J Neurophysiol 110:2337–2349

Ilg W, Golla H, Thier P, Giese MA (2007). Specific influences of cerebellar dysfunctions on gait. Brain. 130(Pt 3):786-98

Igl W, Johansson A, Wilson JF, Wild SH, Polasek O, Hayward C, Vitart V, Hastie N, Rudan P, Gnewuch C, Schmitz G, Meitinger T, Pramstaller PP, Hicks AA, Oostra BA, van Duijn CM, Rudan I, Wright A, Campbell H, Gyllensten U; EUROSPAN Consortium (2010). Modeling of environmental effects in genome-wide association studies identifies SLC2A2 and HP as novel loci influencing serum cholesterol levels. PLoS Genet. 6:e1000798

Ilg W, Timmann D (2013) Gait ataxia–specific cerebellar influences and their rehabilitation. Mov Disord. 28:1566–1575

Inoki K, Ouyang H, Zhu T, Lindvall C, Wang Y, Zhang X, Yang Q, Bennett C, Harada Y, Stankunas K, Wang CY, He X, MacDougald OA, You M, Williams BO, Guan KL (2006). TSC2 integrates Wnt and energy signals via a coordinated phosphorylation by AMPK and GSK3 to regulate cell growth. Cell. 126(5):955-968

Ito M (1984). The Cerebellum and Neural Control. New York, NY: Raven Press

Itier JM, Ibanez P, Mena MA, Abbas N, Cohen-Salmon C, Bohme GA, Laville M, Pratt J, Corti O, Pradier L, Ret G, Joubert C, Periquet M, Araujo F, Negroni J, Casarejos MJ, Canals S, Solano R, Serrano A, Gallego E, Sanchez M, Denefle P, Benavides J, Tremp G, Rooney TA, Brice A, Garcia de Yebenes J (2003). Parkin gene inactivation alters behaviour and dopamine neurotransmission in the mouse. Hum Mol Genet. 12(18):2277-22791

Jaeger PA, Wyss-Coray T (2010). Beclin 1 complex in autophagy and Alzheimer disease. Arch Neurol. 67(10):1181-4

Ji CH, Kim HY, Heo AJ, Lee SH, Lee MJ, Kim SB, Srinivasrao G, Mun SR, Cha-Molstad H, Ciechanover A, Choi CY, Lee HG, Kim BY, Kwon YT (2019). The N-Degron Pathway Mediates ER-phagy. Mol Cell. 75(5):1058-1072.e9

Jia R, Guardia CM, Pu J, Chen Y, Bonifacino JS (2017). BORC coordinates encounter and fusion of lysosomes with autophagosomes. Autophagy. 13(10):1648-1663

Jiao L, Zhang HL, Li DD, Yang KL, Tang J, Li X, Ji J, Yu Y, Wu RY, Ravichandran S, Liu JJ, Feng GK, Chen MS, Zeng YX, Deng R, Zhu XF (2018). Regulation of glycolytic metabolism by autophagy in liver cancer involves selective autophagic degradation of HK2 (hexokinase 2). Autophagy 14(4):671-684

Jin SM, Lazarou M, Wang C, Kane LA, Narendra DP, Youle RJ (2010). Mitochondrial membrane potential regulates PINK1 import and proteolytic destabilization by PARL. J Cell Biol. 191(5):933-942

Jo C, Gundemir S, Pritchard S, Jin YN, Rahman I, Johnson GV (2014). Nrf2 reduces levels of phosphorylated tau protein by inducing autophagy adaptor protein NDP52. Nat Commun. 5:3496

Johansen T, Lamark T (2020). Selective Autophagy: ATG8 Family Proteins, LIR Motifs and Cargo Receptors. J Mol Biol. 432(1):80-103

Jones JP, Nicholas HJ, Ramsey RB (1975). Rate of sterol formation by rat brain glia and neurons in vitro and in vivo. J Neurochem. 24:12312–12316

Jovanović MD, Jelenković A, Stevanović ID, Bokonjić D, Colić M, Petronijević N, Stanimirović DB (2014). Protective effects of glucose-6-phosphate dehydrogenase on neurotoxicity of aluminium applied into the CA1 sector of rat hippocampus. Indian J Med Res. 139(6):864-72.

Jung CH, Jun CB, Ro SH, Kim YM, Otto NM, Cao J, Kundu M, Kim DH (2009). ULK-Atg13-FIP200 complexes mediate mTOR signaling to the autophagy machinery. Mol Biol Cell. 20(7):1992-2003

Kallergi E, Siva Sankar D, Matera A, Kolaxi A, Paolicelli RC, Dengjel J, Nikoletopoulou V (2023). Profiling of purified autophagic vesicle degradome in the maturing and aging brain. Neuron. 111(15):2329-2347.e7

Kang HC, Lee YM, Kim HD, Lee JS, Slama A (2007). Safe and effective use of the ketogenic diet in children with epilepsy and mitochondrial respiratory chain complex defects. Epilepsia. 48(1):82–8

Kang L, Routh VH, Kuzhikandathil EV, Gaspers LD, Levin BE (2004). Physiological and molecular characteristics of rat hypothalamic ventromedial nucleus glucosensing neurons. Diabetes. 53(3):549-559

Karanasios E, Stapleton E, Manifava M, Kaizuka T, Mizushima N, Walker SA, Ktistakis NT (2013). Dynamic association of the ULK1 complex with omegasomes during autophagy induction. J Cell Sci. 126(Pt 22):5224-5238

Kashiwabuchi N, Ikeda K, Araki K, Hirano T, Shibuki K, Takayama C, Inoue Y, Kutsuwada T, Yagi T, Kang Y (1995). Impairment of motor coordination, Purkinje cell synapse formation, and cerebellar long-term depression in GluR delta 2 mutant mice. Cell. 81:245–52

Kashiwaya Y, Bergman C, Lee JH, Wan R, King MT, Mughal MR, Okun E, Clarke K, Mattson MP, Veech RL (2013) A ketone ester diet exhibits anxiolytic and cognition-sparing properties, and lessens amyloid and tau pathologies in a mouse model of Alzheimer's disease. Neurobiol Aging. 34:1530–1539

Kaur D, Yantiri F, Rajagopalan S, Kumar J, Mo JQ, Boonplueang R, Viswanath V, Jacobs R, Yang L, Beal MF, DiMonte D, Volitaskis I, Ellerby L, Cherny RA, Bush AI, Andersen JK (2003). Genetic or pharmacological iron chelation prevents MPTP-induced neurotoxicity in vivo: a novel therapy for Parkinson's disease. Neuron. 37:899–909

Kaushik S, Cuervo AM (2016). AMPK-dependent phosphorylation of lipid droplet protein PLIN2 triggers its degradation by CMA. Autophagy. 12(2):432-438

Keeney JT, Ibrahimi S, Zhao L (2015). Human ApoE Isoforms Differentially Modulate Glucose and Amyloid Metabolic Pathways in Female Brain: Evidence of the Mechanism of Neuroprotection by ApoE2 and Implications for Alzheimer's Disease Prevention and Early Intervention. J Alzheimers Dis. 48(2):411-424

Khaminets A, Heinrich T, Mari M, Grumati P, Huebner AK, Akutsu M, Liebmann L, Stolz A, Nietzsche S, Koch N, Mauthe M, Katona I, Qualmann B, Weis J, Reggiori F, Kurth I, Hübner CA, Dikic I (2015). Regulation of endoplasmic reticulum turnover by selective autophagy. Nature. 522(7556):354-8

Kilpeläinen TO, Lakka TA, Laaksonen DE, Laukkanen O, Lindström J, Eriksson JG, Valle TT, Hämäläinen H, Aunola S, Ilanne-Parikka P, Keinänen-Kiukaanniemi S, Tuomilehto J, Uusitupa M, Laakso M; Finnish Diabetes Prevention Study Group (2007). Physical activity modifies the effect of SNPs in the SLC2A2 (GLUT2) and ABCC8 (SUR1) genes on the risk of developing type 2 diabetes. Physiol Genomics. 31:264–272

Kim M, Sandford E, Gatica D, Qiu Y, Liu X, Zheng Y, Schulman BA, Xu J, Semple I, Ro SH, Kim B, Mavioglu RN, Tolun A, Jipa A, Takats S, Karpati M, Li JZ, Yapici Z, Juhasz G, Lee JH, Klionsky DJ, Burmeister M (2016). Mutation in ATG5 reduces autophagy and leads to ataxia with developmental delay. Elife. 5:e12245

Kimmelman AC, White E (2017). Autophagy and tumor metabolism. Cell Metab. 25(5):1037–1043

King M, Hernandez-Castillo CR, Poldrack RA, Ivry RB, Diedrichsen J (2019). Functional boundaries in the human cerebellum revealed by a multi-domain task battery. Nat Neurosci. 22:1371–1378

Kingwell K (2013). Genetics: Mutations in autophagy gene cause a rare and severe neurodegenerative disease. Nat Rev Neurol. 9(4):182

Kirkin V, Rogov VV (2019). A Diversity of Selective Autophagy Receptors Determines the Specificity of the Autophagy Pathway. Mol Cell. 76(2):268-285

Kitada T, Asakawa S, Hattori N, Matsumine H, Yamamura Y, Minoshima S, Yokochi M, Mizuno Y, Shimizu N (1998). Mutations in the parkin gene cause autosomal recessive juvenile parkinsonism. Nature. 392(6676):605-608

Kitada T, Asakawa S, Hattori N, Matsumine H, Yamamura Y, Minoshima S, Yokochi M, Mizuno Y, Shimizu N (1998). Mutations in the parkin gene cause autosomal recessive juvenile parkinsonism. Nature. 392(6676):605-608

Kleinridders A, Ferris HA, Reyzer ML, Rath M, Soto M, Manier ML, Spraggins J, Yang Z, Stanton RC, Caprioli RM, Kahn CR (2018). Regional differences in brain glucose metabolism determined by imaging mass spectrometry. Mol Metab. 12:113-121

Kletzien RF, Harris PK, Foellmi LA (1994). Glucose-6-phosphate dehydrogenase: a “housekeeping” enzyme subject to tissue-specific regulation by hormones, nutrients, and oxidant stress. FASEB J. 8:174-181

Klockgether T, Mariotti C, Paulson HL (2019). Spinocerebellar ataxia. Nat Rev Dis Primers. 5(1):24

Kobayashi M, Nikami H, Morimatsu M, Saito M (1996). Expression and localization of insulin-regulatable glucose transporter (GLUT4) in rat brain. Neurosci Lett. 213:103–106

Kocaturk NM, Akkoc Y, Kig C, Bayraktar O, Gozuacik D, Kutlu O (2019). Autophagy as a molecular target for cancer treatment. Eur J Pharm Sci.134:116–137

Koike M, Shibata M, Sunabori T, Yamaguchi J, Sakimura K, Komatsu M, Tanaka K, Uchiyama Y (2017). Purkinje Cells Are More Vulnerable to the Specific Depletion of Cathepsin D Than to That of Atg7. The American Journal of Pathology 187 (7):1586-1600

Komatsu M, Waguri S, Chiba T, Murata S, Iwata J, Tanida I, Ueno T, Koike M, Uchiyama Y, Kominami E, Tanaka K (2006). Loss of autophagy in the central nervous system causes neurodegeneration in mice. Nature. 441(7095):880-884

Komatsu M, Waguri S, Koike M, Sou YS, Ueno T, Hara T, Mizushima N, Iwata J, Ezaki J, Murata S, Hamazaki J, Nishito Y, Iemura S, Natsume T, Yanagawa T, Uwayama J, Warabi E, Yoshida H, Ishii T, Kobayashi A, Yamamoto M, Yue Z, Uchiyama Y, Kominami E, Tanaka K (2007a). Homeostatic levels of p62 control cytoplasmic inclusion body formation in autophagy-deficient mice. Cell. 131(6):1149-1163

Komatsu M, Waguri S, Ueno T, Iwata J, Murata S, Tanida I, Ezaki J, Mizushima N, Ohsumi Y, Uchiyama Y, Kominami E, Tanaka K, Chiba T (2005). Impairment of starvation-induced and constitutive autophagy in Atg7-deficient mice. J Cell Biol. 169(3):425-34

Komatsu M, Wang QJ, Holstein GR, Friedrich VL Jr, Iwata J, Kominami E, Chait BT, Tanaka K, Yue Z (2007b). Essential role for autophagy protein Atg7 in the maintenance of axonal homeostasis and the prevention of axonal degeneration. Proc Natl Acad Sci U S A. 2007 Sep 4;104(36):14489-14494

Kondapalli C, Kazlauskaite A, Zhang N, Woodroof HI, Campbell DG, Gourlay R, Burchell L, Walden H, Macartney TJ, Deak M, Knebel A, Alessi DR, Muqit MM (2012). PINK1 is activated by mitochondrial membrane potential depolarization and stimulates Parkin E3 ligase activity by phosphorylating Serine 65. Open Biol. 2(5):120080

Kong MF, Glibert G, Baleanu F, Karmali R (2014). Progressive cerebellar ataxia and new-onset diabetes. Lancet. 383(9912):186

Koppenol WH, Bounds PL, Dang CV (2011). Otto Warburg's contributions to current concepts of cancer metabolism. Nat Rev Cancer. 11:325–337

Kossoff EH, Hartman AL (2012). Ketogenic diets: new advances for metabolism-based therapies. Curr Opin Neurol. 25(2):173–8

Kraus F, Roy K, Pucadyil TJ, Ryan MT (2021). Function and regulation of the divisome for mitochondrial fission. Nature. 590(7844):57-66

Kuhl DE, Markham CH, Metter EJ, Riege WH, Phelps ME, Mazziotta JC (1985). Local cerebral glucose utilization in symptomatic and presymptomatic Huntington's disease. Res Publ Assoc Res Nerv Ment Dis. 63:199-209

Kuhl DE, Metter EJ, Riege WH, Hawkins RA (1984). The effect of normal aging on patterns of local cerebral glucose utilization. Ann Neurol. 15(Suppl):S133–S137

Kulkarni A, Chen J, Maday S (2018). Neuronal autophagy and intercellular regulation of homeostasis in the brain. Curr Opin Neurobiol. 51:29-36

Kullmann S, Kleinridders A, Small DM, Fritsche A, Häring HU, Preissl H, Heni M (2020). Central nervous pathways of insulin action in the control of metabolism and food intake. Lancet Diabetes Endocrinol. 8(6):524-534

Kuma A, Hatano M, Matsui M, Yamamoto A, Nakaya H, Yoshimori T, Ohsumi Y, Tokuhisa T, Mizushima N (2004). The role of autophagy during the early neonatal starvation period. Nature 432(7020):1032-1036

Küper M, Doring K, Spangenberg C, Konczak J, Gizewski ER, Schoch B, Timmann D (2013) Location and restoration of function after cerebellar tumor removal-a longitudinal study of children and adolescents. Cerebellum 12:48–58

Kwon SK, Sando R 3rd, Lewis TL, Hirabayashi Y, Maximov A, Polleux F (2016). LKB1 Regulates Mitochondria-Dependent Presynaptic Calcium Clearance and Neurotransmitter Release Properties at Excitatory Synapses along Cortical Axons. PLoS Biol. 14(7):e1002516

La Spada AR, Taylor JP (2010). Repeat expansion disease: progress and puzzles in disease pathogenesis. Nat Rev Genet. 11(4):247-258

Lamark T, Johansen T (2012). Aggrephagy: selective disposal of protein aggregates by macroautophagy. Int J Cell Biol. 2012:736905

Lamb CA, Yoshimori T, Tooze SA (2013). The autophagosome: origins unknown, biogenesis complex. Nat Rev Mol Cell Biol. 14(12):759-74

Langemeyer L, Ungermann C (2015). BORC and BLOC-1: Shared subunits in trafficking complexes. Dev Cell. 33(2):121-122

Lannoo MJ, Brochu G, Maler L, Hawkes R (1991). Zebrin II immunoreactivity in the rat and in the weakly electric teleost Eigenmannia (gymnotiformes) reveals three modes of Purkinje cell development. J Comp Neurol. 310(2):215-33

Lazarou M, Sliter DA, Kane LA, Sarraf SA, Wang C, Burman JL, Sideris DP, Fogel AI, Youle RJ (2015). The ubiquitin kinase PINK1 recruits autophagy receptors to induce mitophagy. Nature. ;524(7565):309-314

Le Y, Zhang Z, Wang C, Lu D (2021). Ferroptotic Cell Death: New Regulatory Mechanisms for Metabolic Diseases. Endocr Metab Immune Disord Drug Targets. 21(5):785-800

Le Douce J, Maugard M, Veran J, Matos M, Jégo P, Vigneron PA, Faivre E, Toussay X, Vandenberghe M, Balbastre Y, Piquet J, Guiot E, Tran NT, Taverna M, Marinesco S, Koyanagi A, Furuya S, Gaudin-Guérif M, Goutal S, Ghettas A, Pruvost A, Bemelmans AP, Gaillard MC, Cambon K, Stimmer L, Sazdovitch V, Duyckaerts C, Knott G, Hérard AS, Delzescaux T, Hantraye P, Brouillet E, Cauli B, Oliet SHR, Panatier A, Bonvento G (2020). Impairment of Glycolysis-Derived l-Serine Production in Astrocytes Contributes to Cognitive Deficits in Alzheimer's Disease. Cell Metab. 31(3):503-517.e8

Lee DH, Chung MY, Lee JU, Kang DG, Paek YW (2000). Changes of glucose transporters in the cerebral adaptation to hypoglycemia. Diabetes Res Clin Pract. 47(1):15-23

Leloup C, Arluison M, Kassis N, Lepetit N, Cartier N, Ferre P, Penicaud L (1996). Discrete brain areas express the insulin-responsive glucose transporter GLUT4. Brain Res Mol Brain Res. 38:45–53

Leloup C, Arluison M, Lepetit N, Cartier N, Marfaing-Jallat P, Ferre P, Penicaud L (1994). Glucose transporter 2 (GLUT2): expression in specific brain nuclei. Brain Res. 638:221–226

Leloup C, Orosco M, Serradas P, Nicolaidis S, Penicaud L (1998). Specific inhibition of GLUT2 in arcuate nucleus by antisense oligonucleotides suppresses nervous control of insulin secretion. Brain Res Mol Brain Res. 57:275–280

Lewis TL Jr, Turi GF, Kwon SK, Losonczy A, Polleux F (2016). Progressive Decrease of Mitochondrial Motility during Maturation of Cortical Axons In Vitro and In Vivo. Curr Biol. 26(19):2602-2608

Li H, Guglielmetti C, Sei YJ, Zilberter M, Le Page LM, Shields L, Yang J, Nguyen K, Tiret B, Gao X, Bennett N, Lo I, Dayton TL, Kampmann M, Huang Y, Rathmell JC, Vander Heiden M, Chaumeil MM, Nakamura K (2023). Neurons require glucose uptake and glycolysis in vivo. Cell Rep. 42(4):112335

Li M, Sun M, Cao L, Gu JH, Ge J, Chen J, Han R, Qin YY, Zhou ZP, Ding Y, Qin ZH (2014). A TIGAR-regulated metabolic pathway is critical for protection of brain ischemia. J Neurosci. 34(22):7458-71

Li S, Zhang M, Ge L (2021). A new type of membrane contact in the ER-Golgi system regulates autophagosome biogenesis. Autophagy. 17(12):4499-4501

Li X, Yu W, Qian X, Xia Y, Zheng Y, Lee JH, Li W, Lyu J, Rao G, Zhang X, Qian CN, Rozen SG, Jiang T, Lu Z (2017). Nucleus-Translocated ACSS2 Promotes Gene Transcription for Lysosomal Biogenesis and Autophagy. Mol Cell. 66(5):684-697.e9

Li Z, Okamoto K, Hayashi Y, Sheng M (2004). The importance of dendritic mitochondria in the morphogenesis and plasticity of spines and synapses. Cell. 119(6):873-887

Liang Y, Sigrist S (2018). Autophagy and proteostasis in the control of synapse aging and disease. Curr Opin Neurobiol. 48:113-121

Lieberman OJ, Frier MD, McGuirt AF, Griffey CJ, Rafikian E, Yang M, Yamamoto A, Borgkvist A, Santini E, Sulzer D (2020). Cell-type-specific regulation of neuronal intrinsic excitability by macroautophagy. Elife. 9:e50843

Lin W, Wang C, Liu G, Bi C, Wang X, Zhou Q, Jin H (2020). SLC7A11/xCT in cancer: biological functions and therapeutic implications. Am J Cancer Res. 10(10):3106-3126

Liu CC, Hu J, Tsai CW, Yue M, Melrose HL, Kanekiyo T, Bu G (2015). Neuronal LRP1 regulates glucose metabolism and insulin signaling in the brain. J Neurosci. 35(14):5851-5859

Liu D, Pitta M, Jiang H, Lee JH, Zhang G, Chen X, Kawamoto EM, Mattson MP (2013) Nicotonamide forestalls pathology and cognitive decline in Alzheimer mice: evidence for improved neuronal bioenergetics and autophagy procession. Neurobiol Aging. 34:1564–1580

Locasale JW, Cantley LC (2011). Metabolic flux and the regulation of mammalian cell growth. Cell Metab. 14:443–451

Lowry OH, Passonneau JV (1964). The relationships between substrates and enzymes of glycolysis in brain. J Biol Chem. 239:31–42

Luft AR, Skalej M, Schulz JB, Welte D, Kolb R, Bürk K, Klockgether T, Voight K (1999). Patterns of age-related shrinkage in cerebellum and brainstem observed in vivo using three-dimensional MRI volumetry. Cereb. Cortex, 9:712-721

Lunt SY, Vander Heiden MG (2011). Aerobic glycolysis: meeting the metabolic requirements of cell proliferation. Annu Rev Cell Dev Biol. 27:441–464

Lupoli F, Vannocci T, Longo G, Niccolai N, Pastore A (2018). The role of oxidative stress in Friedreich's ataxia. FEBS Lett. 592(5):718-727

Ma T, Tzavaras N, Tsokas P, Landau EM, Blitzer RD (2011). Synaptic stimulation of mTOR is mediated by Wnt signaling and regulation of glycogen synthetase kinase-3. J Neurosci. 31(48):17537-17546

Magistretti PJ, Sorg O, Yu N, Martin JL, Pellerin L (1993). Neurotransmitters regulate energy metabolism in astrocytes: implications for the metabolic trafficking between neural cells. Dev Neurosci. 15:306–312

Maher F, Vannucci SJ, Simpson IA (1994). Glucose transporter proteins in brain. FASEB J. 8:1003–1011.

Majeski AE, Dice JF (2004). Mechanisms of chaperone-mediated autophagy. Int J Biochem Cell Biol. 36(12):2435-2444

Manto M, Bower JM, Conforto AB, Delgado-García JM, da Guarda SN, Gerwig M, Habas C, Hagura N, Ivry RB, Mariën P, Molinari M, Naito E, Nowak DA, Oulad Ben Taib N, Pelisson D, Tesche CD, Tilikete C, Timmann D (2012). Consensus paper: roles of the cerebellum in motor control--the diversity of ideas on cerebellar involvement in movement. Cerebellum. 11(2):457-87.

Marín-Juez R, Rovira M, Crespo D, van der Vaart M, Spaink HP, Planas JV (2015). GLUT2-mediated glucose uptake and availability are required for embryonic brain development in zebrafish. J Cereb Blood Flow Metab. 35(1):74-85

Martínez-Reyes I, Chandel NS (2020). Mitochondrial TCA cycle metabolites control physiology and disease. Nat Commun. 11(1):102

Martinez-Vicente M, Talloczy Z, Wong E, Tang G, Koga H, Kaushik S, de Vries R, Arias E, Harris S, Sulzer D, Cuervo AM (2010). Cargo recognition failure is responsible for inefficient autophagy in Huntington's disease. Nat Neurosci. 13(5):567-76

Marty N, Dallaporta M, Foretz M, Emery M, Tarussio D, Bady I, Binnert C, Beermann F, Thorens B (2005). Regulation of glucagon secretion by glucose transporter type 2 (glut2) and astrocyte-dependent glucose sensors. J Clin Invest. 115(12):3545-3553

Marty N, Dallaporta M, Thorens B (2007). Brain glucose sensing, counterregulation, and energy homeostasis. Physiology (Bethesda). 22:241–251

Maruyama H, Kawakami H (2013). Optineurin and amyotrophic lateral sclerosis. Geriatr Gerontol Int. 13(3):528-532

Masaldan S., Bush A. I., Devos D., Rolland A. S., Moreau C. (2019). Striking while the iron is hot: Iron metabolism and ferroptosis in neurodegeneration. Free Radic. Biol. Med. 133, 221–233

Mauthe M, Orhon I, Rocchi C, Zhou X, Luhr M, Hijlkema KJ, Coppes RP, Engedal N, Mari M, Reggiori F (2018). Chloroquine inhibits autophagic flux by decreasing autophagosome-lysosome fusion. Autophagy 14(8):1435-1455

Mazurek S, Grimm H, Boschek CB, Vaupel P, Eigenbrodt E (2002). Pyruvate kinase type M2: a crossroad in the tumor metabolome. Brit J Nutrition. 87:S23–S29

McBride HM, Neuspiel M, Wasiak S (2006) Mitochondria: more than just a powerhouse. Curr Biol 16(14):R551–R560

McCall AL, Van Bueren AM, Moholt-Siebert M, Cherry NJ, Woodward WR (1994). Immunohistochemical localization of the neuron-specific glucose transporter (GLUT3) to neuropil in adult rat brain. Brain Res. 659:292–297

McDonald WS, Jones EE, Wojciak JM, Drake RR, Sabbadini RA, Harris NG (2018). Matrix-Assisted Laser Desorption Ionization Mapping of Lysophosphatidic Acid Changes after Traumatic Brain Injury and the Relationship to Cellular Pathology. Am J Pathol. 188(8):1779-1793

McMahon J, Huang X, Yang J, Komatsu M, Yue Z, Qian J, Zhu X, Huang Y (2012). Impaired autophagy in neurons after disinhibition of mammalian target of rapamycin and its contribution to epileptogenesis. J Neurosci. 32(45):15704-15714

Mehran AE, Templeman NM, Brigidi GS, Lim GE, Chu KY, Hu X, Botezelli JD, Asadi A, Hoffman BG, Kieffer TJ, Bamji SX, Clee SM, Johnson JD (2012). Hyperinsulinemia drives diet-induced obesity independently of brain insulin production. Cell Metab. 16(6):723-737

Meier-Ruge W, Iwangoff P, Reichlmeier K, Sandoz P (1980). Neurochemical findings in the aging brain. Adv Biochem Psychopharmacol. 23:323–338

Mejías R, Villadiego J, Pintado CO, Vime PJ, Gao L, Toledo-Aral JJ, Echevarría M, López-Barneo J (2006). Neuroprotection by transgenic expression of glucose-6-phosphate dehydrogenase in dopaminergic nigrostriatal neurons of mice. J Neurosci. 26(17):4500-4508

Meles SK, Teune LK, de Jong BM, Dierckx RA, Leenders KL (2017). Metabolic Imaging in Parkinson Disease. J Nucl Med. 58(1):23-28

Menzies FM, Fleming A, Caricasole A, Bento CF, Andrews SP, Ashkenazi A, Füllgrabe J, Jackson A, Jimenez Sanchez M, Karabiyik C, Licitra F, Lopez Ramirez A, Pavel M, Puri C, Renna M, Ricketts T, Schlotawa L, Vicinanza M, Won H, Zhu Y, Skidmore J, Rubinsztein DC (2017). Autophagy and Neurodegeneration: Pathogenic Mechanisms and Therapeutic Opportunities. Neuron. 93(5):1015-1034

Menzies FM, Fleming A, Rubinsztein DC (2015). Compromised autophagy and neurodegenerative diseases. Nat Rev Neurosci. 16(6):345-357

Menzies FM, Huebener J, Renna M, Bonin M, Riess O, Rubinsztein DC (2010) Autophagy induction reduces mutant ataxin-3 levels and toxicity in a mouse model of spinocerebellar ataxia type 3. Brain 133(Pt 1):93–104

Mercer JS, Erickson-Owens DA, Deoni SCL, Dean DC 3rd, Collins J, Parker AB, Wang M, Joelson S, Mercer EN, Padbury JF (2018). Effects of Delayed Cord Clamping on 4-Month Ferritin Levels, Brain Myelin Content, and Neurodevelopment: A Randomized Controlled Trial. J Pediatr. 203:266-272.e2

Metzger S, Walter C, Riess O, Roos RA, Nielsen JE, Craufurd D; REGISTRY Investigators of the European Huntington’s Disease Network; Nguyen HP (2013). The V471A polymorphism in autophagy-related gene ATG7 modifies age at onset specifically in Italian Huntington disease patients. PLoS One. 8(7):e68951

Miall RC (2013). Cerebellum: Anatomy and Function. In: Pfaff DW: Neuroscience in the 21st Century: From Basic to Clinical. Springer: New York. 1149–1167

Middleton FA, Strick PL (2001). Cerebellar projections to the prefrontal cortex of the primate. J Neurosci. 21(2):700-712

Miotto G, Rossetto M, Di Paolo ML, Orian L, Venerando R, Roveri A, Vučković AM, Bosello Travain V, Zaccarin M , Zennaro L, Maiorino M, Toppo S, Ursini F, Cozza G (2020). Insight into the mechanism of ferroptosis inhibition by ferrostatin-1. Redox Biology 28

Mizushima N, Komatsu M (2011). Autophagy: renovation of cells and tissues. Cell. 147(4):728-41

Mizushima N, Yamamoto A, Matsui M, Yoshimori T, Ohsumi Y (2004). In vivo analysis of autophagy in response to nutrient starvation using transgenic mice expressing a fluorescent autophagosome marker. Mol Biol Cell. 15(3):1101-11

Mizushima N. (2005). The pleiotropic role of autophagy: from protein metabolism to bactericide. Cell death and differentiation, 12 Suppl 2, 1535–1541

Montojo MT, Aganzo M, González N (2017). Huntington's Disease and Diabetes: Chronological Sequence of its Association. J Huntingtons Dis. 6(3):179-188

Moore AS, Holzbaur EL (2016). Dynamic recruitment and activation of ALS-associated TBK1 with its target optineurin are required for efficient mitophagy. Proc Natl Acad Sci U S A. 113(24):E3349-3358

Moroo I, Yamada T (1994). Immunohistochemistry using antibody to the glucose transporter 3 in human brainstem and cerebellar tissues. No To Shinkei. 46:1039–1043

Morris RL, Hollenbeck PJ (1993). The regulation of bidirectional mitochondrial transport is coordinated with axonal outgrowth. J Cell Sci. 104(Pt 3):917-27.

Morton SM, Bastian AJ (2004). Cerebellar control of balance and locomotion. Neuroscientist. 10(3):247-59

Morton SM, Bastian AJ (2007). Mechanisms of cerebellar gait ataxia. Cerebellum. 6(1):79-86

Mosconi L, De Santi S, Li J, Tsui WH, Li Y, Boppana M, Laska E, Rusinek H, de Leon MJ (2008). Hippocampal hypometabolism predicts cognitive decline from normal aging. Neurobiol Aging. 29:676–692

Mueckler M, Thorens B (2013). The SLC2 (GLUT) family of membrane transporters. Mol Aspects Med. 34:121–138

Münch G, Westcott B, Menini T, Gugliucci A (2012). Advanced glycation endproducts and their pathogenic roles in neurological disorders. Amino Acids. 42(4):1221-1236

Nagamatsu S, Sawa H, Kamada K, Nakamichi Y, Yoshimoto K, Hoshino T (1993). Neuron-specific glucose transporter (NSGT): CNS distribution of GLUT3 rat glucose transporter (RGT3) in rat central neurons. FEBS Lett. 334:289–295

Nakai A, Yamaguchi O, Takeda T, Higuchi Y, Hikoso S, Taniike M, Omiya S, Mizote I, Matsumura Y, Asahi M, Nishida K, Hori M, Mizushima N, Otsu K (2007). The role of autophagy in cardiomyocytes in the basal state and in response to hemodynamic stress. Nat Med. 13(5):619-24

Nakatogawa H, Suzuki K, Kamada Y, Ohsumi Y (2009). Dynamics and diversity in autophagy mechanisms: lessons from yeast. Nat Rev Mol Cell Biol. 10(7):458-67

Narendra D, Tanaka A, Suen DF, Youle RJ (2008). Parkin is recruited selectively to impaired mitochondria and promotes their autophagy. J Cell Biol. 183(5):795-803

Narendra DP, Jin SM, Tanaka A, Suen DF, Gautier CA, Shen J, Cookson MR, Youle RJ (2010). PINK1 is selectively stabilized on impaired mitochondria to activate Parkin. PLoS Biol. 8(1):e1000298

Negrete-Hurtado A, Overhoff M, Bera S, De Bruyckere E, Schätzmüller K, Kye MJ, Qin C, Lammers M, Kondylis V, Neundorf I, Kononenko NL (2020). Autophagy lipidation machinery regulates axonal microtubule dynamics but is dispensable for survival of mammalian neurons. Nat Commun. 11(1):1535

Nehlig A (1996). Respective roles of glucose and ketone bodies as substrates for cerebral energy metabolism in the suckling rat. Dev Neurosci. 18:426–433

Nehlig A, Pereira de Vasconcelos A (1993). Glucose and ketone body utilization by the brain of neonatal rats. Prog Neurobiol. 40:163–221

Nguyen DKH, Thombre R, Wang J (2019). Autophagy as a common pathway in amyotrophic lateral sclerosis. Neurosci Lett. 697:34-48

Niccoli T, Cabecinha M, Tillmann A, Kerr F, Wong CT, Cardenes D, Vincent AJ, Bettedi L, Li L, Grönke S, Dols J, Partridge L (2016). Increased Glucose Transport into Neurons Rescues Aβ Toxicity in Drosophila. Curr Biol. 26(17):2291-2300

Nixon RA (2007). Autophagy, amyloidogenesis and Alzheimer disease. J Cell Sci. 120(Pt 23):4081-4091

Nixon RA, Yang DS (2011). Autophagy failure in Alzheimer's disease--locating the primary defect. Neurobiol Dis. 43(1):38-45

Noda S, Sato S, Fukuda T, Tada N, Uchiyama Y, Tanaka K, Hattori N (2020). Loss of Parkin contributes to mitochondrial turnover and dopaminergic neuronal loss in aged mice. Neurobiol Dis. 136:104717

Noguchi K, Herr D, Mutoh T, Chun J (2009). Lysophosphatidic acid (LPA) and its receptors. Curr Opin Pharmacol. 9(1):15-23

Nørremølle A, Riess O, Epplen JT, Fenger K, Hasholt L, Sørensen SA (1993). Trinucleotide repeat elongation in the Huntingtin gene in Huntington disease patients from 71 Danish families. Hum Mol Genet. 1993 Sep;2(9):1475-1476

Nthiga TM, Kumar Shrestha B, Sjøttem E, Bruun JA, Bowitz Larsen K, Bhujabal Z, Lamark T, Johansen T (2020). CALCOCO1 acts with VAMP-associated proteins to mediate ER-phagy. EMBO J. 39(15):e103649

Oka M, Suzuki E, Asada A, Saito T, Iijima KM, Ando K (2021). Increasing neuronal glucose uptake attenuates brain aging and promotes life span under dietary restriction in Drosophila. iScience. 24(1):101979

Ordureau A, Paulo JA, Zhang W, Ahfeldt T, Zhang J, Cohn EF, Hou Z, Heo JM, Rubin LL, Sidhu SS, Gygi SP, Harper JW (2018). Dynamics of PARKIN-Dependent Mitochondrial Ubiquitylation in Induced Neurons and Model Systems Revealed by Digital Snapshot Proteomics. Mol Cell. 70(2):211-227.e8

Ordureau A, Sarraf SA, Duda DM, Heo JM, Jedrychowski MP, Sviderskiy VO, Olszewski JL, Koerber JT, Xie T, Beausoleil SA, Wells JA, Gygi SP, Schulman BA, Harper JW (2014). Quantitative proteomics reveal a feedforward mechanism for mitochondrial PARKIN translocation and ubiquitin chain synthesis. Mol Cell. 56(3):360-375

Orenstein SJ, Cuervo AM (2010). Chaperone-mediated autophagy: molecular mechanisms and physiological relevance. Semin Cell Dev Biol. 21(7):719-26

Overhoff M, Tellkamp F, Hess S, Tolve M, Tutas J, Faerfers M, Ickert L, Mohammadi M, De Bruyckere E, Kallergi E, Delle Vedove A, Nikoletopoulou V, Wirth B, Isensee J, Hucho T, Puchkov D, Isbrandt D, Krueger M, Kloppenburg P, Kononenko NL (2022). Autophagy regulates neuronal excitability by controlling cAMP/protein kinase A signaling at the synapse. EMBO J. 41(22):e110963

Page TL, Einstein M, Duan H, He Y, Flores T, Rolshud D, Erwin JM, Wearne SL, Morrison JH, Hof PR (2002). Morphological alterations in neurons forming corticocortical projections in the neocortex of aged Patas monkeys. Neurosci Lett. 317:37–41

Pajak B, Siwiak E, Sołtyka M, Priebe A, Zieliński R, Fokt I, Ziemniak M, Jaśkiewicz A, Borowski R, Domoradzki T, Priebe W (2019). 2-Deoxy-d-Glucose and Its Analogs: From Diagnostic to Therapeutic Agents. Int J Mol Sci. 21(1):234

Palikaras K, Lionaki E, Tavernarakis N (2018). Mechanisms of mitophagy in cellular homeostasis, physiology and pathology. Nat Cell Biol. 20(9):1013-1022

Pankiv S, Alemu EA, Brech A, Bruun JA, Lamark T, Overvatn A, Bjørkøy G, Johansen T (2010). FYCO1 is a Rab7 effector that binds to LC3 and PI3P to mediate microtubule plus end-directed vesicle transport. J Cell Biol. 188(2):253-269

Pankiv S, Clausen TH, Lamark T, Brech A, Bruun JA, Outzen H, Øvervatn A, Bjørkøy G, Johansen T (2007). p62/SQSTM1 binds directly to Atg8/LC3 to facilitate degradation of ubiquitinated protein aggregates by autophagy. J Biol Chem. 2007 Aug 17;282(33):24131-24145

Papa S, Martino PL, Capitanio G, Gaballo A, De Rasmo D, Signorile A, Petruzzella V (2012). The oxidative phosphorylation system in mammalian mitochondria. Adv Exp Med Biol. 942:3-37

Patching SG (2017). Glucose transporters at the blood-brain barrier: function, regulation and gateways for drug delivery. Mol Neurobiol. 54:1046–1077

Pathak D, Shields LY, Mendelsohn BA, Haddad D, Lin W, Gerencser AA, Kim H, Brand MD, Edwards RH, Nakamura K (2015). The role of mitochondrially derived ATP in synaptic vesicle recycling. J Biol Chem. 290(37):22325-22336

Pauwels EK, Ribeiro MJ, Stoot JH, McCready VR, Bourguignon M, Maziere B (1998). FDG accumulation and tumor biology. Nucl Med Biol. 25(4):317-322

Pearson TS, Akman C, Hinton VJ, Engelstad K, De Vivo DC (2013). Phenotypic spectrum of glucose transporter type 1 deficiency syndrome (Glut1 DS). Curr Neurol Neurosci Rep. 13(4):342

Pei Y, Lv S, Shi Y, Jia J, Ma M, Han H, Zhang R, Tan J, Zhang X (2023). RAB21 controls autophagy and cellular energy homeostasis by regulating retromer-mediated recycling of SLC2A1/GLUT1. Autophagy. 19(4):1070-1086

Perry JM, He XC, Sugimura R, Grindley JC, Haug JS, Ding S, Li L (2011). Cooperation between both Wnt/{beta}-catenin and PTEN/PI3K/Akt signaling promotes primitive hematopoietic stem cell self-renewal and expansion. Genes Dev. 25(18):1928-1942

Pfeffer G, Blakely EL, Alston CL, Hassani A, Boggild M, Horvath R et al (2012) Adult-onset spinocerebellar ataxia syndromes due to MTATP6 mutations. J Neurol Neurosurg Psychiatry 83(9):883–886

Pickford F, Masliah E, Britschgi M, Lucin K, Narasimhan R, Jaeger PA, Small S, Spencer B, Rockenstein E, Levine B, Wyss-Coray T (2008). The autophagy-related protein beclin 1 shows reduced expression in early Alzheimer disease and regulates amyloid beta accumulation in mice. J Clin Invest. 118(6):2190-9.

Pickford F, Masliah E, Britschgi M, Lucin K, Narasimhan R, Jaeger PA, Small S, Spencer B, Rockenstein E, Levine B, Wyss-Coray T 82008). The autophagy-related protein beclin 1 shows reduced expression in early Alzheimer disease and regulates amyloid beta accumulation in mice. J Clin Invest. 118(6):2190-2199

Pickles S, Vigié P, Youle RJ (2018). Mitophagy and Quality Control Mechanisms in Mitochondrial Maintenance. Curr Biol. 28(4):R170-R185

Pickrell AM, Youle RJ (2015). The roles of PINK1, parkin, and mitochondrial fidelity in Parkinson's disease. Neuron. 85(2):257-73

Pottier C, Bieniek KF, Finch N, van de Vorst M, Baker M, Perkersen R, Brown P, Ravenscroft T, van Blitterswijk M, Nicholson AM, DeTure M, Knopman DS, Josephs KA, Parisi JE, Petersen RC, Boylan KB, Boeve BF, Graff-Radford NR, Veltman JA, Gilissen C, Murray ME, Dickson DW, Rademakers R (2015). Whole-genome sequencing reveals important role for TBK1 and OPTN mutations in frontotemporal lobar degeneration without motor neuron disease. Acta Neuropathol. 130(1):77-92.

Poretti A, Wolf NI, Boltshauser E (2008). Differential diagnosis of cerebellar atrophy in childhood. Eur J Paediatr Neurol. 12(3):155-67

Puget S, Boddaert N, Viguier D, Kieffer V, Bulteau C, Garnett M, Callu D, Sainte-Rose C, Kalifa C, Dellatolas G, Grill J (2009.) Injuries to inferior vermis and dentate nuclei predict poor neurological and neuropsychological outcome in children with malignant posterior fossa tumors. Cancer 115:1338–1347

Qi J, Leahy RM, Cherry SR, Chatziioannou A, Farquhar TH (1998). High-resolution 3D Bayesian image reconstruction using the microPET small-animal scanner. Phys Med Biol. 43(4):1001-1013

Rabbani N, Xue M, Thornalley PJ (2016). Methylglyoxal-induced dicarbonyl stress in aging and disease: first steps towards glyoxalase 1-based treatments. Clin Sci (Lond). 130(19):1677-1696

Rabinowitz JD, White E (2010). Autophagy and metabolism. Science. 330(6009):1344-1348

Ramsey RB, Jones JP, Naqvi SH, Nicholas HJ (1971). The biosynthesis of cholesterol and other sterols by brain tissue. I. Subcellular biosynthesis in vitro. Lipids. 6(3):154-161

Rangaraju V, Calloway N, Ryan TA (2014). Activity-driven local ATP synthesis is required for synaptic function. Cell. 156:825–835

Rangaraju V, Lauterbach M, Schuman EM (2019). Spatially Stable Mitochondrial Compartments Fuel Local Translation during Plasticity. Cell. 176(1-2):73-84.e15

Rath S, Sharma R, Gupta R, Ast T, Chan C, Durham TJ, Goodman RP, Grabarek Z, Haas ME, Hung WHW, Joshi PR, Jourdain AA, Kim SH, Kotrys AV, Lam SS, McCoy JG, Meisel JD, Miranda M, Panda A, Patgiri A, Rogers R, Sadre S, Shah H, Skinner OS, To TL, Walker MA, Wang H, Ward PS, Wengrod J, Yuan CC, Calvo SE, Mootha VK (2021). MitoCarta3.0: an updated mitochondrial proteome now with sub-organelle localization and pathway annotations. Nucleic Acids Res. 49(D1):D1541-D1547

Ravikumar B, Acevedo-Arozena A, Imarisio S, Berger Z, Vacher C, O'Kane CJ, Brown SD, Rubinsztein DC (2005). Dynein mutations impair autophagic clearance of aggregate-prone proteins. Nat Genet. 37(7):771-776

Ravikumar B, Vacher C, Berger Z, Davies JE, Luo S, Oroz LG, Scaravilli F, Easton DF, Duden R, O'Kane CJ, Rubinsztein DC (2004). Inhibition of mTOR induces autophagy and reduces toxicity of polyglutamine expansions in fly and mouse models of Huntington disease. Nat Genet. 36(6):585-595

Rayner DV, Thomas ME, Trayhurn P (1994). Glucose transporters (GLUTs 1–4) and their mRNAs in regions of the rat brain: insulin-sensitive transporter expression in the cerebellum. Can J Physiol Pharmacol. 72:476–479

Rea SL, Majcher V, Searle MS, Layfield R (2014). SQSTM1 mutations--bridging Paget disease of bone and ALS/FTLD. Exp Cell Res. 325(1):27-37

Reeber SL, Otis TS, Sillitoe RV (2013). New roles for the cerebellum in health and disease. Front Syst Neurosci. 7:83

Reggiori F, Klionsky DJ (2013). Autophagic processes in yeast: mechanism, machinery and regulation. Genetics 194(2):341-61

Ren H, Lu TY, McGraw TE, Accili D (2015). Anorexia and impaired glucose metabolism in mice with hypothalamic ablation of Glut4 neurons. Diabetes. 64:405–417

Ren JX, Sun X, Yan XL, Guo ZN, Yang Y (2020). Ferroptosis in neurological diseases. Front. Cell Neurosci. 14:218

Renna M, Schaffner C, Winslow AR, Menzies FM, Peden AA, Floto RA, Rubinsztein DC (2011). Autophagic substrate clearance requires activity of the syntaxin-5 SNARE complex. J Cell Sci. 124(Pt 3):469-82.

Reno CM, Puente EC, Sheng Z, Daphna-Iken D, Bree AJ, Routh VH, Kahn BB, Fisher SJ (2017). Brain GLUT4 knockout mice have impaired glucose tolerance, decreased insulin sensitivity, and impaired hypoglycemic counterregulation. Diabetes. 66:587–597.

Resnick SM, Pham DL, Kraut MA, Zonderman AB, Davatzikos C (2003). Longitudinal magnetic resonance imaging studies of older adults: a shrinking brain. J Neurosci. 23:3295–3301

Roberts DJ, Tan-Sah VP, Ding EY, Smith JM, Miyamoto S (2014). Hexokinase-II positively regulates glucose starvation-induced autophagy through TORC1 inhibition. Mol Cell. 53(4):521-533

Rocchi A, Yamamoto S, Ting T, Fan Y, Sadleir K, Wang Y, Zhang W, Huang S, Levine B, Vassar R, He C (2017). A Becn1 mutation mediates hyperactive autophagic sequestration of amyloid oligomers and improved cognition in Alzheimer's disease. PLoS Genet. 13(8):e1006962

Rodriguez-Rodriguez P, Fernandez E, Almeida A, Bolaños JP (2012). Excitotoxic stimulus stabilizes PFKFB3 causing pentose-phosphate pathway to glycolysis switch and neurodegeneration. Cell Death Differ. 19:1582-1589

Roostaei T, Nazeri A, Sahraian MA, Minagar A (2014). The human cerebellum: a review of physiologic neuroanatomy. Neurol Clin. 32(4):859-69

Rosenberg GA (2012). Neurological diseases in relation to the blood-brain barrier. J Cereb Blood Flow Metab. 32:1139–1151

Rossetti L, Stenbit AE, Chen W, Hu M, Barzilai N, Katz EB, Charron MJ (1997). Peripheral but not hepatic insulin resistance in mice with one disrupted allele of the glucose transporter type 4 (GLUT4) gene. J Clin Invest. 100(7):1831-1839

Roy CS, Sherrington CS (1890). On the Regulation of the Blood-supply of the Brain. J Physiol. 11(1-2):85-158.17

Ruppert MC, Greuel A, Tahmasian M, Schwartz F, Stürmer S, Maier F, Hammes J, Tittgemeyer M, Timmermann L, van Eimeren T, Drzezga A, Eggers C (2020). Network degeneration in Parkinson's disease: multimodal imaging of nigro-striato-cortical dysfunction. Brain. 143(3):944-959.

Russell RL, Siedlak SL, Raina AK, Bautista JM, Smith MA, Perry G (1999). Increased neuronal glucose-6-phosphate dehydrogenase and sulfhydryl levels indicate reductive compensation to oxidative stress in Alzheimer disease. Arch Biochem Biophys. 370: 236-239

Saitsu H, Nishimura T, Muramatsu K, Kodera H, Kumada S, Sugai K, Kasai-Yoshida E, Sawaura N, Nishida H, Hoshino A, Ryujin F, Yoshioka S, Nishiyama K, Kondo Y, Tsurusaki Y, Nakashima M, Miyake N, Arakawa H, Kato M, Mizushima N, Matsumoto N (2013). De novo mutations in the autophagy gene WDR45 cause static encephalopathy of childhood with neurodegeneration in adulthood. Nat Genet. 45(4):445-9, 449e1

Salameh JS, Brown RH Jr, Berry JD (2015). Amyotrophic Lateral Sclerosis: Review. Semin Neurol. 35(4):469-746

Sankar R, Thamotharan S, Shin D, Moley KH, Devaskar SU (2002). Insulin-responsive glucose transporters-GLUT8 and GLUT4 are expressed in the developing mammalian brain. Brain Res Mol Brain Res. 107:157–165

Santer R, Schneppenheim R, Suter D, Schaub J, Steinmann B (1998). Fanconi-Bickel syndrome - the original patient and his natural history, historical steps leading to the primary defect, and a review of the literature. Eur J Pediatr. 157:783–797

Santer R, Steinmann B, Schaub J (2002). Fanconi-Bickel syndrome—a congenital defect of facilitative glucose transport. Curr Mol Med. 2:213–227

Sarkar S (2013). Regulation of autophagy by mTOR-dependent and mTOR-independent pathways: autophagy dysfunction in neurodegenerative diseases and therapeutic application of autophagy enhancers. Biochem Soc Trans. 41(5):1103-1130

Sarna J, Miranda SR, Schuchman EH, Hawkes R (2001). Patterned cerebellar Purkinje cell death in a transgenic mouse model of Niemann Pick type A/B disease. Eur J Neurosci.. 13(10):1873-80

Sarna JR, Hawkes R (2003). Patterned Purkinje cell death in the cerebellum. Prog Neurobiol. 70(6):473-507

Sarna JR, Larouche M, Marzban H, Sillitoe RV, Rancourt DE, Hawkes R (2003). Patterned Purkinje cell degeneration in mouse models of Niemann-Pick type C disease. J Comp Neurol. 456(3):279-291

Sarraf SA, Raman M, Guarani-Pereira V, Sowa ME, Huttlin EL, Gygi SP, Harper JW (2013). Landscape of the PARKIN-dependent ubiquitylome in response to mitochondrial depolarization. Nature. 496(7445):372-6

Sasabe J, Chiba T, Yamada M, Okamoto K, Nishimoto I, Matsuoka M, Aiso S (2007). D-serine is a key determinant of glutamate toxicity in amyotrophic lateral sclerosis. EMBO J. 26(18):4149-4159

Savova A, Romanov J, Martens S (2020). NBR1 directly promotes the formation of p62–ubiquitin condensates via its PB1 and UBA domains. Preprint at bioRxiv

Schicks J, Müller Vom Hagen J, Bauer P, Beck-Wödl S, Biskup S, Krägeloh-Mann I, Schöls L, Synofzik M (2012). Niemann-Pick type C is frequent in adult ataxia with cognitive decline and vertical gaze palsy. Neurology. 80(12):1169–70

Schmidt O, Pfanner N, Meisinger C (2010). Mitochondrial protein import: from proteomics to functional mechanisms. Nat Rev Mol Cell Biol. 11(9):655-667.

Schmitz AE, de Souza LF, dos Santos B, Maher P, Lopes FM, Londero GF, Klamt F, Dafre AL (2017). Methylglyoxal-induced protection response and toxicity: Role of glutathione reductase and thioredoxin systems. Neurotoxicity Research. 32(3):340–350

Schneider JL, Villarroya J, Diaz-Carretero A, Patel B, Urbanska AM, Thi MM, Villarroya F, Santambrogio L, Cuervo AM (2015). Loss of hepatic chaperone-mediated autophagy accelerates proteostasis failure in aging. Aging Cell. 14(2):249-264

Schniepp R, Möhwald K, Wuehr M (2017). Gait ataxia in humans: vestibular and cerebellar control of dynamic stability. J Neurol. 264(Suppl 1):87-92

Schniepp R, Wuehr M, Huth S, Pradhan C, Schlick C, Brandt T, Jahn K (2014) The gait disorder in downbeat nystagmus syndrome. PLoS One. 9:e105463

Schniepp R, Wuehr M, Neuhaeusser M, Kamenova M, Dimitriadis K, Klopstock T, Strupp M, Brandt T, Jahn K (2012) Locomotion speed determines gait variability in cerebellar ataxia and vestibular failure. Mov Disord. 27:125–131

Schreij AM, Fon EA, McPherson PS (2016). Endocytic membrane trafficking and neurodegenerative disease. Cell Mol Life Sci. 73(8):1529-45

Schwaiger M, Rampler E, Hermann G, Miklos W, Berger W, Koellensperger G. (2017) Anion-Exchange Chromatography Coupled to High-Resolution Mass Spectrometry: A Powerful Tool for Merging Targeted and Non-targeted Metabolomics. Anal Chem 89: 7667-74

Scotter EL, Vance C, Nishimura AL, Lee YB, Chen HJ, Urwin H, Sardone V, Mitchell JC, Rogelj B, Rubinsztein DC, Shaw CE (2014). Differential roles of the ubiquitin proteasome system and autophagy in the clearance of soluble and aggregated TDP-43 species. J Cell Sci. 127(Pt 6):1263-1278

Seibt TM, Proneth B, Conrad M (2019). Role of GPX4 in ferroptosis and its pharmacological implication. Free Radic Biol Med. 133:144-152

Sekine S, Youle RJ (2018). PINK1 import regulation; a fine system to convey mitochondrial stress to the cytosol. BMC Biol. 16(1):2

Semenza GL (2008). Tumor metabolism: cancer cells give and take lactate. J Clin Invest. 118:3835–3837

Sheng S, Clabough EB, Sarkar S, Futter M, Rubinsztein DC, Zeitlin SO (2010). Deletion of the huntingtin polyglutamine stretch enhances neuronal autophagy and longevity in mice. PLoS Genet. 6(2):e1000838

Sheng X, Yung YC, Chen A, Chun J (2015). Lysophosphatidic acid signalling in development. Development. 142(8):1390-1395

Sheng ZH, Cai Q (2012). Mitochondrial transport in neurons: impact on synaptic homeostasis and neurodegeneration. Nat Rev Neurosci. 13(2):77-93

Shibata M, Lu T, Furuya T, Degterev A, Mizushima N, Yoshimori T, MacDonald M, Yankner B, Yuan J (2006). Regulation of intracellular accumulation of mutant Huntingtin by Beclin 1. J Biol Chem. 281(20):14474-14485

Shin BC, Cepeda C, Estrada-Sánchez AM, Levine MS, Hodaei L, Dai Y, Jung J, Ganguly A, Clark P, Devaskar SU (2018). Neural Deletion of Glucose Transporter Isoform 3 Creates Distinct Postnatal and Adult Neurobehavioral Phenotypes. J Neurosci. 38(44):9579-9599

Shleper M, Kartvelishvily E, Wolosker H (2005). D-serine is the dominant endogenous coagonist for NMDA receptor neurotoxicity in organotypic hippocampal slices. J. Neurosci. 25:9413–9417

Sieradzan KA, Mechan AO, Jones L, Wanker EE, Nukina N, Mann DM (1999). Huntington's disease intranuclear inclusions contain truncated, ubiquitinated huntingtin protein. Exp Neurol. 156(1):92-99

Skotte NH, Andersen JV, Santos A, Aldana BI, Willert CW, Nørremølle A, Waagepetersen HS, Nielsen ML (2018). Integrative Characterization of the R6/2 Mouse Model of Huntington's Disease Reveals Dysfunctional Astrocyte Metabolism. Cell Rep. 23(7):2211-2224

Sillitoe RV, Joyner AL (2007). Morphology, molecular codes, and circuitry produce the three-dimensional complexity of the cerebellum. Annu Rev Cell Dev Biol. 23:549-77

Simpson IA, Dwyer D, Malide D, Moley KH, Travis A, Vannucci SJ (2008). The facilitative glucose transporter GLUT3: 20 years of distinction. Am J Physiol Endocrinol Metab. 295:E242–E253

Small SA, Kent K, Pierce A, Leung C, Kang MS, Okada H, Honig L, Vonsattel JP, Kim TW (2005). Model-guided microarray implicates the retromer complex in Alzheimer's disease. Ann Neurol. 58(6):909-919

Smirnova E, Griparic L, Shurland DL, van der Bliek AM (2001). Dynamin-related protein Drp1 is required for mitochondrial division in mammalian cells. Mol Biol Cell. 12(8):2245-2256

Smith HL, Bourne JN, Cao G, Chirillo MA, Ostroff LE, Watson DJ, Harris KM (2016). Mitochondrial support of persistent presynaptic vesicle mobilization with age-dependent synaptic growth after LTP. Elife. 5:e15275

Smith MD, Harley ME, Kemp AJ, Wills J, Lee M, Arends M, von Kriegsheim A, Behrends C, Wilkinson S (2018). CCPG1 Is a Non-canonical Autophagy Cargo Receptor Essential for ER-Phagy and Pancreatic ER Proteostasis. Dev Cell. 44(2):217-232.e11

Smith SM, Nichols TE (2009). Threshold-free cluster enhancement: addressing problems of smoothing, threshold dependence and localisation in cluster inference. Neuroimage. 44 (1):83-98

Sofou K, Dahlin M, Hallböök T, Lindefeldt M, Viggedal G, Darin N (2017). Ketogenic diet in pyruvate dehydrogenase complex deficiency: short- and long-term outcomes. J Inherit Metab Dis. 40(2):237–45

Sonveaux P, Végran F, Schroeder T, Wergin MC, Verrax J, Rabbani ZN, De Saedeleer CJ, Kennedy KM, Diepart C, Jordan BF, Kelley MJ, Gallez B, Wahl ML, Feron O, Dewhirst MW (2008). Targeting lactate-fueled respiration selectively kills hypoxic tumor cells in mice. J Clin Invest. 118(12):3930-3942

Soto M, Cai W, Konishi M, Kahn CR (2019). Insulin signaling in the hippocampus and amygdala regulates metabolism and neurobehavior. Proc Natl Acad Sci U S A. 116(13):6379-6384

Sou YS, Waguri S, Iwata J, Ueno T, Fujimura T, Hara T, Sawada N, Yamada A, Mizushima N, Uchiyama Y, Kominami E, Tanaka K, Komatsu M (2008). The Atg8 conjugation system is indispensable for proper development of autophagic isolation membranes in mice. Mol Biol Cell. 19(11):4762-4775

Spohr TCE, Dezonne RS, Rehen SK, Gomes FC (2011). Astrocytes treated by lysophosphatidic acid induce axonal outgrowth of cortical progenitors through extracellular matrix protein and epidermal growth factor signaling pathway. J Neurochem. 119(1):113-23

Stafford P, Abdelwahab MG, Kim DY, Preul MC, Rho JM, Scheck AC (2010). The ketogenic diet reverses gene expression patterns and reduces reactive oxygen species levels when used as an adjuvant therapy for glioma. Nutr Metab. 7:74

Stahon KE, Bastian C, Griffith S, Kidd GJ, Brunet S, Baltan S (2016). Age-related changes in axonal and mitochondrial ultrastructure and function in white matter. J Neurosci. 36:9990–10001

Stavoe AKH, Holzbaur ELF (2019). Autophagy in Neurons. Annu Rev Cell Dev Biol. 35:477-500

Stolarczyk E, Guissard C, Michau A, Even PC, Grosfeld A, Serradas P, Lorsignol A, Penicaud L, Brot-Laroche E, Leturque A, Le Gall M (2010). Detection of extracellular glucose by GLUT2 contributes to hypothalamic control of food intake. Am J Physiol Endocrinol Metab. 298:E1078–E1087

Stoodley CJ, Schmahmann JD (2009). Functional topography in the human cerebellum: a meta-analysis of neuroimaging studies. Neuroimage 44:489–501

Strata P, Rossi F (1998). Plasticity of the olivocerebellar pathway. Trends Neurosci. 21:407–413

Stromhaug PE, Berg TO, Fengsrud M, Seglen PO (1998). Purification and characterization of autophagosomes from rat hepatocytes. Biochem J. 335 (Pt 2): 217–224

Stuart CA, Ross IR, Howell ME, McCurry MP, Wood TG, Ceci JD, Kennel SJ, Wall J (2011). Brain glucose transporter (Glut3) haploinsufficiency does not impair mouse brain glucose uptake. Brain Res. 384:15-22

Sturrock RR (1989). Age related changes in Purkinje cell number in the cerebellar nodulus of the mouse. J Hirnforsch. 30(6):757-60

Sun X, Li X, Jia H, Wang H, Shui G, Qin Y, Shu X, Wang Y, Dong J, Liu G, Li X (2020). Nuclear Factor E2-Related Factor 2 Mediates Oxidative Stress-Induced Lipid Accumulation in Adipocytes by Increasing Adipogenesis and Decreasing Lipolysis. Antioxid Redox Signal. 32(3):173-192

Sun X, Ou Z, Chen R, Niu X, Chen D, Kang R, Tang D (2016). Activation of the p62-Keap1-NRF2 pathway protects against ferroptosis in hepatocellular carcinoma cells. Hepatology. 63(1):173-84

Szablewski L (2017). Glucose Transporters in Brain: In Health and in Alzheimer's Disease. J Alzheimers Dis. 55(4):1307-1320

Szczepanik JC, de Almeida GRL, Cunha MP, Dafre AL (2020). Repeated methylglyoxal treatment depletes dopamine in the prefrontal cortex, and causes memory impairment and depressive-like behavior in mice. Neurotoxicity Research. 45(2):354–370

Tanaka J, Nakamura H, Miyawaki S (1988). Cerebellar involvement in murine sphingomyelinosis: a new model of Niemann-Pick disease. J Neuropathol Exp Neurol. 47(3):291-300

Tefera TW, Bartlett K, Tran SS, Hodson MP, Borges K (2019). Impaired pentose phosphate pathway in the spinal cord of the hSOD1 G93A mouse model of Amyotrophic Lateral Sclerosis. Mol Neurobiol. 56(8):5844-5855

Terada T, Obi T, Bunai T, Matsudaira T, Yoshikawa E, Ando I, Futatsubashi M, Tsukada H, Ouchi Y (2020). In vivo mitochondrial and glycolytic impairments in patients with Alzheimer disease. Neurology. 94(15):e1592-e1604

Terešak P, Lapao A, Subic N, Boya P, Elazar Z, Simonsen A (2022). Regulation of PRKN-independent mitophagy. Autophagy. 18(1):24-39

Thalman C, Horta G, Qiao L, Endle H, Tegeder I, Cheng H, Laube G, Sigurdsson T, Hauser MJ, Tenzer S, Distler U, Aoki J, Morris AJ, Geisslinger G, Röper J, Kirischuk S, Luhmann HJ, Radyushkin K, Nitsch R, Vogt J (2018). Synaptic phospholipids as a new target for cortical hyperexcitability and E/I balance in psychiatric disorders. Mol Psychiatry. 23(8):1699-1710

Thu DC, Oorschot DE, Tippett LJ, Nana AL, Hogg VM, Synek BJ, Luthi-Carter R, Waldvogel HJ, Faull RL (2010). Cell loss in the motor and cingulate cortex correlates with symptomatology in Huntington's disease. Brain. 133(Pt 4):1094-1110

Tomasi DG, Shokri-Kojori E, Wiers CE, Kim SW, Demiral ŞB, Cabrera EA, Lindgren E, Miller G, Wang GJ, Volkow ND (2017). Dynamic brain glucose metabolism identifies anti-correlated cortical-cerebellar networks at rest. J Cereb Blood Flow Metab. 37(12):3659-3670

Torvik A, Torp S, Lindboe CF (1986). Atrophy of the cerebellar vermis in ageing. A morphometric and histologic study. J. Neurol. Sci., 76:283-294

Uehara Y, Nipper V, McCall AL (1997). Chronic insulin hypoglycemia induces GLUT-3 protein in rat brain neurons. Am J Physiol. 272(4 Pt 1):E716-719

Ulfert G, Schmidt U, Hoyer S (1982). Glucose and energy metabolism of rat cerebral cortex during aging. Exp Brain Res Suppl. 5:102–111

Ullner PM, Di Nardo A, Goldman JE, Schobel S, Yang H, Engelstad K, Wang D, Sahin M, De Vivo DC (2009). Murine Glut-1 transporter haploinsufficiency: postnatal deceleration of brain weight and reactive astrocytosis. Neurobiol. Dis. 36:60-69.

Vaishnavi SN, Vlassenko AG, Rundle MM, Snyder AZ, Mintun MA, Raichle ME (2010). Regional aerobic glycolysis in the human brain. Proc Natl Acad Sci U S A. 107(41):17757-17762

Valbuena GN, Rizzardini M, Cimini S, Siskos AP, Bendotti C, Cantoni L, Keun HC (2016). Metabolomic Analysis Reveals Increased Aerobic Glycolysis and Amino Acid Deficit in a Cellular Model of Amyotrophic Lateral Sclerosis. Mol Neurobiol. 53(4):2222-40

Valente EM, Abou-Sleiman PM, Caputo V, Muqit MM, Harvey K, Gispert S, Ali Z, Del Turco D, Bentivoglio AR, Healy DG, Albanese A, Nussbaum R, González-Maldonado R, Deller T, Salvi S, Cortelli P, Gilks WP, Latchman DS, Harvey RJ, Dallapiccola B, Auburger G, Wood NW (2004). Hereditary early-onset Parkinson's disease caused by mutations in PINK1. Science. 304(5674):1158-60

Valente EM, Abou-Sleiman PM, Caputo V, Muqit MM, Harvey K, Gispert S, Ali Z, Del Turco D, Bentivoglio AR, Healy DG, Albanese A, Nussbaum R, González-Maldonado R, Deller T, Salvi S, Cortelli P, Gilks WP, Latchman DS, Harvey RJ, Dallapiccola B, Auburger G, Wood NW (2004). Hereditary early-onset Parkinson's disease caused by mutations in PINK1. Science. 304(5674):1158-1160

van der Burg JMM, Gardiner SL, Ludolph AC, Landwehrmeyer GB, Roos RAC, Aziz NA (2009). Body weight is a robust predictor of clinical progression in Huntington disease. Ann Neurol. 82(3):479-483

Van Essen DC, Donahue CJ, Glasser MF (2018). Development and Evolution of Cerebral and Cerebellar Cortex. Brain Behav Evol. 91(3):158-169

van Meer G, Voelker DR, Feigenson GW (2008). Membrane lipids: where they are and how they behave. Nat. Rev. Mol. Cell. Biol. 9:112–124

Vannucci SJ, Clark RR, Koehler-Stec E, Li K, Smith CB, Davies P, Maher F, Simpson IA (1998). Glucose transporter expression in brain: relationship to cerebral glucose utilization. Dev Neurosci. 20:369–379

Vannucci SJ, Koehler-Stec EM, Li K, Reynolds TH, Clark R, Simpson IA (1998). GLUT4 glucose transporter expression in rodent brain: effect of diabetes. Brain Res. 797:1–11

Vannucci SJ, Rutherford T, Wilkie MB, Simpson IA, Lauder JM (2000). Prenatal expression of the GLUT4 glucose transporter in the mouse. Dev Neurosci. 22:274–282

Vargas JNS, Hamasaki M, Kawabata T, Youle RJ, Yoshimori T (2023). The mechanisms and roles of selective autophagy in mammals. Nat Rev Mol Cell Biol. 24(3):167-185

Vassar R, Bennett BD, Babu-Khan S, Kahn S, Mendiaz EA, Denis P, Teplow DB, Ross S, Amarante P, Loeloff R, Luo Y, Fisher S, Fuller J, Edenson S, Lile J, Jarosinski MA, Biere AL, Curran E, Burgess T, Louis JC, Collins F, Treanor J, Rogers G, Citron M (1999). Beta-secretase cleavage of Alzheimer's amyloid precursor protein by the transmembrane aspartic protease BACE. Science. 1999 Oct 22;286(5440):735-741

Vaupel P, Multhoff G (2021). The Warburg Effect: Historical Dogma Versus Current Rationale. Adv Exp Med Biol. 1269:169-177

Ventruti A, Cuervo AM (2007). Autophagy and neurodegeneration. Curr Neurol Neurosci Rep. 7(5):443-451

Vilis T, Hore J (1980). Central neural mechanisms contributing to cerebellar tremor produced by limb perturbations. J Neurophysiol. 43(2):279-291

von Leden RE, Moritz KE, Bermudez S, Jaiswal S, Wilson CM, Dardzinski BJ, Byrnes KR (2019). Aging alters glucose uptake in the naïve and injured rodent spinal cord. Neurosci Lett. 690:23-28

von Maltzahn J, Bentzinger CF, Rudnicki MA (2011). Wnt7a-Fzd7 signalling directly activates the Akt/mTOR anabolic growth pathway in skeletal muscle. Nat Cell Biol. 14(2):186-191

Voogd J, Glickstein M (1998). The anatomy of the cerebellum. Trends Neurosci. 21(9):370-375

Waelter S, Boeddrich A, Lurz R, Scherzinger E, Lueder G, Lehrach H, Wanker EE (2001). Accumulation of mutant huntingtin fragments in aggresome-like inclusion bodies as a result of insufficient protein degradation. Mol Biol Cell. 12(5):1393-1407

Wan HZ, Hulsey MG, Martin RJ (1998). Intracerebroventricular administration of antisense oligodeoxynucleotide against GLUT2 glucose transporter mRNA reduces food intake, body weight change and glucoprivic feeding response in rats. J Nutr. 128:287–291

Wang C, Youle RJ (2009). The role of mitochondria in apoptosis*. Annu Rev Genet. 43:95-118

Wang D, Pascual JM, Yang H, Engelstad K, Mao X, Cheng J, Yoo J, Noebel JL, De Vivo DC (2006). A mouse model for Glut-1 haploinsufficiency. Hum. Mol. Genet. 15:1169-1179.

Wang IF, Tsai KJ, Shen CK (2013). Autophagy activation ameliorates neuronal pathogenesis of FTLD-U mice: a new light for treatment of TARDBP/TDP-43 proteinopathies. Autophagy. 9(2):239-240

Wang K, Xu R, Schrandt J, Shah P, Gong YZ, Preston C, Wang L, Yi JK, Lin CL, Sun W, Spyropoulos DD, Rhee S, Li M, Zhou J, Ge S, Zhang G, Snider AJ, Hannun YA, Obeid LM, Mao C (2015). Alkaline Ceramidase 3 Deficiency Results in Purkinje Cell Degeneration and Cerebellar Ataxia Due to Dyshomeostasis of Sphingolipids in the Brain. PLoS Genet. 11(10):e1005591

Wang L, Pavlou S, Du X, Bhuckory M, Xu H, Chen M (2019). Glucose transporter 1 critically controls microglial activation through facilitating glycolysis. Mol Neurodegener. 14:2

Wang T, Morgan JI (2007). The Purkinje cell degeneration (pcd) mouse: an unexpected molecular link between neuronal degeneration and regeneration. Brain Res. 1140:26-40

Wang X, Eno CO, Altman BJ, Zhu Y, Zhao G, Olberding KE, Rathmell JC, Li C (2011). ER stress modulates cellular metabolism. Biochem J. 435(1):285-296

Wang Z, Zou Z, Li Q (2022). Nicotinic acid supplementation contributes to the amelioration of Alzheimer's disease in mouse models. Ann Transl Med.10(19):1049

Wassef M, Sotelo C, Cholley B, Brehier A, Thomasset M (1987). Cerebellar mutations affecting the postnatal survival of Purkinje cells in the mouse disclose a longitudinal pattern of differentially sensitive cells. Dev Biol. 124(2):379-89

Wassef M, Sotelo C, Thomasset M, Granholm AC, Leclerc N, Rafrafi J, Hawkes R (1990). Expression of compartmentation antigen zebrin I in cerebellar transplants. J Comp Neurol. 294(2):223-34

Webb JL, Ravikumar B, Atkins J, Skepper JN, Rubinsztein DC (2003). Alpha-Synuclein is degraded by both autophagy and the proteasome. J Biol Chem. 278(27):25009-25013

Wells C, Brennan SE, Keon M, Saksena NK (2019). Prionoid proteins in the pathogenesis of neurodegenerative diseases. Front. Mol. Neurosci. 12:271

White E, Mehnert JM, Chan CS (2017). Autophagy, Metabolism, and Cancer. Cold Spring Harb Symp Quant Biol.

White JJ, Sillitoe RV (2013). Development of the cerebellum: from gene expression patterns to circuit maps. Wiley Interdiscip Rev Dev Biol. 2(1):149-164

Winkler EA, Nishida Y, Sagare AP, Rege SV, Bell RD, Perlmutter D, Sengillo JD, Hillman S, Kong P, Nelson AR, Sullivan JS, Zhao Z, Meiselman HJ, Wendy RB, Soto J, Abel ED, Makshanoff J, Zuniga E, De Vivo DC, Zlokovic BV (2015). GLUT1 reductions exacerbate Alzheimer's disease vasculo-neuronal dysfunction and degeneration. Nat Neurosci. 18(4):521-530

Winslow AR, Chen CW, Corrochano S, Acevedo-Arozena A, Gordon DE, Peden AA, Lichtenberg M, Menzies FM, Ravikumar B, Imarisio S, Brown S, O'Kane CJ, Rubinsztein DC (2010). α-Synuclein impairs macroautophagy: implications for Parkinson's disease. J Cell Biol. 190(6):1023-1037

Witter L, De Zeeuw CI (2015). Regional functionality of the cerebellum. Curr Opin Neurobiol. 33:150-155

Wong JMT, Malec PA, Mabrouk OS, Ro J, Dus M, Kennedy RT. (2016) Benzoyl chloride derivatization with liquid chromatography–mass spectrometry for targeted metabolomics of neurochemicals in biological samples. J Chromatogr A 1446:78-90

Wong YC, Holzbaur EL (2015). Optineurin is an autophagy receptor for damaged mitochondria in parkin-mediated mitophagy that is disrupted by an ALS-linked mutation. Proc Natl Acad Sci U S A. 111(42):E4439-E4448

Wu HQ, Sha JJ, Wang HQ, Ren B, Zhang GL, Li M (2010). Expression of GLUT 3 in different brain regions of aged rats. Zhejiang Da Xue Xue Bao Yi Xue Ban. 39(1):43-48

Wu L, Zhang X, Zhao L (2018). Human ApoE Isoforms Differentially Modulate Brain Glucose and Ketone Body Metabolism: Implications for Alzheimer's Disease Risk Reduction and Early Intervention. J Neurosci. 38(30):6665-6681

Wu SZ, Bodles AM, Porter MM, Griffin WS, Basile AS, Barger SW (2004). Induction of serine racemase expression and D-serine release from microglia by amyloid beta-peptide. J Neuroinflammation. 1(1):2

Wu Y, Whiteus C, Xu CS, Hayworth KJ, Weinberg RJ, Hess HF, De Camilli P (2017). Contacts between the endoplasmic reticulum and other membranes in neurons. Proc Natl Acad Sci U S A. 114(24):E4859-E4867

Wuehr M, Schniepp R, Ilmberger J, Brandt T, Jahn K (2013) Speed-dependent temporospatial gait variability and long-range correlations in cerebellar ataxia. Gait Posture. 37:214–218

Xiang H, Lu Y, Shao M, Wu T (2020). Lysophosphatidic Acid Receptors: Biochemical and Clinical Implications in Different Diseases. J Cancer. 11(12):3519-3535

Yamamoto Y, Hosoda K, Imahori T, Tanaka J, Matsuo K, Nakai T, Irino Y, Shinohara M, Sato N, Sasayama T, Tanaka K, Nagashima H, Kohta M, Kohmura E (2018). Pentose phosphate pathway activation via HSP27 phosphorylation by ATM kinase: A putative endogenous antioxidant defense mechanism during cerebral ischemia-reperfusion. Brain Res. 1687:82-94

Ye X, Fukushima N, Kingsbury MA, Chun J (2002). Lysophosphatidic acid in neural signaling. Neuroreport. 13(17):2169-75

Yorimitsu T, Klionsky DJ (2005). Autophagy: molecular machinery for self-eating. Cell Death Differ.12 (Suppl 2):1542-52

Yoshii SR, Kuma A, Akashi T, Hara T, Yamamoto A, Kurikawa Y, Itakura E, Tsukamoto S, Shitara H, Eishi Y, Mizushima N (2016). Systemic Analysis of Atg5-Null Mice Rescued from Neonatal Lethality by Transgenic ATG5 Expression in Neurons. Dev Cell. 39(1):116-130

Yu WH, Cuervo AM, Kumar A, Peterhoff CM, Schmidt SD, Lee JH, Mohan PS, Mercken M, Farmery MR, Tjernberg LO, Jiang Y, Duff K, Uchiyama Y, Näslund J, Mathews PM, Cataldo AM, Nixon RA (2005). Macroautophagy--a novel Beta-amyloid peptide-generating pathway activated in Alzheimer's disease. J Cell Biol. 171(1):87-98

Yung YC, Stoddard NC. Chun J (2014). LPA receptor signaling: pharmacology, physiology, and pathophysiology. J. Lipid Res. 55:1192–1214

Zahedi RP, Sickmann A, Boehm AM, Winkler C, Zufall N, Schönfisch B, Guiard B, Pfanner N, Meisinger C (2006). Proteomic analysis of the yeast mitochondrial outer membrane reveals accumulation of a subclass of preproteins. Mol Biol Cell. 17(3):1436-1450

Zavodszky E, Seaman MN, Moreau K, Jimenez-Sanchez M, Breusegem SY, Harbour ME, Rubinsztein DC (2014). Mutation in VPS35 associated with Parkinson's disease impairs WASH complex association and inhibits autophagy. Nat Commun. 5:3828

Zhang J, Ney PA (2009). Role of BNIP3 and NIX in cell death, autophagy, and mitophagy. Cell Death Differ. 16(7):939-946

Zhang S, Hulver MW, McMillan RP, Cline MA, Gilbert ER (2014). The pivotal role of pyruvate dehydrogenase kinases in metabolic flexibility. Nutr Metab (Lond). 11(1):10

Zhang S, Lachance BB, Mattson MP, Jia X (2021). Glucose metabolic crosstalk and regulation in brain function and diseases. Prog Neurobiol. 204:102089

Zhang Y, Chen K, Sloan SA, Bennett ML, Scholze AR, O'Keeffe S, Phatnani HP, Guarnieri P, Caneda C, Ruderisch N, Deng S, Liddelow SA, Zhang C, Daneman R, Maniatis T, Barres BA, Wu JQ (2014). An RNA-sequencing transcriptome and splicing database of glia, neurons, and vascular cells of the cerebral cortex. J Neurosci. 34:11929–11947

Zhao L, Spassieva SD, Jucius TJ, Shultz LD, Shick HE, Macklin WB, Hannun YA, Obeid LM, Ackerman SL (2011). A deficiency of ceramide biosynthesis causes cerebellar purkinje cell neurodegeneration and lipofuscin accumulation. PLoS Genet. 7(5):e1002063

Zimprich A, Benet-Pagès A, Struhal W, Graf E, Eck SH, Offman MN, Haubenberger D, Spielberger S, Schulte EC, Lichtner P, Rossle SC, Klopp N, Wolf E, Seppi K, Pirker W, Presslauer S, Mollenhauer B, Katzenschlager R, Foki T, Hotzy C, Reinthaler E, Harutyunyan A, Kralovics R, Peters A, Zimprich F, Brücke T, Poewe W, Auff E, Trenkwalder C, Rost B, Ransmayr G, Winkelmann J, Meitinger T, Strom TM (2011). A mutation in VPS35, encoding a subunit of the retromer complex, causes late-onset Parkinson disease. Am J Hum Genet. 89(1):168-175

Zlokovic BV (1995). Cerebrovascular permeability to peptides: manipulations of transport systems at the blood-brain barrier. Pharm Res. 12(10):1395-1406

Zlokovic BV (2008). The blood-brain barrier in health and chronic neurodegenerative disorders. Neuron. 57(2):178-201

IX. Acknowledgements

First, I would like to thank Prof. Natalia Kononenko for giving me the opportunitiy to perfom my PhD thesis in her group. Her supervision, scientific input and advice helped me throughout my project.

Additionally, I would like to thank my TAC committee members Prof. Dr. Elena Rugarli and Prof. Dr. Matteo Bergami for their scientific input and helpful feedback. I also want to thank my thesis committee Prof. Dr. Ansgar Büschges and Prof. Dr. Jan Riemer. Additionally, I want to thank my RTG-NCA coordinator Dr. Katerina Vlantis and Kathy Joergens for all their support. Furthermore, I would like to thank my collaborators Prof. Dr. Graziana Gatto, Prof. Dr. Christian Frezza, Dr. Patrick Giavalisco and Dr. Heike Endepols.

I am thankful for all the help and support from Kononenko lab members. I want to thank especially Marianna, Lotte and Ebru for their friendship and lots of joyful moments.

Furthermore, I want to express my gratitude for the constant support and love of my family and friends. And finally, I want to thank my husband for all his love, support and patience!

X. Declaration/ Erklärung

Erklärung zur Dissertation

gemäß der Promotionsordnung vom 12. März 2020

Diese Erklärung muss in der Dissertation enthalten sein.

(This version must be included in the doctoral thesis)

„Hiermit versichere ich an Eides statt, dass ich die vorliegende Dissertation selbstständig und ohne die Benutzung anderer als der angegebenen Hilfsmittel und Literatur angefertigt habe. Alle Stellen, die wörtlich oder sinngemäß aus veröffentlichten und nicht veröffentlichten Werken dem Wortlaut oder dem Sinn nach entnommen wurden, sind als solche kenntlich gemacht. Ich versichere an Eides statt, dass diese Dissertation noch keiner anderen Fakultät oder Universität zur Prüfung vorgelegen hat; dass sie - abgesehen von unten angegebenen Teilpublikationen und eingebundenen Artikeln und Manuskripten - noch nicht veröffentlicht worden ist sowie, dass ich eine Veröffentlichung der Dissertation vor Abschluss der Promotion nicht ohne Genehmigung des Promotionsausschusses vornehmen werde. Die Bestimmungen dieser Ordnung sind mir bekannt. Darüber hinaus erkläre ich hiermit, dass ich die Ordnung zur Sicherung guter wissenschaftlicher Praxis und zum Umgang mit wissenschaftlichem Fehlverhalten der Universität zu Köln gelesen und sie bei der Durchführung der Dissertation zugrundeliegenden Arbeiten und der schriftlich verfassten Dissertation beachtet habe und verpflichte mich hiermit, die dort genannten Vorgaben bei allen wissenschaftlichen Tätigkeiten zu beachten und umzusetzen. Ich versichere, dass die eingereichte elektronische Fassung der eingereichten Druckfassung vollständig entspricht."

Teilpublikationen:

Datum, Name und Unterschrift

Köln, 12.12.23